Ultracold molecules in optical arrays: from laser cooling to molecular collisions

a dissertation presented
by
Loïc G. Anderegg

to
The Department of Physics
in partial fulfillment of the requirements
for the degree of
Doctor of Philosophy
in the subject of
Physics

Harvard University
Cambridge, Massachusetts
September 2019

Ultracold molecules in optical arrays: from laser cooling to molecular collisions

Abstract

Potential wide-ranging scientific applications, spanning fundamental physics to quantum engineering, has led to significant efforts in controlling molecules at the quantum level. The rich internal structure of molecules, that gives rise to these desirable properties also complicates the task of controlling such species. Over the past decade, our ability to produce, control, and detect molecules has advanced tremendously with direct laser-cooling and magneto-optical trapping of diatomic molecules realized by several groups around the world.

In this thesis, we describe the creation of the first RF MOT of CaF, which at the time of the writing of this thesis, remains the largest and densest molecular MOT. New laser cooling techniques for molecules are demonstrated, allowing laser cooling of molecules to 4 μK, 50 times colder than the Doppler limit. Optical trapping of these molecules is also achieved, which, in combination with in-trap laser cooling increased the density of trapped molecules by five orders of magnitude compared to the density in the MOT. We developed methods to cool and detect single molecules with high fidelity, which aided us in the creation of an optical tweezer array of single, ultracold CaF molecules. The densities of molecules (10^{12} cm^{-3}) attained inside the tweezer traps also enabled us to observe both light-assisted and ground state collisions of laser cooled molecules, for the first time. The phase space density within the merged tweezers reached 5×10^{-4}, 10 orders of magnitude larger than the initial MOT. We implemented internal quantum state control of the molecules and dynamical control of the tweezers to build a platform for exploring state-selective ultracold quantum chemistry.

Contents

To my parents.

Citations to Previously Published Work

Parts of this dissertation have been previously reported in the following papers.

1. L. Anderegg, L. Cheuk, Y. Bao, S. Burchesky, K.K. Ni, W. Ketterle, J. M. Doyle "An optical tweezer array of ultracold molecules" *Science*, **365**, 6458, (2019).

2. L. Anderegg, B. Augenbraun, Y. Bao, S. Burchesky, L. Cheuk, W. Ketterle, J. M. Doyle "Laser Cooling of Optically Trapped Molecules" *Nature Physics*, **14**, 890-893 (2018).

3. L. Cheuk, L. Anderegg, B. Augenbraun, Y. Bao, S. Burchesky, W. Ketterle, J. M. Doyle "Λ-Enhanced Imaging of Molecules in an Optical Trap" *Physical Review Letters*, **121**, 8 (2018).

4. L. Anderegg, B. Augenbraun, E. Chae, B. Hemmerling, N. Hutzler, A. Ravi, A. Collopy, J. Ye, W. Ketterle, J. M. Doyle "Radio Frequency Magneto-Optical Trapping of CaF with High Density" *Physical Review Letters*, **119**, 10 (2017).

5. E. Chae, L. Anderegg, B. Augenbraun, A. Ravi, B. Hemmerling, N. Hutzler, A. Collopy, J. Ye, W. Ketterle, J. M. Doyle "One-Dimensional Magneto-Optical Compression of a Cold CaF Molecular Beam" *New Journal of Physics*, **19**, 3 (2017).

6. B. Hemmerling, E. Chae, A. Ravi, L. Anderegg, G. Drayna, N. Hutzler, A. Collopy, J. Ye, W. Ketterle, J. M. Doyle "Laser Slowing of CaF Molecules to Near the Capture Velocity of a Molecular MOT" *Journal of Physics B*, **49**, 17 (2016).

Acknowledgments

I would like to thank first and foremost my advisor, John Doyle, for his guidance and mentorship. From technical tips to an insightful vision of future directions, John's leadership led to our experimental successes. He, somehow, always ensured that we had the funding required to keep the experiment moving forward. I have also benefited greatly from his love of great food and good coffee. Wolfgang Ketterle was a second advisor to me. From the beginning he came to weekly meetings providing both insightful explanations to the fundamental physics and ideas to help solve our technical problems. Additionally, I would like to thank Kang-Kuen Ni for her help with the optical tweezers. I would also like to thank Markus Greiner and Susanne Yelin for being on my thesis committee.

I would like the thank the entire laser cooling team which has evolved over the years. First, to the initial team of Eunmi, Boerge, Garret, and Aakash, who took me in as a new grad student who knew little about atomic physics. A special thanks to Eunmi for teaching me everything there was to know about the experiment, and Boegre, for the long hours spent early on fixing and debugging the dye lasers. Ben, for explaining nearly all of molecular theory to me, and for all of the hard work and long hours spent before we finally got the MOT working. Lawrence, for all his technical knowledge. He

helped transition the experiment into the reliable system it is today. To the newest team of Yicheng, for his willingness to fix everything, and to Sean, and Scarlett, I know the experiment falls in good hands. Finally, thanks to Louis and Ivan, whose experimental proximity made them essentially a part of the experiment, leading to many insightful discussions. I would also like to thank the rest of the members of the Doyle group, who over the years, made the lab a fun environment.

But it was not only the members of the Doyle group which made this work possible. The many staff and contractors at Harvard also played an instrumental role in allowing for experimental progress. I would like to thank Jim MacArthur for all of the electronics help, tips and humorous conversations, Steve for keeping the waterjet operational and running the machine shop with Stan. I would also like to thank Michele Waters and her crew, who on numerous occasion, would put everything down to fix a broken electrical breaker within minutes. Thank you to Lisa Cacciabaudo for dealing with all the paperwork I ever needed and Adam Ackerman and Silke Exner for dealing with all the financial matters. I would like to thank the entire CUA community for the insightful discussions, especially the Greiner group, which allowed us to borrow way more lasers and optics than we could ever afford.

I would also like to thank all the friends I have made from the incoming graduate class of 2014, which have made the past five years truly fun. Finally, to all of those who have guided me over the years. My undergraduate advisor, Holger Müller, without whom, I would not be in AMO today. I am grateful to my parents for their lifelong encouragement. Finally, and most importantly, I would like to thank Urmila for her support and keeping me sane throughout my PhD. The rainbow amoebas would not exist without her.

1

Introduction

Laser cooling of atoms [1] has led to a huge breadth of research and technological applications. As the temperatures of atoms decreased, not only did the precision of spectroscopy increase, but so did the range of applications. From ultra-precise atomic clocks[2] to quantum simulations of condensed matter systems [3], cold atoms have been indispensable. Atoms are relatively simple to cool and manipulate, and weak long-range interactions make them ideal for metrology applications. Molecules, by contrast, have new complexities for cooling and manipulation, with interesting internal structure, strong long-range interactions, and controllable states not found in atoms. This
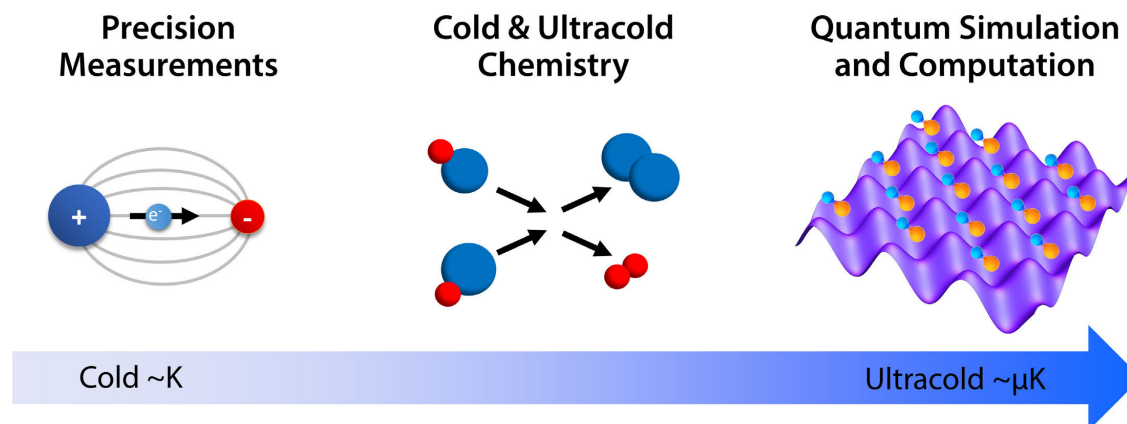
Figure 1.1.1: Applications of cold molecules over a wide span of temperatures.

additional complexity of molecules, which make up most of the world around us, is required for chemistry and the study of quantum many-body physics.

1.1 Why Cold Molecules

Moving from atoms to molecules adds increased complexity, which, while complicating the control of internal and external quantum states, allows them to be used for far reaching applications [4–8] and presents new fundamental scientific questions. From quantum simulation [9–11] and computation [12–17], to ultracold chemistry [18, 19], and precision measurements [5, 20], the field of ultracold molecules is rapidly expanding. These applications arise from the rich internal structure of molecules, most obviously rotational and vibrational modes, and tunable long-range and anisotropic dipolar interactions. But there are others, including bending modes and closely spaced opposite parity levels arising from orbital angular momentum along the internuclear axis. However, controlling molecules remains an experimental challenge despite major recent progress in cooling and trapping.

1.1.1 COLD AND ULTRACOLD COLLISIONS AND CHEMISTRY

What happens when two molecules collide[21], both generically and in specific systems, amazingly remains only poorly answered [19]. For example, various theories indicate the presence of long-lived complexes, so called "sticky collisions"[22], but how this happens, how generic it is, and how it can be controlled, is still frontier work. To make progress one would like to cool molecules down to a single quantum state, so that one can control the inputs to a collisional system in order to gain a better understating of the fundamental processes occurring, e.g. clustering, chemical reactions, resonant states, etc. At ultracold temperatures, quantum effects in ultracold chemistry can also be explored with exquisite control. An interesting goal is to control chemical reactions, with single quantum state preparation and detection of the input and output product states[19]. By controlling the external fields applied on molecules[23], one can try to enhance or suppress various reactions[24]. In doing so, one might modify the collisional proprieties of molecule-molecule[25, 26] and atom molecules collisions. Such studies are not only important for their fundamental interest, they also are key to mastering sympathetic[27] and evaporative cooling, which are routinely used to produce degenerate gases of atoms. The study of these molecular interactions will hopefully lead to a better understanding of not just the fundamental physics occurring but also shed light on the cold and ultracold chemistry occurring within interstellar space.

1.1.2 QUANTUM SIMULATION AND QUANTUM INFORMATION

Due to their long range and tunable interactions, ultracold polar molecules have been proposed to simulate a whole host of Hamiltonians[4, 28, 29]. $^2\Sigma$ molecules, such as CaF, with an unpaired electron spin are predicted to allow for the realization of lattice spin models [9], quantum magnetism [30], dipolar crystals, phase transitions [10, 11, 31–34], and the onset of topologically ordered states [35–37]. The long lifetimes of molecules also allow them to be used a qubits with

long coherence times, orders of magnitude longer than the best solid state systems. Their internal structure are ideal for encoding of quantum bits to these states. One of the long standing goals in quantum information engineering is realizing universal fault tolerant computing. This requires developing a platform where the gate fidelities are sufficiently high. Theoretical work has shown the molecules may be a candidate for such qubits [12–16, 38, 39], with gate error rates as low as 10^{-5}, which is below the threshold for error correction [40]. Molecules have long coherence times and strong coupling allowing for a large number of potential gate operations. Realizing either quantum simulation or computation requires a clean, scalable platform whereby one can trap, manipulate, and image the molecules. Arrays of optical tweezers, which bypass the high phase space necessity of typical optical lattices, are a promising platform[41–43].

1.1.3   PRECISION MEASUREMENTS

Molecules are useful in precision measurements due to the presence of several kinds of nearly degenerate states, which lead to enhanced sensitivities to perturbations [44, 45]. They have been used to search for the electron dipole moments[46–49], which set limits on the Standard Model beyond the energy reach as the LHC[50] for generic CP violating new physics. Polyatomic molecules have recently been proposed to extend these searches to even higher energies near the PeV range [51]. It should be noted that a class of polyatomic molecules can be cooled and controlled with the techniques discussed in this thesis. Molecules can also be used to search for time variation of fundamental constants [52] and the proton-to-electron mass ratio [53, 54]. Remarkably, no precision measurement done with molecules to date has utilized laser cooling, yet they already set many of the most precise limits. If laser cooling can be implemented into precision experiments, huge gains in sensitivities are possible [51, 55].
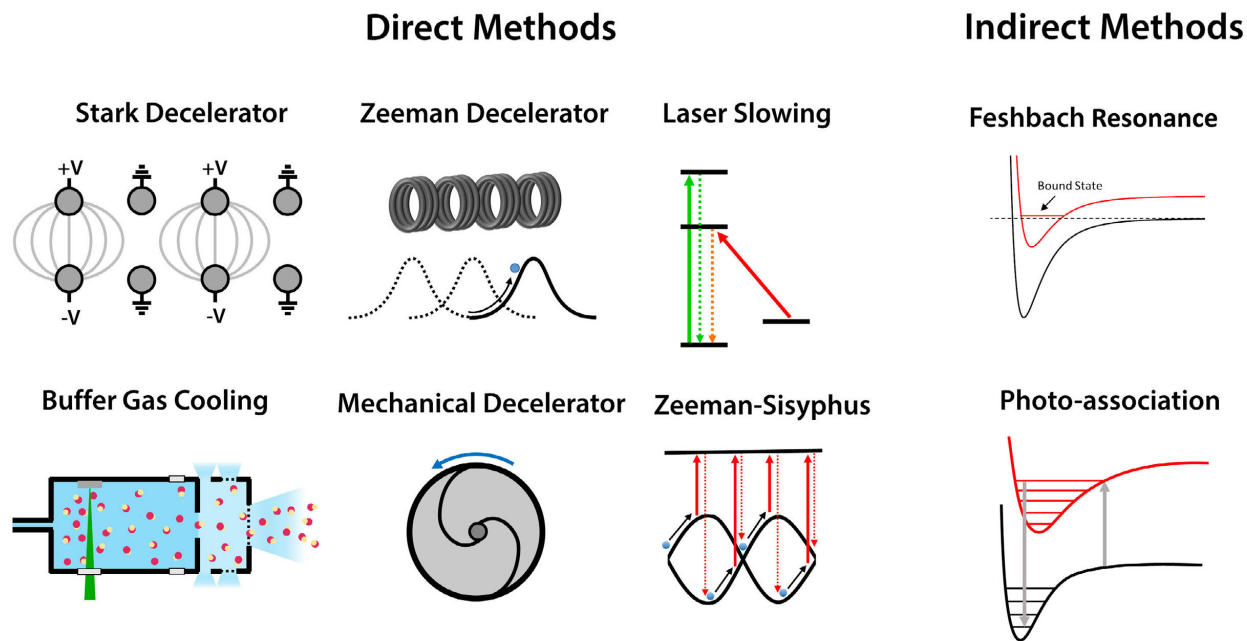
Figure 1.2.1: Methods of creating and slowing molecules.

1.2 Production of Ultracold Molecules

Unfortunately, the qualitatively different level of complexity of molecules comes at a cost to the experimentalist. Even the first, most prosaic step, the producing of gases of molecules is challenging. Atoms may be produced in a single quantum state by simply heating up a sample, but the same is not the case for molecules. At high temperatures, the thermal distribution places molecules in thousands of rotational and vibration states. The challenge is thus to produce high fluxes of molecules (typical reactive radicals) in a single quantum state. There are many approaches to this problem, which can be split into two categories; direct cooling, where one starts with molecules at high temperature and cools them down to ultracold temperatures, and indirect, where molecules are assembled from ultracold atoms. The end goal is to produce samples with high phase space density, defined as [5] $\Omega = n \left(\frac{h}{\sqrt{2\pi m k_b T}} \right)^3$ where Bose-Einstein condensation occurs at $\Omega = 2.612$.

1.2.1   INDIRECT COOLING METHODS

Indirect cooling refers the process of cooling two atomic species down, and then assembling them into a molecule. This method allows one to create molecules that may not be amenable to laser cooling, at the cost of requiring the products be laser coolable. There are two general methods of assembling such molecules, photo-association and magneto-association via Feshbach resonances.

FESHBACH RESONANCE

The pioneering work of the JILA KRb experiment[56] was the first experiment to produce ground state molecules. By tuning a magnetic field to a Feshbach resonance, one can create a weakly bound molecular state, called a Feshbach molecule. These very weakly bound molecules can then be transferred to the ground state with stimulated adiabatic passage, or STIRAP. The first generation KRb experiment was able to produce molecules at 350 nK with a density of 10^{12} cm^{-3} in this fashion[56], and recent results indicate quantum degeneracy[57]. Many experiments around the world now create molecules in this way, with ground state NaK[58], RbCs[59], NaRb[60], and LiNa[61] having been successfully produced in deeply bound molecular states. While this technique has had great success, production is limited to molecules from species that have each been laser cooled to near degeneracy. This method also requires Feshbach resonances that are experimentally accessible.

PHOTO-ASSOCIATION

Molecules can also be produced via photo-association[62] of atoms relying on light to excite two atoms to a molecular bound state. This excited molecular state can then decay into either a bound molecular state, or back into the constituent atoms. Typically, the excited molecular state can decay into a whole host of rovibrational states, limiting the efficiency of this process. Like producing Feshbach molecules, this requires the two constituent atoms to be laser cooled first.

1.2.2 Direct Cooling Methods

Direct cooling of molecules involves first producing the species of interest at an elevated temperature, and then cooling it down towards the ultracold regime. One of they key advantages of this approach is that the molecules can be cooled even after they are produced, which is a critical feature, as most technical noise found in experiments lead to heating.

Buffer Gas Cooling

Buffer gas cooling is a versatile cooling[4, 63] method which relies on elastic collisions with a cryogenic noble gas, such as He or Ne. The cryogenic gas cools both the external and internal degrees of freedom of the molecule, and works on an immense variety of molecules, even very large ones. The target species can be loaded into a buffer gas cell through a variety of methods ranging from laser ablation to oven sources. Cryogenic molecular beams can be created with the use of a cryogenic buffer gas beam source, where a hole inside of a cryogenic cell allows the cooled species of interest be extracted, typically hydrodynamically[64]. This cooling method, in combination with laser ablation, can produces slow bright molecular beams with fluxes over 10^{12}/Sr/pulse in a single quantum state. While this method is typically limited to about one Kelvin, it provides an excellent starting point for further cooling and deceleration methods.

Stark and Zeeman Deceleration

Stark deceleration is based on the principle that the energy levels of a polar molecule in an electric field will be shifted into both high-field and low-field seeking states due to it's electric dipole moment[65, 66]. With the proper application of large electric fields as a function of time, a moving molecule can be made to always see a potential hill it must climb. As a result, the molecule will lose energy as it climbs this potential and be decelerated. The same technique can be done by applying

a magnetic field and relying on the magnetic moment of a molecules to shift the energy levels in a large magnetic field [67]. A variant of this type of cooling is Zeeman-Sisyphus cooling [68] (similar to "optical loading" [69]), which relies on a static magnetic field and the right optical pumping to keep the molecules always climbing up a potential hill.

Mechanical Deceleration

Molecules can also be slowed by simply relying on mechanical forces. Using a centrifuge, molecules injected into this decelerator must loose energy proportionally to the centrifugal energy experienced at the edge of the decelerator [70, 71]. Molecules are electrostatically guided against this potential and lose an amount of energy proportional to the rotational speed. While an engineering challenge, this type of deceleration works for any molecule that can be electrostatically guided.

Other Methods

There are other cooling methods that exist for molecules [72, 73]. Optoelectrical cooling [74] operates via a Sisyphus like cooling effect within an electrostatic trap when pumped from a state with a large stark shift in a low field region and pumped back to a state with a small stark shift in a high field region. As the molecules traverse from the low field to the high field region, they lose kinetic energy and are cooled. Other various methods have also been demonstrated or proposed, such as crossed beam cooling [75], and sympathetic cooling with a laser cooled species [76].

Laser Cooling

Since its conception in 1975 [77, 78], and experimental demonstration in 1978 [79, 80], laser cooling and trapping of atoms as become a vital part of modern AMO experiments [1]. This idea of using the momentum of photons in laser light to apply forces on atoms has allow atoms to be cooled down all the way to a Bose–Einstein condensate [81–83]. With the huge success of laser cooling atoms,

we can apply the same techniques to molecules. Of course, the added complication of additional vibrational and rotational states may seem to be an issue at first glance, but with the correct selection of electronic transitions and right class of molecule, laser cooling becomes not only possible, but immensely successful.

In the seminal paper by Di Rosa in 2004[84], a class of molecules was proposed to be laser coolable due to their electronic structure. These molecules have highly diagonal Frank-Condon factors (decays remain in the inital vibrational state), strong transitions, and no intermediate states below the target excited state, making laser cooling possible. It was further shown that selecting the correct rotational states such that cycling occurs between the N=1 ground state and N=0 excited state, would alleviated the need of rotational repumping due to parity and angular momentum selection rules of $\Delta N = 0, +1$ [85].

Experimental progress followed shortly after. The DeMille group demonstrate the first optical deflection and laser cooling of a SrF beam [86]. 1D and 2D magneto-optical compression were demonstrated in YO [87] and later CaF (Chapter 4 of this thesis) [88]. Laser slowing has been demonstrated for SrF[89], CaF (Chapter 3 of this thesis)[90, 91], and YO. Laser cooling has even been extended to polyatomic species, with SrOH being laser cooled to sub-Doppler temperatures in one dimension [92]. Magneto-optical trapping of molecules was first demonstrated with SrF at Yale[93–96], and then with CaF both at Imperial and here at Harvard (Chapter 5 of this thesis) [97–99], as well as recently with YO at JILA [100]. Just like in atomic experiments, a MOT represents a good starting point for further experiments as it provides as source of a large number of cold, high density molecules.

1.2.3 CONSERVATIVE TRAPS

For many applications of ultracold atoms and molecules, trapping in a conservative trap is necessary. It provides long lifetimes and can to some extent preserve internal state properties. A MOT, on

the contrary, relies on constant photon scattering for molecules to remain confined, limiting the achievable density due to light assisted collisions and the molecular temperature due to the recoil of photons.

Conservative traps in ultracold atom experiments are typically formed from either magnetic or optical fields. Magnetic traps rely on producing a magnetic field minimum and placing particles in low field seeking states. The significant advantages of magnetic traps are large volumes and high trap depths, which open up the possibility of further evaporation or sympathetic cooling. The disadvantage is that DC magnetic traps require trapping of higher energy magnetic states that are unstable to collisions. Magnetic trapping of molecules was first demonstrated with CaH in 1998[101], and recently with laser cooled SrF and CaF[102, 103].

Optical traps rely on the AC Stark shift caused by far detuned light. The light is red detuned such that the ground state energy of the target particles is shifted downwards causing an intensity maxima corresponding to a potential minima. (Note: Optical traps may also operate blue detuned, such that the particle is attracted to an intensity minimum and confined with a doughnut shaped trap.) Despite the much smaller trap volumes and lower trap depths of optical traps, they can be used to trap molecules regardless of their internal state [104]. This can allow for laser cooling and trapping of the absolute ground state.

Microwave traps for molecules have also been proposed[105–107]. These traps can trap the strong field seeking absolute ground state of molecules.

1.3 Platforms for Quantum Simulation

Feynman first proposed the idea of quantum simulation [108] whereby one can study one complex quantum system with another well understood quantum system. Trapped ions [109–111], superconducting circuits [112] and neutral atoms [113–115] have all been used for quantum simulation.
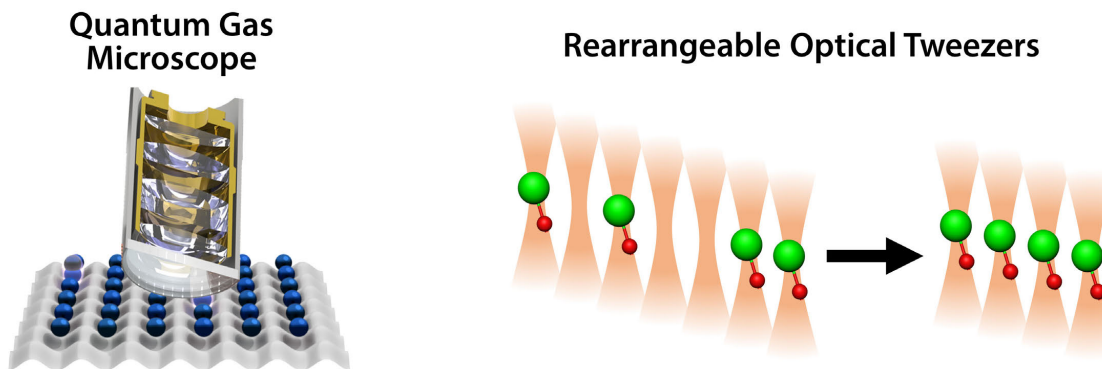
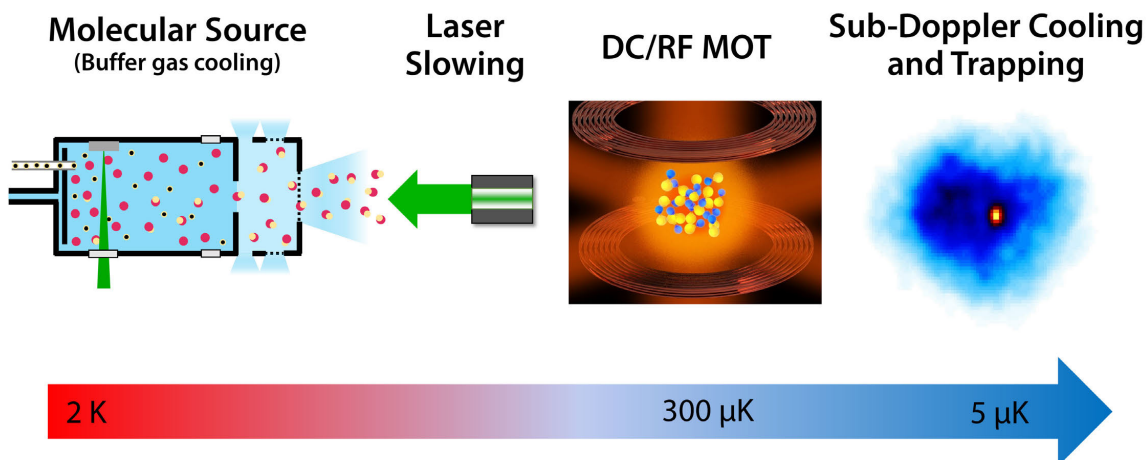**Figure 1.3.1:** Platforms for quantum simulation with atoms and molecules.

Ultracold atoms and molecules have the unique ability to be exquisitely controlled at the quantum level. This makes them ideal candidates as a quantum system that can be used to simulate another more complicated system.

1.3.1 QUANTUM GAS MICROSCOPES

A powerful experimental platform to employ atoms as quantum simulators[113, 114] is the quantum gas microscope[116]. In a quantum gas microscope, atoms are loaded into an optical lattice and imaged with single site resolution. This allows one to study the single particle dynamics in quantum many body systems which would otherwise be impossible in a solid-state system. By tuning the interactions of the particles, one can simulate a wide variety of Hamiltonians.

1.3.2 TWEEZER ARRAYS

Unfortunately, quantum gas microscopes typically require deeply degenerate gasses to have sufficiently filled lattices. A powerful approach that bypasses this requirement are rearrangeable optical tweezer arrays [41, 42] which rely on light assisted collisions[117–121] to ensure single parti-

Molecular Source
(Buffer gas cooling)

Laser Slowing

DC/RF MOT

Sub-Doppler Cooling and Trapping

2 K   300 μK   5 μK

Figure 1.4.1: Overview of the experiential sequence.

cal loading. For molecules, this bottom-up approach of using tweezer arrays combined with laser-cooling is especially important because it bypasses the need for high phase space density samples, which has been a long-standing experimental challenge. Furthermore, this generic approach does not rely on favorable collisional properties necessary for evaporative cooling, and can thus be extended to many other molecular species, including polyatomic ones [51].

1.4   THIS THESIS

In this thesis, we will discuss the production, cooling, trapping and collisional studies with CaF. Chapter 2 will begin with an introduction to molecular theory, laser cooling of molecules, and specifically discuss the relevant properties of CaF. Chapter 3 will discuss production and buffer gas cooling of CaF in our cryogenic molecular source. Laser slowing of the molecular beam is discussed in Chapter 4. Chapter 5 discusses magneto-optical trapping of CaF. Chapter 6 will describe cooling CaF to sub-Doppler temperatures and optical trapping. Chapter 7 will cover the creation of an optical tweezer array, and Chapter 8 will discuss improvements and use this new platform to

study collisions. Finally, in Chapter 9 we will give an outlook of future experiments and discuss a next generation molecular tweezer apparatus.

A diatomic molecule is a molecule with one atom too many.

Arthur Shawlow

2

Laser Cooling Molecules: Theory

In order to laser cool molecules[84], we first need to understand the structure of molecules and the influence of external fields on them. Diatomic molecules have to two additional degrees of freedom that atoms do not possess, vibration and rotation, which are responsible for a molecule's more complex structure compared to atoms. The energy scales of these degrees of freedom are generally well separated, with electronic energy level spacings of 100's of THz, vibration levels at the THz level, and rotational at the 10's of GHz level. This separation in the scale of energy levels allows for
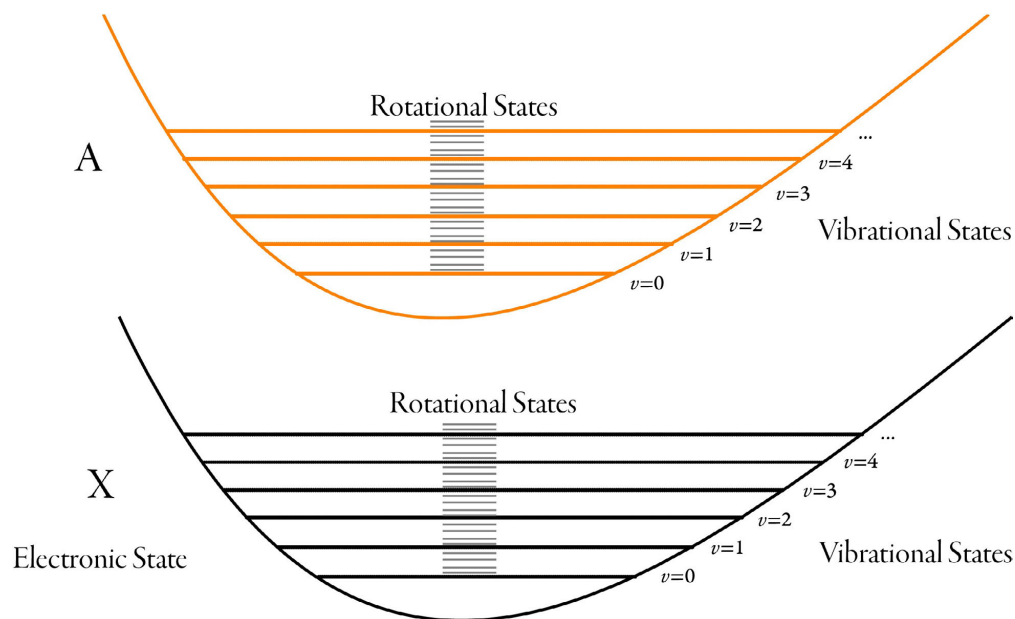
Figure 2.0.1: The energy potential of a diatomic molecule, illustrating the electronic, vibrational and rotational structure.

accurate approximations in characterizing the molecular Hamiltonian.

2.1   Molecular Structure of Diatomics

2.1.1   Born Oppenheimer Approximation

In order to characterize molecular wavefunctions, the Born Oppenheimer approximation is very often applicable. The motion of the nucleus and electrons are treated separately due to large mass difference between them - the nucleus is treated as fixed.

$$|\psi_{molecule}\rangle = |\psi_{electronic}\rangle |\psi_{nuclear}\rangle \tag{2.1}$$

The Hamiltonian for a diatomic molecule can be written in this approximation as a sum

$$H \approx H_{electronic} + H_{vibrational} + H_{rotational} \tag{2.2}$$

A more complete effective Hamiltonian can be found in [122], with the spin-orbit coupling, spin-spin coupling, spin-rotation coupling, centrifugal distortion, Λ doubling, magnetic hyperfine interactions, and other higher order perturbative effects.

2.1.2 QUANTUM NUMBERS

Molecules are described by various quantum numbers. Depending on the relative energy scales of interactions within a molecule, not all quantum numbers remain good quantum numbers. The following table lists the quantum numbers which are relevant in describing our system in this thesis.

Quantum Numbers	Symbol	
Vibration	v	
Electronic Orbital Angular Momentum	**L**	
Rotational Angular Momentum of Nuclei	**R**	
Electronic Spin	**S**	
Nuclear Spin	**I**	
Hunds Case Specific Quantum Numbers	Hunds Case (a)	Hunds Case (b)
Total Angular Momentum	**J=L+S+R**	**J=N+S**
Total Angular Momentum Excluding Electron Spin	Not Valid	**N=L+R**
Total Angular Momentum With Nuclear Spin	**F=J+I**	**F=J+I**
Projection of **L** on internuclear axis	Λ	Λ
Projection of **S** on internuclear axis	Σ	
Projection of **J** on internuclear axis	Ω	

Table 2.1.1: Quantum numbers for diatomic molecules
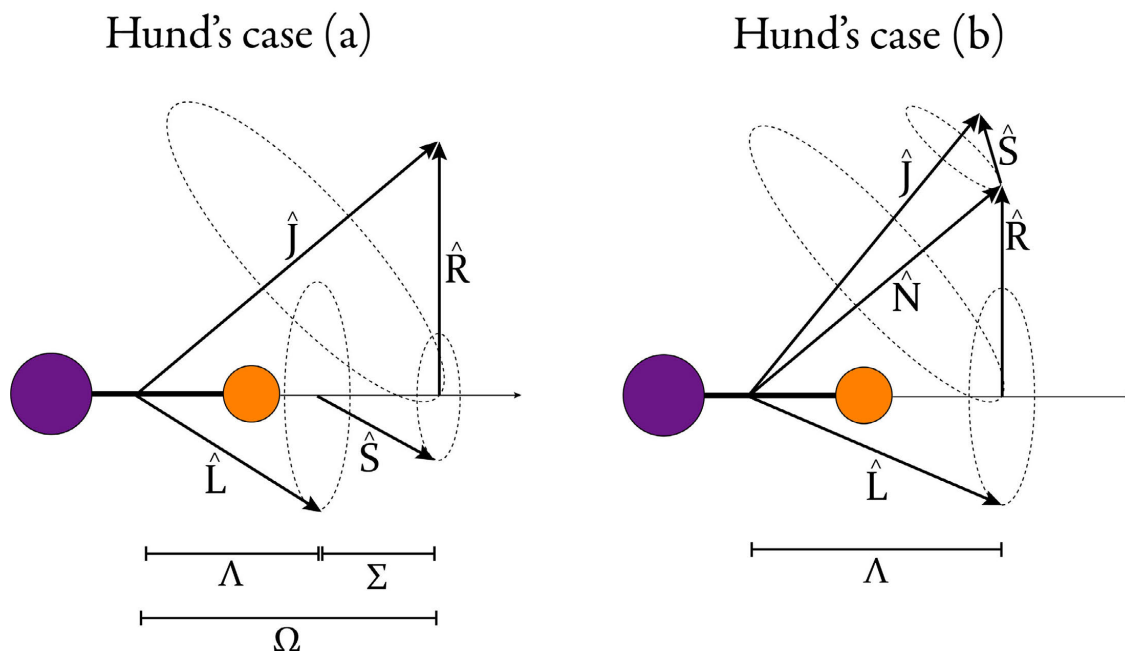
Figure 2.1.1: Hund's cases (a) and (b).

2.1.3 HUND'S CASES

There are various ways in which angular momentum can be coupled in a molecule, the limiting cases of which are called Hund's cases [122]. Here we will only consider Hund's case (a) and (b) (Figure 2.1.1), as all of the relevant levels that we use in CaF fall into one of these two cases. The determining factor that distinguishes these cases is the relative energy spacing of the electronic states, the spin-orbit coupling, and the rotational splitting. Table 2.1.2 shows an overview of which Hund's case is relevant depending on these energies. Note that any molecular state labeled as a Σ, Π, Δ, etc. is written assuming Hund's case (a) or (b), as they are the only cases where Λ is defined. Hund's case (c) molecules have undefined naming due to bad quantum numbers.

Hund's case	Electronic	Spin-Orbit	Rotational	Good Quantum Numbers
(a)	Strong	Intermediate	Weak	$\Lambda, S, \Sigma, J, \Omega$
(b)	Strong	Weak	Intermediate	Λ, N, S, J

Table 2.1.2: Hunds cases relevant to CaF

HUND'S CASE (A)

In Hund's case (a) L is strongly coupled to the internuclear axis. This is due to the electrostatic interactions of the chemical bond, the dominant energy scale, having axial symmetry and causing L to precesses around it [123]. The projection of L on the internuclear axis is called Λ. S is strongly coupled to L due to spin-orbit and its projection on the internuclear axis is called Σ. The sum of Λ and Σ is called Ω. This case describes the CaF A and C states.

HUND'S CASE (B)

In case (b), L is still strongly coupled to the internuclear axis with projection Λ. Due to the weak spin-orbit coupling, L couples to R rather than S to form N=L+R. Physically, this coupling arises from the weak magnetic field generated by the rotation of the molecule [124]. L and N couple to form J=L+N. If a state has $\Lambda = 0$, then there is no spin-orbit interactions, and thus follows case (b). This case describes the CaF X and B states.

2.1.4 LABELING OF MOLECULAR STATES

The typical convention for labeling electronic states of diatomic molecules is for ground states to be labeled as X and the excited states be labeled alphabetically, A,B,C... However, this labeling was done when the states were first discovered, so states may be out of alphabetic order.

Following the labeling structure is the molecular term symbol:

$$2S+1\Lambda_{\Omega,u/g}^{+/-} \tag{2.3}$$

with S displaying the total spin, Λ the orbital angular momentum, Ω the total angular momentum, u/g the parity, and $+/-$ the reflection symmetry through a plane along the nuclear axis.

The orbital angular momentum, Λ, has a basic equivalence to the atomic J angular momentum naming convention. The J=0,1,2,3... states are referred to as S,P,D,F, etc. while $\Lambda = 0, 1, 2...$ are labeled as Σ, Π, Δ, etc. It should be noted that for the projection of S on the molecular axis, labeled Σ, has no relation to the Σ labeling the state of $\Lambda = 0$. This is unfortunately the standard naming convention guaranteed to cause confusion among scientists far into the future.

2.1.5   Vibrational Levels

The vibrational levels of a diatomic molecule can be approximated as a harmonic oscillator with the nuclei oscillating around its equilibrium separation. Unfortunately, from a technical standpoint, molecules are anharmonic oscillators with the vibrational energies described by

$$E_v = \omega_e(v + \frac{1}{2}) - \omega_e x_e(v + \frac{1}{2})^2 + \omega_e y_e(v + \frac{1}{2})^3 + ... \tag{2.4}$$

where v is the vibrational quantum number, ω_e is the vibrational constant, and $x_e, y_e, ...$ are anharmonic constants.

2.1.6   Frank-Condon Factors

Frank-Condon factors are the vibrational wavefunction overlap (more specifically $|\langle \psi'|\psi\rangle|^2$) of two electronic states. This overlap determines the probability that a molecule will decay to a given vibrational state. (This is due to that fact that one can treat electronic transitions as essentially instantaneous compared to the motion of the nucleus.) For practical laser cooling, molecular levels with diagonal Frank-Condon factors are desirable since this limits the number of states that molecules can
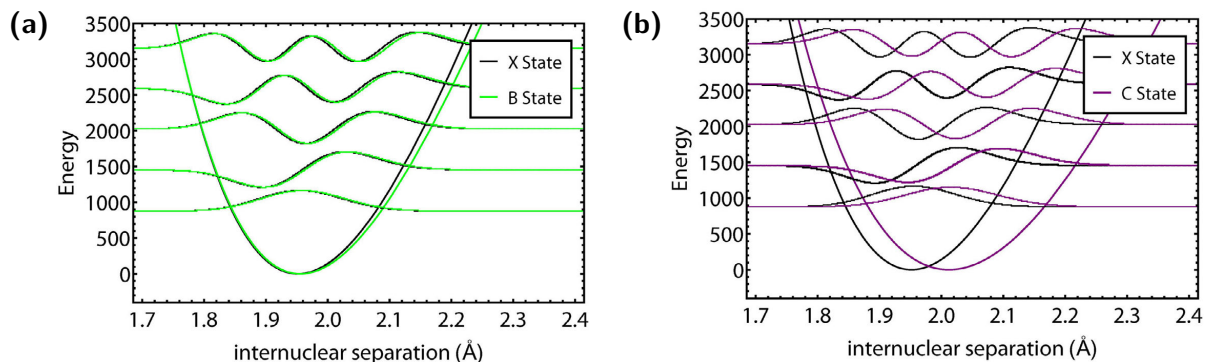
Figure 2.1.2: CaF vibrational wavefunctions. The Frank-Condon principle is well illustrated with CaF by comparing the (a) X-B and (b) X-C transition. The X and B states show good wavefucntion (diagonal Frank-Condon factors), and poor overlap for the X and C State (low Frank-Condon factors).

decay into, and hence, experimentally, limits the number of repumping lasers. It is also important that there be no low lying metastable dark states that an excited molecule can decay to. By diagonal, we mean that the molecule will predominantly decay to one level, and the probabilities of decays to higher and higher vibrational levels falls off quickly. Molecules such as CaF are diagonal due to the electrons dominantly around the metal (Calcium) nucleus (Figure 2.3.1) and little effect of the Halogen (Fluorine) is felt. Another way to think about diagonal Franck Condon factors is that the exited electronic state has the same internuclear spacing as the ground sate. This can very clearly be seen in Figure 2.1.2 for CaF.

2.1.7   LIFETIME OF VIBRATIONAL STATES

Vibrational states are excited states and thus can decay, primarily via E1 transitions. The spontaneous emission rate is [125]

$$\Gamma_{Spont} = \frac{1}{3\pi\varepsilon_o\hbar c^3}\left(\mu_v^2 \omega_v^3\right) \tag{2.5}$$

	$1/\Gamma_{Spont}$ (sec)	$1/\Gamma_{BBR}$ 300K (sec)	$1/\Gamma_{BBR}$ 77K (sec)
$v=1,0$	0.22	3.4	11600
$v=2,1$	0.11	1.7	5800
$v=3,2$	0.073	1.1	3870

Table 2.1.3: Vibrational State lifetimes. These number use the derivative of the dipole moment value of from ref [125]. Ref [126] uses another number, rendering these numbers about 30% longer. For long coherence times in future experiments, cooling will be required.

where the transition dipole moment, μ_v, is from state $v+1$ to v is

$$\mu_v = \sqrt{\frac{(v+1)\hbar}{2m_{reduced}\omega}} \left[\frac{du}{dR}\right]_{R=R_e}$$ (2.6)

The derivative of the dipole moment is used as there is no first order contribution of the dipole operator on the vibrational transition.

Blackbody radiation can also cause stimulated emission and absorption between states at a rate [125]

$$\Gamma_{BBR} = \frac{1}{3\pi\varepsilon_o\hbar c^3}\left(\mu_v^2\omega_v^3\right)\frac{1}{e^{\hbar\omega v/k_BT}-1}$$ (2.7)

Table 2.1.3 shows the lifetimes of both the spontaneous and stimulated decays. Note that since these are E1 transitions, parity is flipped. Hence decay from $v=1$ to $v=0$ will end up in the opposite parity state of the ground state and thus be lost from the optical cycling.

2.1.8 ROTATIONAL LEVELS

Continuing with the simple picture of two masses, the rotational levels of diatomic molecules are to first order that of a rigid rotor. In reality, it is a vibrating rotor and higher order corrections are
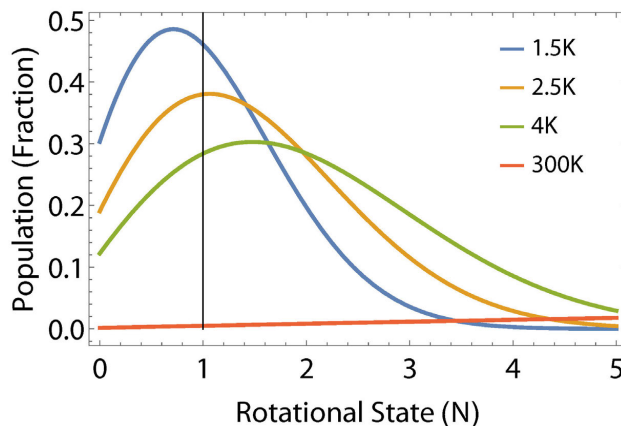
Figure 2.1.3: Thermal occupation of rotational levels for CaF. The temperatures of 1.5, 2.5 and 4 K are those found using a 1 K pumped helium system, a direct connection to the 4 K stage of a pulse tube, and a liquid helium bath, respectively. The vertical line indicates the population in the N=1 state.

needed due to centrifugal distortion. The rotational energy can be expressed

$$E_{rot} = B_v R(R+1) - D_v R^2(R+1)^2 + H_v R^3(R+1)^3 + \ldots \quad (2.8)$$

where R is the rotational quantum number, and B_v, D_v, R_v all depend on the vibrational level v.

$$B_v = B_e - a_e\left(v + \frac{1}{2}\right) + \gamma_e\left(v + \frac{1}{2}\right)^2 \ldots \quad (2.9)$$

This dependence on the vibrational level can intuitively be understood due to a changing moment of inertia as a molecule vibrates, thus affecting the rotational levels.

The spacing of rotational levels is on the order of 10's of GHz and therefore can be manipulated with microwaves. This energy scale is also on the thermal scale of a few Kelvin. Figure 2.1.3 shows the population in rotational states as a function of temperature. To have sufficient population in the N=1 state, temperatures of 4 K or less are desired.

2.1.9 SELECTION RULES

The selection rules for diatomic molecules mirror those of atoms for electric dipole ($E1$) transitions. Parity must change and $\Delta J = 0, \pm 1$ ($J'=0$ to $J=0$ is forbidden). We can use these selection rules to our advantage by cycling from $J=1$ to $J'=0$. Based on these selection rules, $J'=0$ must decay to $J=1$, and hence rotational closure (where the molecule can be driven repeatably to and from the excited electronic state) is achieved.

Higher order transitions may also occur. For example, the rate of electric quadrupole ($E2$) transitions compared to $E1$ transitions can be estimated as

$$\frac{R_{E2}}{R_{E1}} \sim \frac{\omega^2 \langle f|r^2|i\rangle}{c^2 \langle f|r|i\rangle} \sim \left(\frac{a}{\lambda}\right)^2 \sim \left(\frac{1.95\ nm}{606\ nm}\right)^2 \sim 10^{-7} \tag{2.10}$$

where a is the molecular bond length and λ is the transition wavelength. The rate of magnetic dipole transitions can be estimated as

$$\frac{R_{M1}}{R_{E1}} \sim \frac{\langle f|\mu|i\rangle}{\langle f|\mathbf{d}|i\rangle} \sim a^2 \sim 5 \times 10^{-5} \tag{2.11}$$

where a is the fine structure constant. This rate holds for decays between states of the same angular momentum, such as the decays from B-X. For the A state however, this decay is further suppressed, as M1 transitions can not change total angular momentum, and only causes decay within the A state, leading to a relative rate on the order of 10^{-9}. Thus it appears these decays are not a limiting factor for the time being.
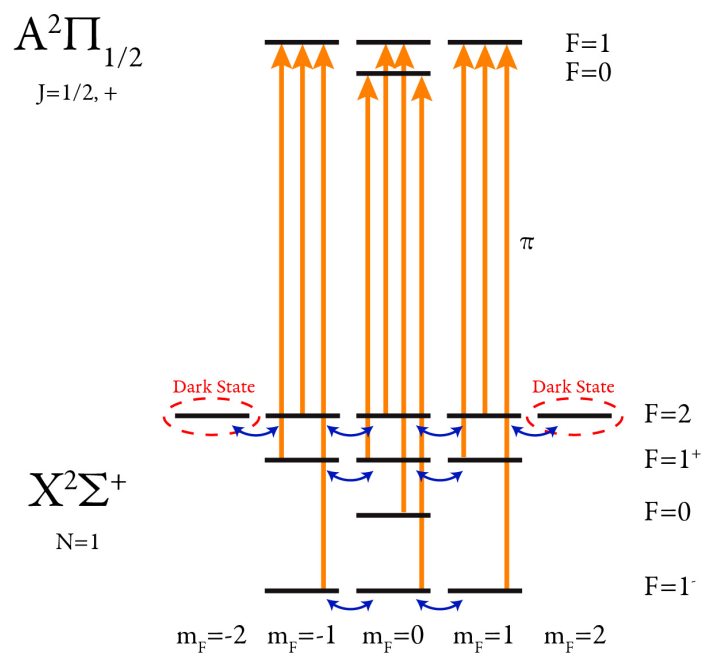
Figure 2.1.4: Dark states in CaF when driven with linearly polarized light. Dark states are also present with the application of circular polarized light, not shown. The dark state can be remixed with a static magnetic field (blue arrows).

2.1.10 Dark States

One consequence of cycling from J=1 to J'=0 to attain rotational closure is the presence of dark states. Figure 2.1.4 depicts this problem in CaF. There are a number of ways to remix dark states: magnetic fields, polarization switching, or microwaves. The application of a static magnetic field is the simplest method. A magnetic field will cause Larmor precession of the Zeeman sublevels in the ground state. If a magnetic field is applied at an angle Θ to that of the laser polarization, the precession rate will be

$$\omega_B = \mu_B g_F m_F B_0 \sin \Theta \tag{2.12}$$

The optimal value of Θ can be calculated to be $63°$. The precession rate should be set such that the remixing occurs at a rate similar to that of the pumping into the dark states.

2.1.11 Λ Doubling

The projection of Λ can be either positive or negative, with these two eigenstates degenerate when the molecule is not rotating. However, with molecular rotation, this degeneracy is lifted due to the perturbing Σ state, and the energy splitting between these two eigenstates is called Λ doubling. The Λ doubling splitting scales with N (or J). An intuitive picture of this splitting is to visualize a P shaped orbital (non-zero angular momentum) rotating along either along its lobe axis or perpendicular to it. These two axes have different moments of inertia, and as a result different energies.

The most significant effect of lambda doubling is the creation of an opposite parity state close to the excited state. This small splitting, 1.3 GHz in the case of CaF, allows stray electric fields to mix these opposite parity states, causing decays to unrepumped states, and thus loss from the laser cooling cycle. This effect will be discussed further in Chapter 5.

2.2 INTERACTION WITH EXTERNAL FIELDS

2.2.1 SCATTERING RATE AND SATURATION INTENSITY

For a system that can decay to multiple states, the saturation intensity is

$$I_s = \frac{\pi hc}{\lambda^3 \tau r} \tag{2.13}$$

where τ is the lifetime of the excited state and r is the branching ratio to the original state. For a multilevel system, as is found in CaF, the two level scattering rate equation is modified to

$$R_{scat} = \Gamma \frac{n_e}{(n_g + n_e) + 2\sum_{j=1}^{n_g}(1 + 4\Delta_j^2/\Gamma^2)I_{s,j}/I_j} \tag{2.14}$$

Where I_j is the intensity of the light driving transition j with detuning Δ_j and saturation intensity $I_{s,j} = \frac{\pi hc}{\lambda_j^3 \tau_j}$.

   We can then make the following assumptions. Since the v=1 repumping laser is on resonance and the main line (v=0) is detuned, the transitions are dominated by the main line cycling terms and we can drop the effects of the v=1 repump. Assuming all the transitions are driven with an intensity that is divided evenly between all ground states, and all state have the same Δ and I_s, then this simplifies to [99]

$$R_{scat} = \frac{\Gamma_{eff}}{2} \frac{s_{eff}}{1 + s_{eff} + 4\Delta^2/\Gamma^2} \tag{2.15}$$

where the effective linewidth is

$$\Gamma_{eff} = \frac{2n_e}{n_g + n_e}\Gamma \tag{2.16}$$

and the effective saturation rate is

$$s_{eff} = \frac{2(n_g + n_e)}{n_g^2}\frac{I}{I_s} \tag{2.17}$$

In CaF, we have 12 Zeeman sublevels in the ground state, 4 in the excited state, and 12 in the v=1 ground state. Hence $n_e = 4$ and $n_g = 24$.

The Doppler limit due to the linewidth of a laser cooling transition sets a minimum temperature for Doppler cooling of $T_D = \frac{\hbar\Gamma}{2k_B}$. For CaF, the Doppler limit for the X-A transition is 200μ K. The recoil limit due to scattering a single photon is given by $T_r = \frac{\hbar^2 k^2}{2k_B m}$ which for CaF on the X-A transition is 440 nK.

2.2.2 ZEEMAN SHIFTS

The presence of an external magnetic field causes energy shifts to the molecular states, called Zeeman shifts. The Hamiltonian for this is given by [122]

$$H_Z = g_s \mu_B S \cdot B + g_l \mu_B L \cdot B - g_I \mu_N I \cdot B \qquad (2.18)$$
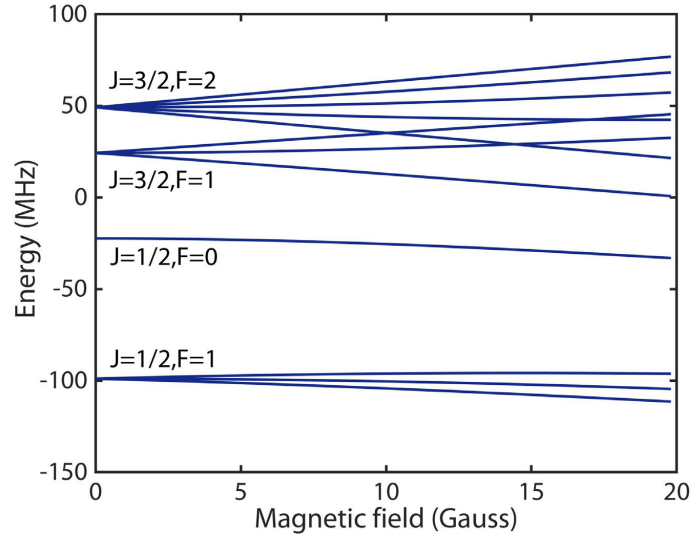
where $g_S \approx 2$, $g_L \approx 1$, $g_I \approx 5.585$ and the I term is suppressed by $\mu_N \approx \frac{\mu_B}{1836}$. For small shifts with respect to the hyperfine levels,

$$H_z \approx g_F \mu_B F_z B_z \qquad (2.19)$$

with the g-factor

$$g_F \simeq g_s \frac{S(S+1) + J(J+1) - N(N+1)}{2J(J+1)} \frac{F(F+1) - I(I+1) + J(J+1)}{2F(F+1)} \qquad (2.20)$$

For fields beyond about 5 Gauss, this approximation begins to break down and a full calculation is required [127]. The Zeeman shifts for CaF at low fields is shown in Figure 2.2.1.

Figure 2.2.1: CaF Zeeman shifts for the X state (N=1).

2.2.3 AC Shifts and Polarizability

When an atom or molecule is illuminated by a laser beam, the electric field of the light will cause the molecule's dipole moment to oscillate at the driving frequency. Here we will follow the derivation of [128] to calculate the polarizability. The interaction potential U_{dip} is

$$U_{dip} = -\frac{1}{2}\langle pE \rangle = -\frac{1}{2\varepsilon_o c}Re(a)I \qquad (2.21)$$

Where the polarizability is defined as $p = a(\omega)E$, where p is the induced dipole moment from an electric filed E. The factor of 1/2 comes from the fact that it is an induced dipole, not a permanent one and $I = 2\varepsilon_o c|E|^2$ is the intensity of the trapping light. This potential leads to a force $F_{dip} = -\nabla U_{dip}$ which we can see that if $Re(a)$ is positive, as is the case for red detuned light, there is a net force towards the point of highest intensity. From the Lorentz model,

$$a = \frac{e^2}{m_e}\frac{1}{\omega_o^2 - \omega^2 - i\omega\Gamma_\omega} \qquad (2.22)$$

28

where Γ_ω is the classical damping rate due to radiative loss

$$\Gamma_\omega = \frac{e^2 \omega^2}{6\pi\varepsilon_0 m_e c^3} \tag{2.23}$$

Substituting this in, we find the polarizability is

$$\alpha = 6\pi\varepsilon_0 c^3 \frac{\Gamma/\omega_0^2}{\omega_0^2 - \omega^2 - i(\omega^3/\omega_0^2)\,\Gamma} \tag{2.24}$$

This formula breaks down for high intensities where the excited state becomes strongly populated, but in the case of dipole trapping, we are far from this regime. Semiclassicaly, the damping rate is replaced with the following

$$\Gamma = \frac{\omega_0^3}{3\pi\varepsilon_0 \hbar c^3} |\langle e|\mu|g\rangle|^2 \tag{2.25}$$

however the classical approach leads to a polarizability correct at the percent level. This leads to a polarizability in the case of large detuning and small saturation parameters [128],

$$U_{\mathrm{dip}}(\mathbf{r}) = -\frac{3\pi c^2}{2\omega_0^3} \left(\frac{\Gamma}{\omega_0 - \omega} + \frac{\Gamma}{\omega_0 + \omega} \right) I(\mathbf{r}), \tag{2.26}$$

For a multilevel system, the damping rate simply becomes a sum over all of the relevant states:

$$\Gamma = \frac{\omega_0^3}{3\pi\varepsilon_0 \hbar c^3} \sum_g \sum_j |\langle e|\mu_j|g\rangle|^2 \tag{2.27}$$

where we sum over all electronically excited states $|e_j\rangle$.

For X-A the transition dipole matrix element is $\langle \Lambda = \pm 1|T_{\pm 1}^1(d)|\Lambda = 0\rangle$ due to the degeneracy of $\Lambda = \pm 1$, this gives a factor of 2/3. For the X-B transition, $\langle \Lambda = 0|T_{\pm 1}^1(d)|\Lambda = 0\rangle$, which gives a factor of 1/3. We can continue adding in the effects of other states, with the C state being a Π
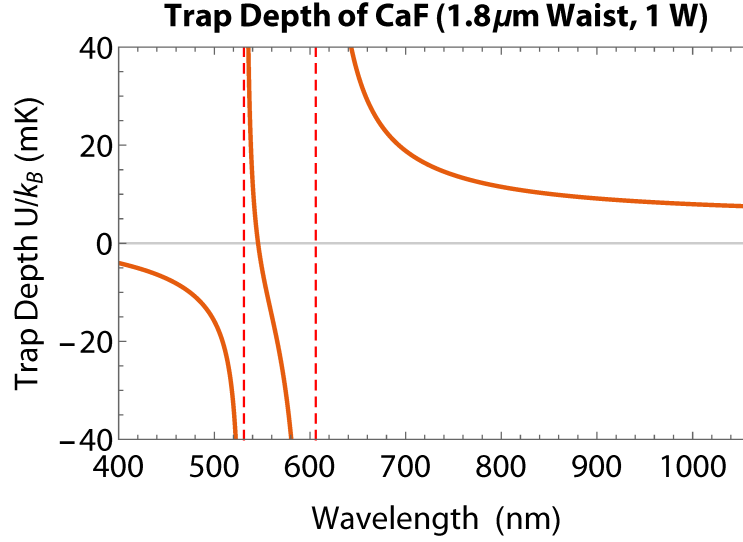
Figure 2.2.2: CaF polarizability as a function of wavelength. The trap depth is plotted here for a 1.8 μm waist with 1 W of power.

state, hence having a factor of 2/3, and the D states, which is a Σ state, giving a factor of 1/3. This combines to give an overall polarizability of CaF of:

$$
\begin{aligned}
6\pi\varepsilon_0 c^3 \Big(\frac{2}{3} & \frac{\Gamma/\omega_0^2}{\omega_0^2 - \omega^2 - I(\omega^3/\omega_0^2)\Gamma} + \frac{1}{3}\frac{\Gamma/\omega_2^2}{\omega_2^2 - \omega^2 - I(\omega^3/\omega_2^2)\Gamma} \\
\frac{2}{3} & \frac{\Gamma/\omega_3^2}{\omega_3^2 - \omega^2 - I(\omega^3/\omega_3^2)\Gamma} + \frac{1}{3}\frac{\Gamma/\omega_4^2}{\omega_4^2 - \omega^2 - I(\omega^3/\omega_4^2)\Gamma} \Big) \times 0.931
\end{aligned}
\tag{2.28}
$$

The factor of 0.931 comes from the full state dependent treatment of the stark shifts. The trap depth for CaF arising from this polarizability as a function of wavelength is shown in Figure 2.2.2.
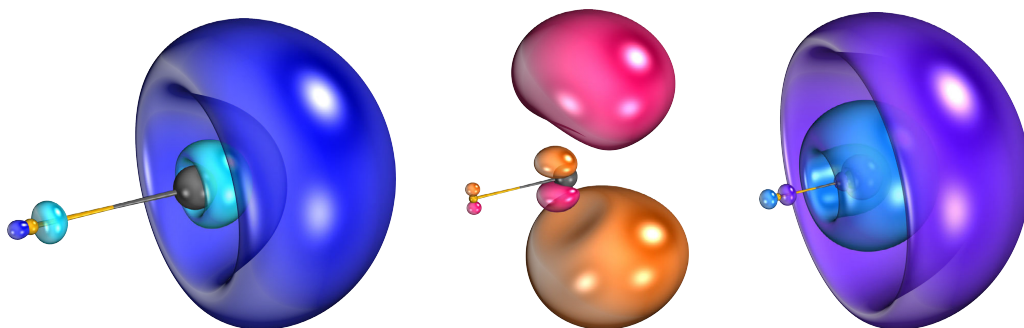
Figure 2.3.1: CaF orbitals for the $X\Sigma$, $A\Pi$, and $B\Sigma$ states. Calculated in Gaussian using the EOM-CCSD method and the cc-pVTZ basis set. The calcium atom, in black, is on the right of the molecule around which the electron wavefunction is localized.

2.3 CaF

CaF was selected for laser cooling due to its diagonal Frank Condon factors, accessible laser transitions, low mass (59 amu), and reasonable dipole moment (3 D). The low mass hinted at possibly lower inelastic collisional processes. A large amount of prior spectroscopy had been done on CaF, which greatly simplified the task of finding transitions. The ground state is a $^2\Sigma$ state due to the 1/2 nuclear spin of the fluorine atom. This nuclear spin gives rise to hyperfine structure, splitting the ground state into 4 hyperfine manifolds. This splitting is addressable with AOMs. The ground state also has a magnetic moment of 1 μ_b, useful for potential magnetic trapping and future quantum simulation.

The main cycling transition is the X-A transition at 606 nm and and X-B transition is at 531 nm. The X-A transition is fairly diagonal, with 3 vibrational repump required to scatter $\sim 150,000$ photons. While the X-B is very diagonal, at the 10^{-5} level with only one repump, the B state can decay thought the A state at a rate of

$$\frac{R_{B\to A}}{R_{B\to X}} = \frac{\omega_{BX}^3 \, d_{BX}}{\omega_{BA}^3 \, d_{BA}} \approx 1.2 \times 10^{-4} \tag{2.29}$$
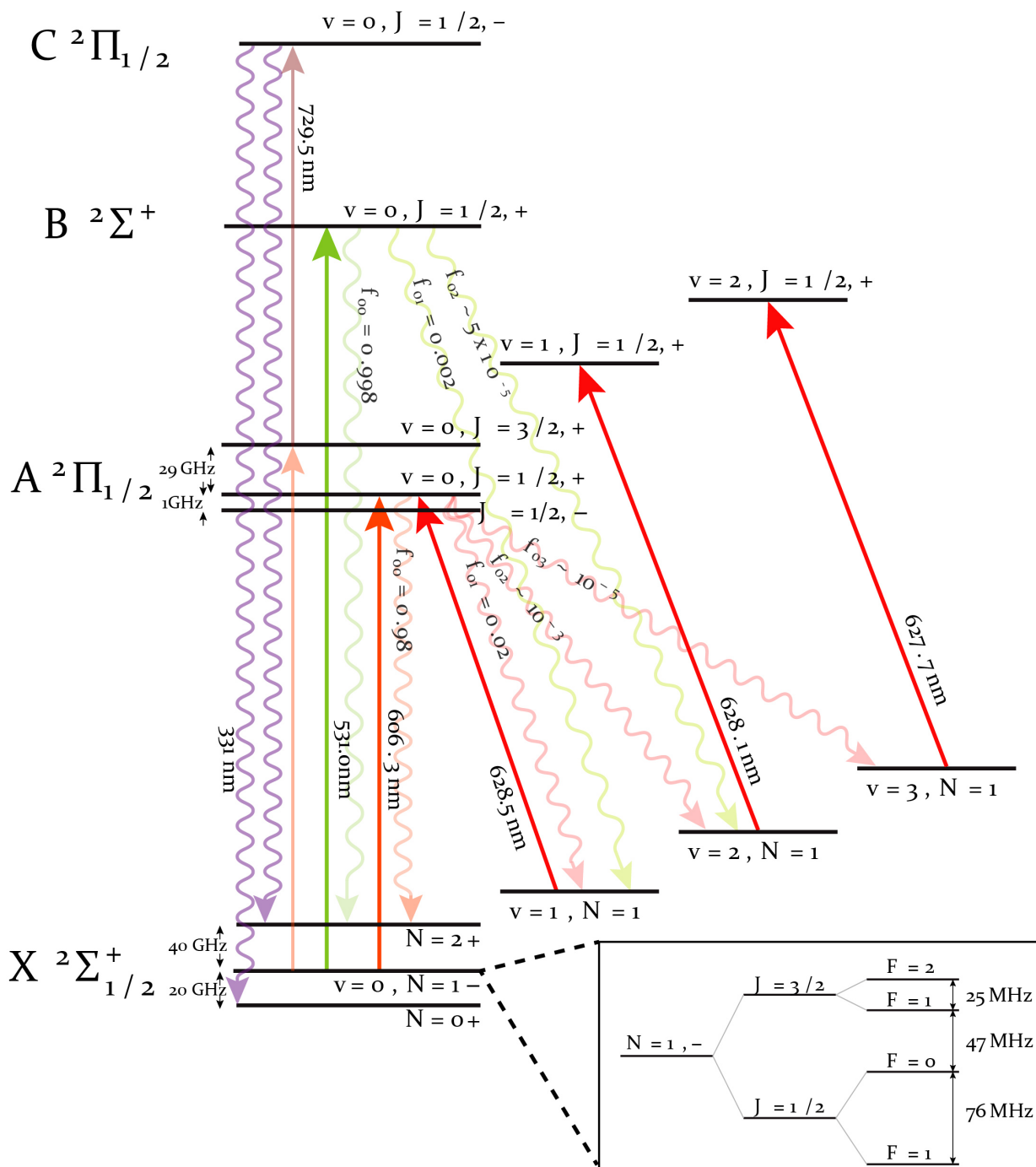
Figure 2.3.2: CaF levels relevant in this thesis.

Transition	Frequency (THz)	Wavelength (nm)	Lifetime (ns)	$T_{Doppler}$ (μK)	T_{recoil} (μK)	I_{sat} (mW/cm^2)	P_{Recoil} (cm/s)
X-A	494.432203	606.3	25.1	240	0.44	15	1.1
X-B	564.582695	531.0	19.2	320	0.6	12	1.3

Table 2.3.1: The main CaF laser cooling transitions.

This two photon process will flip the parity of the molecule causing loss. This loss rate is tolerable for the laser slowing step, but not the MOT.

There is also a higher lying C state (and a D state which is very close by, but slightly below the C state.) that can be used for background free detection via a two photon excitation. This will be discussed later for slowing detection. The C and D state are both "back-polarized" [129], meaning the electron wavefunction is no longer localized around the Calcium atom. This leads to very poor Frank Condon factors for these states, decaying into the next vibrational state after about three photons.

The relevant energy levels and decays for the discussion in this thesis is shown in Figure 2.3.2. Table 2.3.1 gives an overview of the two main cycling transitions. Appendix A contains an overview of the CaF constants and properties.

What happened to the ablation?

A Daily Question

3

Cryogenic Molecular Source

In order to laser slow and trap CaF, a source producing slow, cold molecules is required. We rely on a combination of chemistry and sympathetic cooling in our molecular source to realize high fluxes of cold CaF. Using a cryogenic buffer gas cooling, we produced $\sim 10^{12}$ CaF molecules in a beam with a temperature around 2 K. The initial design of this source was detailed in Eunmi's thesis [127]. Here we will briefly review the original design of our buffer gas source, and enhancements made to the flux and most importantly, reliability. An overview of the experiential apparatus is shown in Figure
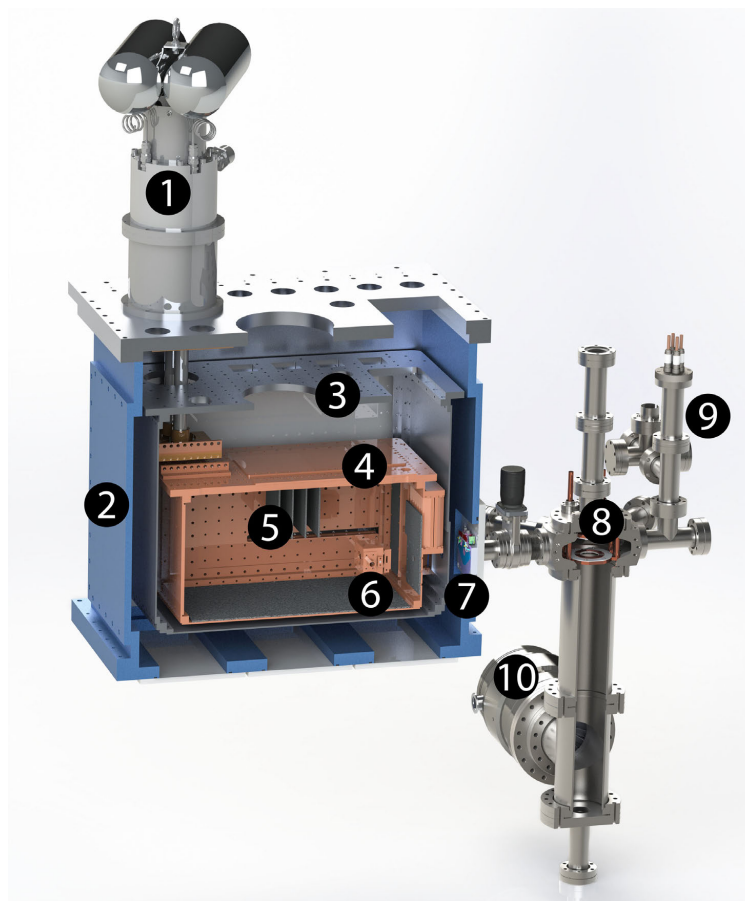
Figure 3.0.1: Cross section of the experimental apparatus. (1) pulse tube (PT415) (2) beambox (3) 77 K shields (4) 4 K shields (5) coconut charcoal sorbs (6) cell (7) UHV shutter (8) detection region (9) Ti-sublimation pump (10) turbomolecular pump

3.0.1.

3.1 CaF$_2$ Based Cryogenic Buffer Gas Source

A cryogenic buffer gas source relies on sympathetic cooling of a buffer gas with the target species. It is a versatile method able to cool both the internal and external degrees of freedom for a wide range of molecules. To produce a molecular beam, a hole is introduced into a cell, though which the molecules and buffer gas escape. Depending on the buffer gas flow rates, various flow regimes may be used to produce such a beam, as detailed in [64]. Here we mostly operate in the effusive regime, to attain the slowest exit velocities of the molecules. Experimentally, this is achieved with a "two stage" cell, where a second stage is added to reduce the boosting effect found at the exit of the of the first stage aperture. This boosting is due to the preferentially forward velocity of the helium gas in the cell's exit aperture. In the second stage, the helium density is lower by order an order of magnitude and the molecules undergo a few additional collisions in random directions. The two stage cell used in shown in Figure 3.1.1. The single stage version is identical without parts (9) and (10). The helium density in the first stage is on the order of 10^{15} cm^{-3}, providing 1000's of collisions necessary to thermalize both the external motion as well as the internal degrees of CaF into the N=1 rotational state.

The initial design relied on laser ablation (532 nm Minilite) of a hot vacuum pressed CaF$_2$ target made by American Elements. The cryogenic buffer gas cell was cooled to 1 K via a thermal connection to a 1 L pot of liquid helium which was pumped on. This provided a run time of about 6 h between refills. The cell is surrounded with coconut charcoal [130] cooled with a Cryomech PT415 pulse tube to 4 K to act as a cryopump for the helium flowed into the cell. The 4 K and 40 K stages of the pulse tube are connected to radiation shields to decrease the black-body heat load onto the cell (Figure 3.0.1).
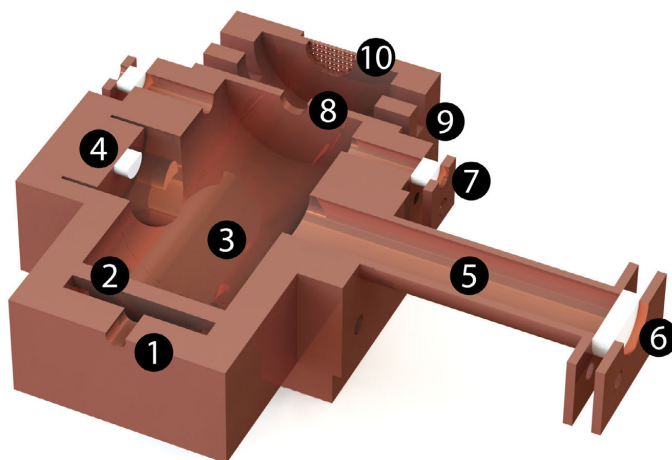
Figure 3.1.1: Cross section of the two stage cell. (1) Helium fill line inlet. (2) Diffuser, which helped thermalized the ablated CaF and lowered forward velocity of the beam. (3) 1 in ID bore, 2 in long. (4) Ca/CaF$_2$ target glued with Stycast 2850. (5) Snorkel to reduce dust on the (6) Yag window. (7) In-cell absorption windows. (8) 6 mm first stage aperture. (9) The second stage. (10) 9 mm second stage aperture with 50% filling copper mesh.

With the two stage cell, and 7 mJ of ablation energy at 4 sccm (typical running conditions which were found to produce the optimal beam in terms of flux versus fraction at low velocities) the mean beam velocity was 90 m/s, with a tail all the way down to 50 m/s. A typical flux of $\sim 10^{10}$ molecules per pulse in N=1 were produced and the velocity distribution is shown in Figure 3.2.1(a). This molecular source was used in all of the initial whitelight slowing work, Chapter 4.

All CaF velocity plots show a very quick decay of the low velocity tail below 50 m/s or so. This is even more striking for slower moving species, such as Yb due to its heavy mass. One can compare the velocity profile out of the cell versus downstream to see that low velocity atoms/molecules are preferentially kicked out. This is due to two contributing factors. First, slower moving molecules will have more time to plume out and will not make it into the downstream region. Secondly, sufficient pumping of the helium is required as to not interfere with the molecular beam. The helium that is most detrimental to the molecular beam is any helium moving either against or transverse to
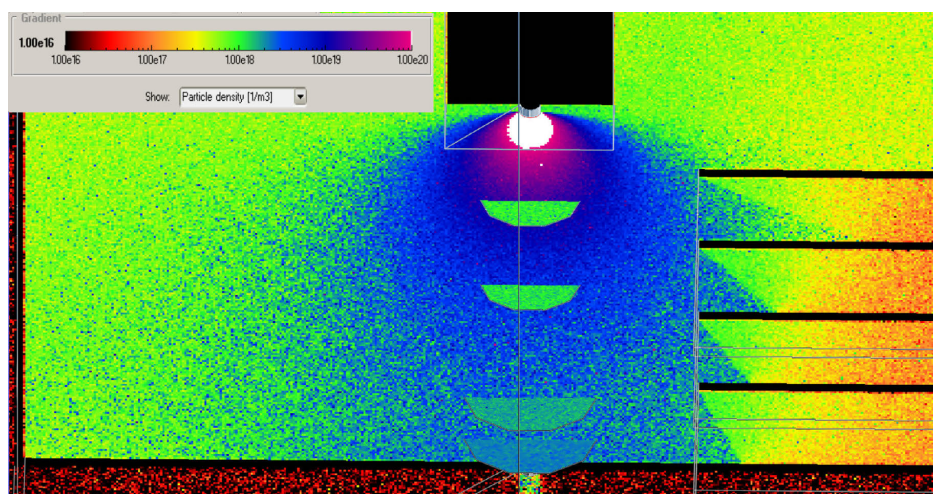
Figure 3.1.2: Simulation of helium pressure inside the beam source. This assumes 10 sccm flow, which is equivalent of 2 sccm and the increase from the helium released during the ablation. The particle density plotted is calculated from particles crossing the boundary. The vertical circles show the helium back pressure, i.e. the helium density moving backwards against the beam. This assumes that the front plate and all the other sorbs have a sticking fraction of 0.5.

the beam, which can kick molecules out, rather than the one co-propagating with the beam. The helium back-pressure is determined by the helium flow rate, the spacing between the cell and the 4 K shield, the sorb placement, etc. The fact that slower moving molecules spend more time in the high-pressure region cause them to be preferentially kicked out. Figure 3.1.2 shows a simulation of the helium back-pressure within the 4 K shield. It is worth noting that due to the pressure being much lower outside the 4 K shields, even with the limited conductance out into a turbo pump or the MOT region, chevron baffles should not be added to the 4 K shields.

3.2 DRAWBACKS OF CaF$_2$ ABLATION

While the pressed powder ablation allowed us to generate fairly high fluxes, there was a major issue in terms of stability and reliability of this source. The pressed powder targets only lasted about 5 days, and the beam velocity would increase dramatically each running day. On top of this, the ablation

(a)

(b)
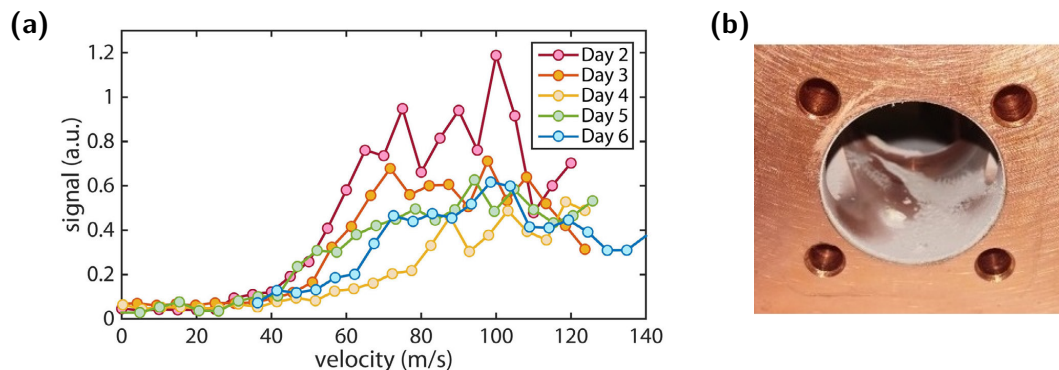
Figure 3.2.1: (a) Beam velocity and flux vs experimental run day. Days 1-4 used one target and days 5-6 used the second target. The flux of the source degrades on this short timescale and the velocity profile is differently everyday. While there is some ability in regaining the low velocity tail after switching to the new target, the overall flux is significantly lower than the early run days. (b) Dust accumulation inside the first stage after two weeks of running.

spot needed constant tuning, with each spot on a target only lasting about 50 shots before in-cell absorption degraded.

Figure 3.2.1(a) shows the changes in beam flux and velocity as a function of running days. The leading theory behind this change in beam dynamics is due to the buildup of dust on the cell walls, decreasing the thermalization rate of the ablated molecules. Figure 3.2.1(b) clearly shows the coating of dust after two weeks of running (time for two targets to be depleted).

Clearly if we wanted any hope of achieving reliably slowing and a MOT, a new source was needed.

3.3 $Ca + SF_6$ Source

To solve our degrading beam problem, we opted for chemical source using a calcium target and SF_6 gas, which had been used in the Tarbutt group for some time[131]. The ablation of metals in buffer gas source is very reliable and provides high fluxes (some metals reach $> 10^{14}$ atoms per pulse!). The reaction of calcium with SF_6 had first been studied much earlier in molecular beams [132, 133]. We decided to modify our current two stage cell in order to accommodate a heated fill line, needed to
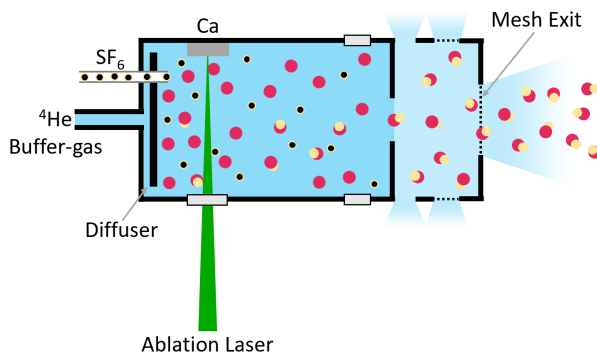
Figure 3.3.1: Overview of Ca + SF$_6$ source.

deliver SF$_6$ gas into the cell, Figure 3.3.1.

3.3.1 DESIGN

While SF$_6$ sublimates at 210 K, we thought that the vapor pressure at 160 K ($\sim$20 torr) would be high enough to prevent clogging. We also wanted to design the fill line such that we could preload SF$_6$ into the cell in the morning and run the entire day with the need of flowing any extra SF$_6$ gas. In this way, the fill line could be cooled to 4 K, alleviating any extra heat load on the cell which would decrease running time and potentially increase the beam velocity.

We designed the heated fill line with a target heat load of $\sim$ 250 mW into the 50 K shield, $\sim$ 100 mW in the 4 K shield, and 10 mW into the cell while at 160 K. In order to ensure the heated fill line would cool when the heaters were turned off, weak thermal connections were made between the fill line and both the 50 K shield and the 4 K shield. 250 mW of heat flow into 50 K shield with a 12 AWG stainless steel wire corresponds to a 1.6 cm long connection. For 100 mW of heat flow into 4 K shield, a 4.5 cm long 12 AWG stainless steel wire was used.

The fill line was made of a 316 stainless steel tube, 1/16" OD with an 11 mil thick wall. Thin film SMD resistors were attached as heating elements. Thin film resistors were used as their value remains
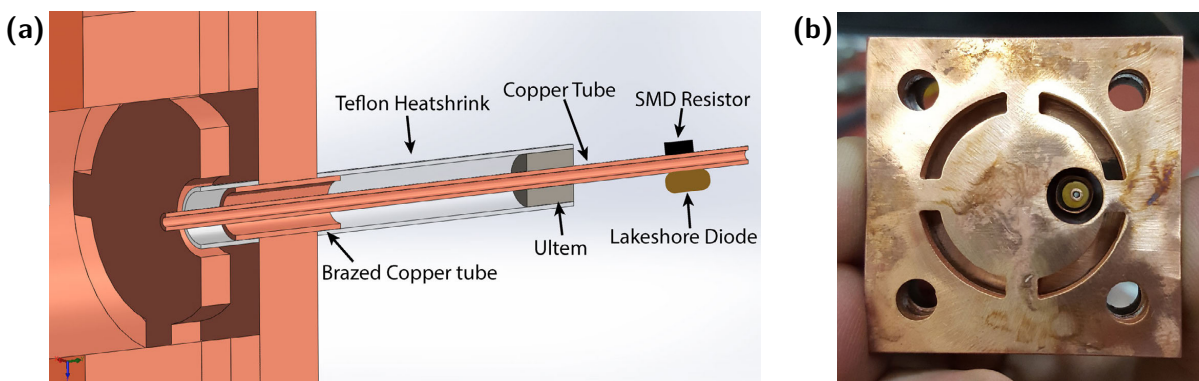
Figure 3.3.2: (a) The heated fill line has one resistor glued with Styast 2850 on the copper tube on the right end. A layer of Kapton tape insulates the resistor from shorting with the tube. This copper tube is attached with a round Ultem holder with an outside diameter matching the Teflon tube. The tube is Teflon heat shrink which is was heated to match the diameter of the brazed copper for a tight press fit. A small Teflon tube on the inside of the cell ensures the helium buffer gas is not heated by the fill line. (b) View of the back assembly. Note: prior to cool-downs, ensure that the heated fill line is well centered to prevent it touching the cell during cool-down.

nearly constant, even at cryogenic temperatures. Thermal cycling to cryogenic temperatures does run the risk of introducing small cracks into the film, slowing increasing the resistance as the cracks enlarge. Each SMD resistor (100 Ohm) is Stycasted (2850) on to a loop of Kapton tape to prevent shorts. This stainless steel fill line was then connected with a small Teflon tube to a copper fill line which enters into the cell. A hole in the diffuser allows the SF_6 to be delivered into the main cell region without freezing onto the diffuser. The copper tube has a 1 kOhm SMD resistor attached to it to heat it as it is thermally disconnected from the stainless steel fill line. The copper tube is stood off from the cold cell with a Teflon heat-shrink tube and a small Ultem insert. Teflon was selected due to its low thermal conductivity and large thermal contraction at cryogenic temperatures as to make a leak tight seal. Figure 3.3.2 shows a drawing of the fill line entering the cell.

Thermal simulations were performed to ensure that the thermal load on the cell was manageable, shown in Figure 3.3.3. In theory, this heated fill line should have caused a 20 mW increase in thermal heat load onto the cell. In reality, the thermal load from the fill line appeared to be closer to 100 mW.
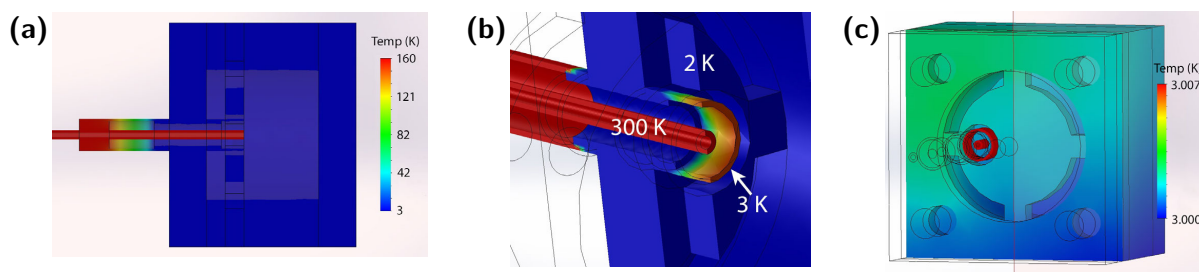
Figure 3.3.3: Thermal simulations of the heated fill line. Thermal radiation is included. (a) Overview of the heated fill line entering the cell. (b) Thermal radiation heating the Teflon guard inside the cell by about 1 K. (c) Diffuser showing no elevated temperatures from the fill line.

It remains unclear as to what caused this discrepancy. One possible explanation is that the PTFE (Teflon) heat shrink may not be pure PTFE, causing a much larger heat flux into the cell. It is also possible that there are some hot-spots on the fill line which produce a much high radiation flux than anticipated. This issue could be resolved by wrapping the fill line in super-insulation. We refrained from implementing this due to the fear of introducing shorts and the fact that the total heat flux still leaves us with 90 minutes of run time between transfers when pumping and 3.5 hours running at 4 K.

3.3.2   Performance

As we hoped, the new source leads to a much more stable beam where ablation can last 1000's of shots per spot on the target, and increased flux. Figure 3.3.4 shows the beam flux versus velocity of the old and new sources.

We found that the SF_6 gas was depleted quite quickly ($\sim$30 min) if simply pre-loaded into the cell. As a result, we ran with the fill line continuously hot and with low flow. Initially, we used an SF_6 flow rate of 0.2 sccm. However, this caused clogs in the fill line and a large accumulation of "snow" in the cell, which degraded the beam. Figure 3.3.5 shows this snow after a few days of running. We solved these problems by running the fill line slightly warmer (closer to 200 K) and decreasing the
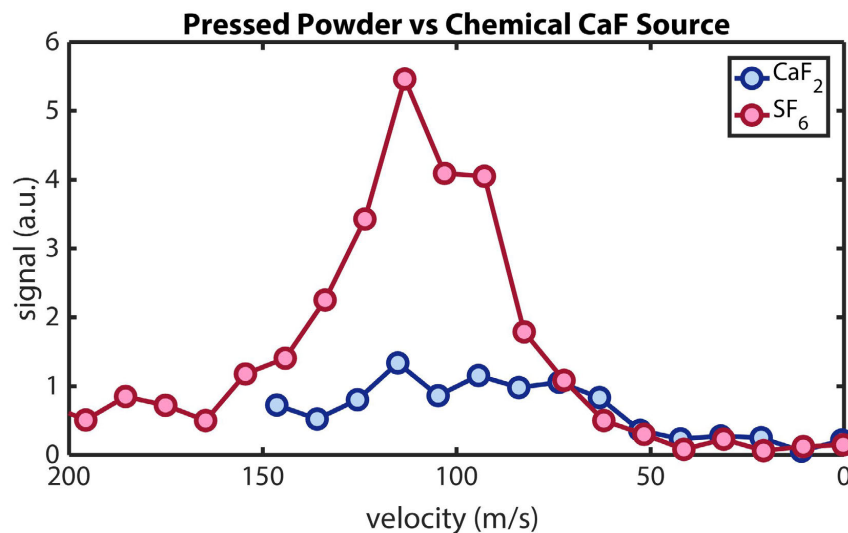
Figure 3.3.4: Flux versus velocity from both the SF_6 and CaF_2 source. Note this is comparing the flux of the chemical source early on day 2 of running. We now know that the flux degrades over two time scales, bi-weekly between SF_6 melting, and overall on the few month timescale (about a factor of 2-3).

flow rate to 0.02 sccm. With these parameters, we are able to run for two full weeks and melt the ice over the weekend. We also tried CF_4 gas rather than SF_6, however, this reduced the beam flux by about a factor of two. Other more volatile fluorine containing gasses may be more reactive with the calcium, however, they tend to be highly toxic.

Each calcium target lasts about 3-6 months. Figure 3.3.5 shows a partly used target after about two months of continuous data acquisition. We found that with a new calcium target, the molecular beam is much more uniform as the Yag is moved to various spots on the target. However, the flux of slow-able molecules (as detected by the number in the MOT) is slightly lower than a partly used target. After a few weeks, the target becomes pitted and "magic spots" appear where the flux can increase by many factors. However, these regions are small and finding them can be difficult.

We also find that what we refer to as the "day one" effect, where the flux from the source is substantially lower on the first day of running after the cell is cleaned, is still present. This was seen with both the CaF_2 pressed targets as well as the SF_6 source, where it can take up to a week of running
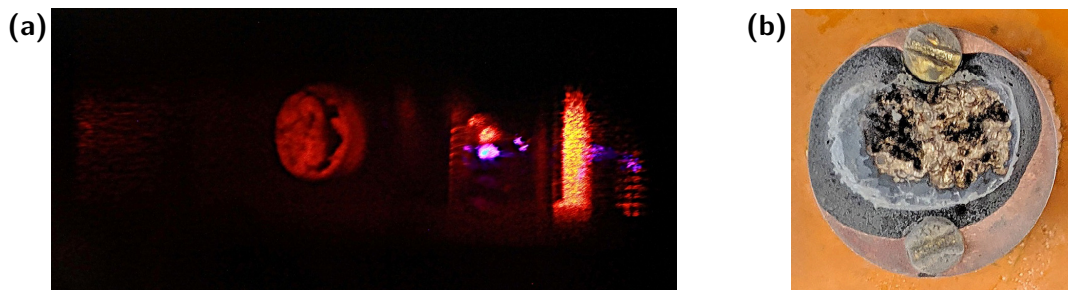
Figure 3.3.5: (a) SF6 "snow" buildup in the cell, seen on the side of the Yag snorkel entrance. (b) A calcium target after a few months of data acquisition. Heavy pitting leads to the creation of "magical spots" which produces a substantially larger MOT.

before the flux stops growing. Both the Imperial and JILA groups have seen a similar effect. An explanation for this effect is yet to be determined. In fact, the YO experiment coats their cell with YO powder to increase flux [134].

The cell produced a beam with a velocity profile quite similar to the CaF_2 ablation source. The following section will discuss the molecular beam in detail. However, the beam flux and velocity distribution does vary dramatically on the ablation spot. (This became even more striking once we moved to making a MOT, discussed in Chapter 5). Figure 3.3.6 shows various beam velocity distributions versus different ablation spots on the target.

3.4 MOLECULAR BEAM CHARACTERIZATION

The tunable parameters affecting the molecular beam include primarily the helium flow, ablation spot, and Yag energy. For the SF_6 source we find that even low flows (0.01 sccm) of SF_6 saturates the production. We can operate both with a single stage and two stage cell. The addition of the second stage moves the peak velocity down from 150 m/s down to 90 m/s at the cost of a factor of five in flux. Initially, we found this trade-off to be beneficial, due to the limited slowing power
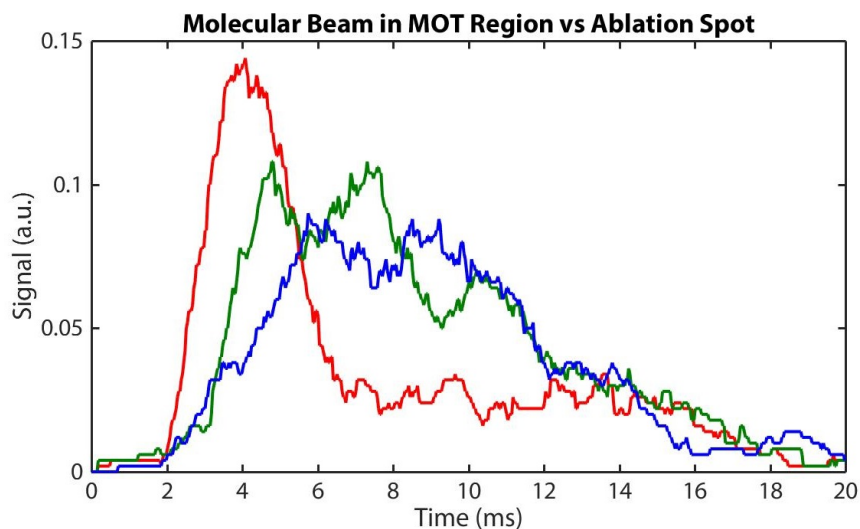
Figure 3.3.6: Molecular beam time of arrival in the MOT region versus ablation spot. Radically different beam shapes can be created with very small changes to the ablation location on the calcium target.
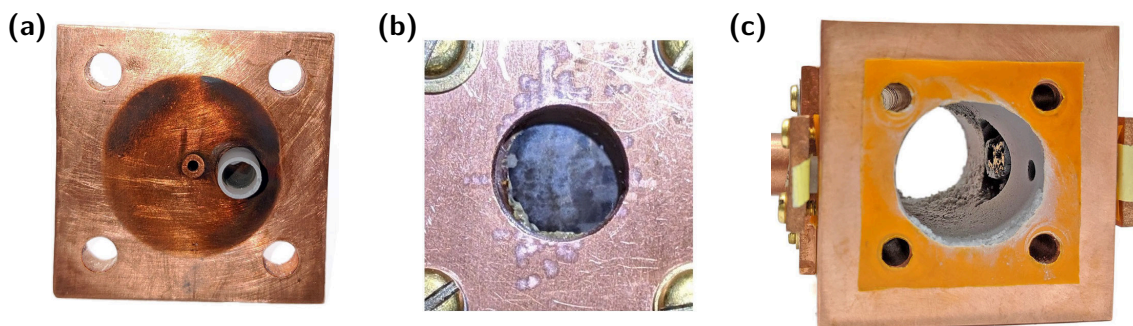
Figure 3.3.7: Cell after 2 months of heavy data taking. (a) Oxidation on the back of the cell. Based on the oxidation pattern, it seems like it comes from the main cell area, possibly a reaction of the SF_6 with something during ablation. (b) Yag window at the end of the snorkel becomes fairly dusty. (c) Inside of cell is covered with dust.
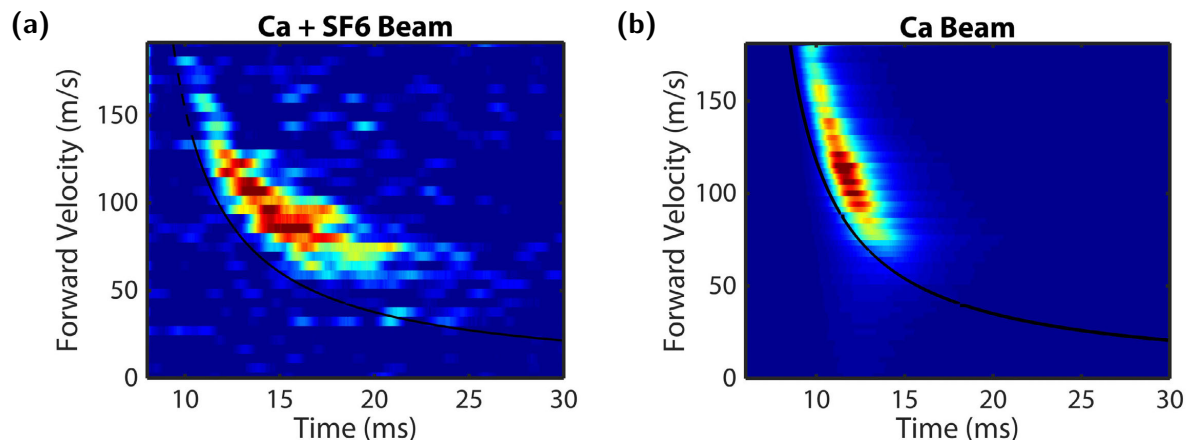
Figure 3.4.1: (a) Forward velocity of the CaF beam vs time of arrival. The dotted line represent the time of flight arrival time beginning at the time of the Yag pulse. (b) Forward velocity of the calcium beam.

available at the time. Using a single stage source would have increased the slowing distance, and thus decreased the flux.

3.4.1 TWO STAGE BUFFER GAS CELL

Figure 3.4.1 shows the forward velocity and time of arrival for both the CaF beam (a) and the calcium beam (b). An interesting difference is that there appears to be a 1 ms delay in the production of the CaF beam with respect to the calcium beam. The absence of a high velocity thermal trail indicates that the molecular beam is well thermalized. There is a sharp cut off on the low velocity side, due to the previously mentioned reasons.

We characterized our molecular beam by scanning the helium flow rate and the ablation energy. While the ablation spot can have large impact, it is not a well controlled parameter, and thus ignored for the time being. Figure 3.4.2 displays the molecular beam flux and velocity verses the flow rate while operating at 14 mJ. We find that a flow rate of 4 sccm seemed to be optimal in producing a bright and slow beam, with a peak around 90 m/s. Figure 3.4.2 shows the effect of ablation power at
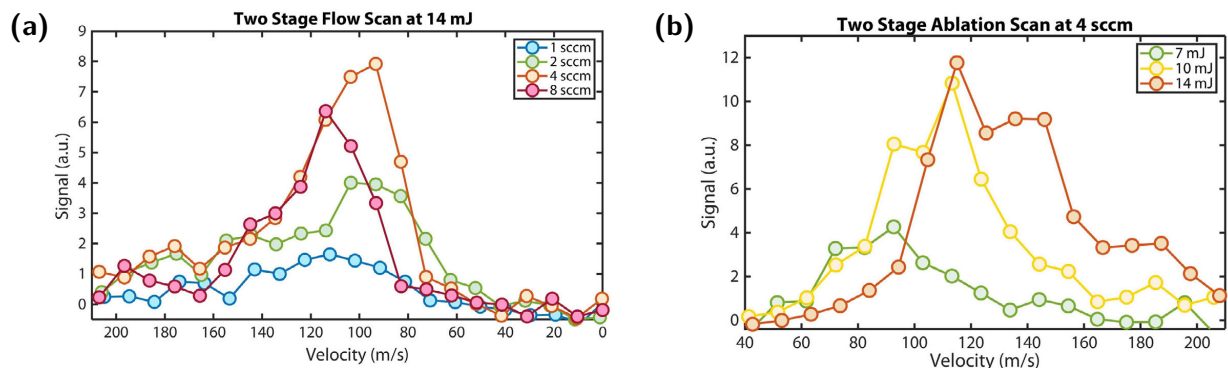
Figure 3.4.2: Two stage source. (a) Helium flow scan of flux vs velocity. (b) Ablation energy scan of flux vs velocity.
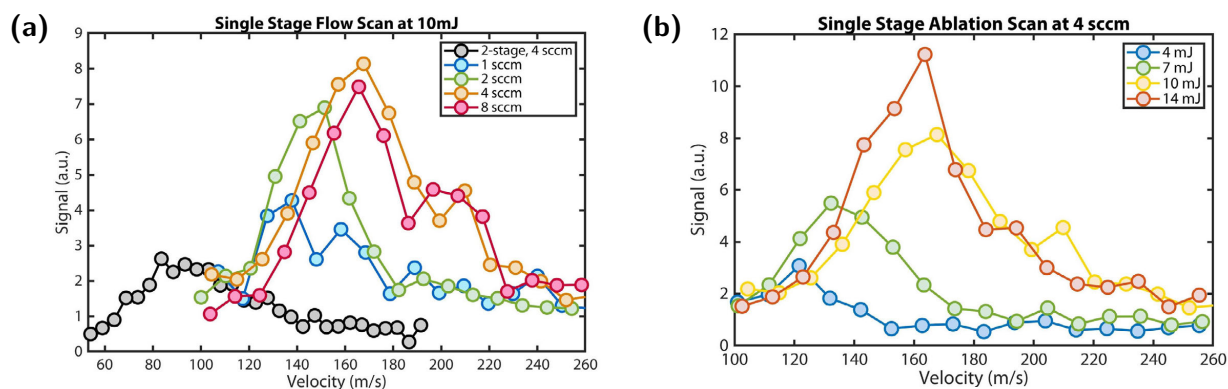
Figure 3.4.3: Single stage source. (a) Helium flow scan of flux vs velocity. (b) Ablation energy scan of flux vs velocity.

4 sccm of helium. Once can see a strong threshold effect around 7 mJ which is the minimum energy for production of CaF with the chemical source. (This threshold is most likely due to the energy required to excite the meta-stable state of Ca, which reacts with the SF_6. This is on the order of 2 eV, or 20,000 K.) Increased Yag energy increases total flux, but also eliminates the low velocity tail of the distribution.

3.4.2 Single Stage Buffer Gas Cell

The initial slowing, MOT, and ODT data were taken with a two stage source. However, we recently (during the optical tweezers, mid 2019) switched to a single stage source due to increased slowing power, as discussed in Chapter 5. Figure 3.4.3 (a) displays the molecular beam flux and velocity versus the flow rate while operating at 10 mJ. A two stage trace is included to show the effects of the second stage. Figure 3.4.3 (b) displays the molecular beam versus ablation energy at 4 sccm. Again, a strong threshold behavior is present, with a cutoff around 7 mJ. One caveat of the single stage source is that it also produces larger pulses of helium downstream, which could become a problem in some situations. This source produces on the order of 10^{12} molecules per pulse in the N=1 state.

4

Laser Slowing

While the molecular source produces molecules moving at around 100 m/s, the MOT capture velocity is only on the order of 5 m/s. In order to slow the molecules down, we rely on laser slowing. While in most AMO experiments laser slowing is a trivial task, the case is not the same for molecules. Slowing the molecules down to the MOT capture velocity (5 m/s) was by far the most challenging task of making this experiment work and remains, to this day, the most inefficient step. This was in part due to the limited laser power available and the method used. This inefficiency should be celebrated by future graduate students, as there are large gains to be made in the future.

4.1 LASER SLOWING CaF

Atomic experiments typically rely on Zeeman slowers [135], a clever design to slow atoms from a range of initial velocities to a single final velocity all at the same location, typically into a MOT. This works by utilizing a large spatially varying magnetic field to Zeeman detune the atoms by the full range of their Doppler shift. The field generated is tailored to the atomic species such that the atoms experiences a constant deceleration by remaining in resonance with the slowing beam. This slowing design relies on the fact that atoms have a large Zeeman shift in the excited state and due to a sparsity of ground states, always fall back into the same ground state the majority of the time. Unfortunately, as discussed previously, photon cycling of molecules realizes on going from the $N=1$ ground state to an $N=0$ excited state. This means that we have many more ground state than excited states. It also leads to the fact that molecules can decay into both high and low field seeking states. In addition, CaF has a very small excited state g factor, making such a Zeeman slowing difficult. Recently there has been schemes proposed to use a Zeeman slower for molecules [136–138], however the laser intensities required for large gains are not feasible with the available power, although this is rapidly changing.

4.2 DETECTION OF SLOWED MOLECULES

The detection of the slowed molecules proved to also be a tricky task. The main issue is that the slowing efficiency was very low; of the molecules that reach the MOT chamber, only about 0.001 of them are slowed to the desired velocity under optimal conditions. The detection was done with a Doppler sensitive beam at 45 degrees. However, due to fact that CaF is a multi-level system, with the multiple hyperfine states of CaF ranging 150 MHz (translating to 65 m/s at 45 degrees detection), care must be taken to ensure velocity sensitivity. We use a single frequency detection to solve
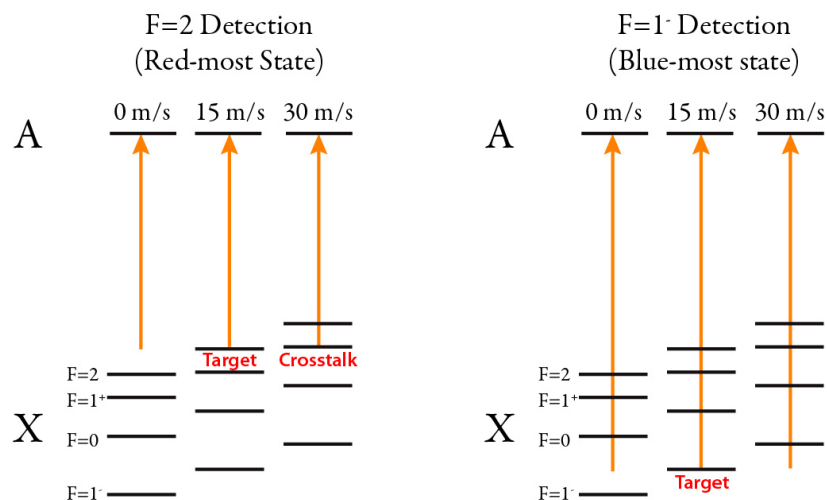
Figure 4.2.1: Single frequency velocity detection crosstalk. Here molecules at 15 m/s are targeted with detection at 0 degrees. If using the red most F=2 state, there is crosstalk with 30 m/s molecules. By contrast, when using the blue most F=1⁻ state, there is no crosstalk from higher velocity molecules. There can be crosstalk from lower velocities, but since the flux at low velocities is always lower than higher velocities for slowed molecules in the region of interest, this is not a problem. Also, for CaF, the crosstalk would occur from molecules moving 45 m/s slower than the target velocity. Since we are interested in molecules moving at 5-30 m/s this can be ignored.

this, eliminating crosstalk, as shown in Figure 4.2.1. The bluest hyperfine state, F=1-, is used to detect the slowed molecules. Due to the much larger population of high velocity molecules than low velocity molecules, the off-resonant florescence of the faster unslowed molecules is combined with the slowed molecules, leading to an overestimate of the slowing efficiency. Finally, single state detection means that the slowing detection is sensitive to the distribution of hyperfine states, which changes due to optical pumping during the slowing process (see [127]).

Experimentally however, looking for slowed molecules directly with single frequency detection is hopeless due to scattered light. While photon cycling could be done, this still does not generate enough photons to overcome the scattered light problem. As a result, we opted for a two photon background free detection scheme to detect the slow molecules, Figure 4.2.2.
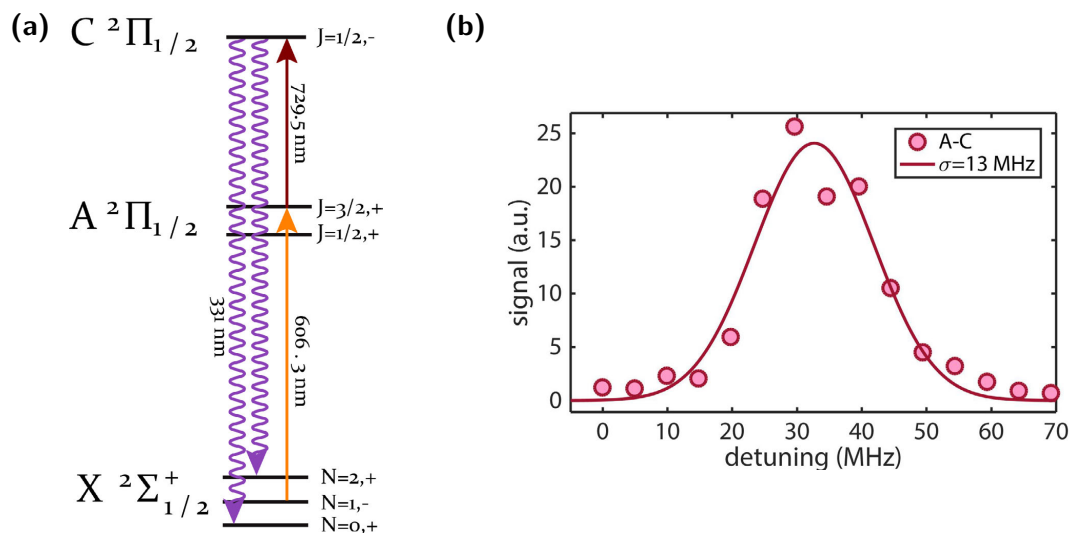
Figure 4.2.2: (a) Two Photon Detection levels. Typically the X-A beam is transverse and the A-C beam was at 45 degrees for velocity sensitivity. (b) Scan of the A-C transition transverse to the molecular beam.

The molecules in the $X^2\Sigma(N = 1, F = 1-)$ ground state are excited to the $A^2\Pi_{1/2}(J = 3/2, +)$ state with X-A (606 nm) light orthogonal (velocity insensitive) to the molecular beam. Before the molecules can decay back to the $X^2\Sigma$ state, they can be excited up from the $A^2\Pi_{1/2}$ state to the $C^2\Pi_{1/2}(J = 1/2, -)$ state with a velocity sensitive beam (729.5 nm) at 45 degrees. The intensity of the A-C beam must be high enough to excite a significant fraction up to the C state before the 19 ns lifetime of the excited A state. However too much power broadens the range of velocity detection. With the typical power used, the fluorescence linewidth is about 15 MHz, Figure 4.2.2b. The fluorescence from the $C^2\Pi_{1/2}$ to the $X^2\Sigma$ decay at 331 nm collected onto a PMT (Hamamatsu R7600P) with a low dark count rate (45 Hz) operated in photon counting mode. Two interference filters (Brightline 335/7) with color glass (FGUV11) sandwiched in between prevented unwanted light leakage. It should be noted that only one photon per molecule may be emitted as due to parity selection rules, molecules decay from the $C^2\Pi_{1/2}$ state to the $X^2\Sigma(N = 0, 2)$ states.

The PMT signal in sent to a preamplifier (SRS SR445A) and then to a fast comparator (AD-

(a)

(b)
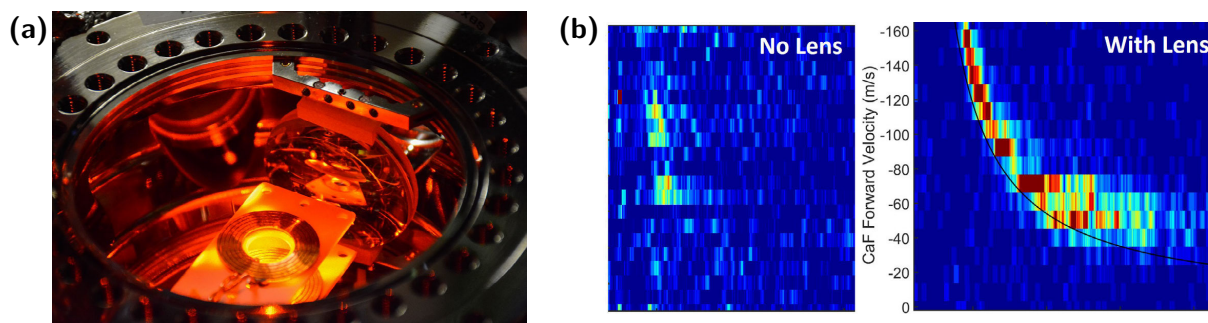
Figure 4.2.3: In-vacuum lens for higher NA. (a) Lens is mounted in the UHV chamber. (b) Molecular beam signal with and without the lens.

CMP552) which sets the threshold for photon counting. The output pulses are then counted by the DAQ card. One important thing to note is that a typical RG-58 BNC cables only has about 45 dB of shielding. When trying to count single photons in a noisy lab environment, this becomes as problem. We replaced the RG-58 cables with RG-405 semi rigid coax which has a shielding value of 100 dB. This fixed nearly all of the noise pickup problems.

An in-vacuum lens (Newport SBX049) increased the numerical aperture of our collection optics allowing us to collect one in every 30 photons emitted, Figure 4.2.3. Without this lens, we could not detect molecules at below 30 m/s.

4.3   WHITELIGHT SLOWING

Laser slowing was initially done using whitelight slowing, where the frequency of the slowing light is broadened to cover the entire range of Doppler shifted velocities. With a two level system and flat intensity versus frequency slowing beam, all of the population would be slowed until the atoms or molecules fall out of resonance with the slowing beam. The width of the final velocity distribution is set by the linewidth of the transition. Unfortunately, the reality is much less efficient. The broadening of the slowing light is never perfectly flat with sharp edges. The broadening of the slowing light

(a)

(b)
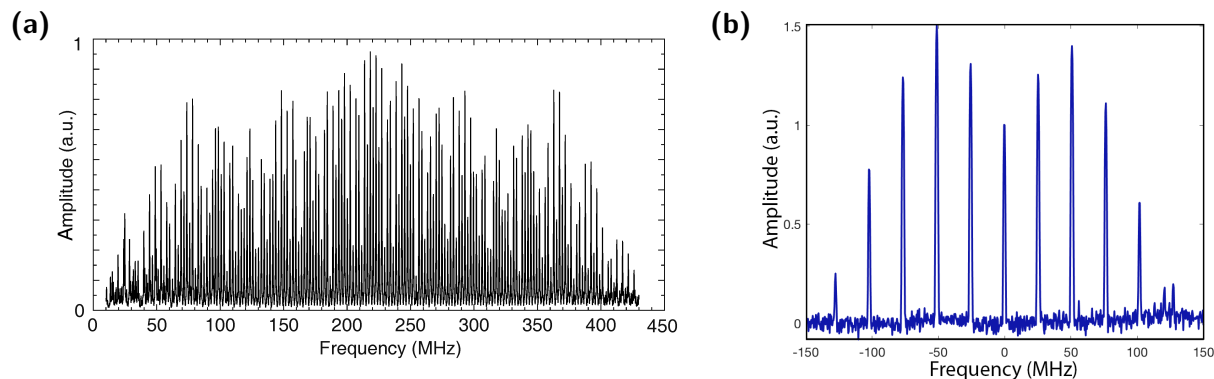
Figure 4.3.1: (a) Whitelight slowing laser spectrum. The laser is broadened about 350 MHz using two sequential EOMs, one at 24.8 MHz for the hyperfine spectrum, and the other at 4.5 MHz with a $\beta = 17$, half of the CaF linewidth. This spectrum was measured by beating the modulated light with unmodulated light from the same laser, allowing the individual peaks to be resolved. (b) Hyperfine only EOM spectrum.

is done with an EOM driven with a high modulation index. The frequency of the EOM is 4.5 MHz, less than the linewidth of the transition, and spans $\sim$ 350 MHz. The high modulation index EOM renders the edges of this slowing light quite broad. The four hyperfine ground state ground states of CaF also affect the slowing efficiency somewhat, however the population is essentially just pumped into the F=1- state as the other states remain in resonance with the light. The spectrum of the slowing light and repump lasers is shown in Figure 4.3.1. The maximum initial velocity is set by the width of the broadening, which is typically restricted due to power limitations. A $\sim$ 5 Gauss transverse magnetic field is applied to remix dark magnetic states along the slowing region.

Slowing was originally done on the X-A transition, Figure 4.3.2(a). For optimal slowing to low velocities, the slowing laser was applied starting 4 ms after the ablation pulse and was on for 13 ms. The intensity of the slowing beam was 260 mW/cm² for both the main and $v = 1$ beams. The slowing beam was slightly focused, giving rise to an effective transverse force to decrease pluming out. The slowing was far from efficient with most of the molecules remaining at around 70 m/s and only a very small tail extending down towards the MOT capture velocity, Figure 4.3.9. This translated to around 6×10^4 molecules slowed to a velocity of 10 ± 4 m/s. We also tried using helium-3 as the

(a)

(b)
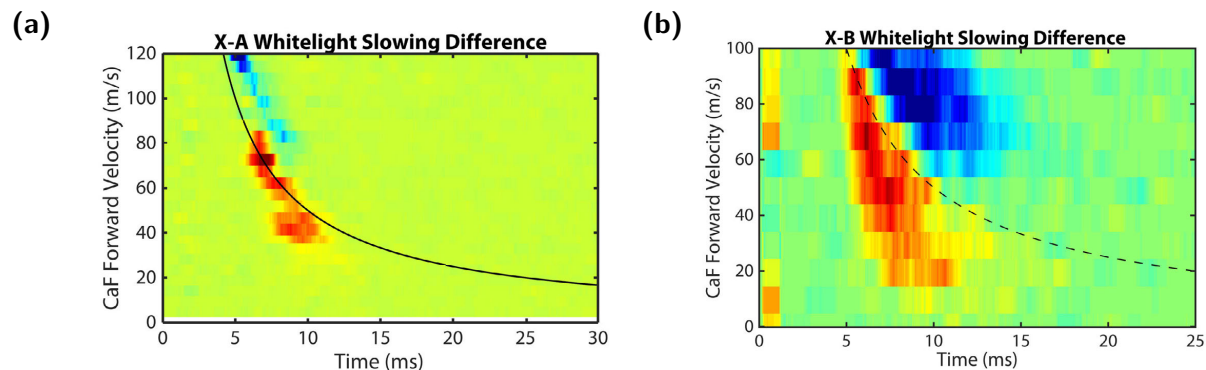
Figure 4.3.2: Comparison of (a) X-A and (b) X-B slowing. The forward velocity of CaF is measured with and without the slowing and the difference is plotted. Red represent accumulation of molecules and blue represents depletion. One can see that higher velocity molecules are depleted and an accumulation of low velocity molecules is seen. The dotted line represents the time-of-flight arrival time for that velocity. Slowed molecules arrive before this line as they initially were traveling at a higher velocity.

buffer gas. This resulted in roughly a factor of 2 increase in flux of slow molecules.

4.3.1   X-B SLOWING

We then switched to slowing on the X-B transition, giving us an enhanced scattering rate. This is due to the fact that when cycling on X-A, one also couples in the v=1 vibrational state thought the repumping laser addressing the same excited state. From Equation 2.14, we see that by switching to X-B, we now have 12 ground states rather than 24, giving us a factor of two in scattering rate, allowing us to slow closer to the peak of the velocity distribution rather than just the tail, Figure 4.3.2(b). As for the number of MOT capturable molecules, this increased by an order of magnitude, Figure 4.3.3(b). This is due to several factors. First, we now had enough scattering rate to decelerate the peak of the initial distribution. Second, the increased scattering rate decreased the slowing distance. By decreasing the slowing distance, the effect of pluming loss is reduced, Figure 4.3.3(a). The number of molecules captured in the MOT versus slowing duration and power is shown in Figure 4.3.4.
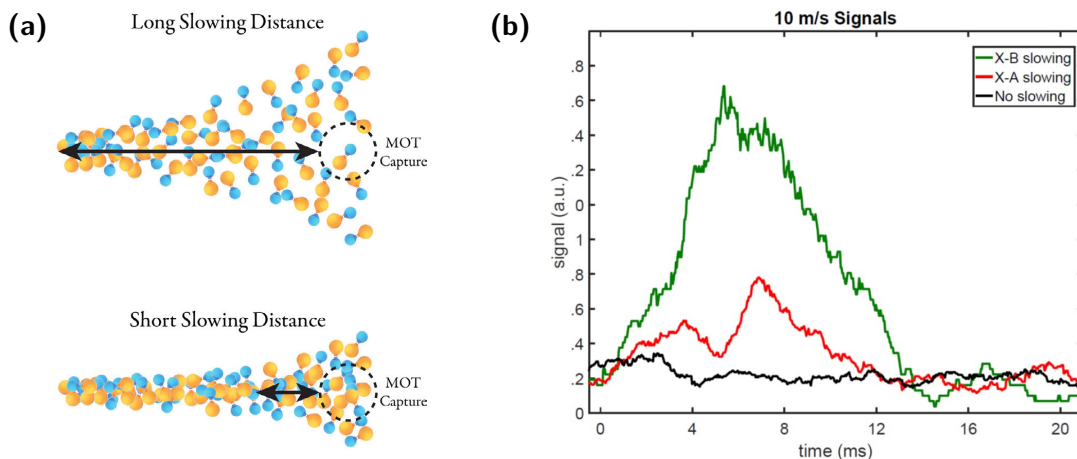
Figure 4.3.3: (a) Pluming vs slowing distance. A short slowing distance allows the molecules to travel at a higher forward velocity for longer and only causes transverse heating near the end, reducing the loss from pluming. (b) 10 m/s molecules with X-A and X-B slowing. The green trace corresponds to 5×10^5 slowed molecules.
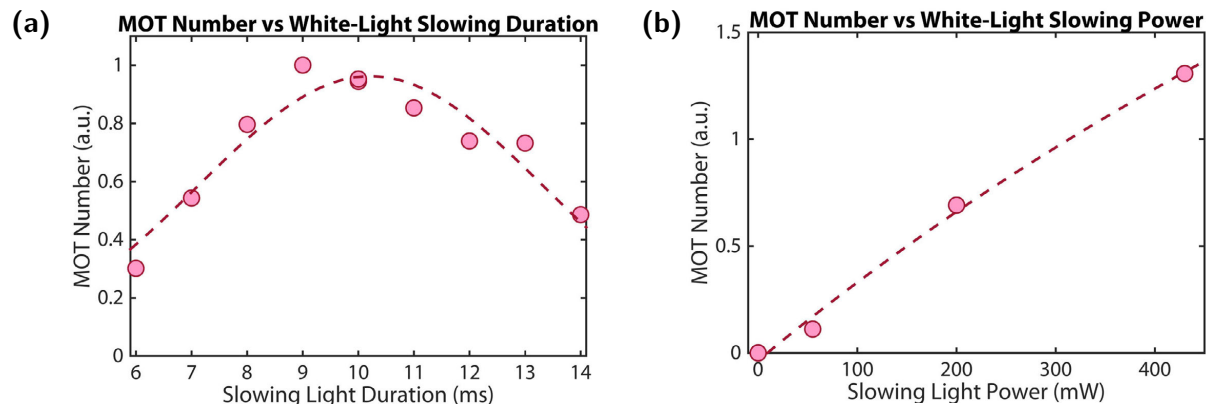
Figure 4.3.4: X-B whitelight slowing parameter scan. (a) The MOT number vs slowing duration. (b) The MOT number vs X-B slowing power.

We find that we were still limited by slowing power.

4.3.2 CHIRPED SLOWING

Rather than frequency broadening the slowing light to address different velocity classes, one could also sweep the frequency of the slowing light to track the deceleration of the molecular pulse. In the limit of an infinitely short pulse and narrow initial velocity dispersion, chirped slowing can be highly efficiency, as the only broadening in velocity is due to the shot noise of the number of photons scattered. In reality the molecular beam has a large velocity and exit time dispersion which limits this efficiency. Numerical simulation and results from the Tarbutt group [131] indicated that a large gain was possible over whitelight slowing. This type of slowing was only implemented after we attained our first molecular MOT.

To chirp the slowing laser frequency, we modulate the piezo input of the NKT seeding the Elysa lasers. Unfortunately, this raises several complications. First, we find that the NKT has high amounts of hysteresis when an external input voltage is applied. This can be solved by always applying the same initial lock voltage and tuning the NKT wavelength internally. Also limiting the output voltage of the lock prevents larges changes in frequency.

A more fundamental problem is one due to amplitude modulation induced by the frequency modulation when sweeping the frequency of the NKT. According to Quantel, in the gain fiber of the amplifier, the light creates an effective grating. When the frequency of the light is changed quickly in the wrong direction, the amount of back reflected light from the grating increases, and the amplifier detects this as increased back reflection and shuts off. The NKT itself also has an FM to AM conversion problem, which arises from the cavity inside NKT. If the sweep rate is faster than the ring down time of this cavity, that leads to amplitude noise, which can also shut down the amplifier.

These problems were mitigated by installing a 4 Hz analog filter into the analog piezo input of
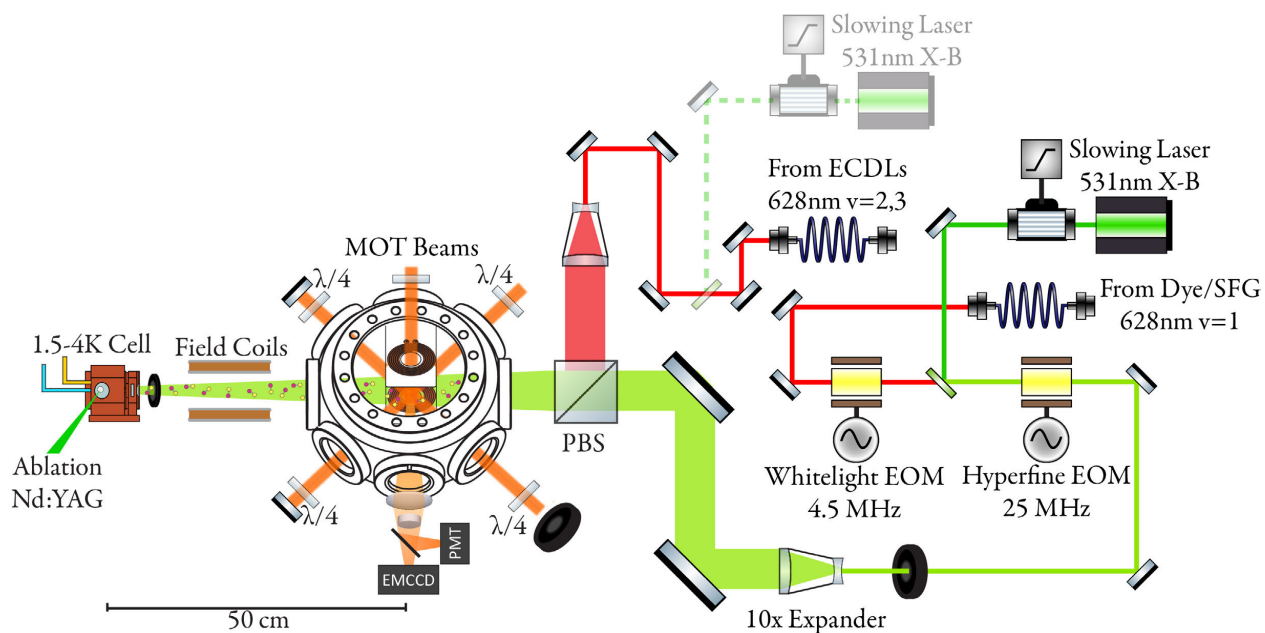
Figure 4.3.5: Slowing laser table for chirped slowing. The X-B slowing light is sent though a hyperfine EOM, with a spectrum shown in Figure 4.3.1(a). The ν=1 repump laser is sent though the whitelight EOM, whose spectrum is show in Figure 4.3.1(b). The grayed out beam path was a second slowing beam we added. This is discussed further in the following chapter.
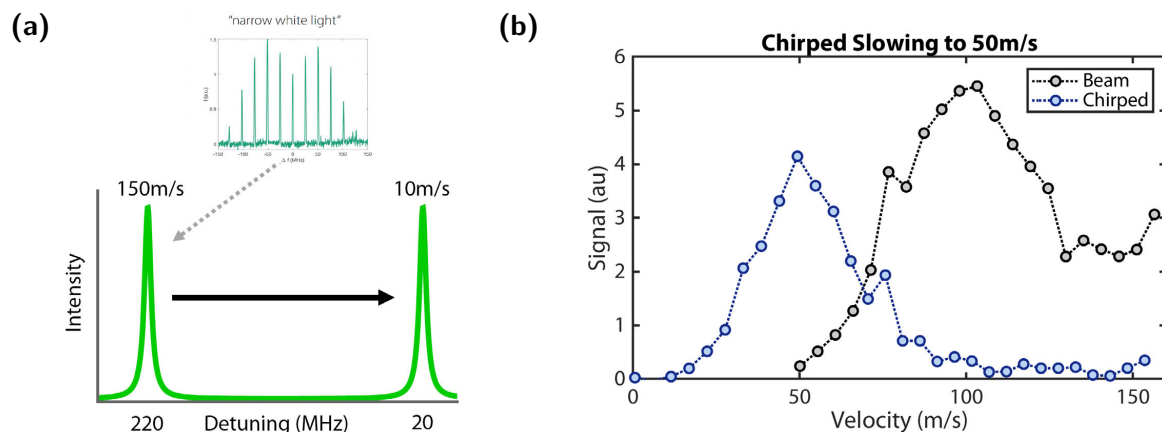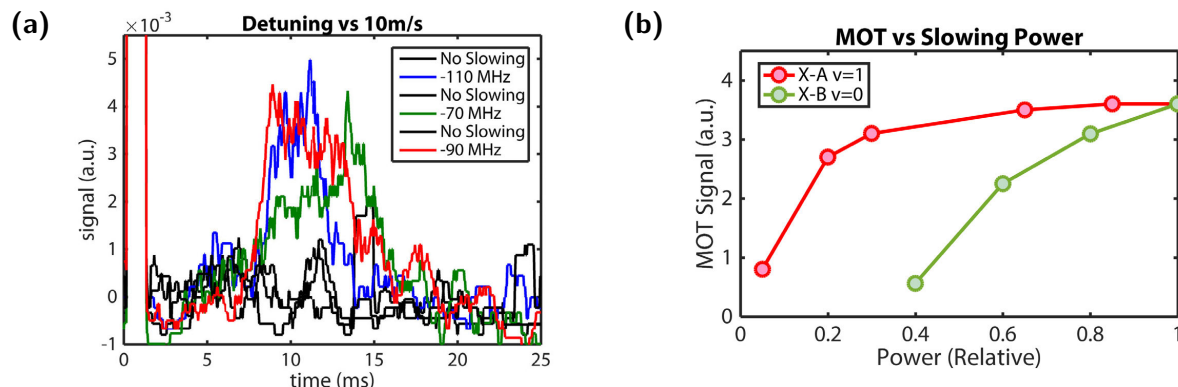
Figure 4.3.6: Chirped slowing of CaF (a) Chirped laser slowing. The frequency chirp was done with a analog pulse from Cicero fed into the NKT seed of the Eylsa laser. For optimal slowing, the chirp rate should be set to the highest deceleration possible, as determined by the scattering rate. (b) Slowing molecules to 50 m/s with chirped slowing where we moved the frequency in two steps. (Parameters: Initial wait of 2 ms, then 1 ms preslow, then step down after 2 ms reaching the final frequency in 4.2 ms later.)

the NKT, limiting the PID speed, adding a digital filter to the LabView locking software to prevent jumps, and ramping the sweep back to the initial frequency over 100 ms. In order to sweep the laser while keeping it locked, we installed a sample and hold circuit (LF398), which kept the analog value of the laser lock point sent from LabView until after the chirp was done.

The slowing light was setup to bypass the whitelight EOM crystal, but left to go through the hyperfine EOM to ensure closure in order to cycle photons, Figure 4.3.5. The optimal hyperfine EOM power which led to the most slow molecules is shown in Figure 4.3.1(b).

We first optimized the chip slowing by trying to efficiently transfer molecules to 50 m/s. We applied a "preslowing" initial pulse for 1.5 ms as a way of trying to compress the initial velocity distribution, and then chirped the frequency of the light linearly (Note: Linear here means linear in the control voltage. We don't have good way of measuring what the actual frequency of the laser is during the rapid chirp). This turned out to be remarkable efficient, as shown in Figure 4.3.6(b).

Having successfully slowed to 50 m/s we then then optimized the slowing down to 10 m/s, shown

Figure 4.3.7: (a) 10($\pm$5) m/s signal from slowed molecules vs initial slowing detuning. We found that the signal is surprisingly insentive to the initial detuning of the slowing laser. (b) Required slowing power for v=0 and v=1 with chirped slowing. Full power is 300 mW of X-A and 1 W of X-B.

in Figure 4.3.6. We had learned that the signal at 10 m/s is not a very reliable proxy for an optimal MOT loading back from our initial slowing work. Rather we scanned all of the parameters of the slowing at looking at these 10 m/s molecules and then applied this knowledge of the slowing parameters when optimizing the MOT with this chirped slowing. Of course, this time, we had the luxury of knowing that our MOT worked and all the beams per already optimally aligned.

We found initially that due to the high scattering rate of this chirp slowing, we became limited by $v = 1$ laser power. This manifested itself has being able to slow to about 30 m/s in the half meter distance, but no slower. If a higher chirp rate was used, most of the molecules would be lost. We focused the repump laser beam down to match the main-line and improved the fiber coupling such that the X-B slowing power was the limiting factor. Figure 4.3.7 shows the $v = 1$ repump power requirement versus chirp rate.

While optimizing the slowing down to low velocities, we found that programming an exponential ramp improved the slow molecule number. This was true also for the MOT signal. Again, this may be due simply to how the voltage input of the NKT is converted to frequency.

An interesting discovery was that the slowing had an optimal start time, Figure 4.3.8, usually on
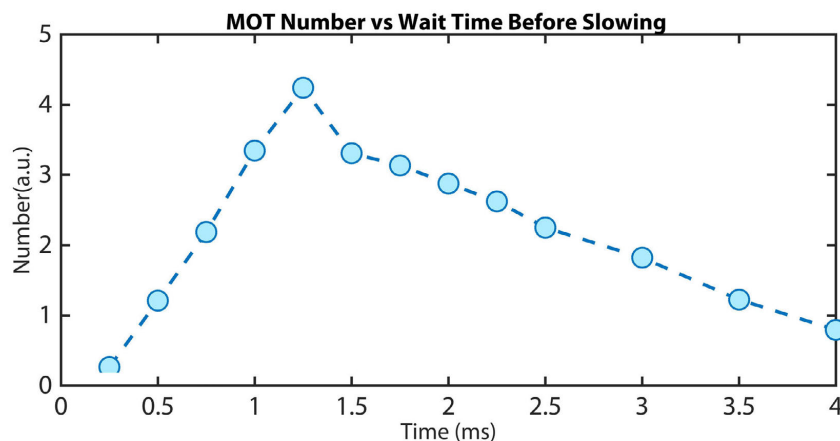
Figure 4.3.8: Wait time before slowing vs MOT signal. This optimal is dependent on Yag energy, ablation spot, and amount of days run. This scan was taken on the 5th run between cell cleanings on day 2 after an SF_6 melt.

the order of 1-2 ms after the Yag pulse. This is most likely due to a combination of the exit time of the CaF molecules from the cell and an optimal slowing distance. We find that later in a data taking run (∼week), this optimal wait time decreases, evidence that the molecular beam speeds up. The optimal wait time also depends on ablation spot and Yag energy.

4.3.3 A Comparison of Chirped and Whitelight Slowing

The overall performance of all three types of slowing is shown in Figure 4.3.9. In terms of MOT capturable molecules, X-B chirped slowing was about twice as good as X-B whitelight and 20 times better than X-A whitelight slowing.

The benefits of chirped slowing however are most likely experiment dependent. It depends on the amount of power available and the velocity and time profile of the molecular pulse. In terms of optimization, chirped slowing has many more parameters than that of whitelight slowing. For whitelight there are 3 main parameters; slowing duration, frequency, and power. For chirped slowing there are 6; start time, slowing duration, start frequency, end frequency, ramp shape, and power.
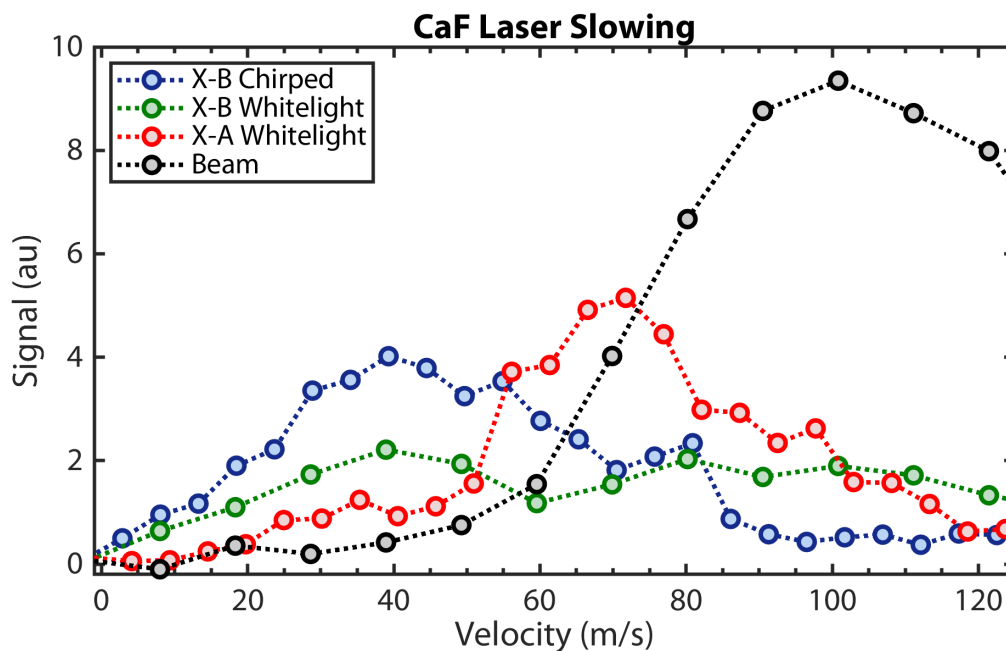
Figure 4.3.9: Laser slowing of CaF. All curves here represent the optimal slowing parameters for producing low velocity molecules. These traces show the integrated number of molecules reaching the detection region from 2 ms to 30 ms. The beam shown represents a typical two-stage molecular beam profile.

This means the optimization goes from 3 to 6 dimensional. This is manageable when optimizing to have the best MOT possible, but more difficult when searching for initial MOT signal. If whitelight slowing could be optimized to have a steeper cutoff in its spectrum, large gains could result. Ideas for future improvements to slowing is discussed in Chapter 9.

It's On Fire!!!

-High-Tech Debugging Process

5

Magneto Optical Trapping of CaF

5.1 MAGNETO-OPTICAL TRAPPING OF MOLECULES

A magneto-optical trap (MOT) relies on a combination of magnetic field gradients and laser beams with the proper polarization to generate a confining and cooling force[139]. A magnetic field gradient, created with an pair of anti-Helmholtz coils, Zeeman shifts the magnetic sublevels. For a J=0 to J=1 transition, the magnetic field splits the excited state into three magnetic sublevels, $m_J = +1, 0, -1$, while the ground state does not split. Counter propagating laser beams with σ^+ and

64
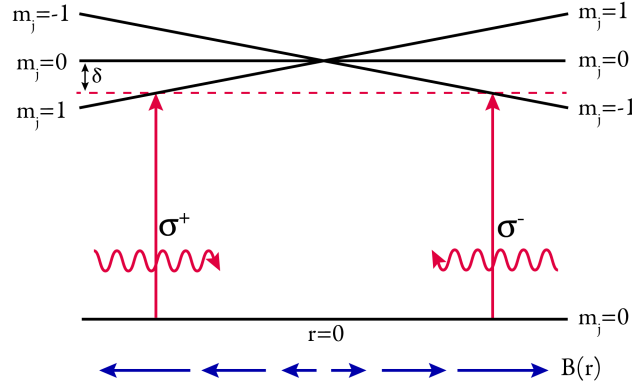
Figure 5.1.1: MOT laser and atomic state configuration. With the circular polarized light red detuned, atoms preferentially scatter a specific polarization dependent on their position.

σ^- polarizations are red detuned of the transition frequency, as shown in Figure 5.1.1. Due to angular momentum conservation, exciting an atom from $m_j = 0$ to $m_J = 1$ requires absorbing a photon with σ^+ polarization, while driving from $m_j = 0$ to $m_J = -1$ requires absorption of a σ^- photon. As an atom moves out away from the center, for example, to the left in Figure 5.1.1, the σ^- beam, which is moving to the right, shifts into resonance with the atom and is absorbed. By contrast, the σ^+ beam is shifted out of resonance. After absorbing a photon, the atom then decays back down into the J=0 state. The force experienced by the atoms in the MOT is a sum of left and right moving beams [140],

$$F_{scat}(\delta) = \hbar k \frac{\Gamma}{2} \frac{I/I_{sat}}{1 + I/I_{sat} + 4\delta^2/\Gamma^2} \tag{5.1}$$

$$
\begin{aligned}
F_{MOT} &= F_{scat}\big(\omega - kv - (\omega_o + \beta z)\big) - F_{scat}\big(\omega - kv - (\omega_o - \beta z)\big) \\
&\simeq -\alpha v - \frac{\alpha\beta}{k}z
\end{aligned}
\tag{5.2}
$$

where a is an effective damping coefficient and β is the Zeeman shift.

$$a = \frac{-8\hbar k^2 s \Delta}{\Gamma (1 + s + \frac{4\Delta^2}{\Gamma^2})^2} \tag{5.3}$$

$$\beta = \frac{g\mu_B}{\hbar} \frac{dB}{dz} \tag{5.4}$$

The maximum velocity which a MOT can capture will be dependent on the spontaneous decay rate, Γ, of the excited state, which will limit the maximum number of photons which can be scattered over the diameter D of the beam. This leads to a capture velocity of [140]

$$v_c = \sqrt{\frac{\hbar k \gamma D}{m}} \tag{5.5}$$

Assuming a scattering rate on the order of 2 MHz, and 1 cm beams, leads to a maximum capture velocity for CaF of 10 m/s.

5.1.1 Dark States and the RF MOT

As described in the previous section, a typical atomic MOT uses a DC field and operates by cycling photons on a $F \rightarrow F + 1$ transition (often called a type-I MOT), where F is the total angular momentum. However, in order to ensure rotational closure for molecules, photons must be cycled on a $F \rightarrow F - 1$ transition, a type-II MOT, and hence have more ground states than excited states. As a result, for a given polarization of light, there exists ground states which are dark to the MOT light. Without a form of remixing, all of the molecules would be pumped to a dark state where they would be lost [141].

The solution to this is to use what is called an RF or AC MOT [142]. Here, rather than using a
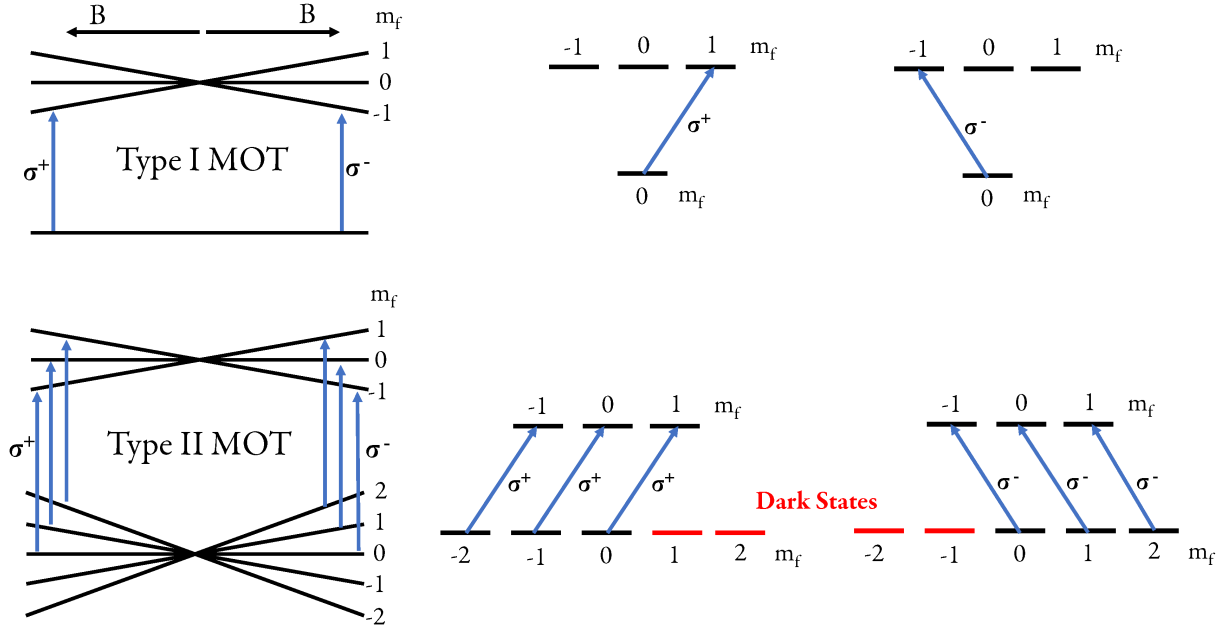
Figure 5.1.2: Type-I vs Type-II MOTs. The presence of more ground states than excited states in type-II MOTs lead to the existence of dark states for a given polarization.

static DC field, the magnetic field and polarization are switched at a similar rate to the pumping rate into these dark states [87, 143], remixing dark states.

In some cases, a DC MOT can still be achieved due to remixing that occurs naturally in the multi-level structure of molecules. CaF offers this structure due to the spacing of the $F = 1$ and $F = 2$ hyperfine ground states, where one can exploit a "dual frequency" [144] effect to achieve strong trapping and cooling forces, Figure 5.1.3(b), discussed below. The relevant energy levels for CaF are shown in Figures 5.1.3(a).

5.1.2 Polarization of MOT Beams

For a DC MOT, the optimal choice of circular polarization depends on the angular momentum of the ground and excited state, F_e and F_g as explained in [145]. When $F_e < F_g$, a type II MOT, the polarization should be reversed from a typical MOT. The polarization should also be reversed if the
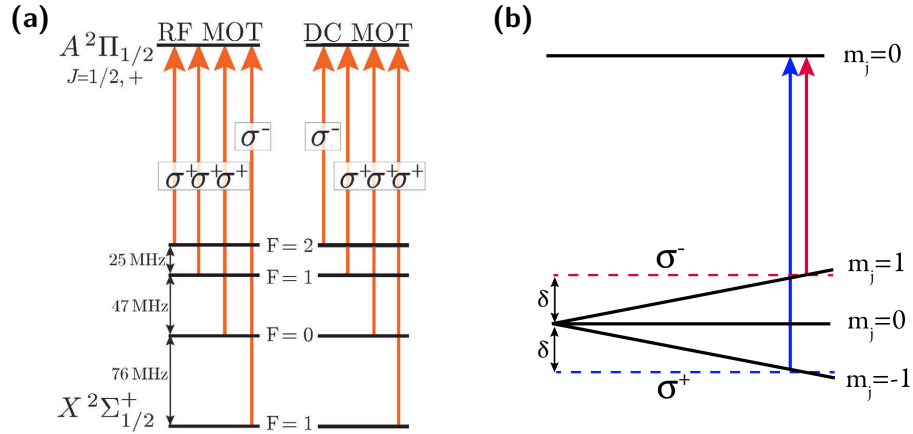
Figure 5.1.3: The optimal polarization scheme for a CaF MOT. The RF MOT polarizations are what one would naively expect from the g factors of CaF. The DC MOT polarization is due to the fact that one wants opposite polarizations around the top F=2 state. The polarization of the F=0 and F=1-states do not play a significant role as they only provide repumping and not a force. (b) The dual frequency MOT.

excited state g factor is negative. The excited state used for CaF is an $A^2\Pi_{1/2}$ state where the g-factor is very small (0.02) since the magnetic moments of the spin and orbital angular momentum are in opposite directions with nearly equal magnitudes (mixing with $^2\Sigma_{1/2}$ state increases the g factor slightly). By contrast, $g \sim 1$ for the lower state, so the ratio of g_e to g_g is small, leading to a very weak trapping. One solution is to use an RF MOT and switch polarizations and the field gradient. The switching must be fast enough for the change to be non-adiabatic, with the strongest force obtained when the switching frequency is on the order of the pumping time. The other solution is to make use of a dual frequency effect as pointed out in [144]. This effect can provide strong MOT forces even when the excited state g factor is very small. The idea is as follows. Let's assume we have a ground state with F=1 and an excited state with F=0. If one applies σ^+ light blue detuned and σ^- red detuned, then a restoring force is present regardless of what internal state the molecule falls down to (m_f=0 obviously provides no force). This can very easily be implemented in CaF without the addition of any new beams simply from the fact that the spacing between the top F=2 state and the next F=1 state is 25 MHz, approximately twice of the typical MOT detuning. Then simply
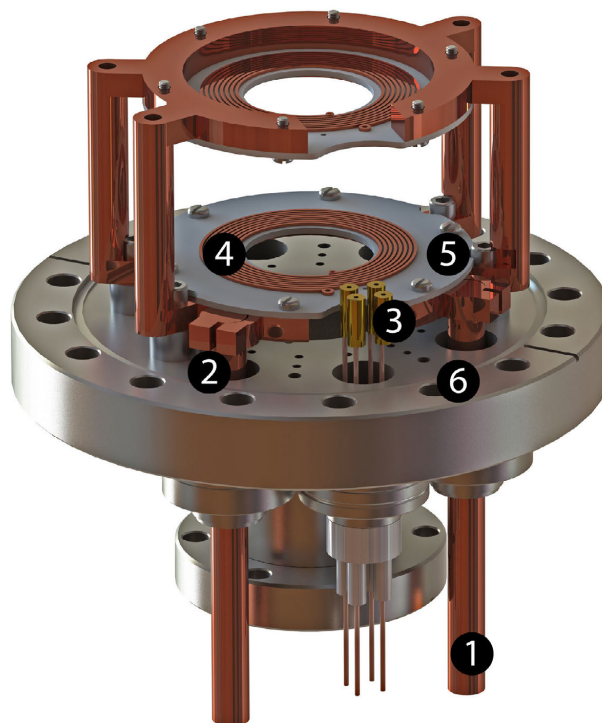
Figure 5.2.1: MOT coils for an RF MOT of CaF. (1) Copper feedthrough water-cooled outside the chamber. (2) Clamp to water cooling. A layer of gold foil helps the thermal contact. (3) Electrical feedthroughs. Lead-free solder is used to attach the coils to the wires. (4) MOT coils attached with ceramic adhesive. (5) Alumina boards. (6) UHV flange with tapped holes to mounts coils.

applying opposite polarization for the top two states is enough to give a MOT force. The other states do not provide a force and simply remix the system. The recommended polarizations for CaF are shown in Figure 5.1.3.

5.2 Experimental Realization

5.3 RF MOT Coil Design

While for typical MOTs the anti-Helmholtz coils are trivial to design, it is not the case for an RF MOT. For the CaF RF MOT, we needed to produce an axial field gradient of at least 10 G/cm RMS

for loading the MOT, and as high as possible for compressing it. The difficulty comes about due to switching high currents at megahertz speed. This switching gives rise to a large inductive spike, which creates high voltages (we drive up to 200,000,000 A/s, so the inductance should be on the order of μH). These high voltages can then create high electric field which can cause mixing of states with opposite parities and decays to states not repumped in the cycling scheme used. The high frequency also means the skin depth is very small, which causes additional heating in the coils. Thus, one can optimize for the lowest inductance while keeping the current low enough to prevent excessive heating. The coils are small, order inches, and situated inside the vacuum chamber to minimize the inductance and arcing risks. However, this placement complicates the heat management.

While many iterations of the MOT coils took place, we will primary discuss the coils that were used in making a 3D MOT. The previous coils used to make the 1D MOT had a smaller inner diameter (ID) of 15 mm. A spiral coil with a wire width of 1 mm was mounted on a 1.5 mm thick alumina substrate. Each side had 12 turns with the boards spaced by 16 mm.

The 3D MOT coils, Figure 5.2.1, consist of two pairs of OFHC copper spirals which were photochemically etched (Newcut), each mounted on each side of two alumina boards with ceramic adhesive (Cotronics 940). Each coil is 1/32" thick and has 8 turns with a coil width of 0.03" and a gap of 0.02" and an ID of 1.4". The spacing between the coils is 1.6". These coils create a field gradient of 10 G/cm with 4.6 A.

At RF frequencies, due to eddy currents within a conductor, the current in a wire is localized to the surface with a thickness called the skin depth. The skin depth is defined as

$$\delta_s = \sqrt{\frac{2}{\omega\mu\sigma}} \tag{5.6}$$

where ω is the frequency, μ is the permeability, and σ is the conductivity. The skin depth of copper
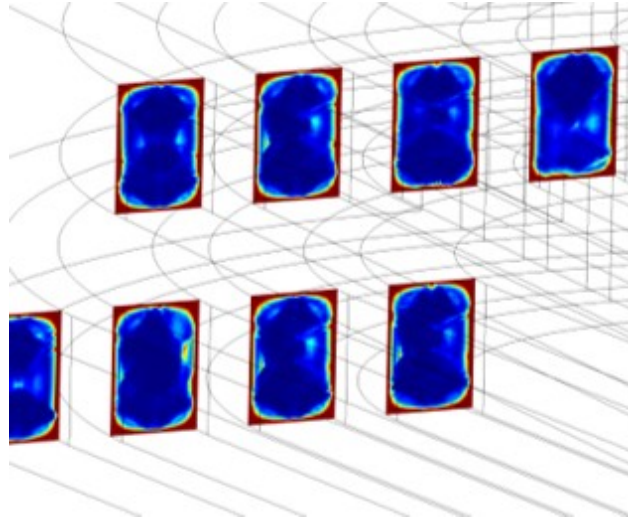
Figure 5.3.1: Simulation of the heat dissipation in the RF Coils at 1 MHz. Due to the small skin depth at this frequency, the current is localized to a thin 65 μm layer, drastically increasing the heat dissipation of the coils.

at 1 MHz is only 65 μm. This means that the resistivity goes up substantially since only a small fraction of the cross-section is responsible for carrying the current. Figure 5.3.1 shows the power loss in a simulation of the MOT coils at 1 MHz.

When driving the coils with 15 g/cm RMS, each coil generates nearly 50 W of heat - proper heatsinking was critical in the UHV chamber to prevent high outgassing rates as well as preventing thermal runways and changes in impedance matching. The alumina boards which mount the coils were attached onto two copper rings, which was connected to two 0.5" copper feedthroughs. A gold foil layer was added between the clamp and the feedthrough to increase thermal conduction. These copper feedthroughs were water cooled on the outside of the MOT chamber.

The thermal performance of the system was verified with a thermal imaging camera, shown in Figure 5.3.2. One can see fairly large gradients which arise from the limited thermal conductivity of alumina (25 W/(m K)). In future design aluminum nitrite (200 W/(m K)), which has almost an order of magnitude higher thermal conductivity, may be used. Figure 5.3.3 shows thermal sim-
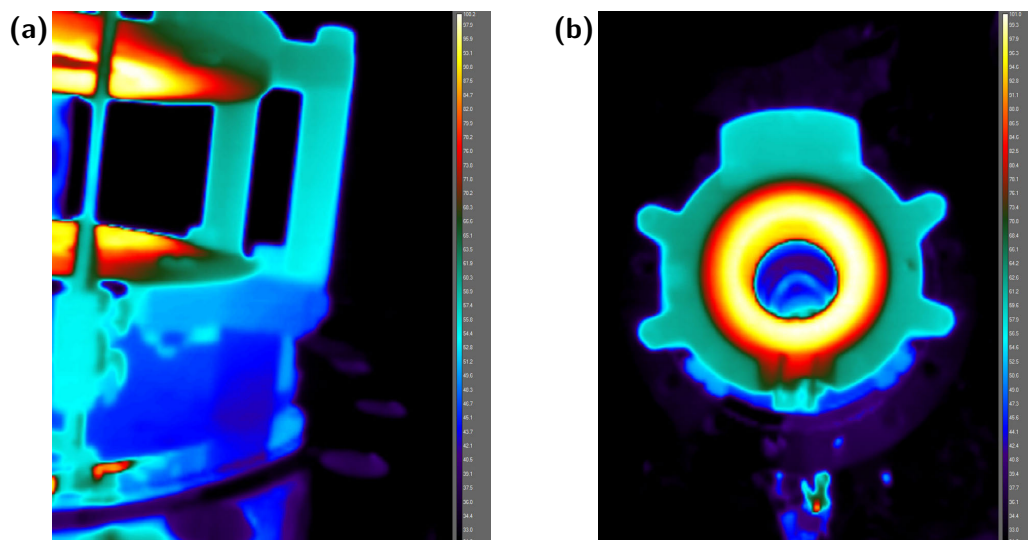
Figure 5.3.2: Thermal images of the MOT coils tested in air with 5 amps confirming good thermal contact to the water cooled feedthroughs.

ulations of the increased heat-sinking capability if AlN was used. This would become important for future designs where very high gradients from a compression stage may be added.[1]

5.3.1 ELIMINATING THE ELECTRIC FIELD REMIXING

To eliminates any RF electric fields, which would mix opposite parity states of the Λ-doubled A-state, $J = 1/2(+)$ and $J = 1/2(-)$ (Figure 5.3.4), split by 1.3 GHz, we use symmetric amplifiers. This prevents unwanted decay to the dark $X(N = 0, 2)$ rotational states. Previous RF molecular MOTs [95] required microwaves to remix these dark states, which reduced the overall scattering rate due to coupling of additional ground states, or complex winding patterns [146] which only reduced the electric field. The problems can most clearly be understood by considering the electric potential which is being applied on the MOT coils when driving a sinusoidal current through the coils. A large voltage is created due to the inductance of the coils. The voltage on the input of the

---

[1]AlN is very difficult to machine. It is possible to use machinable ceramics such as Shapal™, which has nearly as high thermal conductivity as AlN.
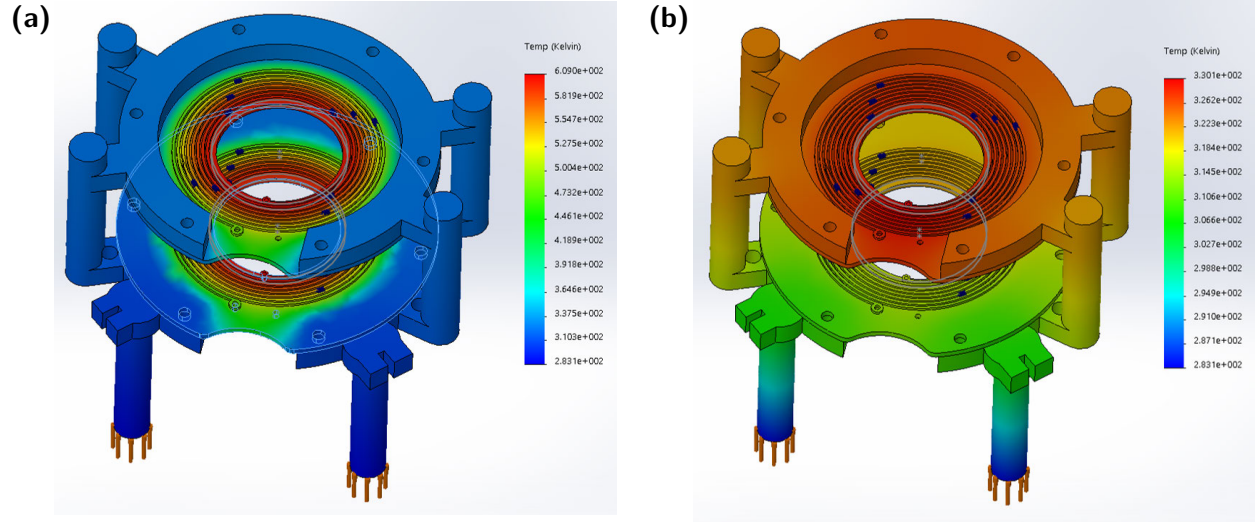
Figure 5.3.3: Thermal simulation of the cooling of the MOT coils with (a) aluminum nitride ($\Delta = 50$ K) and (b) alumina ($\Delta = 300$ K).

coils is the highest and the output is the lowest. If both anti-Helmholtz coil are connected in series, then the first coils will have a net positive voltage with respect to the second coils. This net potential difference between the top and the bottom creates an electric field, which is found at the center on the MOT. Figure 5.3.5 shows the potential and field from driving the coils in series

This electric field causes a remixing rate [146]

$$\tau_{Mix} = \frac{4 \times \omega_\Lambda^2 + \Gamma/4}{R_{scat}(d_A E/3)^2} \tag{5.7}$$

where $\omega_\Lambda = \frac{1}{2}\Lambda$ doubling splitting $= 650$ MHz, $d_A =$ A state electric dipole moment $= 4.1$ D, and $R_{scat} = 1.4$ MHz.

For the original 1D MOT coils run at 1 MHZ with a 12 G/cm field, an electric field of 2000 V/m translates to a lifetime of 2.7 ms. For the new larger 3D MOT coils, at 1 MHz with 5.4 A to give 12 G/cm, leads to a 13000 V/m field, or a 0.07 ms lifetime. With a semi modified wiring of half the top coil, bottom coil, rest of the top coil, the field is reduced to 3000 V/m, which is still only

$$A\ ^2\Pi_{1/2}$$

J=1/2,+
J=1/2,-
1GHz

$$X\ ^2\Sigma^+_{1/2}$$

N=2,+
N=1,-
N=0,+
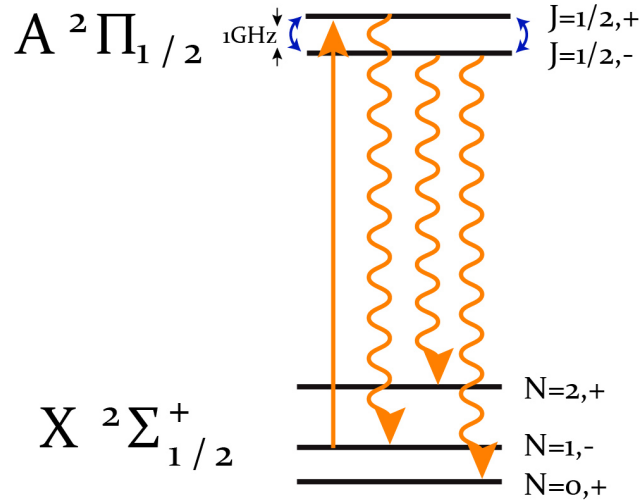
Figure 5.3.4: Mixing of opposite parity states caused by an electric field, in blue. This mixing causes decays to opposite rotational states which are not repumped.

1.4 ms. By contrast, using the parallel wiring there is only around 10 V/m, Figure 5.3.6, which gives a lifetime of 130 seconds. At this point the lifetime will be limited by other factors, such as losses to higher vibrational levels or collisions with background gas.

5.3.2 High Power Drivers and Impedance Matching

To produce the field gradient necessary for the RF MOT, we use two RF amplifiers (ENI 550L) each producing ∼150 W (one for each pair of coils), resulting in a field gradient of 14 G/cm RMS at ∼1.4 MHz. To match the impedance of the coils to that of the amplifier, we used an LC impedance matcher, shown in Figure 5.3.7. The impedance matcher consists of an air core inductor and high voltage capacitors. No ferrite core was able to produce high enough Q-factors and not catch on fire. Vacuum variable capacitors are used to tune the capacitance because they are resistant to arcing and melting at the voltages and currents used. Fixed high voltage doorknob capacitors are used to increase the capacitance beyond the tuning range of the vacuum variable capacitor. The impedance
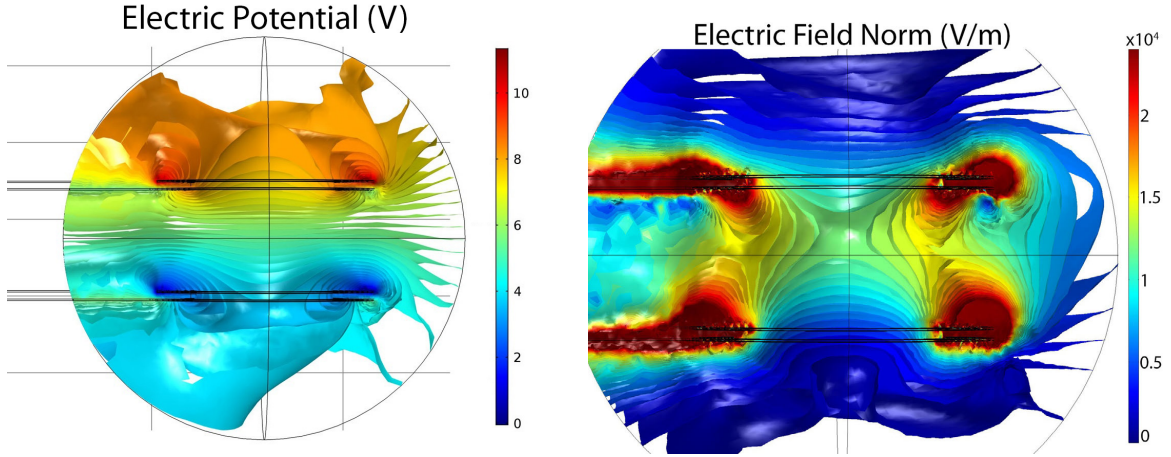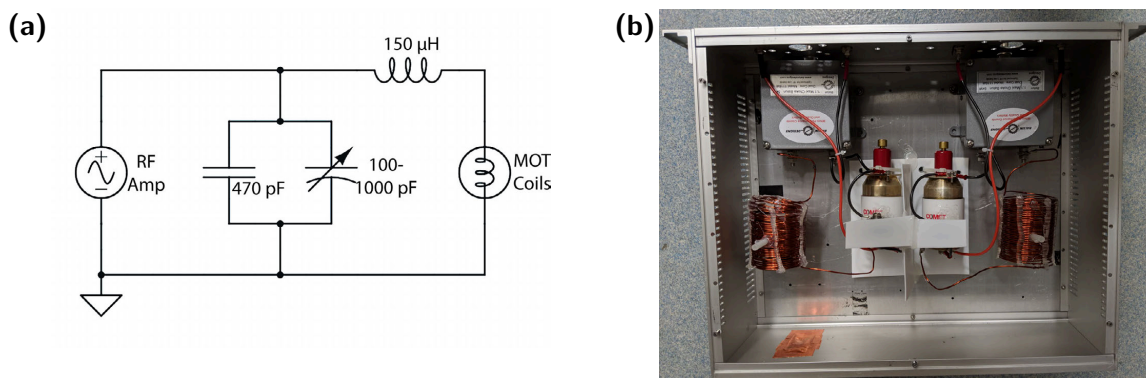
Figure 5.3.5: Electric potential and field generated by the MOT coils. Simulation is run at 1 MHz, 5.4 amp, 8 turn wire. The electric field in the center of the MOT is 13000 V/m.
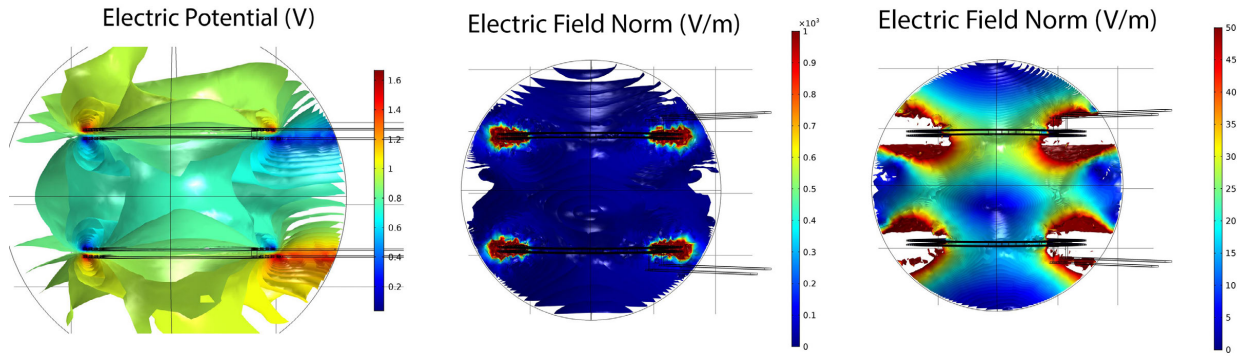
Figure 5.3.6: Electric potential and field generated by the MOT coils in parallel. Simulation is run at 1 MHz, 5.4 A, 8 turn wire. The electric field in the center of the MOT is 10 V/m.

(a)

(b)

**Figure 5.3.7:** (a) Impedance matching circuit diagram for 3D MOT coils. (b) Built circuit.

matcher is housed inside of a metal case to shield it from leaking noise across the entire lab. BNC cables with high shielding are used to deliver the current to the coils. The impedance matcher when properly tuned has a voltage standing wave ratio (VSWR) of 1.2 (21 dB return loss) at the desired 1.4 MHz.

5.4 MOT Detection

The molecules in the MOT are detected via their fluorescence (X→A transition at 606 nm), which is simultaneously recorded on both a PMT and an EMCCD for time and spatial information, respectively. A multi-lens objective in front of both devices is used to image and spatially filter the MOT fluorescence. The signal to noise is limited by background scattered light. Due to this, we went to great lengths to decrease the scattered light to be maximally sensitive to a very small MOT signal.

5.4.1 Scattered Light Reduction

One of the primary motivations for moving to the large 3D MOT coils was to increase the distance between the MOT beams and the MOT coils. Everything in the chamber, including the coils, was

(a) **(b)**
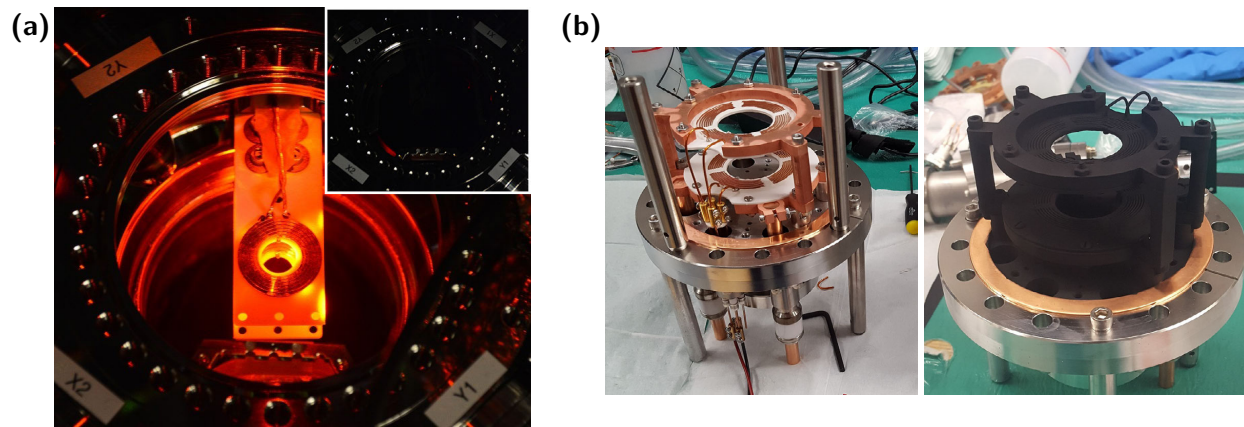
Figure 5.4.1: Blackening of MOT coils to reduce scattered light. (a) Old 1D MOT coils before and after blackening. (b) New 3D MOT coils before and after blackening.

blackened to reduce stray light. Various method of blackening exist. Appendix C gives a comparison of various blackening methods and outgassing measurements. Due to good performance and ease of application, we opted to cover everything in the chamber with MH2200 paint from Alion. This is UHV compatible silica-based paint which is nonconductive. Figure 5.4.1 shows the 1D and 3D MOT coils before and after blackening.

Custom windows were also used to further decrease scattered light. Unfortunately, during the brazing process, most commercial UHV windows become covered with a thin layer of grime which causes high scatter, as seen in Figure 5.4.2(a). The DeMille group had solved this problem by gluing their own windows [147]. We did the same, with a 10-5 substrate (CVI PW1-2037-UV) coated with a 606 nm V coating(Thin Film Labs) on a CF to KF adapter. One very important thing to note is that after the AR coating run, the windows should be re-cleaned prior to gluing. It is exceedingly difficult to clean the inside of the windows properly after gluing. We tried various types of glue to be able to bake the chamber. One candidate, Epotek 353ND can operate at temperatures up to 250 °C. Unfortunately, it requires a minimum cure temperature of 80 °C, and 150 °C for full strength, according to the specification sheet. When we tried curing at these temperatures, large stresses formed in the window, Figure 5.4.2(b/c). We then tried to do a two-part cure, first at 55 °C,
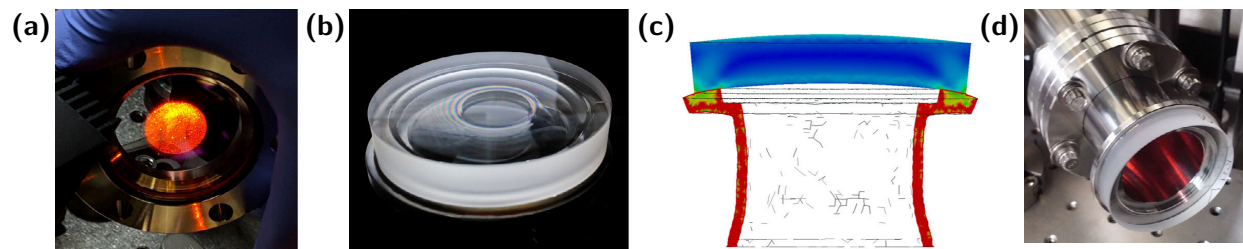
Figure 5.4.2: (a) Scattered light from a commercial window. (b) Stress in the glued Epotek window. (c) FEM simulations of the stresses due to the curing schedule. (d) Scattered light from a homemade window.

and then a post cure at 80 °C. After curing with this process, all eight windows held vacuum[2]. Later on, we had to replace these windows and switched to a lower temperature epoxy. We found that the use of Epotek 302-3M was much easier to use as it is able to cure at room temperature. These glued windows reduced our scattered light by nearly an order of magnitude over commercial windows, Figure 5.4.2(d).

5.4.2   MOT Imaging System

The imaging system underwent many iterations, from first having to detect both 331 nm and 606 nm florescence, but without much care given to resolution, to imaging both the MOT and an ODT 40 μm in size simultaneously. This final iteration is shown in Figure 5.4.3. With it we are able to image both the 780 nm light from an ODT or tweezer as well as the MOT/molasses after 30 ms drop times. This large field of view is very important for measuring low temperatures. The camera used is a Luca R EMCCD and the PMT is a Hamamatsu R7600.

---

[2]While the Epotek 353ND windows never cracked while under use, even with several vacuum cycles, after they were removed and sat on a shelf for about two years, they had all cracked. It is not clear what caused this, but something to be aware of.
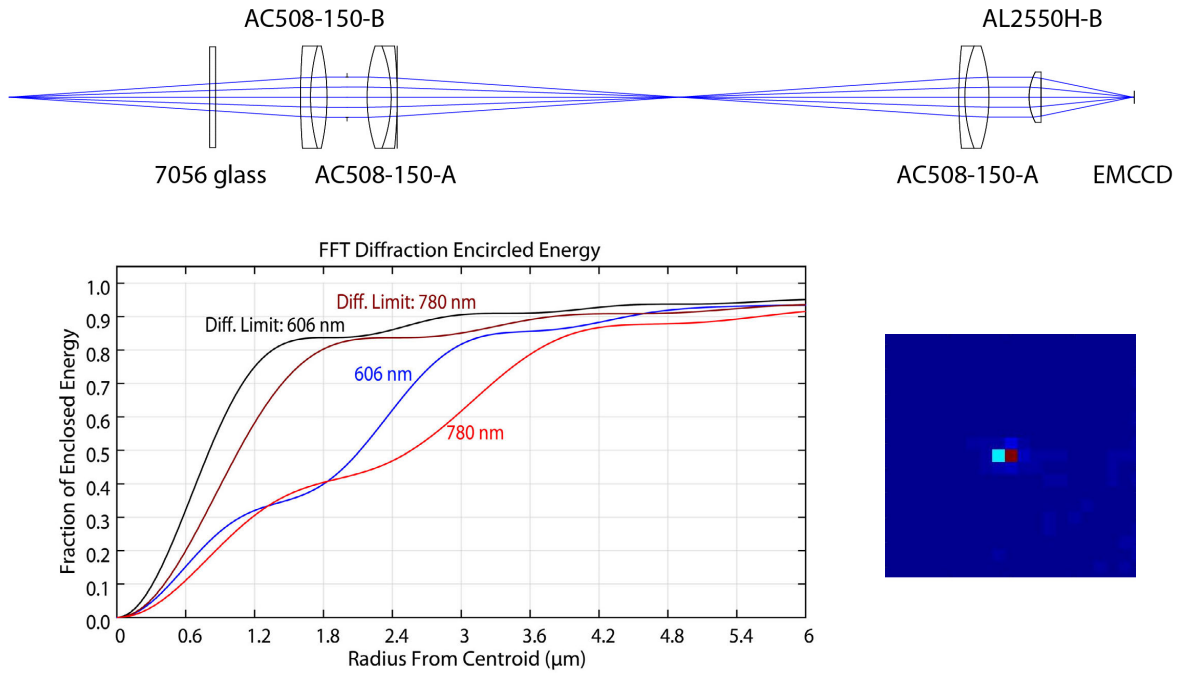
Figure 5.4.3: Luca imaging system for the MOT and ODT. This imaging system has a wide field of view and is nearly diffraction limited. The pixel size of the Luca R camera is 8x8 μm. The system is able to image both 780 nm light, for ODT/tweezer positioning purposes, as well as 606 nm fluorescence from the MOT and ODT. Note there is a chromatic shift between the two wavelengths which shifts the focus slightly. Bottom right: Image of the 780 nm light.
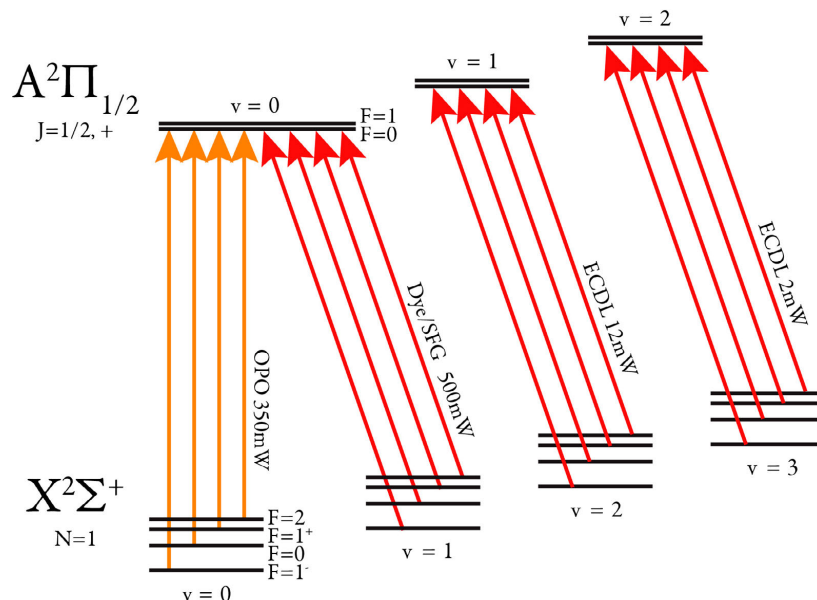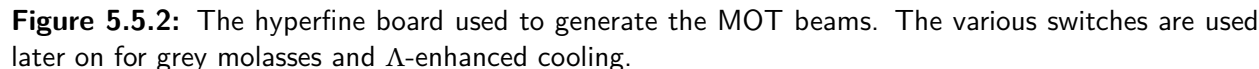
Figure 5.5.1: Transitions addressed in the experiment for the 3D MOT. The hyperfine sidebands of the main and $v{=}1$ are generated by the hyperfine board, Figure 5.5.2. The $v{=}2$ and $v{=}3$ repumps have sidebands created by an EOM. The laser generating the light and the approximate total power seen by the molecules is labeled next to each transition.

5.5 LASERS

The MOT is operated on the $X^2\Sigma^+ \to A^2\Pi_{1/2}$ transition. All of the addressed transitions are shown in Figure 5.5.1. RF sidebands produced by a series of acousto-optic modulators (AOMs) address all hyperfine transitions. This is done with what is referred to as the hyperfine board, shown in Figure 5.5.2. This allows us to set the polarization and frequency of each hyperfine component independently, allowing the use of the optimal polarization scheme for both the DC and RF MOTs. It also allows us to change the relative powers and frequencies need for Λ-cooling, discussed in later chapters. At full power, each MOT beam contains 60 mW of $X(v = 0) \to A(v = 0)$ light and 80 mW of $X(v = 1) \to A(v = 0)$ light.

Figure 5.5.2: The hyperfine board used to generate the MOT beams. The various switches are used later on for grey molasses and Λ-enhanced cooling.

5.5.1 606nm OPO Laser $\left(X(v=0)\rightarrow A(v=0)\right)$

The $X(v=0)\rightarrow A(v=0)$ light is generated by an Acculight Argos SF OPO. This is an monolithic MgO:PPLN OPO-SFG system which is pumped with a 15 W 1064 nm IPG fiber laser. The 1064 nm light is split into two IR photons, at 1407 nm and 4365 nm, in an OPO. The longer wavelength photon is dumped and the other is then recombined with a 1064 nm photon in an SFG process to generate 606nm light. Unfortunately this laser is little more than an overpriced price of junk. The fundamental issue is that the laser relies upon a cavity to ensure the OPO process and SFG process happens for a single wavelength only. While the laser appears to be single frequency if looked at on a wavemeter, it is far from it when monitored on a high finesse cavity, Figure5.5.3(b). The laser is very often multimode, and these additional frequencies can easily destroy the MOT. Many hours were wasted due to this unknown behavior early on, with the experiment working for a few hours,
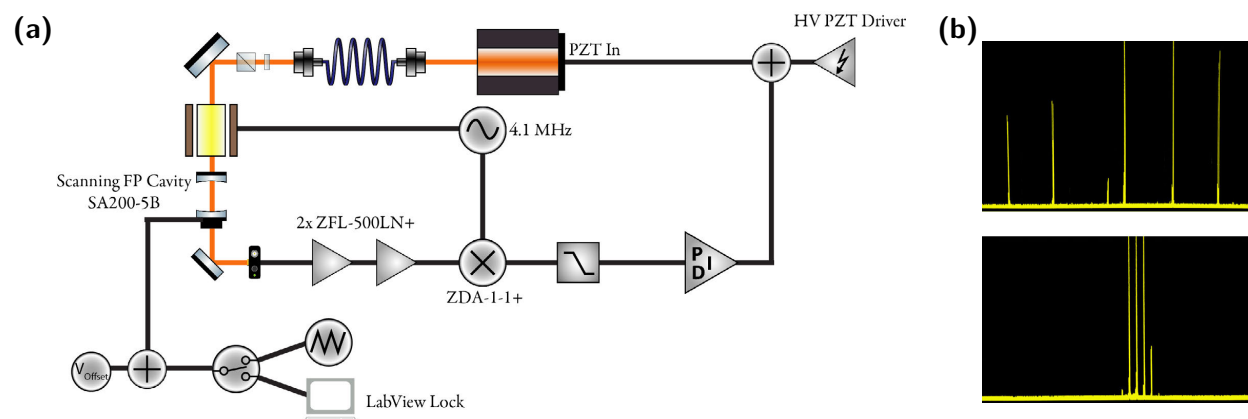
Figure 5.5.3: (a) OPO locking setup. An EOM adds sidebands to the laser which enters a scanning Fabry–Perot cavity. The OPO is locked in transmission by demodulating the light that makes it through the cavity with the sideband frequency. The RF portion is amplified, mixed, and low pass filtered to create an error signal. This error signal is then locked with a home built PID lockbox and fed back to the piezo of the OPO. The wide bandwidth tuning is done by the wavemeter/LabVIEW which moves the cavity to the desired wavelength and provides the long term locking feedback. (b) OPO spectrum when multimode on a high finesse cavity.

then not working, and some days not working at all. The OPO must also be continuously purged to prevent absorption of a water line at the infrared wavelength used. The wavelength of the laser drifts so quickly when not locked, that the wavemeter PID feedback (10-20 Hz) from the wavemeter is too slow to lock the laser to less than the 10 MHz level. As a result, an analog prestabilization step was added to the OPO, where by the laser is first locked to a scanning cavity which provides a short term reference. The locking scheme is detailed in Figure 5.5.3(a). When the laser is single mode, it has a narrow linewidth, but it may not 30 seconds later. The selling point of this laser was that it was fairly tunable. However, because Acculight used the wrong glue inside the cavity heater, the range is far more limited. If one wants tunability (and a always single mode laser), an 899 Dye laser is far superior and more reliable. If one simply wants a narrow linewidth laser with high power, a Raman fiber amplifier should be used. These are cheaper and deliver much higher powers at 606 nm. I have been told that Acculight no longer sells the visible OPO-SFG modules, probably for a good reason...
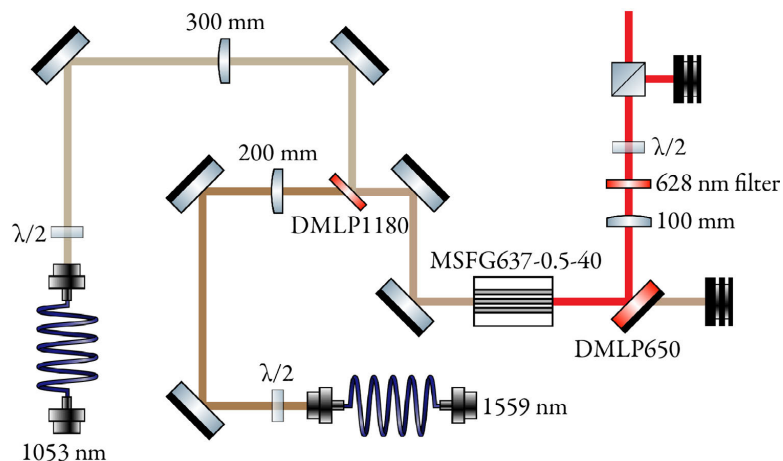
Figure 5.5.4: 628 nm SFG system. With 10 W of 1053 nm and 10 W of 1559 nm light, 7+ W of 628 nm light is produced. The SFG crystal is held at 63.77 °C.

5.5.2 628NM DYE AND SFG LASERS $(X(v=1) \rightarrow A(v=0))$

The $X(v = 1) \rightarrow A(v = 0)$ light for both the MOT and the slowing repump was generated until recently by two Coherent 899 dye lasers. These lasers are amazingly versatile, producing up to several watts of power tunable throughout the visible spectrum. Appendix D gives a guide to how these lasers work and some tips and tricks. Recently we replaced both of our dye laser with a single SFG system due to other experiments needing our dye laser and the ability to produce higher powers with the new system. The layout of the system is shown in Figure 5.5.4. This SFG system uses a periodically poled non linear crystal to achieve quasi-phase matching, the periodicity of which can be tuned using temperature. Since the nonlinear coefficient of lithium niobate is anisotropic, the polarization of the light should match this crystal axis. The crystal used is a doped MgO:PPLN with an effective nonlinear coefficient of 14 pm/V. The 5% MgO doping increases the resistance to photorefractive damage significantly. For optimal SFG efficiency, the light should be focused such that the ratio of crystal length to confocal parameter $(2\times$ Rayleigh range)is a factor of 2.84 (Boyd and Kleinmann model [148]). The optics were setup to achieve close to this condition, but slightly

off in favor of slightly larger beams. This was done to reduce the risk of crystal damage. The system is pumped with two 10 W fiber amplifiers at 1053 nm and 1559 nm[3], and produces up to 7.5 W of 628 nm light.

5.5.3 628.5 NM INJECTION LOCKED ECDL LASERS $(X(\nu = 2, 3) \rightarrow A(\nu = 1, 2))$

The light for the ν=2 and ν=3 repumpers is generated by two injection locked pairs of ECDLs. To hit the desired wavelength, one needs to cool the laser diodes slightly. This was originally done with a homebuilt -40°C ECDL using the HL63133DG diode (λ =638 nm, P=170 mW). We found it beneficial to replace this with a HL63163DG(λ =633 nm, P=100 mW) since it did not have to be cooled as much. We also replaced all of the ECDLs to unibody Steck design ECDLs [149]. This dramatically increased the stability of the lasers, allowing them to remain locked for days rather than ∼hour time scales. Both lasers have injection locked pairs to increase the power of the system. This allows us to run the seed ECDLs at lower current, increases their long-term stability and reliability. These lasers are then combined into a single polarization to go through a hyperfine EOM. This method of combination is highly inefficient. A future experiment with more optical access would be able to send two independent beams into the MOT chamber with higher power and without the need of the injection locked pairs.

5.6   1D MOT

Before directly looking for a 3D MOT of CaF, we first looked at a 1D MOT. To ensure the MOT coils were properly wired and producing the desired gradient in the chamber, we began by looking at the fluorescence of the molecular beam with the coils turned on. The large magnetic field, much

---

[3]Avoid NP lasers at all cost. It took 10 months for them to deliver a 1559 nm laser with a lead time of 3 months and it which never reached the specified power of 10 W, even after shipping it back twice.

**(a)** BOP Off   **(b)** BOP On   **(c)**
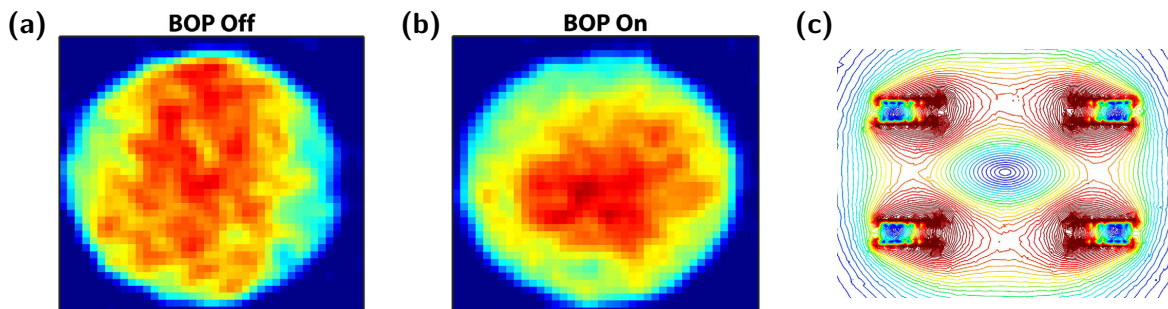
Figure 5.6.1: Zeeman detuning of the molecular beam. (a) Molecular beam illuminated with the z beam with no field. (b) Molecular beam detuned with the anti-Helmholtz MOT coils. (c) Magnetic field profile over detection area.

(a)   **(b)**   **(c)**
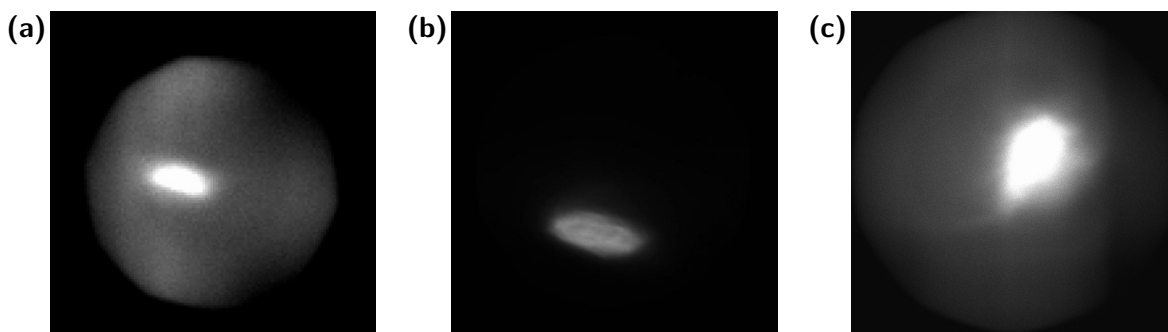
Figure 5.6.2: Atomic MOTs. (a) Erbium DC MOT (b) Ytterbium DC MOT (c) Ytterbium RF MOT

larger than the MOT field, allowed us to Zeeman detune the molecules away from the center out of resonance, as shown in Figure 5.6.1. We also made a few atomic MOTs to ensure that all of the beams for the 3D MOT were well aligned, shown in Figure 5.6.2. In doing so we also found an error in the optics. Namely that circular polarized light is not an eigenvalue of a 45 degree mirror. This means that to create clean circularly polarized light, the waveplate should be the last element before the MOT. We had hoped to avoid this since the waveplates were a large contributor to scattered light into the MOT chamber due to their relatively poor surface quality[4]. Optimization was also much easier as the atomic MOT could be seen in a single shot. (This would not be the case for CaF for
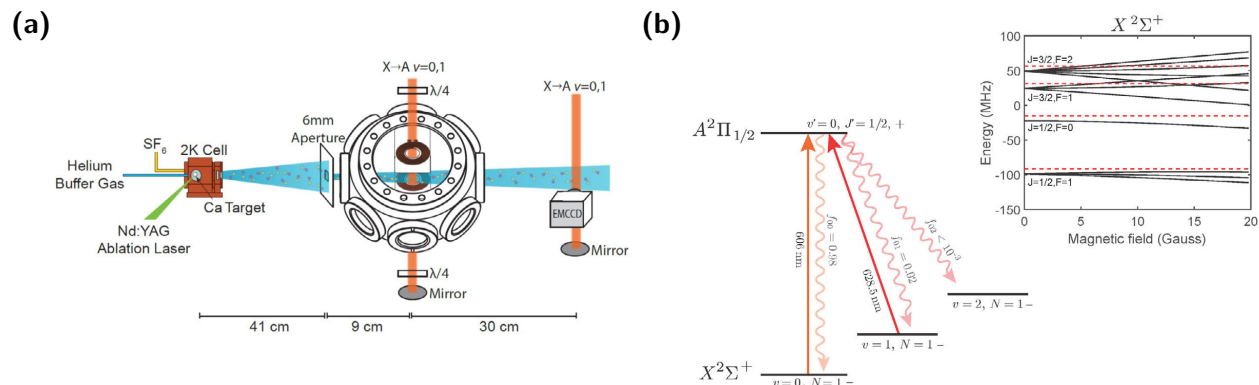
Figure 5.6.3: (a) Setup for looking at both deflection and the 1D MOT. (b) Transitions addressed for the 1D MOT. Inset: Zeeman structure of the ground state with the red lines showing the detuning used for the 1D MOT.

quite some time).

With the optics correctly ordered, we then looked for deflection of the molecular beam. We sent a single transverse beam into the MOT chamber and looked at the florescence downstream to verify we could apply forces on the molecules and detect it. The setup and transitions addressed are shown in Figure 5.6.3. Figure 5.6.4 shows the the deflected molecular beam downstream. The observed deflection corresponds to around 300 scattered photons.

We then looked for magneto-optical compression of the molecular beam. For this we use the $X(v = 0) - A(v' = 0)$ transition along with one vibrational repumper. When red detuned, the transverse beams Doppler cool the beam. The addition of a magnetic field gradient allows not just cooling, but compression of the molecular beam. With an RF MOT, we expect the compression to occur when the polarization and field gradient are in phase, while when out of phase, anti-compression should be present. By observing the molecular beam downstream from the 1D MOT region, we were able to observe these changes in the molecular beam width.

---

[4]Foctek's optically contacted waveplates exhibit much less scatter than Thorlabs waveplates.

(a)

(b)
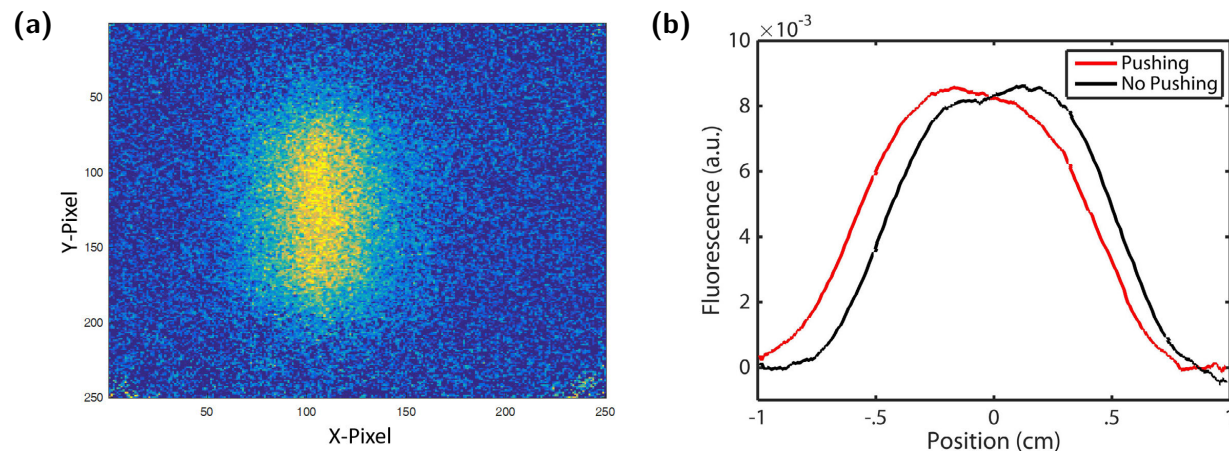
Figure 5.6.4: (a) Molecular beam imaged 39 cm downstream of the aperture. Imaging beam is vertical. The molecular beam width is the distance from top to bottom. (b) Deflection of the molecular beam with a single beam in the MOT region.

We then turned on the RF coils and search for a phase (between the magnetic field and polarization) dependent force. Figure 5.6.5 shows the width of the molecular beam as set by the upstream aperture. In the absence of the magnetic field, Doppler cooling (heating) is observed with red(blue)-detuning of lasers. The direction of the magneto-optical force is seen to reverse with blue-detuning of the lasers compared to the case with red-detuning as expected. The data was fitted to a Monte-Carlo simulation, Figure 5.6.5. The solid lines of the simulation agree with scattering 150 photons, which corresponds to a photon scattering rate of 2 MHz. This agrees with the expected scattering rate based on the measured laser powers and transition strengths.

At a detuning of 7 MHz, the optimal compression is achieved with a magnetic field gradient of 7.3 Gauss/cm. Several other field gradients were tested but the compression effects were significantly reduced compared to the optimal gradient. This is due to the small hyperfine splitting of CaF which leads to level crossings between magnetic sublevels of different hyperfine states around the 5 Gauss level. This increases the probability of scattering anti-confining photons, and thus weakens the compression effect.
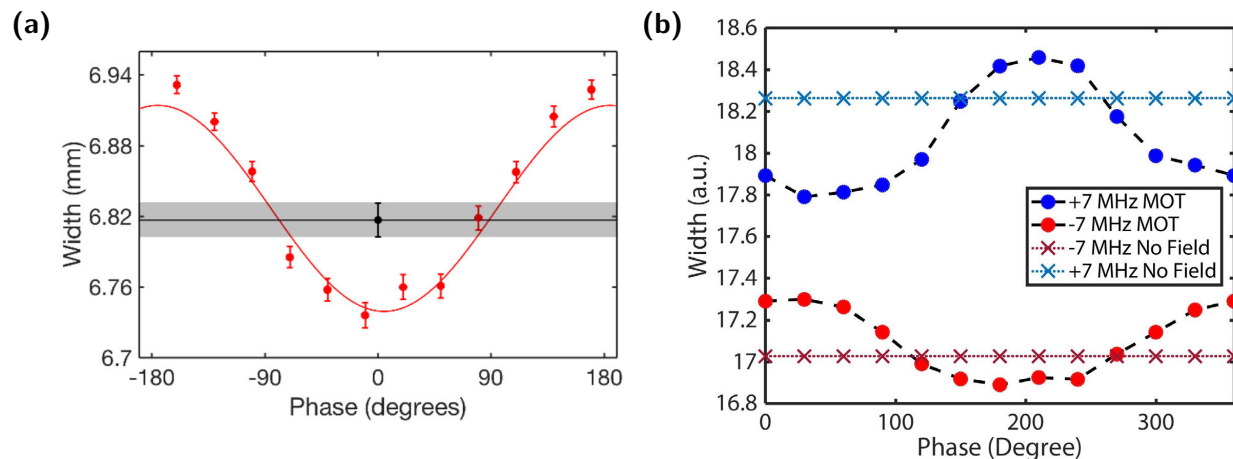
Figure 5.6.5: (a) 1D MOT phase vs beam waist. The black line shows the no field width (Doppler cooling). Each point has a few hundred averages. The measured beam profiles are fit using super-Gaussian functions of order 4 with their amplitudes, beam widths, and centers as free parameters. (b) Magneto-optical compression for both blue and red detuned light centered about the Doppler heating and cooling widths. The sign of the compression versus phase is flipped.

From the 1D MOT, we could estimate that an on-axis molecule would have a capture velocity for the 3D is about 10 m/s. With a 3D MOT Monte-Carlo simulation of trap loading we find that the capture velocity averaged over all transverse positions of the trap is about half of the ideal on-axis estimation, resulting in an effective capture velocity of about 5 m/s for the molecular beam as a whole.

5.7   3D MOT

After realizing the 1D MOT, we installed the new SF_6 source (see Chapter 3), switched to slowing on the X-B transition (see Chapter 4), and installed the new larger RF MOT coils into the vacuum chamber. We began by first verifying that we could see slow molecules down to about 30 m/s (We no longer had an in-vacuum lens so we could not see molecules much slower than this). We also first looked for a DC MOT rather than the RF MOT as that had less parameters which had to be adjusted
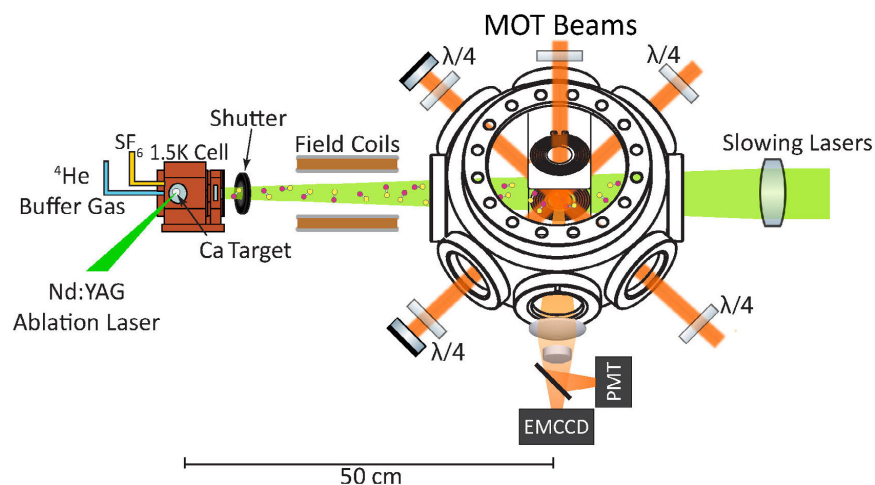
Figure 5.7.1: Experimental layout for the 3D MOT.

(namely the lack of the phase between the field and polarization). The initial search for the MOT used a PMT where we looked for a decaying signal of trapped molecules. The experiential layout is shown in Figure 5.7.1.

We saw our first 3D MOT signal when we significantly extended the slowing duration. Based on our slowing data, it seemed like molecules traveling at around 10 m/s would arrive about 5-7 ms after the slowing light was turned on. It became clear that whatever population we were monitoring with our slowing detection was not the one which was loaded into the MOT. Figure 5.7.2 shows a scan of the slowing duration the molecules loaded into the MOT. The optimal slowing time of 16 ms was almost three times longer than what we had seen as the arrival time of 10 m/s molecules. The most logical explanation of this is that the capture velocity of this original MOT was much lower than we though, probably closer to 2-3 m/s level. This was mostly likely due to the fact that the MOT was far from optimized at this time (polarizations[5], MOT beam alignment, and gradient were not optimal).

---

[5]To reduce the effect of reflected light adding scatter, the quarter wave-plates were angled slightly in the retro-reflected arms. This unfortunately made them no longer act as perfect quarter wave-plates. Straightening them increased the MOT lifetime and the number loaded by about a factor of two.
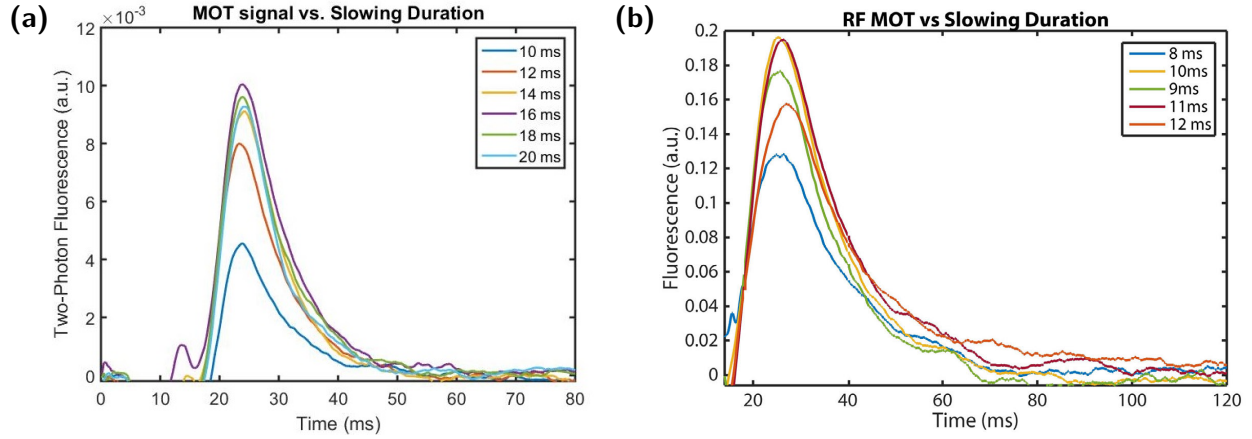
Figure 5.7.2: (a) Scan of the slowing duration vs loading of the original DC MOT. (b) Scan of the slowing duration vs loading of the original RF MOT.
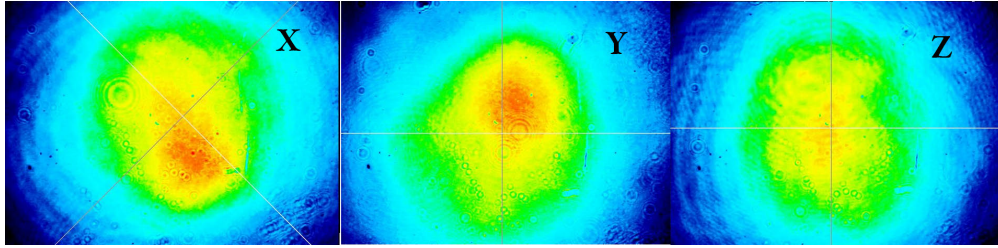

Figure 5.7.3: Beam profiles of the MOT beams. The $1/e^2$ diameter is 11 mm.

The MOT beams have a $1/e^2$ diameter of 11 mm; the beam profiles are shown in Figure 5.7.3. The peak intensity driving the $X(v = 0) \rightarrow A(v = 0)$ transition at the center of the MOT is $I_0 \equiv$ 750 mW/cm^2. The intensity among hyperfine components are distributed by degeneracy, hence 5,3,1,3 for F=2,1,0,1 respectively. We checked this dependence by looking at the fluorescence of the molecular beam, as shown in Figure 5.7.4. Attenuating the intensity of the F=0 beam by a factor of 4 has nearly no effect, while attenuating the F=2 states does.

Initially insufficient gradients cause very odd shaped MOTs initially. Increased gradients helped both the loading of the MOT and the density, Figure 5.7.5.

After characterizing the DC MOT, we switched to the RF MOT. At this point, the MOT beams
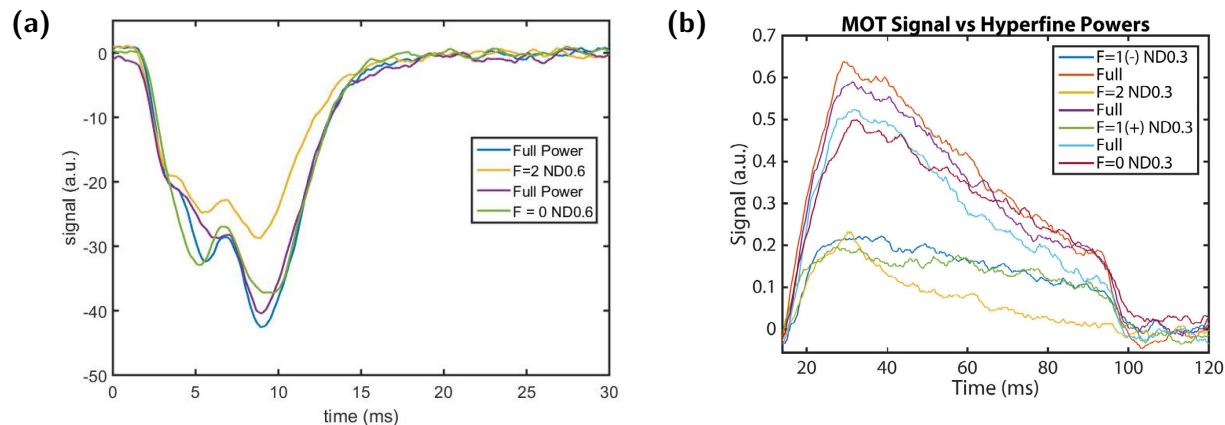
Figure 5.7.4: (a) Effect of the molecular beam fluorescence when attenuating various Hyperfine components. The observed effect is consistent with the fact that the intensities should be distributed by the number of m_F states rather than evenly among F states. (b) Effect while looking at the 3D MOT fluorescence.
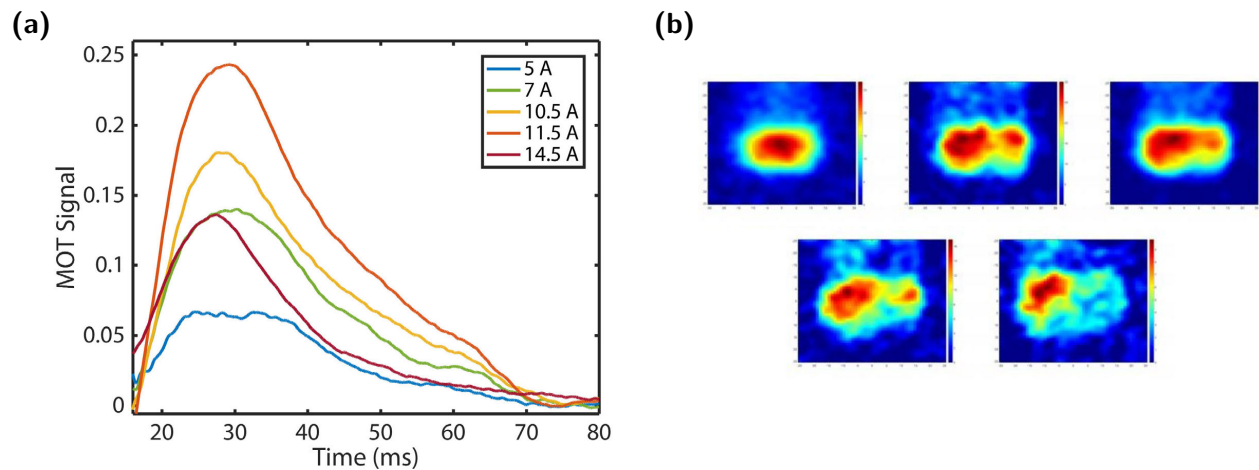

Figure 5.7.5: (a) MOT fluorescence vs various MOT gradients. (b) Images of the MOT with the various gradients plotted in (a).
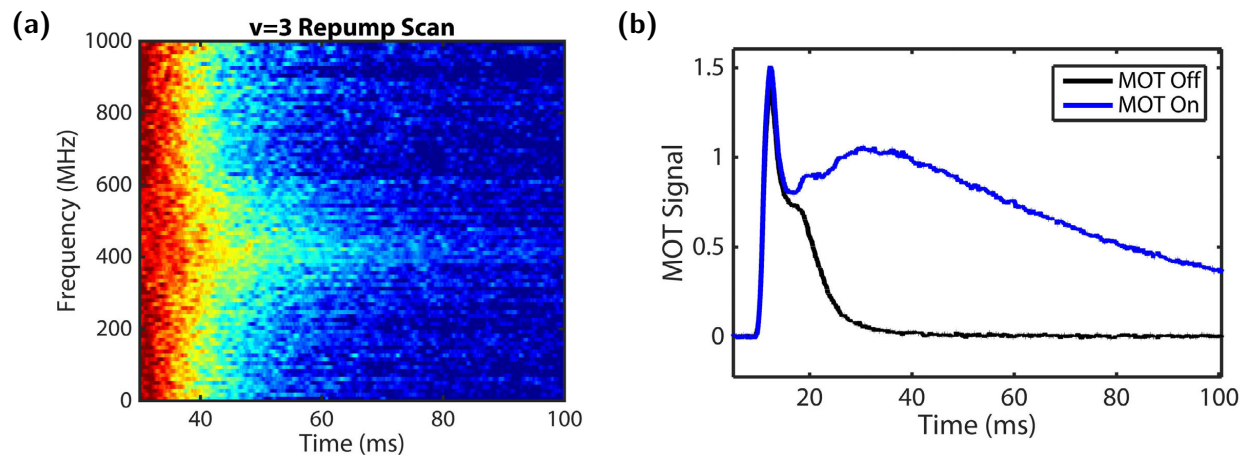
Figure 5.7.6: (a) $v=3$ vibrational repump scan observing the MOT fluorescence. The $v=3$ frequency shows an increase in the MOT lifetime. (b) PMT trace of the MOT lifetime with the $v=3$ vibrational repump.

were better aligned, and the RF MOT gave a higher capture velocity than the DC MOT. This translated into an optimal slowing duration was around 10 ms, Figure 5.7.2, much closer to what we had seen from our slowing optimization.

The MOT lifetime was determined by measuring the decay of the fluorescence on the PMT. Decreasing the intensity of the MOT beams, and thus the scattering rate, increased the MOT lifetime inversely proportionally to the scattering rate. We found a MOT lifetime of $\tau = 20$ ms at high intensity without repumping the $v = 3$ state, in line with expectations based on CaF's Franck-Condon factors. Adding a $v = 3$ repump laser, we find a lifetime of $\tau = 85$ ms, Figure 5.7.6. We found that DC and RF MOT have roughly equal lifetimes at the same scattering rate, confirming the electric field in the RF MOT is suppressed to a level less than one tenth of the decay rate into $v = 3$, as expected from the use of the symmetrical amplifier configuration.
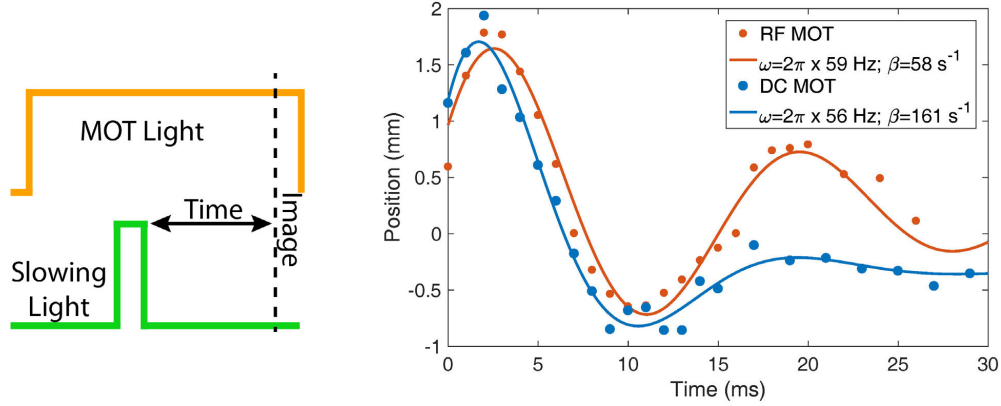
Figure 5.8.1: MOT trap frequency measured following a 1 ms push with the slowing laser. The equilibrium positions of the RF and DC MOTs are different since the dc remixing field in the slowing region shifts the center position of the DC MOT.

5.8 COMPARISON OF AN RF VERSUS A DC MOT OF CaF

With the ability to create both an RF and DC MOT, we could directly compare the performance of each. It should be noted that the MOT may have been improved since some of these measurements were taken, due to improvements in beam alignments, frequency, cancellations of stray fields, etc.

The trap frequency and damping constant were determined by recording the position of the molecular cloud following a 1 ms pulse with the slowing beam (Figure 5.8.1). At a gradient of 14 G/cm and the MOT beams at an intensity of I_0, the molecular cloud in the DC MOT oscillates in an underdamped fashion at $2\pi \times 56(2)$ Hz with a damping coefficient of $161(20)$ s^{-1}. The RF MOT with a 14 G/cm RMS field gradient oscillates at $2\pi \times 59(2)$ Hz and a damping coefficient of $58(10)$ s^{-1}.

The temperature of the MOT was determined by time-of-flight (TOF) expansion (Figure 5.8.2). The MOT beams and magnetic field are turned off for varying lengths of time, τ_{TOF}, followed by a 1 ms MOT laser imaging pulse. A laser intensity of $I_0/32$ is used to reduce any heating effects during imaging. This also ensures we image the MOT below saturation. We fit the radial and axial
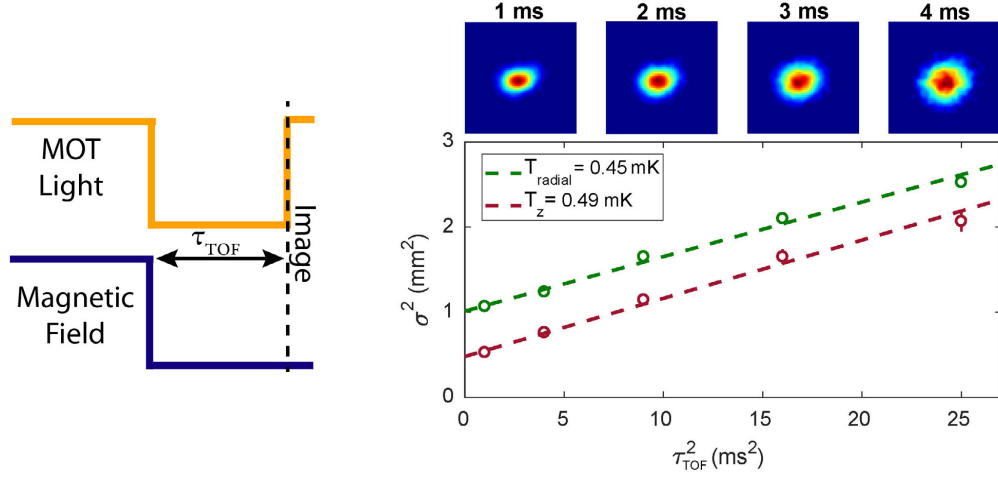
Figure 5.8.2: Time-of-flight expansion of the molecular cloud to measure temperature. The slope of the plot of the diameter squared vs time squared is proportion to the temperature. Image field of view is 10 × 10 mm.

temperatures to a 2D Gaussian with the difference of initial and final widths after expansion,

$$\sigma^2 - \sigma_o^2 = k_B T \tau_{TOF}^2 / m_{CaF} \tag{5.8}$$

The temperature is then $T_{axial}^{2/3} T_{radial}^{1/3}$.

The high temperatures measured of the MOT can be explained by a Sisyphus heating mechanism as described in more detain in the following chapter. To achieve lower temperatures and higher densities, while maximizing the number of trapped molecules, we load our MOT at full intensity and hold until any initial oscillation damps out. We then ramp down the intensity of the X($v = 0$)→A($v = 0$) transition over 15 ms and hold for 10 ms to ensure thermalization at the lower intensity. In the DC MOT, we find the temperature decreases with decreasing intensity from $T = 5$ mK to $T = 560(110)$ μK at $I_o/64$. At lower intensities, the cloud size rapidly grows due to the limited restoring force (Figure 5.8.4). The RF MOT reaches lower temperatures than the DC
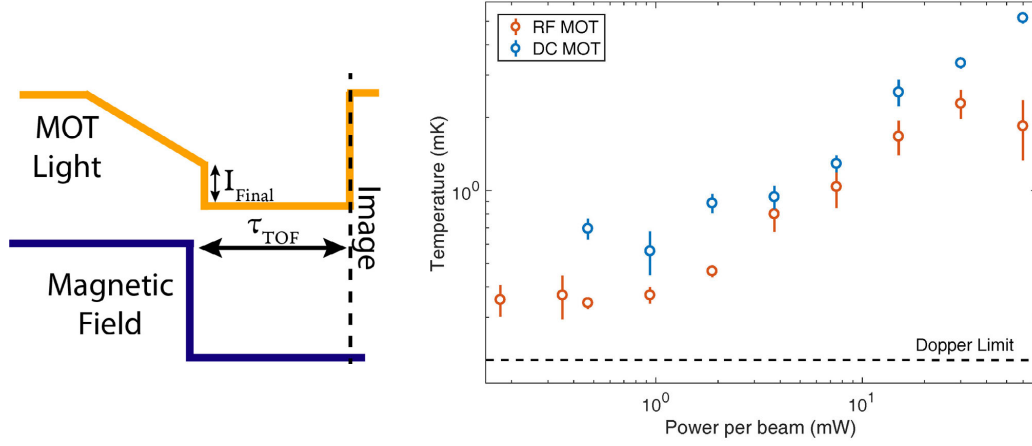
Figure 5.8.3: MOT temperature vs MOT beam intensity following as 15 ms intensity ramp and 10 ms of holding.
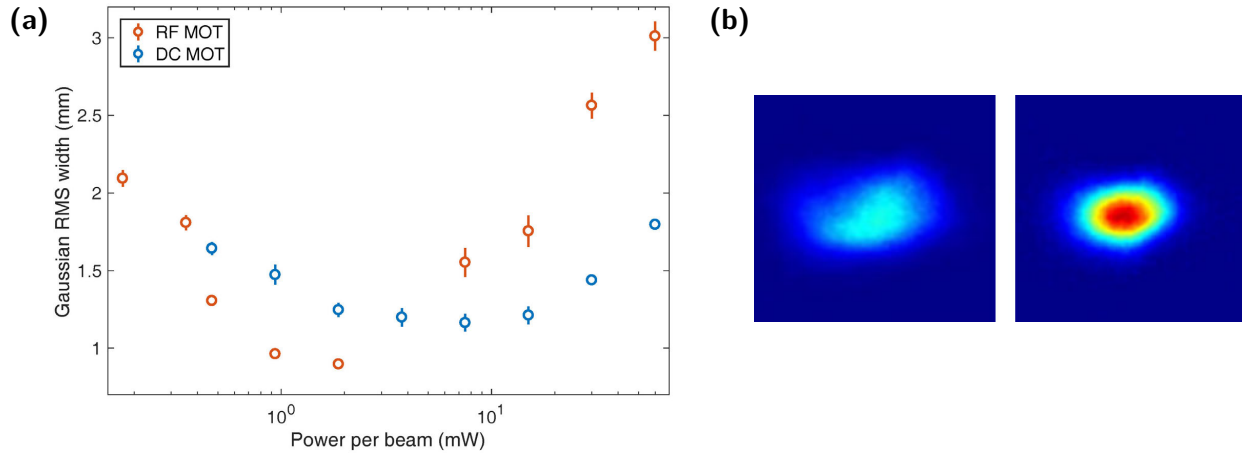
Figure 5.8.4: (a) MOT size (Gaussian rms width) vs MOT beam intensity following as 15 ms intensity ramp and 10 ms of holding. (b) Images of the before and after the intensity decrease showing the increased in density.

	RF	DC
Number	1.1×10^5	0.7×10^5
Minimum Temperature	$340\ \mu K$	$560\ \mu K$
Minimum Size	0.9 mm	1.2 mm
Peak Density	7×10^6 cm^{-3}	2×10^6 cm^{-3}

Table 5.8.1: Optimal MOT properties when loaded with whitelight slowing and no compression stage.

MOT. At $I_o/128$, $T = 340(20)\ \mu K$, close to the Doppler limit of $200\ \mu K$ (Figure 5.8.3).

In order to estimate the number of molecules in the MOT, we measured the scattering rate by shuttering the $X(v = 2) \rightarrow A(v = 1)$ repump and monitoring the decay of fluorescence as the molecules were pumped into $v = 2$. With a MOT beam intensity of I_o, we find a scattering rate of $1.7(1) \times 10^6$ s^{-1} and determine a peak MOT number of $7(2) \times 10^4$ molecules for the DC MOT and $1.1(3) \times 10^5$ molecules in the RF MOT, saturating with field gradient around 12 G/cm RMS. Following a ramp down to $I_o/32$, we retain $\sim 90\%$ of the molecules, with a peak density in the RF MOT of $n_o = 7(3) \times 10^6$ cm^{-3}.

Table 5.8.1 give a comparison of the RF vs the DC MOT loaded with whitelight slowing and no additional compression. While improvements have been made since to the MOT, as discussed below, no systematic comparison between both the RF and DC MOT was undertaken. On average the RF MOT is about an order of magnitude denser than the DC MOT. This is fairly easy to understand as in the DC MOT, the only restoring force is coming from the top most F=2 state, while in the RF MOT, all the states contribute. This can be verified experimentally by operating the DC MOT with opposite polarization for the F=1- or F=0 state. No noticeable difference is seen, confirming the fact that these states do not contribute substantially to the force of the MOT. The typical powers in each MOT beam is shown in Table 5.8.2.

	MOT Main (mW)				v=1 Repump (mW)			
	F=2	F=1+	F=0	F=1-	F=2	F=1+	F=0	F=1-
X	10.1	9.75	4.7	7.1	10.1	38.0	6.6	7.9
Y	9.8	10.3	4.7	7.4	10.52	15.4	6.5	21.4
Z	11.1	9.6	4.6	7.3	16.9	24.6	4.1	13.3

**Table 5.8.2:** MOT beam powers for a typical day after the AOM for sub-Doppler cooling was added.
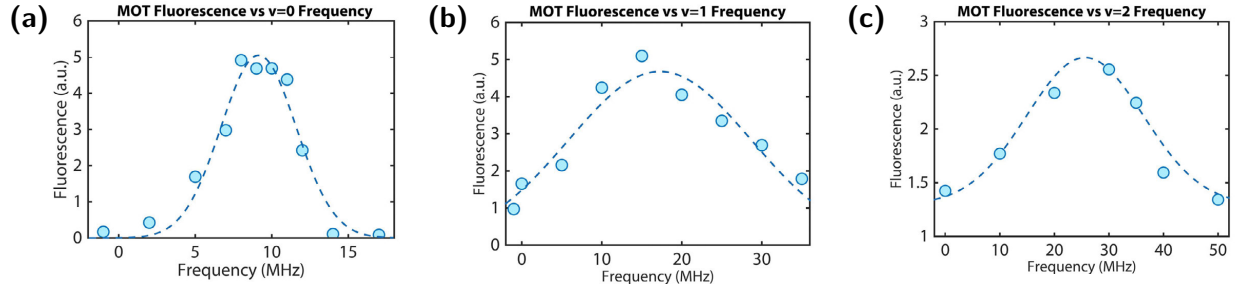
Figure 5.9.1: MOT Fluorescence vs frequency for (a)v=0 (b)v=1 (c)v=2.

5.9 DETAILED CHARACTERIZATION OF THE CaF MOT

Here we discuss the many optimization scans we did for the MOT parameters. Scanning the frequency of the X($v = 0$)→A($v = 0$) transition showed a maximum MOT fluorescence signal at a detuning $\Delta = -8$ MHz from the transition center frequency and a FWHM of ~ 7 MHz. Similar scans of both the first and second repump lasers showed peaks at $\Delta = 0$ MHz from their centers, with FWHMs of 30 and 40 MHz respectively, Figure 5.9.1.

MOT VS POWER

The MOT number as a function of the main line v=0 light saturates at around 25 mW for our MOT beam size, Figure 5.9.2(a). The v=1 beams requires a similar amount of power, Figure 5.9.2(b). The lifetime of the MOT at a scattering rate of around 2 MHz is shown in Figure 5.9.3 for v=2 and v=3
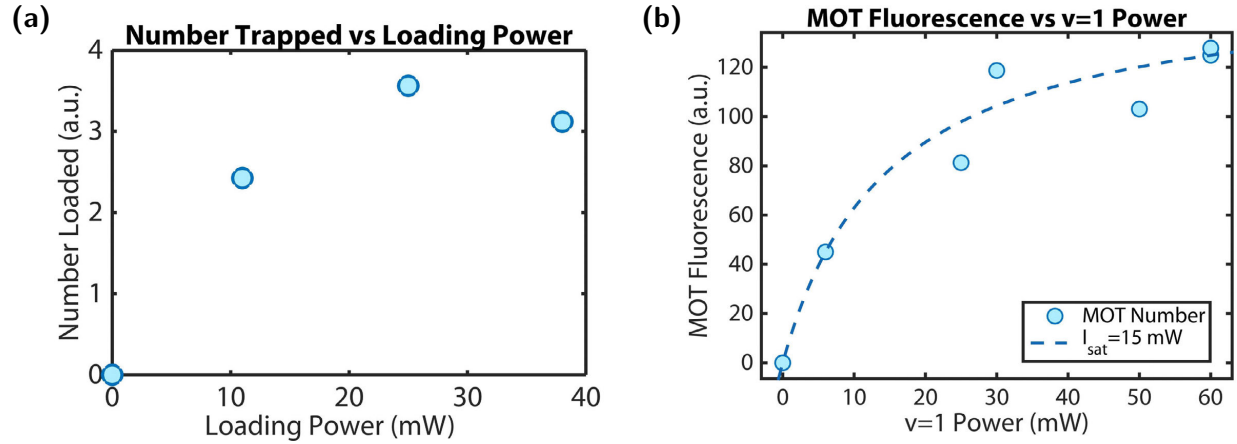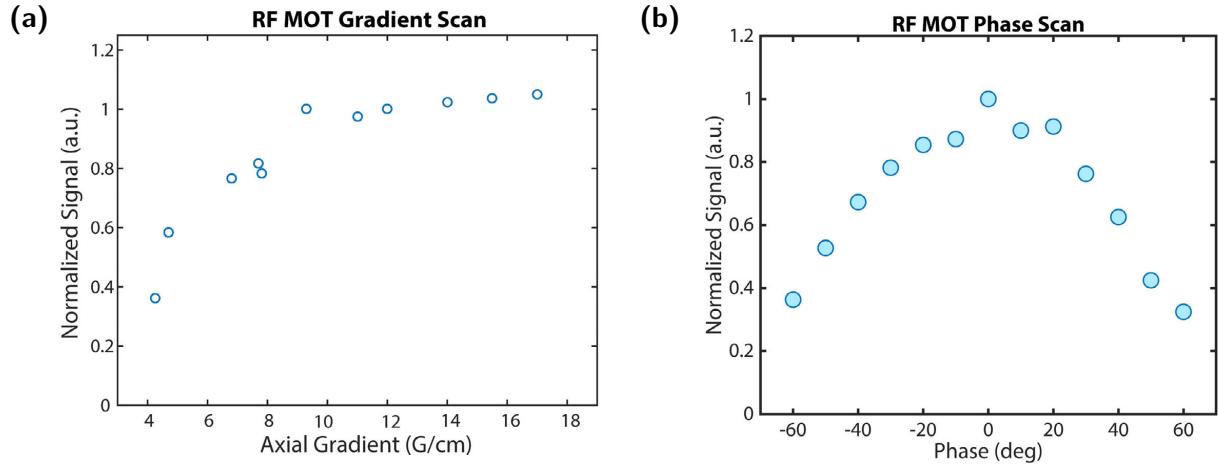
Figure 5.9.2: (a) MOT number vs power for $v=0$. (b) MOT fluorescence vs $v=1$ power.
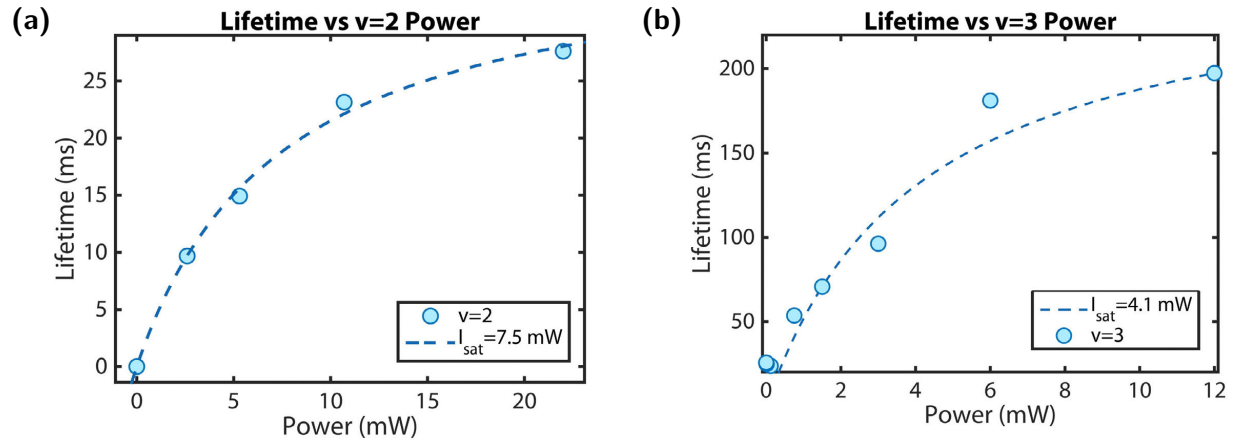
Figure 5.9.3: (a) MOT Lifetime vs $v=2$ power, without $v=3$. (b) MOT lifetime vs $v=3$ power, with $v=2$.

(a)

(b)

Figure 5.9.4: (a) RF MOT number vs field gradient. (b) RF MOT number vs phase of the magnetic field and polarization switching.

rempump power. The scattering rate in the RF MOT versus power is shown in Figure 5.9.5(a).

MOT vs RF Phase and Field Gradient

The number loaded in the RF MOT as a function of gradient is show in Figure 5.9.4(a). The gradient required for loading is around 10-15 g/cm. Higher gradients begin hurting the MOT since level crossing among hyperfine states begin to occur. The number loaded in the MOT is also shown as a function of the phase of the field versus that of the light, Figure 5.9.4(b). For the optimal MOT loading, the phase needs to be stable to around ±10 degrees. If the relative phase of the current between the two coils is out of phase, electric fields also occur, which can substantially shorten the lifetime of the MOT.

Compression of the RF MOT

The density of the RF MOT scales as the field gradient to the 3/2, as shown in Figure 5.9.5(b). This can be derived from the trap frequency as follows,
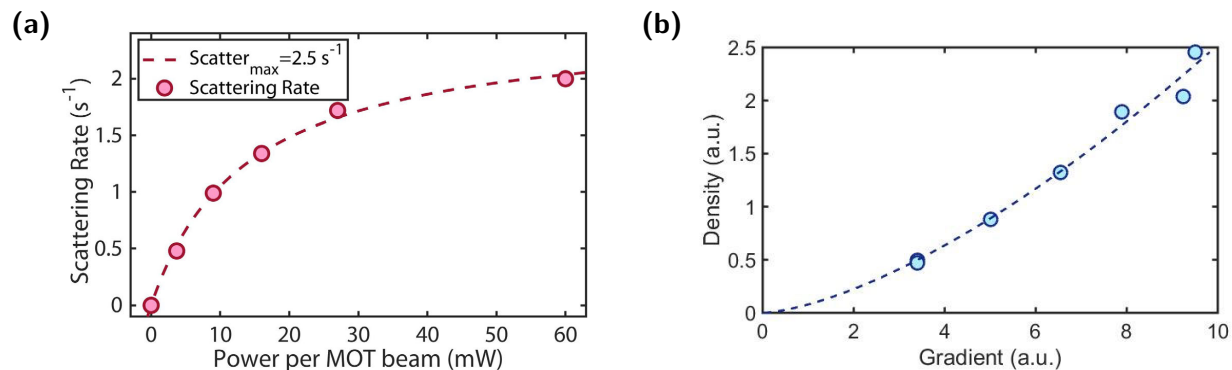
Figure 5.9.5: (a) Scattering rate of the RF MOT vs MOT beam power. (b) Density of the RF MOT vs gradient. The fit shows this scales as gradient to the 3/2.

$$\omega^2 \sim -\frac{\Gamma_{eff} k(\Delta/\Gamma) g\mu A s_{eff}}{\Gamma(1 + s_{eff} + 4\Delta^2\Gamma^2)^2} \tag{5.9}$$

$$\omega = \sqrt{\frac{k_b T}{m\omega^2}} \tag{5.10}$$

$$\omega \propto A^{3/2} \tag{5.11}$$

While large improvements are attainable in the future, improvements to the RF amplifiers and heat dissipation are required.

MOT vs In-cell Absorption

While one may naively expect that some knowledge may be gained from the in-cell absorption signal as to the number of molecules that may be loaded into the MOT, there is no correlation of any form (yes, even seemingly no incell absorption can lead to a MOT). Figure 5.9.6 shows some examples of incell absorption and MOT fluorescence. This should be something that is kept in mind when first searching for a MOT. It is possible that the lack of a MOT may simply be due to the spot on the target which is being ablated (factors of 100× are common depending on the spot ablated). The
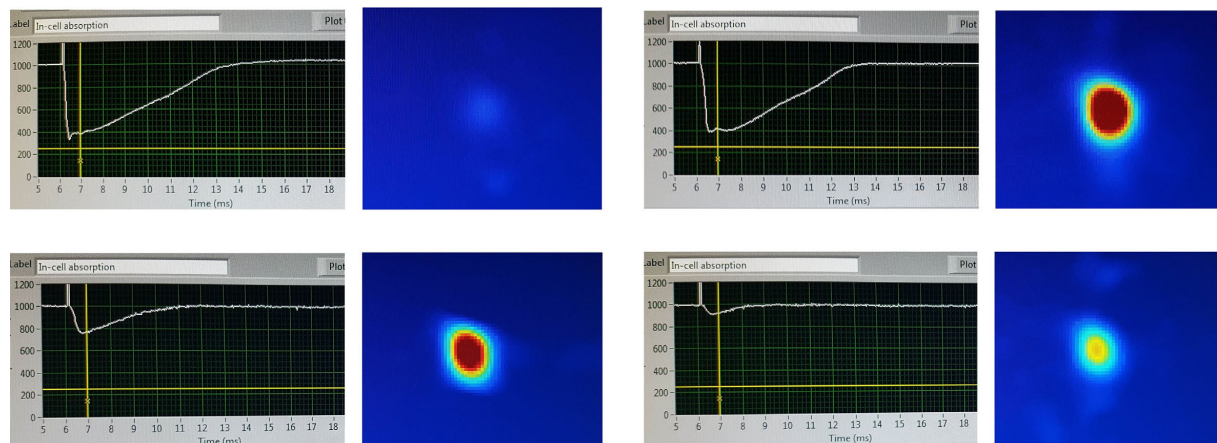
Figure 5.9.6: In-cell absorption vs MOT signal. No other parameters were changes besides the ablation spot hit. Nearly a factor of 100x exist between "magical spots" and "bad spots".

creation of these "magical spots" and "bad spots" are more pronounced when the target has been ablated for a while. However, the MOT signal from these "magical spots" are often better than the anywhere on a new target.

5.9.1 Helium Pressure Management

The MOT chamber pressure is at 2×10^{-8} Torr when the buffer gas flow is on and rises slightly when the laser ablation takes place. To prevent the helium buffer gas from limiting the MOT lifetime, a shutter was installed in-vacuum between the output of the source and the MOT. It is opened for 8 ms following ablation, prior to molecule slowing. The shutter initially used was a Uniblitz VS14S1T0-ECE. This was rated at 1 million shots MTBF. In the first iteration the coil burned out quite quickly as it was not property heat sunk. This was fixed, Figure 5.9.7, and over the course of a few more of these shutters, we found that they would fail around one to two million shots. The method of failure was always the same. One of the blades would get stuck open, at first intermittently, and finally permanently. This is due to the design of these Uniblitz shutters. The shutter blades have a raised
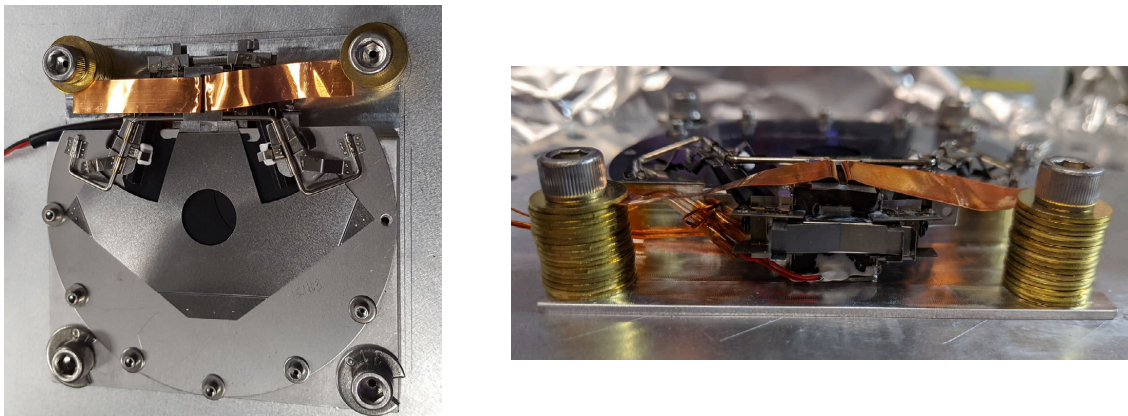
Figure 5.9.7: UHV Shutter. The shutter is thermally heatsunk with some brass washers to the aluminum beam box. Underneath the coil, a layer of indium foil also increases the thermal heat transfer. Finally, Torr-Seal is added to prevent the copper sheet from separating from the coil and a thermistor is added.

triangular back which hits a rubber stopper when the blades are opened. Overtime the metal clip holding this rubber stopper slowly gets pushed up, allowing the blade to become logged underneath the stopper. We found that prebending the shutter stopper down helped, thereby work-hardening the metal clip and delaying this failure mechanism. Eventually we move to the VS14E1T0-ECE driven with the D880C driver. This is a constant current driver rather than a capacitive discharged one. This seems to dramatically increase the shutter lifetime to around the 10 million shot level. However, failures still occurred, sometimes in dramatic fashion. The D880C driver has no output protection and at some point, failed to properly regulate the current it was delivering to the shutter. This caused the encapsulated coil to vaporize and coat the inside of the beambox with burnt epoxy. A thermistor and temperature interlock have now been added to prevent this failure mode from reoccurring. Torr-Seal epoxy was also added to the copper wrap around the coil to prevent it from separating and causing a thermal runaway. With the shutter in place, the MOT chamber pressure is 2×10^{-9} Torr with spikes when the shutter opens. The pump out time of the chamber was simulated in Molflow+ and found to be under 100 ms, Figure 5.9.8. This matches the timescale measured by the ion gauge in the MOT chamber.
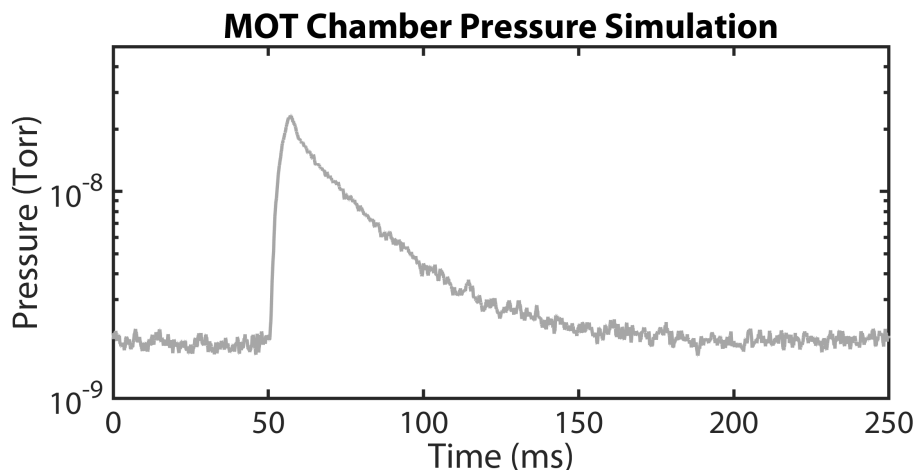
Figure 5.9.8: Simulation of the helium pump out time after the UHV shutter is closed. A base outgassing rate to match that of the MOT chamber was added.

5.9.2   DOUBLE LASER SLOWING

We recently added a second slowing laser which we combine with the original one with opposite polarization, shown in Figure 5.9.9. We also no longer fiber couple the slowing lasers over to the experiment, gaining us nearly another factor of two in power. With the two improvements we have nearly four times the original slowing power. As explained in the previous chapter, the shorter the slowing time, the more molecules that can be loaded into the MOT. The higher slowing power allowed us to ablate at higher energies which lead to a larger MOT signal. Now only 4-5 ms of slowing is required for the optimal MOT signal. This also allowed us to switch from the two-stage cell to a one-stage, taking advantage of the higher flux. The result was a factor of about 10 in molecules loaded into the MOT.
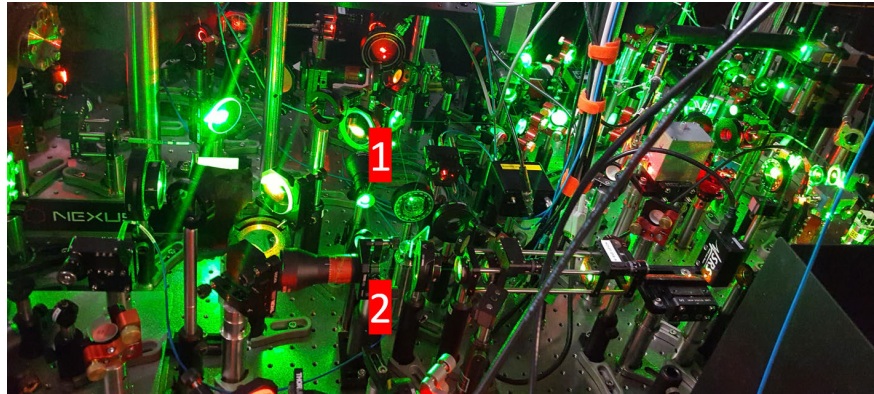
Figure 5.9.9: Dual laser slowing optics. The two slowing beams are labeled as 1 and 2.

The test of all knowledge is experiment. Experiment is the sole judge of scientific truth.

Richard Feynman

6

Optical Trapping and Sub-Doppler Cooling of Molecules

Having realized a MOT, the focus shifted to cooling the molecules further and loading them into a conservative trap. This was done in parallel, with our ability to optically trap molecules increasing every time an improvement in cooling was made. The parameter space for optimal cooling is vast and while simulations qualitatively reproduce the results seen, it is difficult to predict ahead of time what the optimal cooling parameters are. Here we first discuss two methods of sub-Doppler cooling:
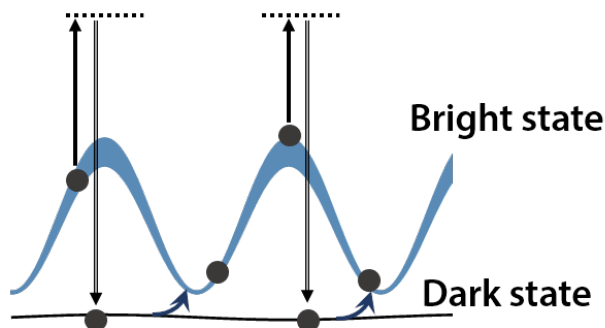
Figure 6.1.1: Grey molasses cooling for $lin \perp lin$ light. An atom or molecule is initially in the dark state, and undergoes motional coupling into a bright state. The atom/molecule then rides up this potential hill, loosing energy and is then driven to an excited state, where it then decays back into the dark state. This cycle repeats, with the particle loosing an energy set by the ac stark shift of the bright state.

grey molasses cooling and Λ-enhanced grey molasses. We then discuss optical trapping of these molecules.

6.1 Sub-Doppler Cooling

6.1.1 Theory of Grey Molasses Cooling

Since we cycle photons on an $F \rightarrow F$ or $F \rightarrow F - 1$ transition, where F denotes angular momentum, for any polarization of light, dark states exists. There are two type of sub-Doppler cooling which can arise depending on the polarization. The first is $lin \perp lin$, which is the most commonly explained type of Sisyphus cooling, Figure 6.1.1. Due to aforementioned dark states, the ground state manifold splits into both a bright and dark state. Because of the blue detuning, all bright states are always Stark shifted towards the upwards above the dark state. An atom or molecule in the ground state will move across this spatially varying potential. The atom/molecule will undergo motional coupling from the dark state to be bright state, ride up the potential hill, and be driven to the excited state when it will then decay back into the dark state. This cycle repeats itself, each time cooling the particle by an
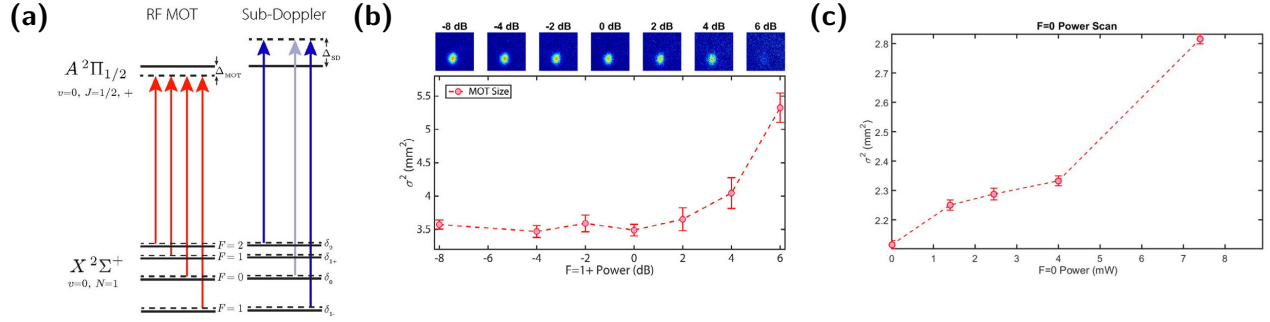
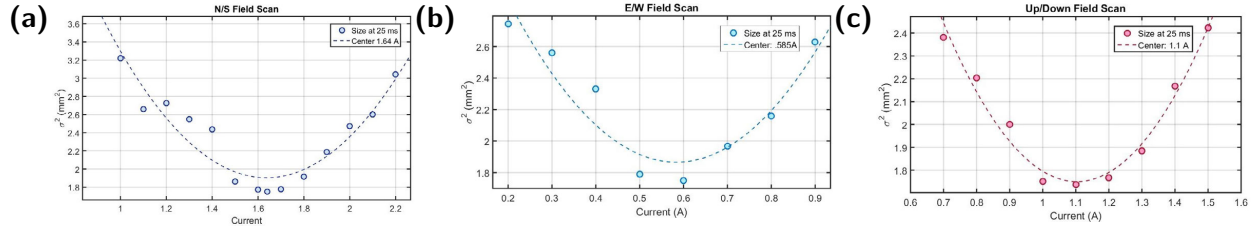**Figure 6.1.2:** Grey molasses cooling of CaF. (a) Levels addressed for the grey molasses cooling. (b) Scan of temperature vs F=1+ power. (c) Scan of temperature vs F=0 power.

energy proportional to the the height of the ac modulation, which depends on its polarizability. The brighter the cooling light, the higher the potential, but also the quicker the molecule gets optically pumped back into the dark state. This gives cooling for the $lin\perp lin$ situation. This is in contrast to $F \to F+1$ systems that do not have dark states. Here, the explanation is a bit subtle, since selection rules also matter[150]. For circular polarization, $\sigma^+\sigma^-$, in the $F \to F$ or $F \to F-1$ case, there is no spatial variation as the ac Stark shifts are constant and no cooling effect is present in 1D. However, in 3D, atoms/molecules will move though intensity and polarization gradients, recovering a spatially varying ac Stark shifts [145], and hence the cooling force. It turns out that for transitions from $F \to F$ and $F \to F-1$, both the $lin\perp lin$ and $\sigma^+\sigma^-$ configurations provide exceedingly similar cooling forces, as calculated by Mike Tarbutt [145].

The inverted angular momentum structure of CaF is similar to the D1-line in alkali atoms, and allows for this type of blue detuned cooling [97, 151–155]. It should be noted that the multiple hyperfine states complicate this simple picture and allows for off resonant excitations. This sets a limit on the lowest achievable temperature.

Figure 6.1.3: Magnetic field shim coil scans. The slowing remixing coil was turned on to 6.04 A. (a) North/South coil (b) East/West coil (c) Up/Down coil.

6.1.2 GREY MOLASSES COOLING OF CaF

To perform sub-Doppler cooling on CaF, the MOT beams and the MOT magnetic gradient are switched off for 200 μs, during which time the laser is detuned to the blue, $\Delta_{SD} \approx +3\,\Gamma$ with a double pass AOM in a cat eye setup. The MOT beams, with polarization switching turned off, are then switched back on at full intensity, but without the $F = 1+$ component (Figure 6.1.2(a)), which can lead to heating as it is red-detuned relative to the $F = 0$ transition. Figure 6.1.2(b) shows the temperature of the molasses vs the power of the F=1+ component. Repumping out of $F = 1+$ is still accomplished, albeit at a reduced rate by off-resonant light that nominally addresses the $F = 2$ state. The vibrational repumpers for all the components are still on as the beams are switched off with shutters after dichroics in the 606 nm beam path. The magnetic field of the earth was nulled, to less than 0.1 G by minimizing the temperature of the molasses. Stray magnetic fields remixe the bright and dark states, reducing efficiency of the cooling. It should be noted that the field cancellation was repeated multiple times, since the lower in temperature we got, the more sensitive we became to this field. Figure 6.1.3 shows the square of the MOT diameter after a fixed expansion time, which is proportionate to temperature. These coils primarily cancel out the Earth's field and the small residual field from the remixing coils in the slowing region. In a time of $\sim$100 μs, the molecules are cooled to 40 μK, much lower than the Doppler cooling limit of 200 μK.

We found that as we decreased the power of the F=0 hyperfine component, the molecules became
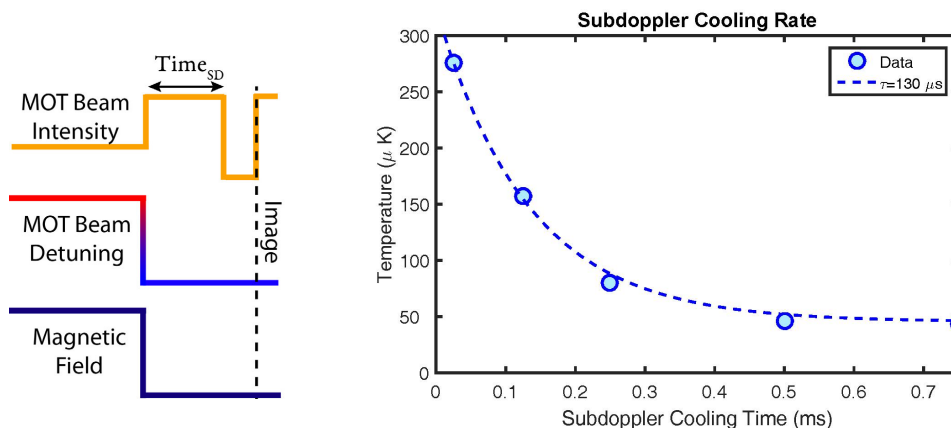
Figure 6.1.4: Sub-Doppler cooling timescale in free space. Note this temperature equilibrium was higher as with was taken before we turned off the F=0 component.

colder and colder. The optimal sub-Doppler cooling was found to be with only F=2 and F=1- components on. This can also be explained by the fact that at the sub-Doppler detunings used (30 MHz blue), this component becomes red detuned of the $F = 1$-. After this was done the lowest temperature reached with sub-Doppler cooling was 9 μK, at a sub-Doppler detuning of 27 MHz, and F=2(F=1-) power of 16 mW (7.6 mW) per MOT arm. The cooling timescale, Figure 6.1.4, was measured to be similar to that for the unoptimized sub-Doppler cooling, with this low temperature reach under 2 ms. This rapid cooling is the most important part of the sub-Doppler cooling step. Since the molecules out of the MOT are at a relative high temperature (300 μK), they need to be cooled on a time scale fast enough such that the density does not decrease significantly.

We found that decreasing the power of the remaining two beams did not help when looking at the MOT size after a 25 ms TOF period, Figure 6.1.5. This could be from either slow cooling out of the hot MOT, or worse final cooling temperatures. The temperature versus sub-Doppler detuning is shown in Figure 6.1.6(a). We found that larger detuning led to colder temperatures. Going much beyond 35 MHz increased the cooling time and thus decreased the final density. The best sub-Doppler cooling in free space gave temperatures of 9 μK, shown in Figure 6.1.6(b). This cooling is
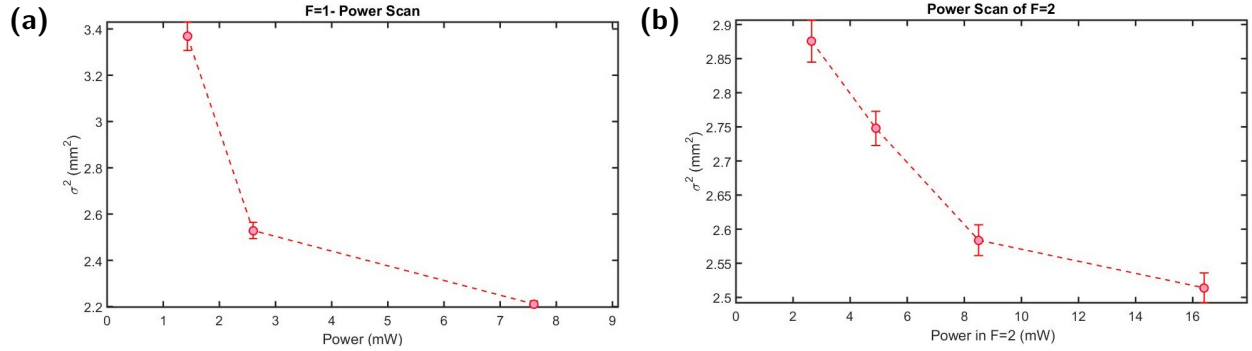
Figure 6.1.5: (a) Temperature vs F=1- power. (b) Temperature vs F=2 power.
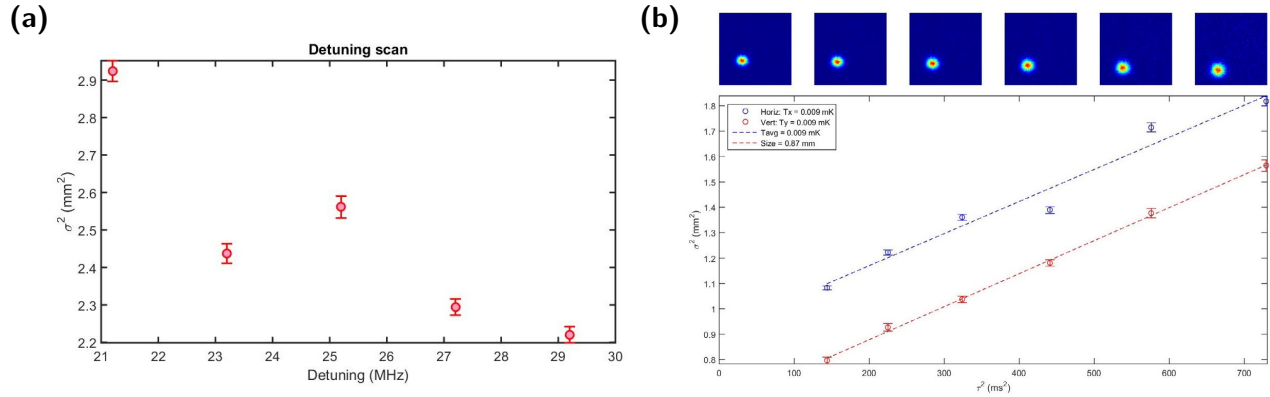
Figure 6.1.6: (a) Temperature vs sub-Doppler detuning. (b) TOF temperature measurement following sub-Doppler cooling with optimized parameters fits to a temperature of 9 μK.

done with full power for the F=1- and F=2 transitions as a sub-Doppler detuning of 35 MHz.

6.2   Λ-Enhanced Grey Molasses Cooling

6.2.1   Theory

Λ-enhanced grey molasses cooling combines grey molasses cooling with an additional cooling mechanism: velocity selective coherent population trapping (VSCPT) [156]. VSCPT relies on coherent dark states. It can be understood in a three level system, shown in Figure 6.2.1. For two circularly
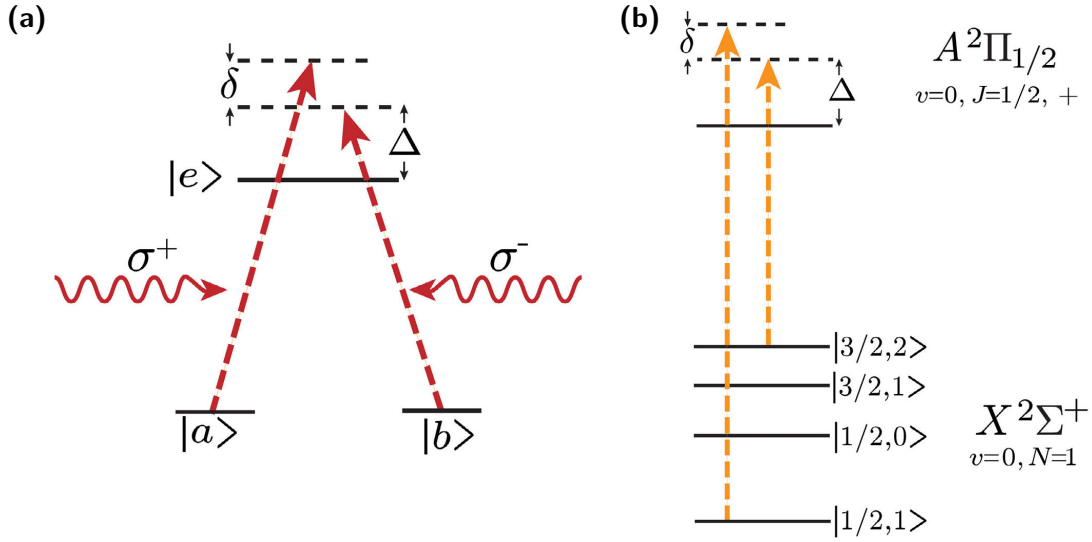
Figure 6.2.1: (a) 3-level system exhibiting velocity-dependent dark states. Two ground states $|a\rangle$ and $|b\rangle$ are addressed separately by two counter-propagating laser beams. (b) Λ-cooling scheme of CaF. The cooling light consists of two components addressing the F=2 and F=1- hyperfine manifolds. The single-photon detuning for F=2 and two-photon detuning between F=2 and F=1- are denoted by Δ and δ respectively.

polarized counter propagating beams of equal frequency, there exists a coherent dark state at zero velocity. This state is a superposition of the $|a\rangle$ and $|b\rangle$ states, where the transition amplitudes destructively interfere, forming the dark state. For non-zero velocities, the two beams are no longer at the same frequency due to opposite Doppler shifts, and thus the dark state no longer exists. This cooling can be characterized by a two photon detuning, δ, which sets the velocity around which the cooling is centered. VSCPT cooling can reach very low temperatures, but is not efficient typically due to relying only on random walks to cool the population to zero velocity. By combining this cooling with grey molasses cooling, the cooling no longer realizes solely on a random walk, as the grey molasses provides a resorting force towards zero velocity and the VSCPT effect traps the atoms or molecules near zero velocity. Of course, this also means that the zero-velocity state is no longer as dark, raising the minimum temperature achievable by this type of cooling.
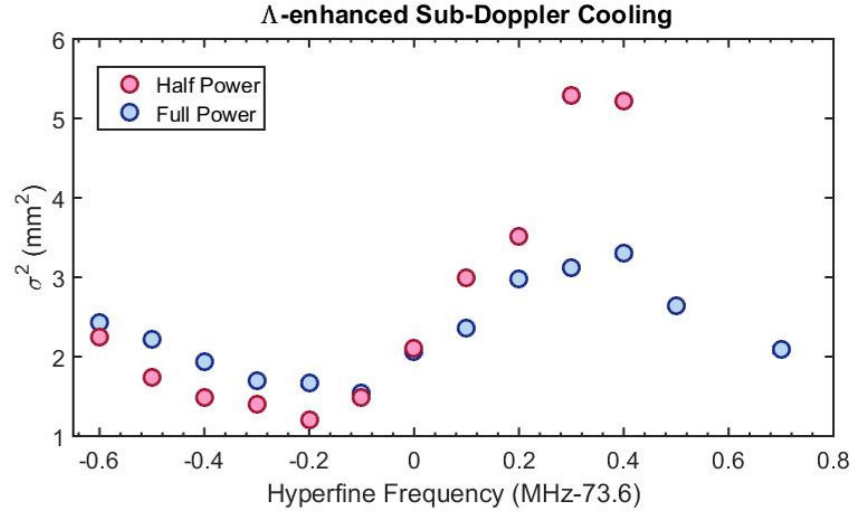
Figure 6.2.2: Λ-enhanced grey molasses cooling of CaF. The two intensities are at the full MOT power and half power.

VSCPT was first demonstrated for helium [157], and Λ-enhanced grey molasses was first demonstrated on the D1 lines of alkali atoms [158], which features an $F \rightarrow F$ transition for grey molasses cooling and a second state used to create a coherent VSCPT dark state. In CaF, since our grey molasses was already only using two frequencies, we could easily implement this type of cooling by scanning the relative frequencies of our two cooling transitions. While coherent effects with more frequencies could also be tried, limiting the number of frequency components to two significantly reduces the parameter space to search. The grey molasses cooling had used hyperfine frequencies which were not matched to hyperfine interval of CaF due to historical reasons. We moved the relative hyperfine frequencies by about 2 MHz and began scanning for an effect on the temperature. Figures 6.2.2 shows the results. For all intensities used, Figure 6.2.3, we observe a temperature minimum near the two-photon resonance ($\delta = 0$), surrounded by a heating feature, which is more pronounce at lower intensities. This can be qualitatively explained by a 3-level model. Away from resonance, the VSCPT dark states that are formed are at a finite velocity given by $\delta/(2k)$. Molecules accumulate in these longer-lived states at higher velocities, resulting in a higher average kinetic energy.
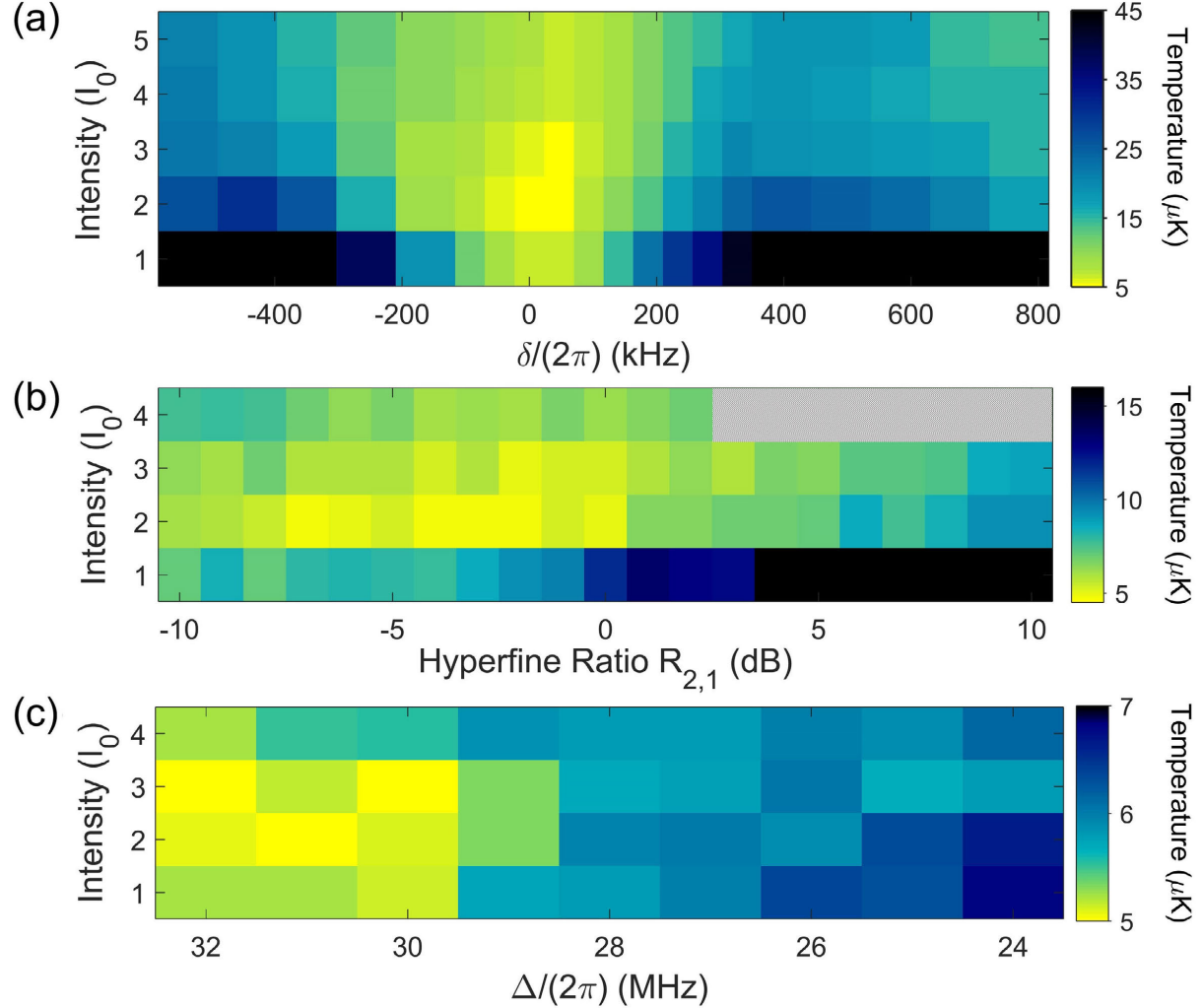
Figure 6.2.3: Dependence of Λ-cooling in free space on various parameters. (a) Temperature versus intensity I and two-photon detuning δ at fixed single-photon detuning ($\Delta = 2.9\,\Gamma$) and hyperfine ratio ($R_{2,1} = 0.92$). (b) Temperature versus I and $R_{2,1}$ with $\Delta = 3.4\,\Gamma$ and $\delta = 0$. $R_{2,1}$ is shown on a logarithmic scale. (c) Temperature versus Δ and I with $R_{2,1} = 0.92$ at $\delta = 0$. For all plots, I was varied in steps of $I_0 = 6.8\,\mathrm{mW/cm^2}$.
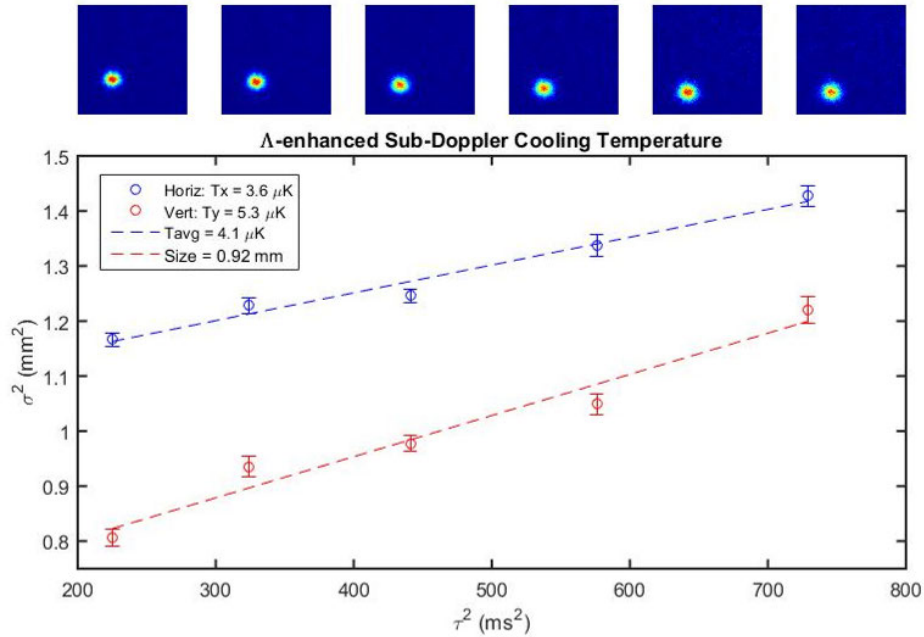
Figure 6.2.4: Time of flight of the Λ-enhanced grey molasses.

We also observe that the width of the cooling feature increases with intensity, typical of VSCPT, where higher intensities increase the pumping rate into dark states. In a 3-level model, the bright state admixture scales as $(\delta/\Omega)^2$, Ω being the single-photon Rabi frequency. Features that vary as a function of δ should broaden with increasing values of Ω^2. Since the intensity is proportional Ω^2, these features are expected to broaden with intensity, in agreement with our observations. This also mimics the behavior seen in the alkali atoms.

Demonstrations of Λ-enhanced cooling of alkali atoms have shown optimal cooling when the ratio of the intensities between the hyperfine components was large [158, 159]. Which of the components was stronger, however, was not found to be crucial [154]. In molecules, the dependence on hyperfine ratio can be different because of additional nearby hyperfine manifolds. We thus explored the dependence of Λ-enhanced cooling on $R_{2,1}$, the ratio of F=2 light to F=1- light. In contrast to observations in alkali atoms, we observed a strong asymmetry with respect to $R_{2,1}$ (Figure 6.2.3(b)).

	MOT Main (mW)				$v{=}1$ Repump (mW)			
	F=2	F=1+	F=0	F=1-	F=2	F=1+	F=0	F=1-
X	1.8	0	0	11.7	0.34	0	8.5	13.6
Y	1.8	0	0	11.9	0.34	0	7.9	40.3
Z	1.5	0	0	8.3	0.58	0	5.3	17.3

**Table 6.2.1:** Beam powers for Λ-cooling.

Optimal cooling occurs when $R_{2,1}$ is 0.5, at a total intensity of $I \approx 14 \, \text{mW/cm}^2$. Cooling is much reduced when $R_{2,1} \gg 1$. One possible explanation is that while the F=1- component is blue-detuned relative to all hyperfine states and always provides Sisyphus cooling, the F=2 component is red-detuned relative to the F=0 and F=1- states and can cause Sisyphus heating.

After optimization of the temperature with respect to the single-photon detuning Δ and the total intensity I, we are able cool the molecules to $4.0(5)\mu$ K in free space (Figure 6.2.4), about 9 times the recoil limit. We observe a slight dependence on Δ (Figure 6.2.3(c)), and optimal cooling is achieved at $\Delta = 3.9 \, \Gamma$, $I = 14 \, \text{mW/cm}^2$, $R_{2,1} = 0.92$, with an optimal two-photon detuning of $\delta_{\text{opt,fs}} = 0$. With the measured free-space density of $1.4(3) \times 10^7 \, \text{cm}^{-3}$, the corresponding phase space density is $1.4(4) \times 10^{-8}$.

Table 6.2.1 contains the typical powers in each MOT beam used for the Λ cooling.

6.3   Optical Trapping

Transferring molecules into a conservative trap is important to be able to use the molecules in future experiments and can be used to increase both density and, with compatible cooling, phase space density. There are two main types of traps used in the cold atom community; magnetic and optical traps. While magnetic traps offer large volumes and high trap depths, they can only trap high field seeking states. By contrast optical trapping can trap molecules regardless of their internal state, assuming sufficient detuning. This is critical to studying ground state collisions between molecules.

(a)

(b)
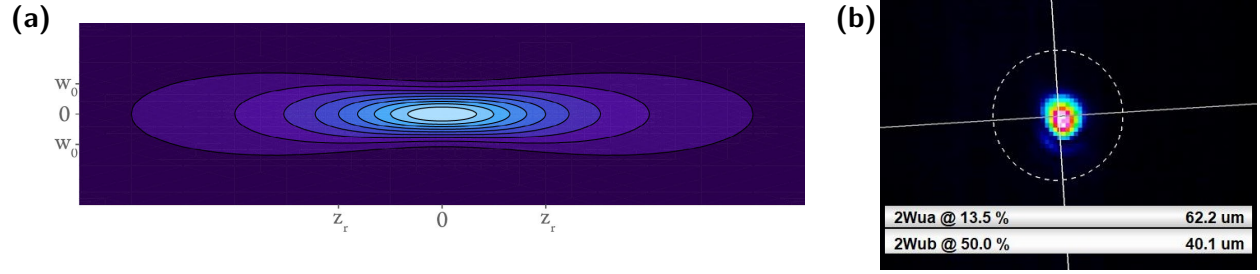
Figure 6.3.1: (a) Gaussian beam intensity profile transversely. (b) ODT beam profile measured at the focus.

It also allows for laser cooling of trapped samples, leading to enhancement in density and phase-space density as well as all optical routes towards quantum degeneracy, which can occur on much shorter time scales and be more efficient than evaporative cooling [160]. However, cooling in an optical trap can fail due to differential ac Stark shifts of the ground and excited states.

The polarizability of CaF was derived in chapter 2. We found that the trap depth scales as $1/\Delta$ while the scattering rate scales as $1/\Delta^2$. While further detuning will help lower the scattering rate, it comes at the cost of needing more power. There is also an experiential consideration which comes into play, which is the fact that very high power lasers (50 W+) tend to exist at 532 nm, 1064 nm, 1550 nm, and 10.6 μm.

Optical dipole traps are focused Gaussian beams, Figure 6.3.1, whose intensities follow

$$I(r, z) = I_0 \left(\frac{w_0}{w(z)} \right)^2 \exp\left(\frac{-2r^2}{w^2(z)} \right) \tag{6.1}$$

In the harmonic approximation, the relevant trap properties are:

$$z_r = \frac{\pi w_{\mathrm{o}}^2}{\lambda} \qquad \text{(Rayleigh range)} \tag{6.2}$$

$$\omega_r = \sqrt{\frac{4 U_{dip}}{m w_{\mathrm{o}}^2}} \qquad \text{(Radial Frequency)} \tag{6.3}$$

$$\omega_z = \sqrt{\frac{2 U_{dip}}{m z_r^2}} \qquad \text{(Axial Frequency)} \tag{6.4}$$

$$n_{\mathrm{o}} = N \left(\frac{m \left(\omega_r^2 \omega_z \right)^{2/3}}{2 \pi k_B T} \right)^{3/2} \qquad \text{(Peak Density)} \tag{6.5}$$

For a fixed number of particles in the optical trap, the following scaling arise as a function of trap power, P, trap waist, w_{o}, and temperature, T.

$$U_{Depth} \propto \frac{P}{w_{\mathrm{o}}^2} \qquad \text{(Trap Depth)} \tag{6.6}$$

$$\omega_r \propto \frac{\sqrt{P}}{w_{\mathrm{o}}^2} \qquad \text{(Radial Frequency)} \tag{6.7}$$

$$\omega_z \propto \frac{\sqrt{P}}{w_{\mathrm{o}}^3} \qquad \text{(Axial Frequency)} \tag{6.8}$$

$$n_{\mathrm{o}} \propto \left(\frac{P}{T} \right)^{3/2} \frac{1}{w_{\mathrm{o}}^7} \qquad \text{(Peak Density)} \tag{6.9}$$

At high temperatures and low trap depths, as was the case in the first optical traps, this approximation breaks down and the full Gaussian potential must be considered. This was done with Monte Carlo simulations. For a T/T_{Trap} of 0.25, the harmonic approximation overestimates the trap frequency by about 20%. For low trap depths, the effect of gravity must be taken into account.
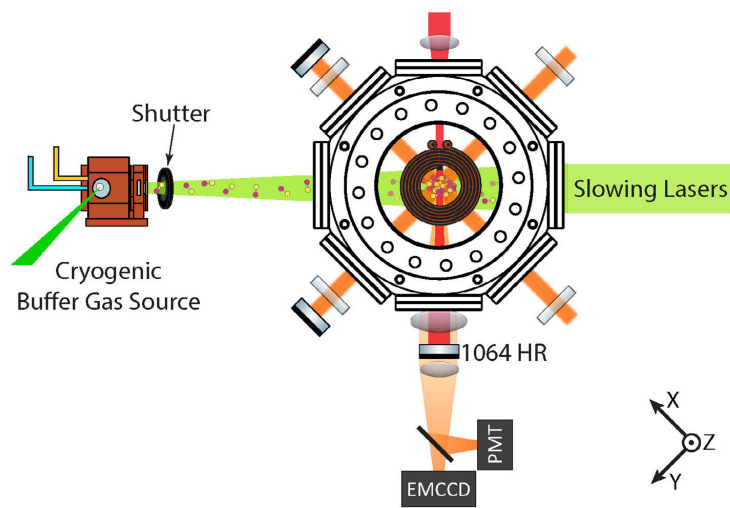
Figure 6.3.2: Schematic of experimental apparatus for optical trapping of CaF. The 1064 nm light is generated by a 50W fiber amplifier and focused into the chamber. A high reflectivity mirror on the opposite size allows us to create either a lattice or a single pass ODT depending on its orientation.

6.3.1   1064NM ODT WITH GREY MOLASSES

We decided to optically trap CaF Molecules using 1064 nm light due to the availability of high power, low noise, single frequency fiber lasers. The apparatus for all initial optical trapping experiments is shown in Figure 6.3.2. Using a 1064 nm fiber amplifier (Nufern), we focused 12.7 W of single-frequency light to a beam waist of 29 μm. This produces a trap depth of 380(60) μK, with radial (axial) trap frequencies of $\omega_r(\omega_z) = 2\pi \times 2.5\,\mathrm{kHz}$ (21 Hz). The ODT light was reflected by a dichroic mirror that transmits the fluorescence of the molecules, but reflects the ODT beam either onto a beam dump away from the trapped molecules, or directly back to form a lattice.

The 1064 nm light is delivered to the experimental chamber via a photonic crystal fiber. A typical optical fiber cannot carry more than about 2 W of power due to several factors, including damage of the core, facets, and stimulated Brillouin scattering or SBS. SBS arises from the light coupling to phonon modes. These phonon modes generate an effective grating (density modulation) which reflects the light back. The effective gain of this SBS grows exponentially with the length of the fiber

and the power sent into the fiber. At about 5-10 meters in length, this limits the power to on the order of 1-3 W. At shorter lengths, SBS no longer become a limitation and rather thermal damage of the fiber becomes the dominant failure mechanism. To get around these problems, we use a photonic crystal fiber (LMA-PM-15 with AlphaNov SMA-6 connector), in which a photonic structure guides the light over a large mode area (12.6 μm), allowing for high power capabilities. Fused silica end caps cover the input and output ends of the fiber to minimize the risk of damage from dust burning. Care must be taken to ensure the fiber remains aligned at high power. Poor coupling at high powers leads to the power being dumped into the cladding, heating the fiber which can lead to damage. Preparation and fiber coupling of the 1064nm Nufern is shown in Figure 6.3.3. Care must also be taken to prevent thermal lensing at higher power and back reflection into the amplifier, especially when creating a lattice. A Thorlabs high power isolator, IO-5-1064-HP, was modified to prevent back reflection into the amplifier and lensing by removing the input and output polarizing beam cubes and replacing them with Brewster angle polarizing plates. The Nufern amplifier was originally seeded with an NP Rock module, which had very poor RIN properties and the tendency to become multimode. This was later replaced by a RIO Orion seed.

The ODT was imaged with a similar optical system described in the previous chapter for the MOT. It should be noted however, that unlike the large MOT, here the focus was important for optimal signal to noise. Figure 6.3.4 shows a simulation of the ODT as imaged by the imaging system at various focus positions. One challenge was the lack of an in-vacuum reference to which we could focus this imaging system.

In order to capture molecules in the optical trap, the ODT light was switched on at the start of the sub-Doppler cooling. The sub-Doppler light, simply grey molasses with all 4 hyperfine components at this point in time, was then ramped down in intensity by 30% in the first 10 ms and left on for a further 5 ms. We waited for 50 ms to allow untrapped molecules to fall from the imaging region,
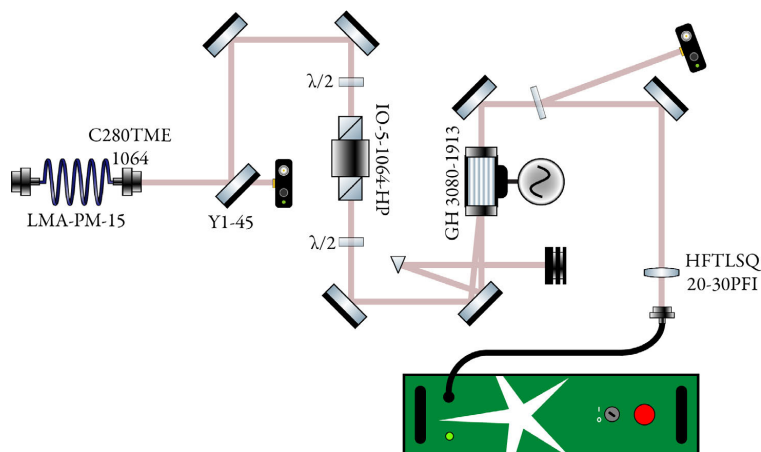
Figure 6.3.3: Preparation of the 1064 nm ODT light. The GH3080-1913 AOM is used to turn the ODT on and off. The beam dump is water cooled to prevent temperature changes misaligning the optics. This setup remains fiber coupled for several months, but does requite a short warm-up period after the Nufern is switch on for the polarization out of the amplifier to settle. Some thermal lensing does occur, most likely due to the AOM, made of TeO_2 ($\frac{dn}{dT} = 16 \times 10^{-6}$ /°C[161]), or possibly in the C280TME asphere, which is made of ECO550 glass ($\frac{dn}{dT} = -1.3 \times 10^{-6}$ /°C)
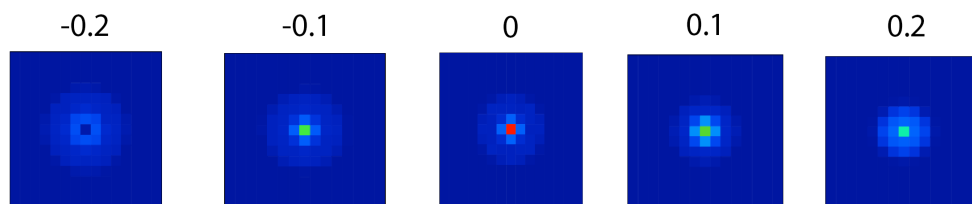
Figure 6.3.4: Simulation of the ODT signal vs camera focus. Distance of the first lens is plotted above in millimeters, showing the focus need to be within 100 μm for efficient detection.
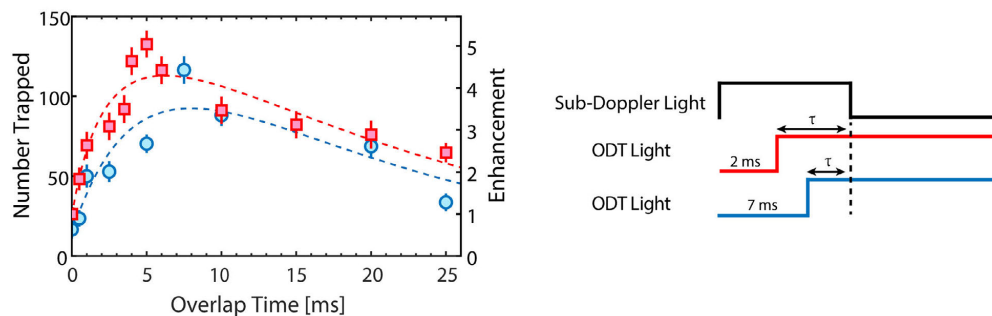
**Figure 6.3.5:** Loading of molecules into the ODT as a function of overlap time, τ, with the sub-Doppler light. Shown in red squares (blue circles) is the number loaded when the cooling light is turned on 2 ms (7 ms) prior to the ODT light. The number of molecules loaded into the ODT is enhanced by up to a factor of 5 with sub-Doppler light. The enhancement is relative to no cooling light overlap.

before imaging using a 0.5 ms pulse of light resonant with the X→A transition. With optimal parameters, 150(30) molecules were transferred into the ODT. The number of transferred molecules is determined by the size of the optical trap (29 μm waist), which is much smaller than the size of the initial sub-Doppler cooled cloud ($\sim$ 2 mm FWHM).

We next varied the overlap duration of the cooling light and the ODT. This was accomplished as follows. We shorten the sub-Doppler intensity ramp to 2 ms with the ODT off. Subsequently, the ODT was switched on, and we varied the amount of time that the sub-Doppler light overlaped with the ODT light. Zero temporal overlap corresponds to direct capture of sub-Doppler cooled molecules. As shown in Figure 6.3.5, we found that the number of trapped molecules increased by up to a factor of 5 and reaches a peak at 5 ms. To verify that the enhancement was not due to additional sub-Doppler cooling in free space, we increased the duration of the free space sub-Doppler cooling by an additional 5 ms before switching on the ODT. With the additional free-space cooling, we found a smaller initial number of loaded molecules, likely due to a lower central density resulting from the longer sub-Doppler cooling time. Despite a smaller initial number, the number of loaded molecules again rose as a function of overlap time. The peak number is reached at $\sim$ 10 ms, at a similar level to the case without extra sub-Doppler cooling.
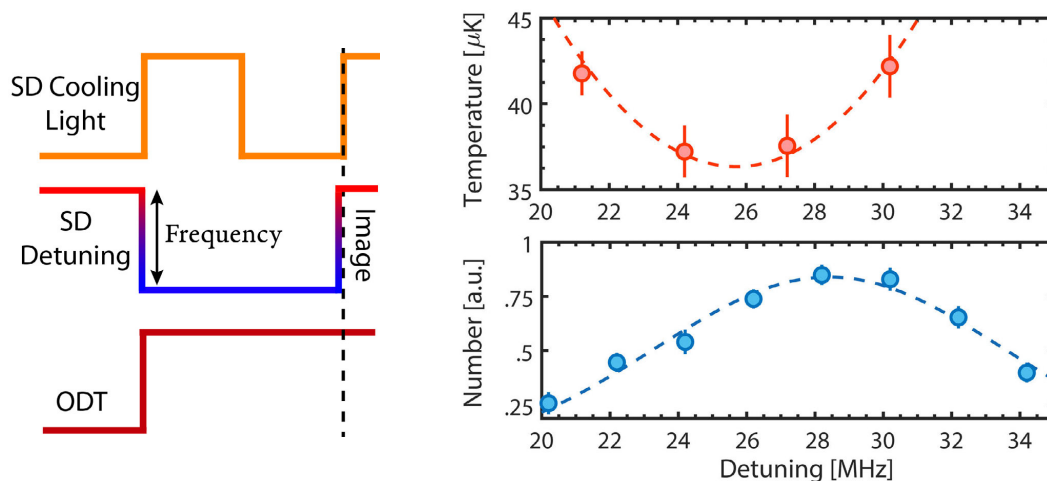
Figure 6.3.6: Dependence of sub-Doppler cooling and ODT loading on laser detuning. Top Right: Free-space sub-Doppler temperature as a function of detuning Δ_{SD}. The dashed line shows a quadratic fit. Bottom Right: Number of trapped molecules in the ODT as a function of Δ_{SD}. We observe a 3 MHz shift between optimal ODT loading and optimal free-space sub-Doppler cooling, which is consistent with the estimated ac Stark shift due to the ODT.

The initial rise at short times indicates that there is a time window of $\sim$ 10 ms when molecules that pass by the ODT can be cooled by sub-Doppler light into the trap. The optimal loading time coincides with the average time it takes for a molecule on one edge of the initial sample to traverse the optical trap, where it can be cooled into the trap. Since the ODT is a conservative trap, the enhanced loading suggests that cooling is occurring at least in some region of the trap. Another indication of sub-Doppler cooling of trapped molecules is that the measured temperature of $60(5)\,\mu$K is significantly lower than that expected from direct capture ($100\,\mu$K).

We further characterized the effect of the sub-Doppler light on the ODT loading process. We varied the frequency of the sub-Doppler cooling light during ODT loading. As shown in Figure 6.3.6, optimal loading occurs when the sub-Doppler cooling light is detuned +3 MHz relative to the free-space cooling frequency that produces the lowest temperature. The detuning is consistent with estimates of the ac Stark shift on the X→A transition arising from the ODT.
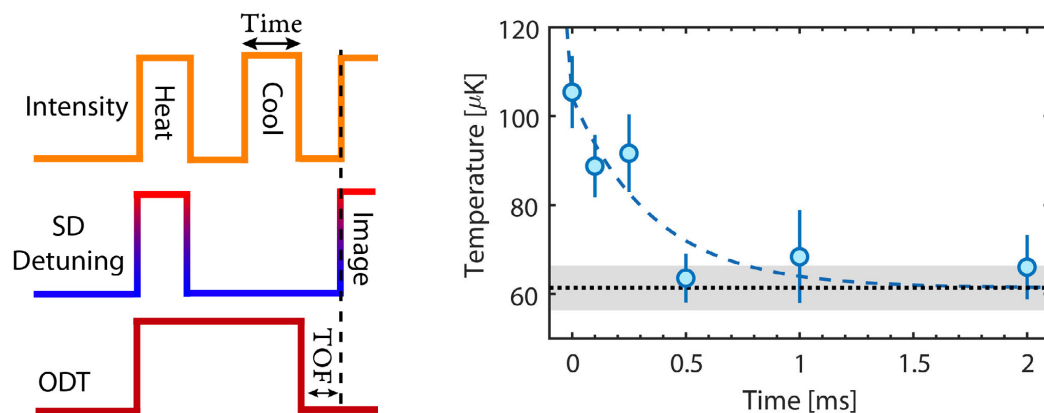
Figure 6.3.7: Cooling of optically trapped molecules. Trapped molecules are heated by a $40\,\mu s$ pulse of resonant light at time $t = 0$. Shown is the temperature as a function of varying sub-Doppler cooling time beginning at $t = 0.2\,\mu s$. An exponential fit, shown by the dashed blue line, yields a $1/e$ time constant of $\sim 300\,\mu s$. The temperature prior to heating is indicated by the black dotted line.

To demonstrate that cooling occurs within the ODT and measure the cooling timescale in the ODT, we heated the CaF molecules to $\sim 100\,\mu K$ by applying a $40\,\mu s$ pulse of resonant light (detuned by $+3\,MHz$ to compensate for the Stark shift of the ODT beam) . To ensure that the heated molecules are trapped, we measured the molecule number after waiting $50\,ms$. After the resonant heating pulse, half of the trapped molecules remained. We then applied a pulse of sub-Doppler cooling light and observed that the molecules are re-cooled to $\sim 60\,\mu K$ with a $1/e$ time of $\sim 300\,\mu s$ (Figure 6.3.7). This verified that sub-Doppler cooling worked for molecules trapped in the ODT. This was an important initial demonstration which showed that laser cooling an optical trapping were compatible.

The lifetime of trapped molecules was measured to be $750(40)\,ms$ ($1/e$ decay time), shorter than the calculated lifetime ($\gg 1\,s$) due to heating from off-resonant photon scattering of the $1064\,nm$ ODT light. To determine what limited the lifetime, we varied the flow rate of helium into the buffer gas cell, with no appreciable effect on the lifetime (Figure 6.3.8(a)inset). The UHV shutter that is open for $< 10\,ms$ during each experimental cycle eliminates the effects of buffer gas collisions on the

(a)

(b)
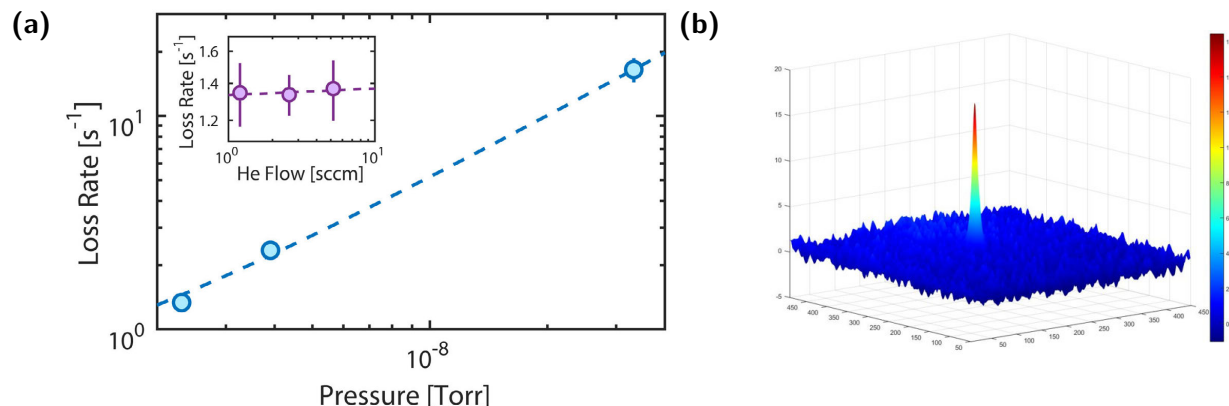
Figure 6.3.8: (a) Loss rate of molecules trapped in the ODT vs Pressure. The inset shows the loss rate as a function of the buffer gas flow rate. The dependence of loss rate on buffer gas flow was measured to be consistent with zero, $0.0(2)\,\mathrm{s^{-1}sccm^{-1}}$, while the dependence on background pressure was $5.5(1) \times 10^8\,\mathrm{s^{-1}torr^{-1}}$. (b) Image of the ODT.

(a)

(b)
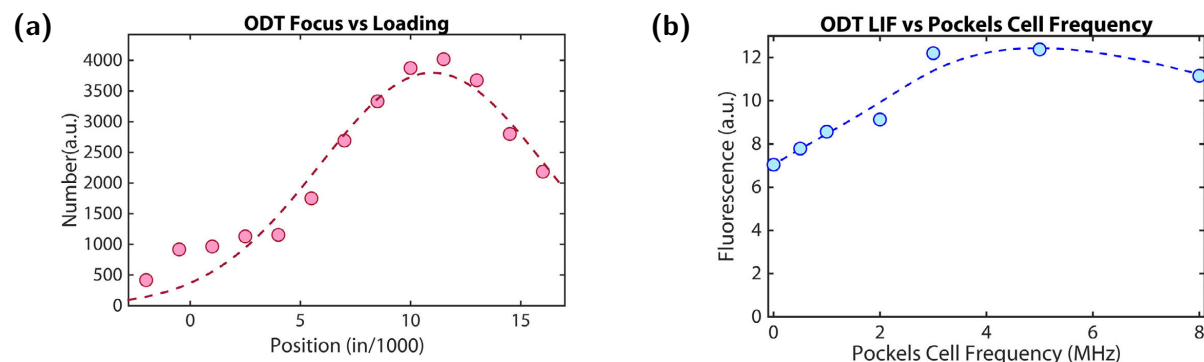
Figure 6.3.9: (a) Number loaded in the ODT vs focus. (b) LIF vs Pockels cell frequency.

1 s timescale. To explore the dependence of loss rate on background pressure, we varied the MOT chamber pressure from 1×10^{-9} torr to 3×10^{-8} torr and find a dependence of $5.5(1) \times 10^8\,\mathrm{s^{-1}\,torr^{-1}}$ (Figure 6.3.8).This was done by spinning the turbo pump down and taking data as the chamber pumped back out. This indicated that at our typical pressure of 1×10^{-9} torr, the loss rate of molecules from the ODT is dominated by collisions with background gas.

The number loaded is also dependent on the focus of the ODT vs the MOT position, as shown
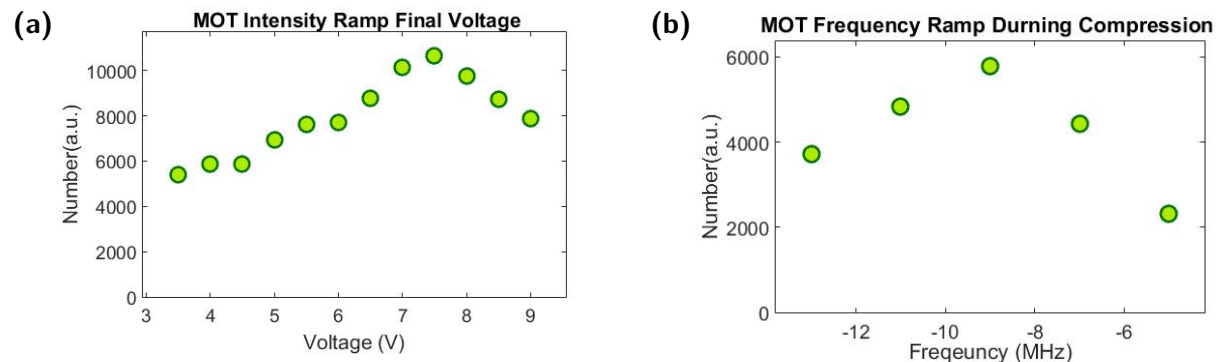
Figure 6.3.10: (a) MOT intensity ramp final voltage vs number in the ODT. (b) MOT frequency compression vs number in the ODT.

in Figure 6.3.9(a). Surprisingly, the sensitivity to the focus position is much higher than one would naively expect from the Rayleigh range of the trap. The optimal Pockels cell switching frequency for imaging the molecules with all 3 beams is shown in Figure 6.3.9(b). The scattering rate in this condition is on the order of 2×10^6 s^{-1}. This indicates that the optimal Pockels cell remixing frequency is about twice that of the scattering rate.

We also optimized the number of molecules in the ODT versus the final intensity of the MOT, Figure 6.3.10. In atomic MOTs, it is typical to add a compression stage to the MOT by detuning to the optimal cooling detuning at $\Gamma/2$. We tried ramping the frequency while monitoring the ODT signal (Figure 6.3.10) and found it was best to simply leave the MOT frequency at the optimal loading frequency.

6.3.2   1064nm ODT with Λ-Enhanced Grey Molasses

After we demonstrated Λ-enhanced cooling in free space, we now had the ability to cool the molecules nearly a factor of 10 times colder than when we were optimizing the initial ODT. This led to an order of magnitude increase in the number of trapped molecules in the ODT. The rest of the experiential setup remained the same from what was described previously.
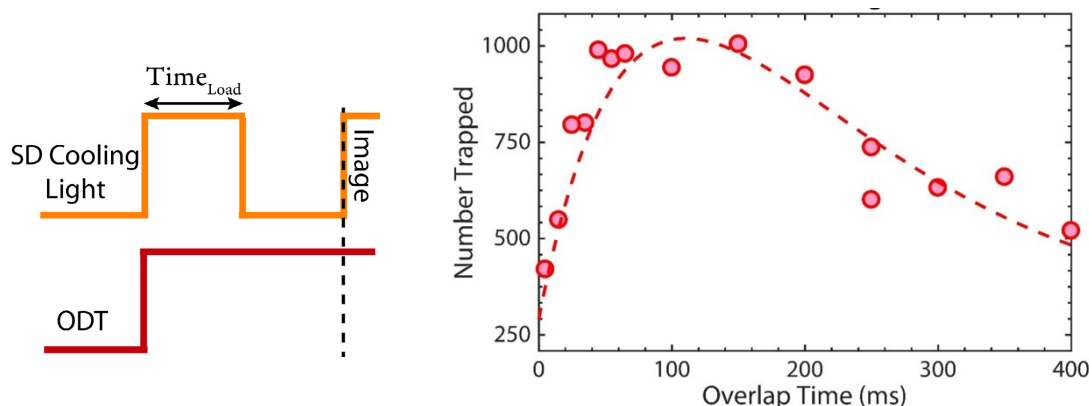
Figure 6.3.11: ODT loading curve with Λ-cooling light. The optimal time is a combination of the ODT lifetime in the presence of Λ-cooling light and the decreasing loading rate due to an expanding molasses cloud.
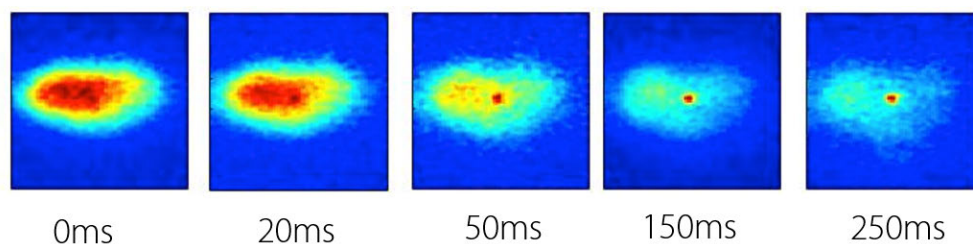
Figure 6.3.12: ODT overlap with molasses as a function of time. One can see the molasses slowly expand out, decreasing the ODT loading rate.

   With the Λ-cooling we rescanned the loading curve for the ODT. We found that now the peak occurred after around 100 ms, rather than 5-10 ms, Figure 6.3.11. This longer time scale can be explained by the fact that the molasses remains at high densities for much longer due to the lower temperature. As shown in figure 6.3.12, the molasses lifetime has a similar time scale as the ODT loading. The increase in trapped molecule number can also be seen as the intensity of the ODT matches that of the molasses, albeit over a much smaller region. The size mismatch can also be directly seen here. Future improvements in transfer efficiency could come in the form of either more MOT compression, or sweeping the ODT position to increase the overlap volume.
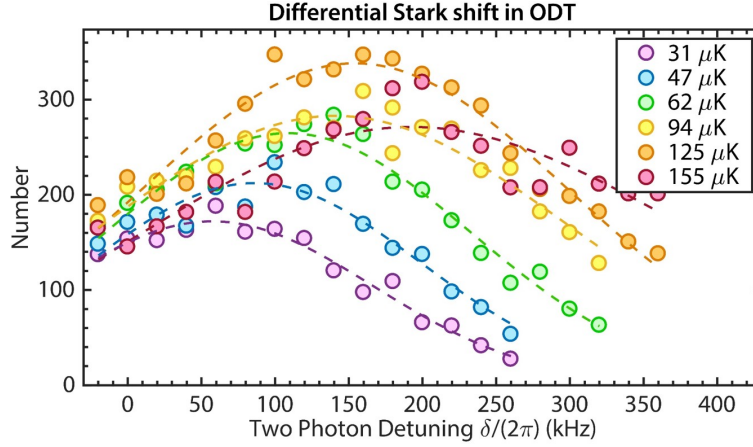
Figure 6.3.13: Number of molecules transferred into the ODT versus two-photon detuning δ at various trap depths V. With the exception of δ, Λ-cooling parameters are set to the free-space optimum ($\Delta = 3.9\,\Gamma$, $I = 14\,\text{mW/cm}^2$, $R_{2,1} = 0.92$).

We scanned the dependence of trapped number versus two-photon detuning at different trap depths. This was done by switching on the ODT and initially cooling the molasses with high intensity, $\Delta = 2.9\,\Gamma$ and $I = 34\,\text{mW/cm}^2$, quickly cooling the molecules to $\sim 10\,\mu\text{K}$, significantly reducing the expansion due to finite temperature. Then, after $1.5\,\text{ms}$, optimal free-space cooling parameters ($\Delta = 3.9\,\Gamma$, $I = 14\,\text{mW/cm}^2$, $R_{2,1} = 0.92$) are used for the next $35\,\text{ms}$ with a varying two photon detuning (not only $35\,\text{ms}$ loading was used at this time because we had scanned the loading curve prior to the optimized parameters used in Figure 6.3.11 and found a shorter optimal). The cooling light is then switched off for $50\,\text{ms}$ to allow untrapped molecules to fall away before the number of trapped molecules is measured. As shown in Figure 6.3.13, as a function of trap depth, the optimal two-photon detuning for maximal trap loading, δ, is shifted from the optimal free space δ. The shift in optimal detuning matches the estimated differential Stark shifts between hyperfine states. At the trapping wavelength, $1064\,\text{nm}$, the differential Stark shifts between ground hyperfine states are as large as $\sim 20\%$ of the trap depth. These differential Stark shifts arise because of the non-zero tensor polarizability of the states relevant for laser cooling in $^2\Sigma$ molecules. The saturation of the number of
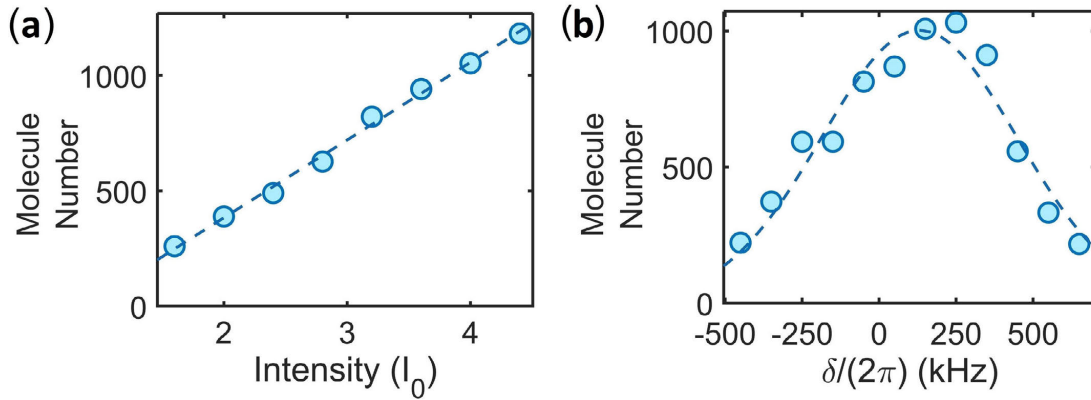
Figure 6.3.14: (a) Molecule number in the ODT vs Λ-cooling light intensity during the loading process. (b) Molecule number in the ODT vs Λ detuning.

trapped is most likely due to the competition between the optimal cooling in free-space and inside the trap. For deeps traps, the optimal becomes so different from the free space value, no reasonable compromise can be made.

In order to optimize for both free-space and in-trap cooling, one can use higher intensities of the cooling light to broaden the Λ-enhanced cooling feature at the expense of minimum attained temperature (Figure 6.2.3(a)). The number loaded increases with intensity (Figure 6.3.14(a)), consistent with this model. To verify that the two-photon resonance remains a key factor at high intensities, we measure the loaded number versus δ at the maximum intensity available ($I = 31\,\mathrm{mW/cm^2}$). As shown in Figure 6.3.14(b), we observe a broad enhancement feature with a width in δ of $\sim 2\pi \times 1\,\mathrm{MHz}$.

With optimized parameters ($\Delta = 3.9\,\Gamma$, $\delta = 2\pi \times 90\,\mathrm{kHz}$, $I = 31\,\mathrm{mW/cm^2}$, trap depth$= 130\,\mu\mathrm{K}$), 1300 molecules are transferred with a temperature of $21\,\mu\mathrm{K}$. The peak trapped density of $6\times10^8\,\mathrm{cm^{-3}}$ and phase space density of 8×10^{-8}.

One experimental difficulty we ran into was that the ODT often seem to disappear. This was when we discovered the multimode issue of the OPO mentioned in the previous chapter. The ODT
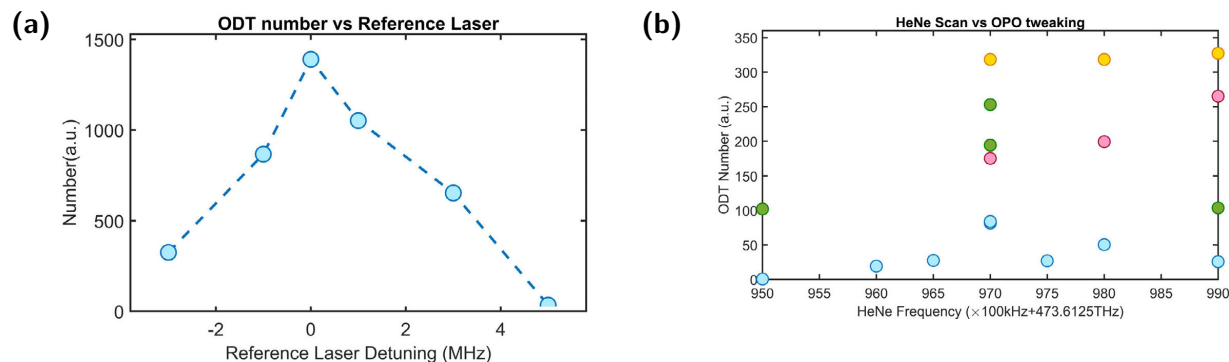
Figure 6.3.15: (a) ODT Sensitivity vs frequency (b) ODT signal vs OPO tweaking. This is due to the multimode nature of this poorly designed laser, as discussed in the previous chapter.

signal was quite sensitive to the overall frequencies of the laser. Figure 6.3.15(a) shows a detuning scan of the reference laser frequency versus ODT signal. This indicates that the frequencies need to be locked to within 500 kHz or so. Figure 6.3.15(b) shows the ODT signal while we tweaked the OPO to different modes. This was done before we had a high finesse cavity that we could carefully monitor the output of the OPO.

6.3.3 IMAGING OF TRAPPED MOLECULES

Non destructive imaging of trapped molecules is a critical part to making use of the molecules for future applications. To show that Λ-cooling could be used for non-destructive detection, we first measured the trapped number as a function of cooling time. Molecules were loaded into the ODT using 150 ms of Λ-cooling, which was then switched off for 50 ms to allow untrapped molecules to fall away. Λ-cooling was subsequently applied for a variable time. To normalize out losses due to collisions with background gas, the samples are always held for the same total time. At the optimal ratio ($R_{2,1} = 0.16$), the lifetime is $370(60)$ ms (Figure 6.3.16(a)). By comparing the collected fluorescence with that of resonant imaging, the scattering rate for Λ-cooling is found to be $\Gamma_\Lambda = 70(10) \times 10^3 \, \mathrm{s}^{-1}$. We could thus scatter 2700 photons per molecule with 10% loss. With resonant imaging (scattering
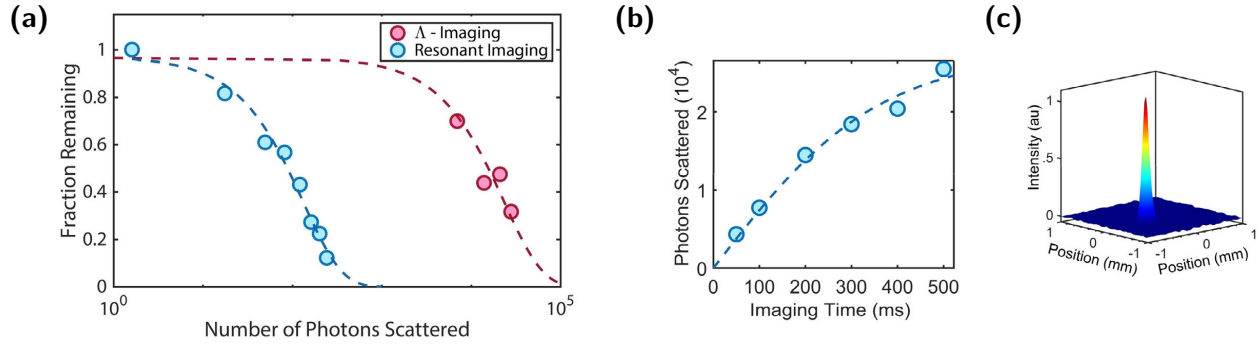
Figure 6.3.16: (a) Fraction of molecules remaining versus imaging time for Λ-imaging shown (blue circles) and resonant imaging (red squares). (b) Total number of photons scattered versus imaging time (c) In-situ Λ-imaging of trapped molecules ($\Delta = 3.9\,\Gamma$, $\delta = 2\pi \times 90\,\text{kHz}$, $I = 31\,\text{mW/cm}^2$ and $R_{2,1} = 0.16$). The exposure time is 200 ms, and 50 individual images are averaged.

rate of $1.6(2) \times 10^6\,\text{s}^{-1}$), the imaging lifetime is $80(5)\,\mu$s (Figure 6.3.16(a)), corresponding to the scattering of $13(2)$ photons per molecule with 10% loss. Λ-imaging thus provides 200 times more photons. It should also be noted that the temperature after lambda imaging is unchanged, staying at $20(3)\,\mu$K, 6 times below the trap depth. By contrast, resonant fluorescent imaging applied for $60\,\mu$s increases the temperature to $50\,\mu$K and leads to significant losses.

The main loss mechanism is thought to be spatial diffusion during Λ-cooling, which arises when Γ_Λ is much larger than the trap frequencies, which are $\omega_{x,y,z} = 2\pi \times \left(1.5 \times 10^3, 1.5 \times 10^3, 12\right)\text{s}^{-1}$ in our setup. This effect can be captured by a simple model where the velocity of a molecule is described by a Boltzmann distribution at a temperature of $20\,\mu$K, and randomized at the scattering rate Γ_Λ. A Monte-Carlo simulation taking into account trap dynamics and gravity yields a lifetime of $700(100)$ ms, 2 times longer than observed. We believe that this model captures the dominant loss mechanism, and differences are likely explained by spatially inhomogeneous cooling. This diffusive loss could be reduced by lowering Γ_Λ at the expense of longer photon collection time.

This was the initial confirmation what we could non-destructively image molecules trapped in optical tweezers. In Chapter 8 we will discuss improvements to the imaging lifetime, allowing us to
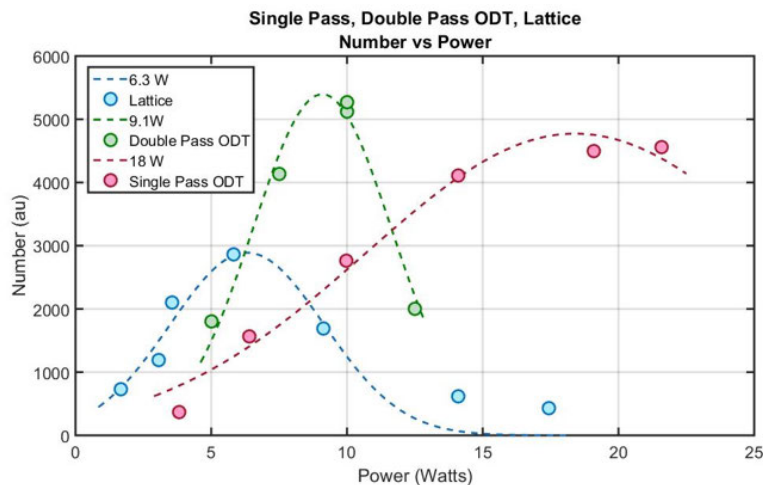
Figure 6.3.17: Number of molecule loaded into a single pass ODT, a double pass ODT, and a lattice as a function of 1064 nm Power.

match the vacuum lifetime.

6.3.4   1064 nm Optical Lattice

If the retro-reflecting mirror shown in Figure 6.3.2 is properly aligned, and the polarization is the same, then a standing wave creates a lattice. This optical lattice has the advantage that now molecules feel a strong confinement in the axial direction, which used to be weak. This stronger confinement allows for an increase in density as well as a deeper trap depth. This means that with the same amount of optical trapping power, a larger volume trap with more molecules may be loaded.

Figure 6.3.17 shows the loading of molecules into a single pass ODT, a double pass ODT, where the retro-reflection has the opposite polarization to prevent the creation of a lattice, and a lattice. As expected, the double pass ODT required half the power of the single pass one. The optimal loading power for a lattice is 4 times lower than that of a single pass ODT, as expected, however fewer molecules are loaded. The lower loading number came from the fact that we saw loss some heating in the lattice on a time scale similar to that of the loading time. We will discuss this heating
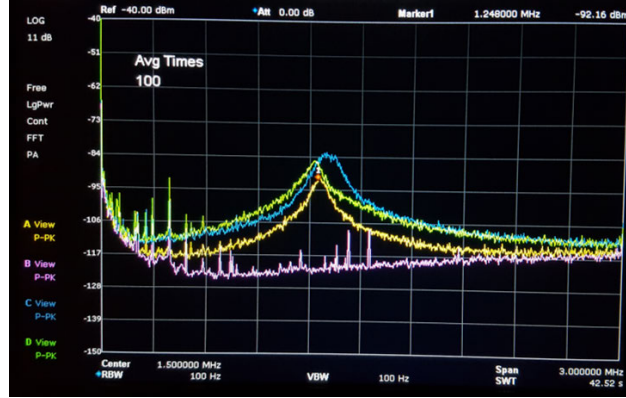
Figure 6.3.18: RIN spectrum of the Nufern with the NP Rock seed laser.

next.

The fundamental problem comes about from intensity noise on the optical trapping light, Figure 6.3.18. This noise, which comes predominantly from the seed laser, causes parametric heating of the molecules. Due to the fact that the peak of this noise is close to that of the radial frequency, the molecules are very efficiently heat out of the lattice. This can be solved by simply using a more quiet seed laser, such as a Rio Orion. The Nufern also adds intensity noise, characterized by [162].

The heating rate can be calculated as follows [163]. The Hamiltonian for the trapped molecule is

$$H = \frac{p^2}{2m} + \frac{1}{2}m\omega^2 \left[1 + \varepsilon(t)\right] x^2 \tag{6.10}$$

where $\varepsilon(t)$ is a factional fluctuation to the spring constant due to the changing trap depth, $\varepsilon(t) = \frac{I(t)-I_0}{I_0}$. Using 1st order time dependent perturbation and bit of math, one finds that the heating rate is

$$\Gamma_{heating} = \pi^2 \nu^2 S_I(2\nu) \tag{6.11}$$

where ν is the trap frequency in Hz, and S_I is the power spectral density at twice the trap frequency

132
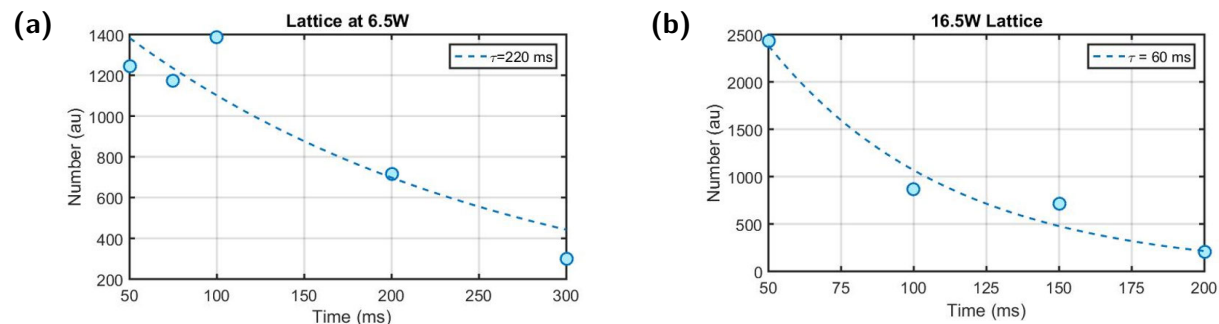
Figure 6.3.19: Loss curves of molecules trapped in the 1064 nm lattice at 6.5 W (a) and 16.5 W (b). The loss rate is higher for deeper traps, as the trap frequency moves toward the peak of the RIN spectrum.

(in units of faction/Hz, or $\left(10^{dBc/10}/\text{Hz}\right)$. $1/\Gamma_{heating}$ is the time to increase the energy by e. This heating rate is exponential since the fluctuating force increase as the square of the distance from the trap center. In three dimensions, one takes the mean of the heating along each axis [163].

Pointing fluctuations may also result in heating. This rate may be expressed as

$$\Gamma_{pointing} = \pi^2 \nu^2 \frac{S_x(2\nu)}{\langle x^2 \rangle} \tag{6.12}$$

were $\langle x^2 \rangle$ is the mean square position of the molecule in the trap and $S_x(2\nu)$ is the power spectrum of the position fluctuations.

The loss rate versus depth is shown in Figure 6.3.19. The loss rate measured agrees well with the calculated heating rate from the RIN spectrum. The loss rate increased as the trap depth increased since twice the trap frequency moved toward the peak of the RIN spectrum at 1.2 MHz.

6.3.5 High Power Multimode Trapping Laser

This was very bad. Don't try it.

Singe frequency, single mode 1064 nm fiber lasers were limited to about 50 W at the time (now

(a)

(b)
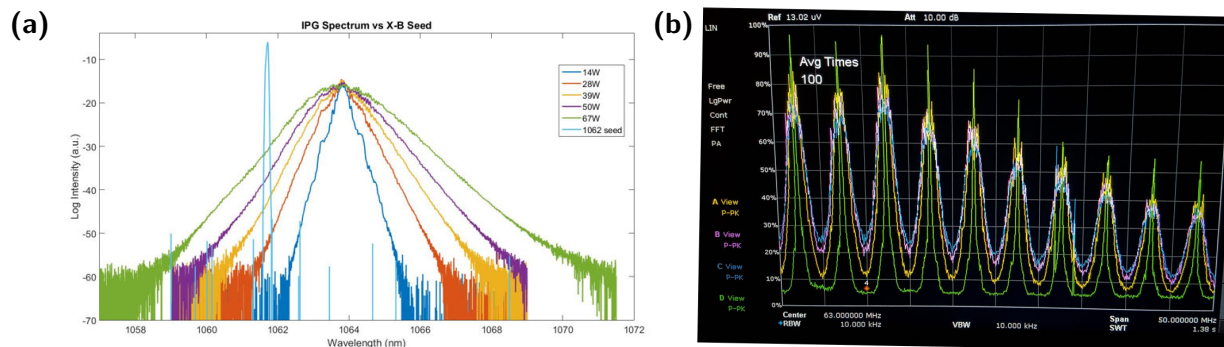
Figure 6.3.20: (a)IPG spectrum vs ouput power (b)IPG spectrum measured on photodiode vs power. The narrow green peaks are at low power, and the broader blue trace is at the lightest power.

days 100 W can be bought). Since we knew that we could load more molecules if we had a larger and deeper trap, we borrowed a 300 W IPG 1064 nm laser (Thank you Greiner Lab, Lithium!). At these powers, the lasers are not single frequency, but are rather quite broad in frequency. Figure 6.3.20 (a) shows the spectrum of a 300 W IPG vs power. We see that the linewidth increased significantly at higher intensities. On top of that we also found that the spectrum was not actually flat, but rather had many different intensity peaks Figure 6.3.20(b), spaced by 5 MHz.

We tried to load molecules into this trap but found extremely short lifetimes. This can be traced to two problems. First, we can drive a two-photon transition from light at 1062 nm to drive the X-B transition. Because this is a two-photon process, the parity is flipped and these molecules would decay to the opposite parity states and become dark. This was solved by added a Semrock filter to suppress this by over 40 dB, Figure 6.3.21.

The other larger problems is fundamentally due to the fact that the laser is very broad in wavelength, but enhanced by the fact that there is this 5 MHz noise peak substructure. Since the laser is broader than the rotational spacing of 20 GHz, the laser can drive Raman transitions from one rotational state to the next. Because the rate of this Raman process is proportional to the square of the intensity, the higher intensities generated due to the sub-peaks in the IPG enhances this rate
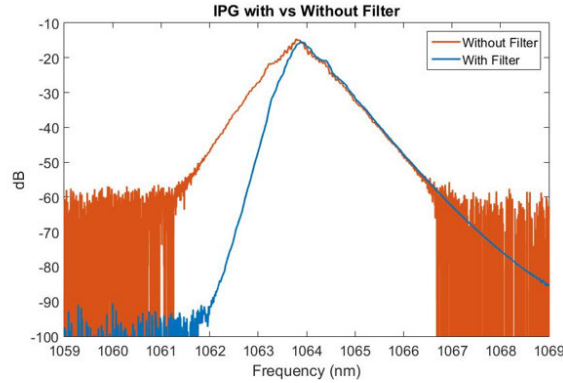
Figure 6.3.21: IPG Spectrum before and after the insertion of a 531nm notch filter to prevent X-B transitions.

significantly.

The two photon rate[164, 165] for driving the X-B transition with a narrow laser is

$$\Gamma = 18\pi^2 \frac{\omega^3 c^4}{\hbar^2 \omega_{XA}^6 \omega_{XB}^3} \Gamma_A^2 \Gamma_B \kappa \eta^2 \left| \frac{1}{(\omega_{XA} - \omega)} \frac{1}{(\omega_{XB} - 2\omega)} \right|^2 I^2 \qquad (6.13)$$

where κ is a numerical factor from matrix elements of .62 and $\eta^2 = 0.184^2$ is the square of the ratio of the dipole matrix elements of B-A and X-A.

For broadband excitation, this expression is modified to:

$$\Gamma = 18\pi^3 \frac{c^4}{\hbar^2 \omega_{XA}^6} \Gamma_A^2 \kappa \eta^2 \frac{I_o^2}{(\omega_{XA} - \omega_{XB}/2)^2} \int d\omega_1 r(\omega_1) r(\omega_{XB} - \omega_1) \qquad (6.14)$$

where I_o is the total intensity and $r(\omega) = I(\omega)/I_o$ is the relative spectral intensity.

This Raman transition rate for rotational levels can be calculated as follows:

$$\Gamma = \frac{9\pi^3}{4} \frac{\Gamma_A^2 c^4}{\omega_{XA}^6 \hbar^2 \Delta^2} \zeta I_o^2 \int d\omega_1 r(\omega_1) r(\omega_1 - \omega_o) \qquad (6.15)$$

where Δ is the single photon detuning from X-A an ζ is a numerical factor of .18.

135

(a)

(b)
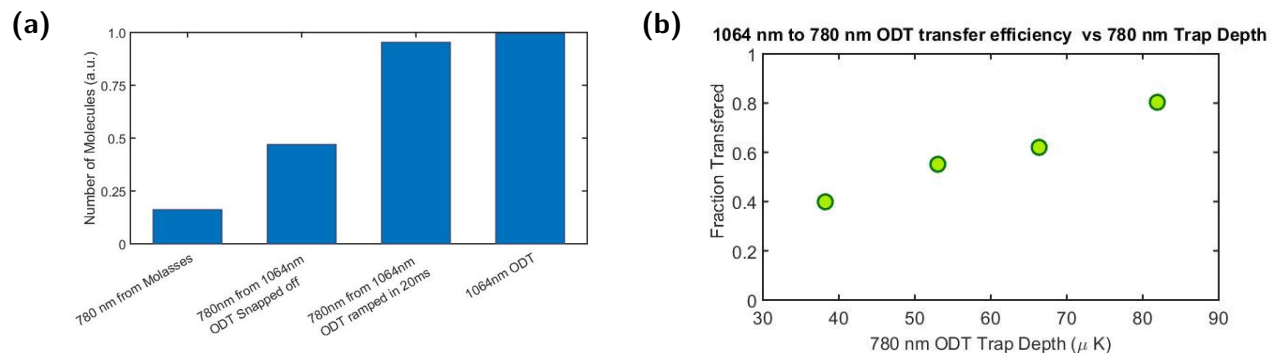
Figure 6.3.22: (a) Transfer efficiency from the 1064 nm ODT to the 780 nm ODT. (b) Transfer efficiency vs 780 nm ODT depth.

The off resonance scattering rate for the trapping light is

$$\Gamma = \frac{3\pi c^2 \omega^3}{2\hbar \omega_{X-X'}^6} \left[\frac{\Gamma_{X'}}{(\omega_{X-X'} - \omega)} + \frac{\Gamma_{X'}}{(\omega_{X-X'} + \omega)} \right]^2 f_{X-X'} \eta I \qquad (6.16)$$

were η is 2/3 for X-A and 1/3 for X-B.

6.3.6 TRANSFER TO A 780 NM ODT

The final thing we wanted to test was whether we could transfer molecules from a larger 1064 nm ODT into a smaller 780 nm ODT. This was the final proof of principle test we needed to do to make sure we could load tweezer arrays of single molecules.

To do this, we overlapped both the 1064 nm and 780 nm traps co-propagating, overlapped with a dichroic. The 780 nm light was created by a Ti:Sapphire laser. We first loaded a 780 nm ODT from the molasses to make sure 780 nm light could be used for optical trapping. We then used the molecular signal to overlap the 780 nm ODT and the 1064 nm ODT since we had no direct reference and chromatic shifts meant we could not fully trust the position of the trap light on the cameras. We first transferred the molecules from one ODT to the other by snapping off the 1064 nm trap. Doing
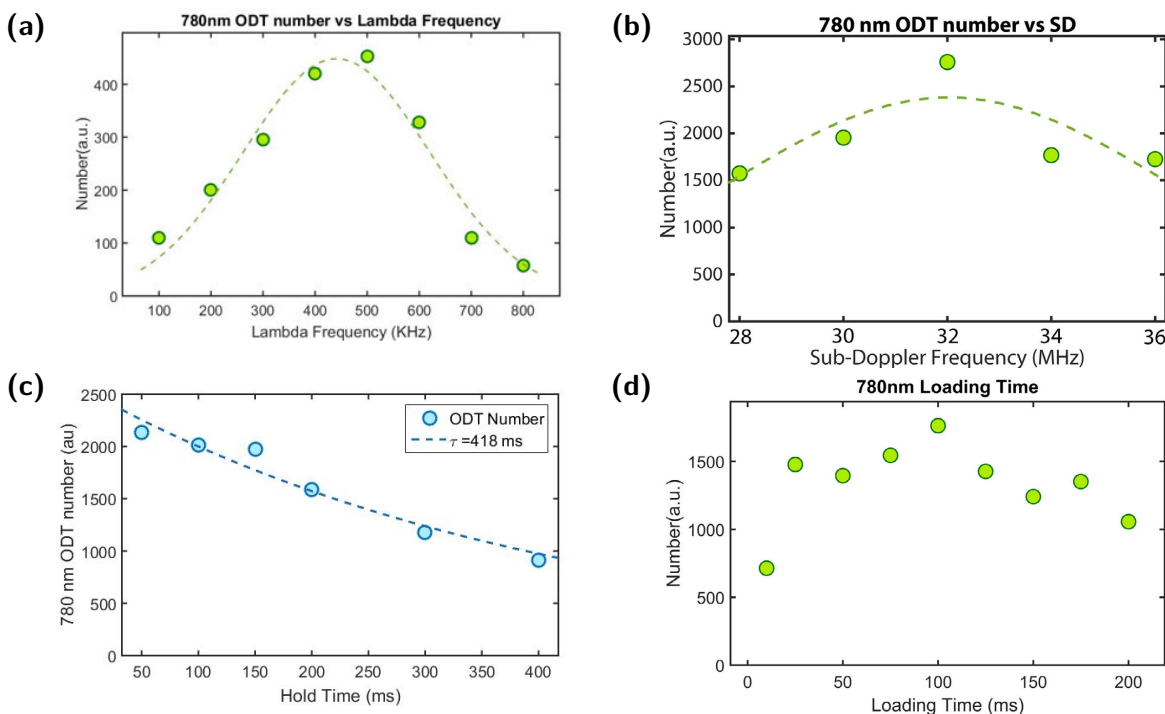
Figure 6.3.23: Loading and characterization of the 780 nm ODT. (a) 780 nm ODT loading vs Λ frequency (two photon detuning). (b) 780 nm ODT loading vs Sub-Doppler frequency. (c) 780 nm ODT lifetime. (d) 780 nm ODT loading curve.

this resulted in roughly half the molecules being transferred. We then ramped down the intensity of the 1064 nm trap and found that we were able to transfer molecules efficiently, Figure 6.3.22. Due to the high transfer efficiency and the smaller volume of the 780 nm ODT, doing so increased the density by an order of magnitude. This thus showed that we would be able to load the molecules from the 1064 nm ODT into the tweezers, once they were overlapped.

We also characterized the direct loading of the 780 nm trap, Figure 6.3.23, as a function of Λ frequency, sub-Doppler detuning, and loading time.

This was supposed to just work, and yet it caught on fire.

-The Author

7

An Optical Tweezer Array of Ultracold Molecules

Optical tweezer arrays [41–43] of laser-cooled molecules are a powerful platform that may bypass existing experimental hurdles. In this approach [16], one can fully control and detect individual molecules. Such individual particle control is a key tool for quantum science and engineering, as it opens up the assembly of complex quantum systems from the bottom up, as exemplified by work with atoms in rearrangeable optical tweezer arrays [41, 42] and assembly of a molecule from two atoms [166]. For molecules, the bottom-up approach of using tweezer arrays combined with laser-cooling is especially important because it bypasses the need for high phase space density samples,
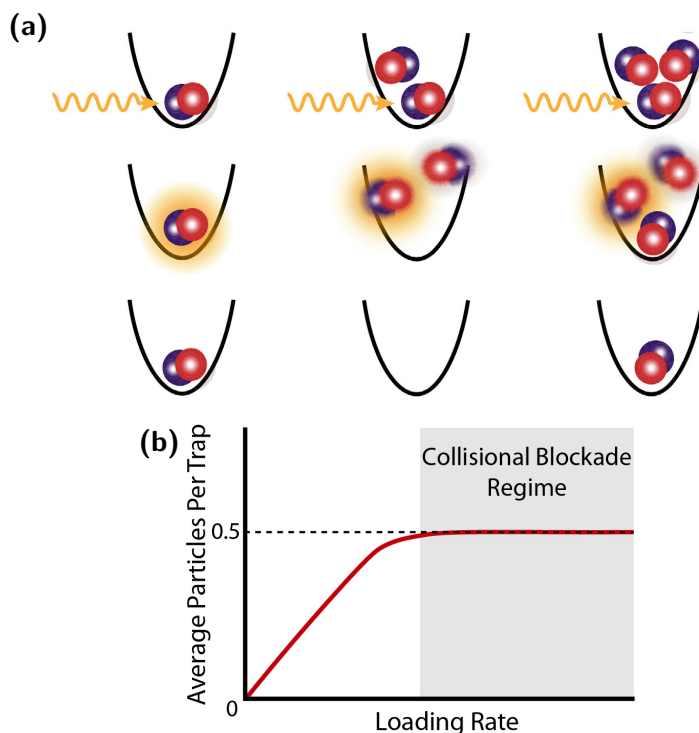
Figure 7.1.1: (a) Light induced collisions in an optical microtrap giving rise to a collisional blockade. (b) Average number of particles loaded in a microtrap versus loading rate showing the collisional blockage regime [121].

which has been a long-standing experimental challenge for molecules in general. Furthermore, this generic approach does not rely on favorable collisional properties necessary for evaporative cooling, and can thus be extended to many other molecular species including polyatomic ones [51]. Optical tweezer arrays of laser-cooled molecules may thus help to realize the full potential of molecules in quantum science.

7.1 THEORY

Single particle loading of optical tweezers is made possible by light induced collisions [117–121]. In the "collisional blockade" regime [121], the loading per trap saturates to one half, Figure 7.1.1. This
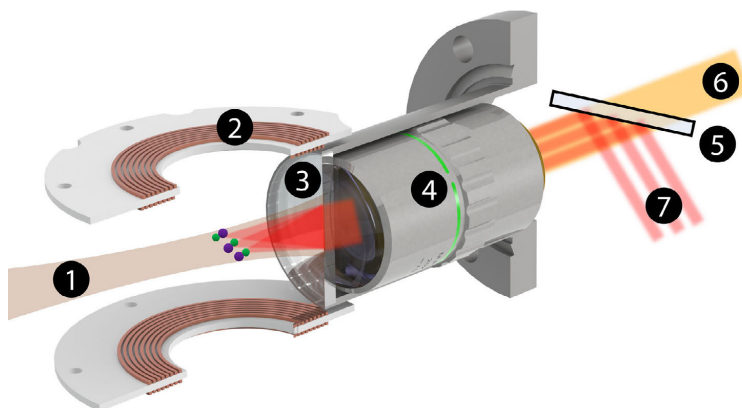
Figure 7.2.1: Experimental setup. An optical dipole trap formed by a focused beam of 1064 nm light (1) intersects the MOT, and is reflected off the re-entrant window (3) at an angle to prevent the formation of a lattice. A microscope objective (4) is placed inside a re-entrant housing between the MOT coils (2). Fluorescence from the molecules (6) is collected through the objective and imaged onto a camera. The optical tweezer traps are generated using an acousto-optic deflector (AOD) (7) and are combined into the imaging path using a dichroic mirror (5).

occurs when the small volume of optical tweezers ensures that the rate of light induced collisions is much higher than the loading rate into the trap. As a result, each trap will always end up with either one or zero particles. The rate of light induced collisions for molecules was not known prior to this experiment, and it was not clear if additional light pulses would need to be applied to ensure parity projection(meaning 0 or 1).

7.2 DESIGN

The plan was to use a microscope objective to project small optical tweezers at 780 nm into the ODT. We choose 780 nm due to the fact it is the peak power of the Ti:sapphire laser, and commercial objectives still transmit at that wavelength. One can estimate the density required to ensure sufficient loading of the tweezer traps from initial density and temperature arguments, and it was found that loading directly from the molasses was on the edge of being sufficient. The MOT density
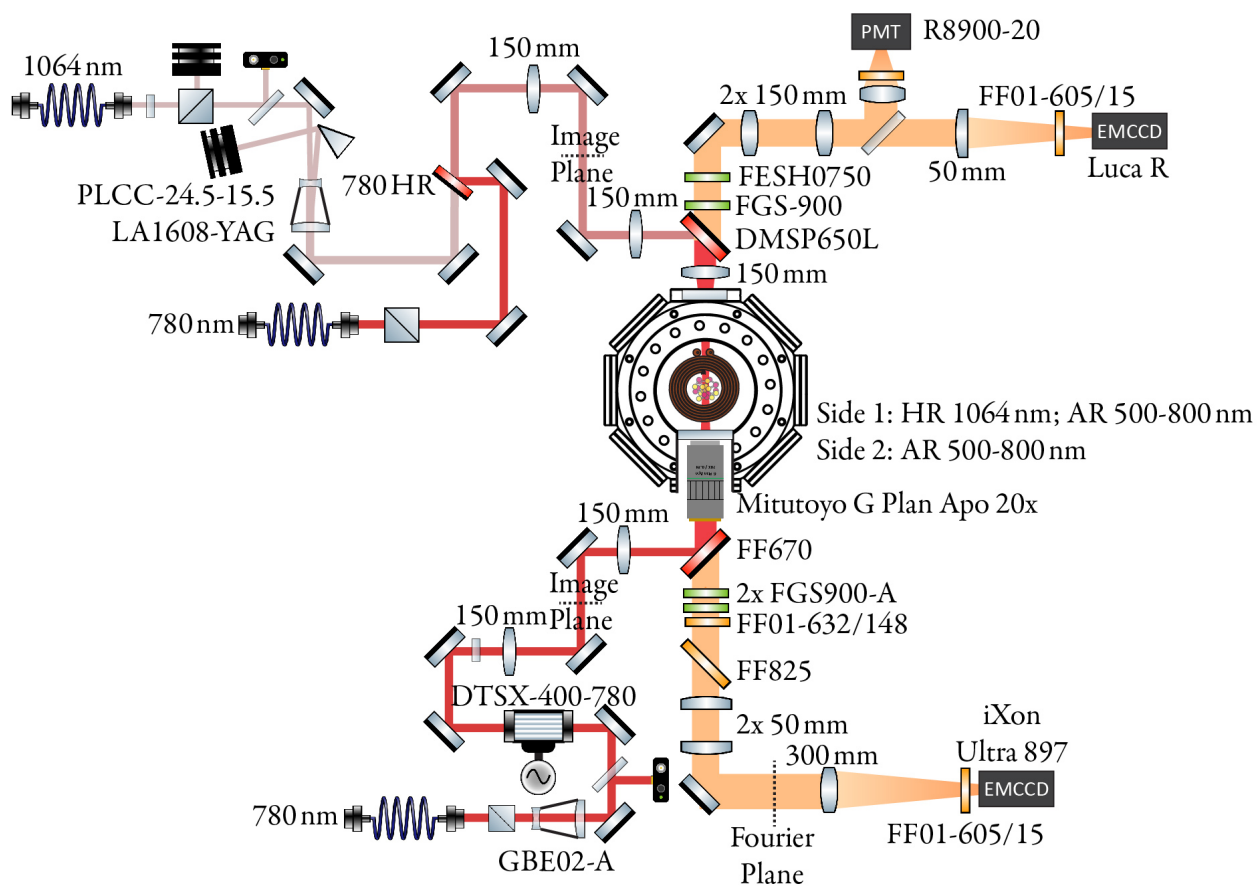
Figure 7.2.2: Tweezer optics beam paths and imaging optics.

of 10^5 cm^{-3} is too low for direct capture into μm-sized optical tweezers. As a result, we decided to first transfer molecules from the MOT into an optical dipole trap. We would then load the optical tweezers from the ODT, which we knew had a two to three order of magnitude higher density than the molasses. To reach loading probabilities of order unity, one would require densities of $\sim 10^{11}$ cm^{-3}, more than four orders of magnitude higher than the MOT density. However, because the laser cooling continues to work inside the trap, large density enhancements can be obtained, so lower initial densities are needed. The molecules trapped inside the 1064 nm ODT are subsequently transferred into the smaller micron sized optical tweezers (780 nm). In order to get the microscope objective close enough to the molecules, we needed to install a re-entrant window into our chamber. Since the MOT beams of centimeter size are at 45 degrees, the highest NA that could be used was about 0.3. The objective we used was a glass compensated long working distance objective (Mitotoyo G Plan Apo 20X) (NA=0.28) with a working distance of 29.4 mm, which is compensated for a glass thickness of 3.5 mm. This meant we could use it outside the vacuum chamber without the need of a custom objective to correct for the viewpoint glass thickness. It is $\sim$73% transmissive at 780 nm and was tested to produce a near diffraction limited spot size with beam waist of 1.4 μm. The experimental setup is shown in Figure 7.2.1.

To generate the multiple tweezer traps, we used an AOD (DTSX-400-780) driven with multiple frequencies generated by a software defined radio (USRP X310) with a 160 MHz bandwidth transceiver (UBX-160)[1]. The initial phase of each trap frequency is optimized to reduce the amplitude of the amplified signal to prevent saturation of the RF amplifier, which can lead to excess noise [42]. The AOD is placed in the Fourier plane such that an angular displacement leads to a position displacement of the trap at the focus. An overview of the beam path is show in Figure 7.2.2. Molecules loaded into the optical tweezers are imaged with the Λ-enhanced grey molasses

---

[1]This transceiver has a low quality PLL, adding considerable phase noise. This in turn leads to heating of the trapped molecules. Switching daughterboards eliminated this heating.
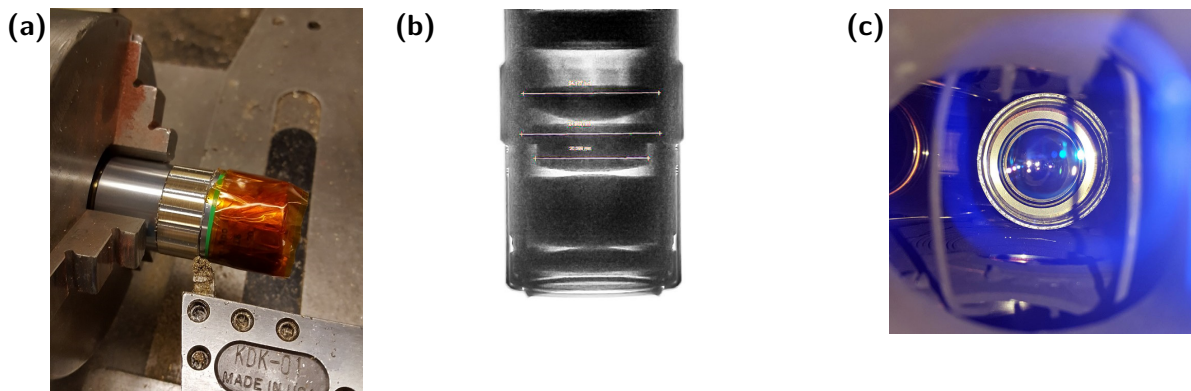
Figure 7.2.3: (a) Machining the objective down. (b) An X-ray image taken of the objective to figure out how much more material we could remove. (c) Final position of the objective, showing the left right offset.

light. The light emitted by the molecules is collected by the objective and split with a dichroic filter from the tweezer light. This light is then sent onto an EMCCD (iXon Ultra 897) for high signal to noise detection.

The position of the MOT coils with respect to the re-entrant window had been checked with a small millimeter sized pickup coil. However, when we began looking at the relative alignment of the MOT and objective, we found it was off very slightly. Unfortunately, the objective's large outer diameter gave us very little adjustment room for the re-entrant tube's inner diameter. We solved this by machining the objective down on a lathe, Figure 7.2.3, such that we could translate it laterally and properly align it with the MOT center.

7.2.1   Imaging

With the goal of detecting single molecules, efficient photon detection becomes crucial. For high fidelity detection, we would like to be in a regime where we need to scatter far fewer photons than that needed to decay into a dark state. With the limited numerical aperture and losses in the system, we collect about one in every 100 photons scattered and have a photon budget on the order of 10^5

photons. We found that the background noise was mainly limited by camera noise rather than background scatter. We spent some time characterizing the camera to find the optimal parameters. The imaging optics are shown in Figure 7.2.2 and 7.2.9.

EMCCD Readout Optimization

To achieve the best signal to noise detection in our low photon count regime, we use an EMCCD (Electron Multiplying CCD). Here we will briefly review why an EMCCD improves detection efficnty at low photon numbers. In a CCD, an array of photodiodes converts photons to electrons which are stored in a capacitor, or well. To read out the image, these charges are then shifted down one line at a time and read out in an output amplifier. There are various noise sources present in this type of device, primary dominated by readout noise from the output amplifier, and dark noise from leakage current. Cooling the camera reduces the dark current exponentially, but does not eliminate the readout noise. This is where an EMCCD helps. Here, in the horizontal readout, rather than simply transferring the electron charge to the final output amplifier, large clocking voltages (voltages used to move charge from one well to the next) are used to multiply the charge in a stochastic fashion. The noise of an EMCCD is set by the dark current, the readout noise, a stochastic noise factor from the amplification stage of a factor of $\sqrt{2}$, and clock induced charge. The stochastic noise can be eliminated in photon counting mode, which requires a photon flux much less than 1 photon per pixel. It turns out that for many EMCCDs, CIC (Clock induced charge) becomes the dominant noise source. So, what is CIC? It arises from impact ionization of electrons as they move across the Si-SiO$_2$ interface[167]. This is the same mechanism as is found in the EM registers, but here it leads to unwanted noise during the vertical shifting. High clock voltages and fast clock rise time will increase CIC since it scales with the applied electric field. However, if the clock voltage is too low, not all of the charge will be transferred from one well to the next. Since CIC is from electrons leaving the traps, the longer the electrons are held in each well, the higher the chance the electron
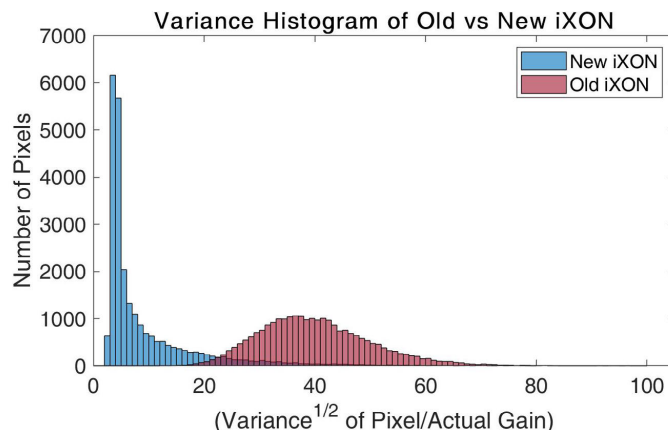
Figure 7.2.4: New iXon Ultra 897 vs old iXon3

can escape and impact ionization can occur [168]. For this reason, faster vertical shift speeds will lead to lower CIC.

EMCCDs have made remarkable progress over the past decade. We upgraded our old EMCCD for a new one and gained a factor of 2.6 in signal to noise, Figure 7.2.4. The EMCCD used (iXon Ultra 897) is back illuminated, meaning the wiring and wells are on the opposite side to which the light enters. This unobstructed view allows for quantum efficiencies at our wavelength of 93%. We characterized the noise properties of our EMCCD versus readout rate, temperature, vertical shift speed, and preamp gain. Since our method of detecting molecules is to set a florescence threshold, above which we count a tweezer as occupied, we are interested in noise at these higher count thresholds. Figure 7.2.5 shows the error rate vs threshold used for various camera settings. For optimal signal to noise, but retaining the ability to align the trap position carefully, we operate with a hardware binning of 2 pixels in the vertical direction, and 8 pixels in the horizontal direction. The readout rate of the EMCCD is affected by the number of rows read out, but not the number of columns. The EMCCD is cleaned from bottom to top, so to make sure the camera is clean, the pixels of interest are placed at the bottom of the sensor. A shutter should also be installed in the future to not be sen-
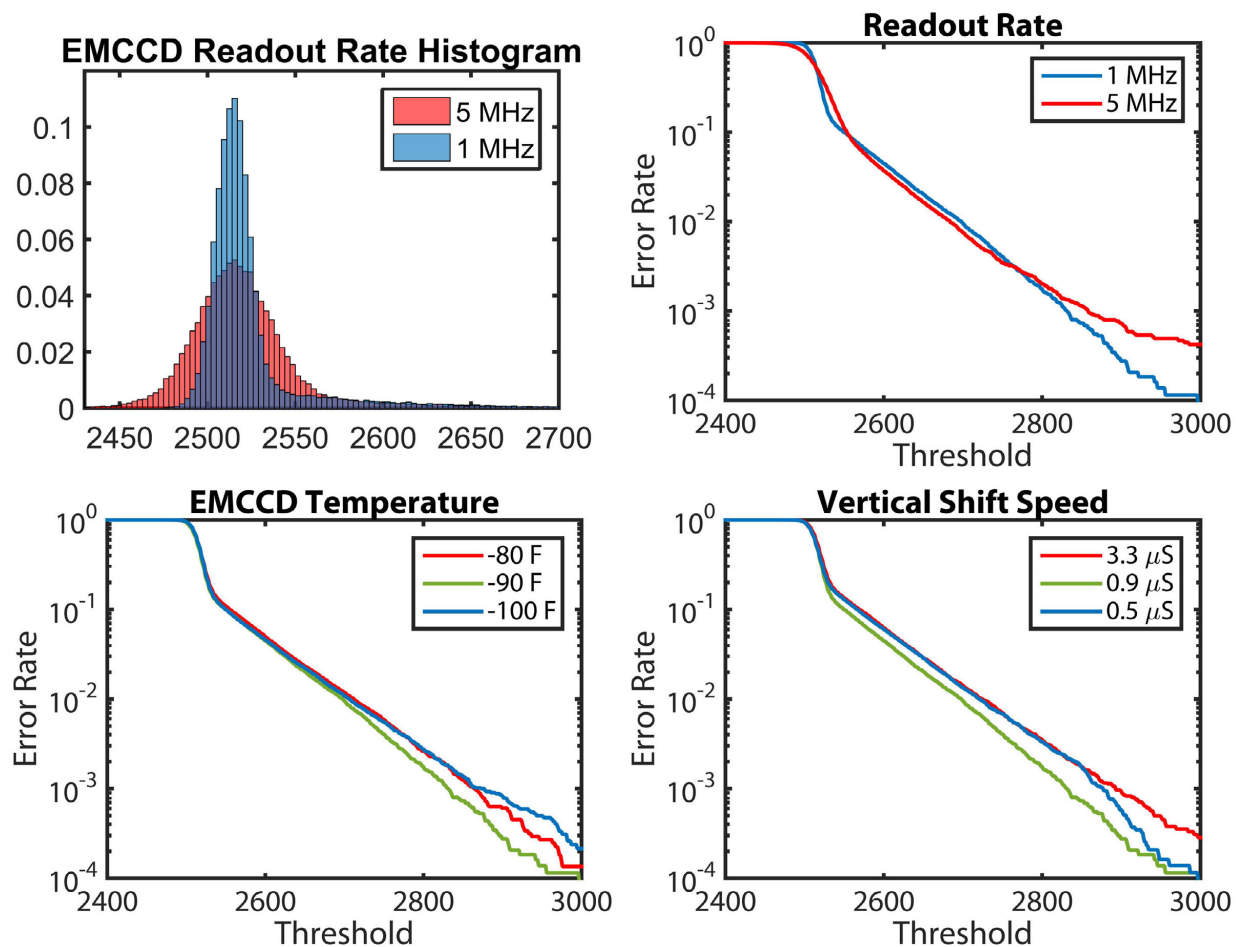
Figure 7.2.5: EMCCD settings vs error rates. For the exposures used, 25 ms, we typically operate with a threshold of 3000.
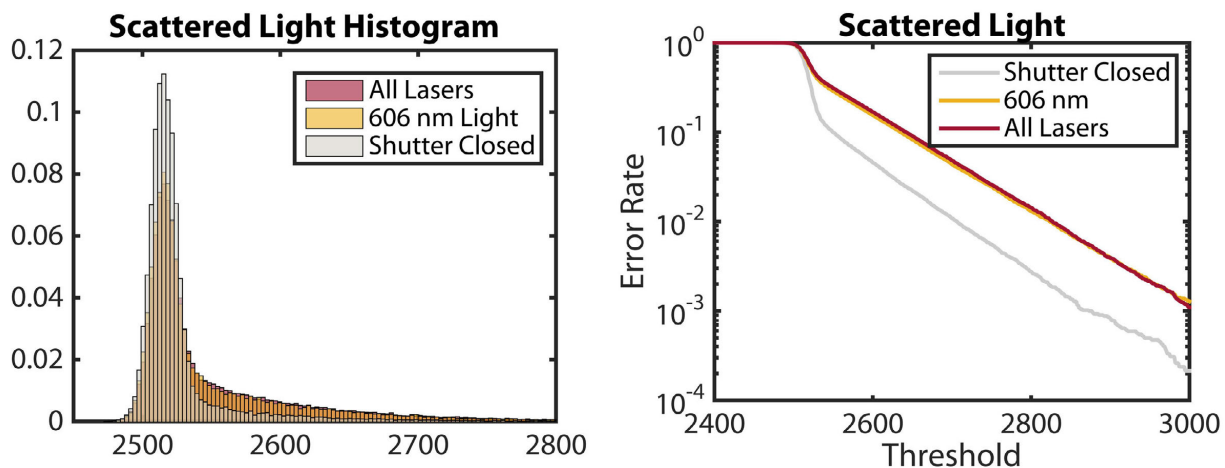
Figure 7.2.6: Error rate vs threshold with the measured scattered light.

sitive to stray light prior to the exposure. The optimal parameter we ended up using for detection is shown in Table 7.2.1.

iXon Parameter	Setting
Vertical shift speed	0.9 μS
Horizontal shift speed	1 MHz
EM gain	500
Preamp gain	3 (4.21 e/ADU)
Temperature	-90 °C
Horizontal Binning	2
Vertical Binning	8

Table 7.2.1: Optimal EMCCD parameters used.

Figure 7.2.6 shows a histogram and error rate due to scattered light. We find that we are currently dominated by scattered light. A 4f Fourier filtering system has been built into the system, but we have not yet inserted a mask into the Fourier plane.

(a)
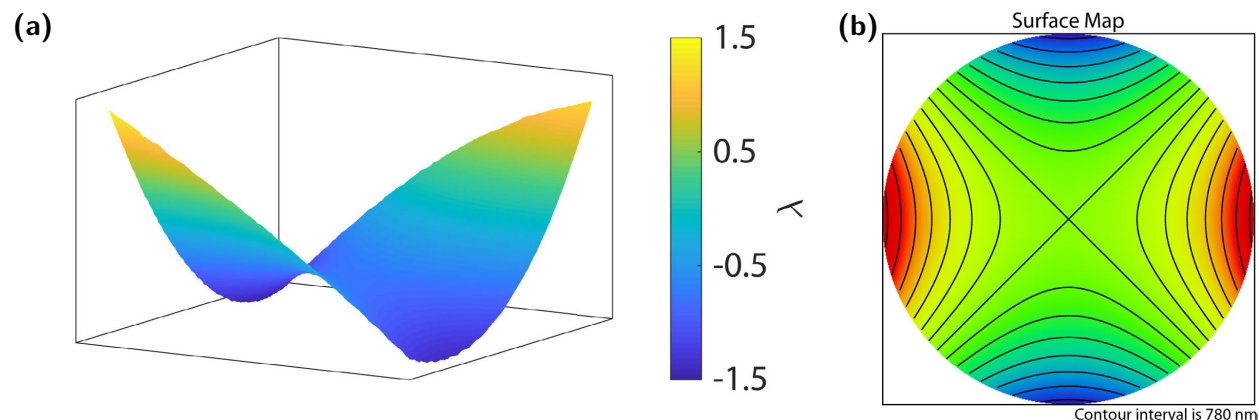
Figure 7.2.7: (a) Measured ISI window curvature over an 8x8 mm region. (b) Surface used in ray tracing simulation, matching the curvature measured.

7.2.2   RE-ENTRANT WINDOW

There are two ways of getting an objective close enough to the molecules to have a high NA. The first option is an in-vacuum lens and the second is an outside of vacuum lens with the molecules close to a window. Having the lens outside of the vacuum allows for much greater flexibility and the ability to align the objective to the molecules. This proved to be a very valuable asset. The objective we decided to use was corrected for a 3.5 mm thick piece of glass, so we needed a re-entrant window of this thickness. We also wanted the ability to reflect the 1064 nm ODT light off of it so it had to be coated with a high reflectivity 1064 nm coating. We had this window made by ISI (subdivision of MDC) with a specification of $\lambda/10$ for the flatness of the window substrate.

Unfortunately, when we measured the flatness of the re-entrant window we received, we found that due to the brazing process used, a large saddle shape curvature on the window was present. Figure 7.2.7 shows the curvature of the window surface as measured with an interferometer using a superluminescent diode (QSDM-680-2). (This source has a coherence length on the order of $15\mu m$ to prevent inference from the second surface of the window or any other part of the interferometer.)
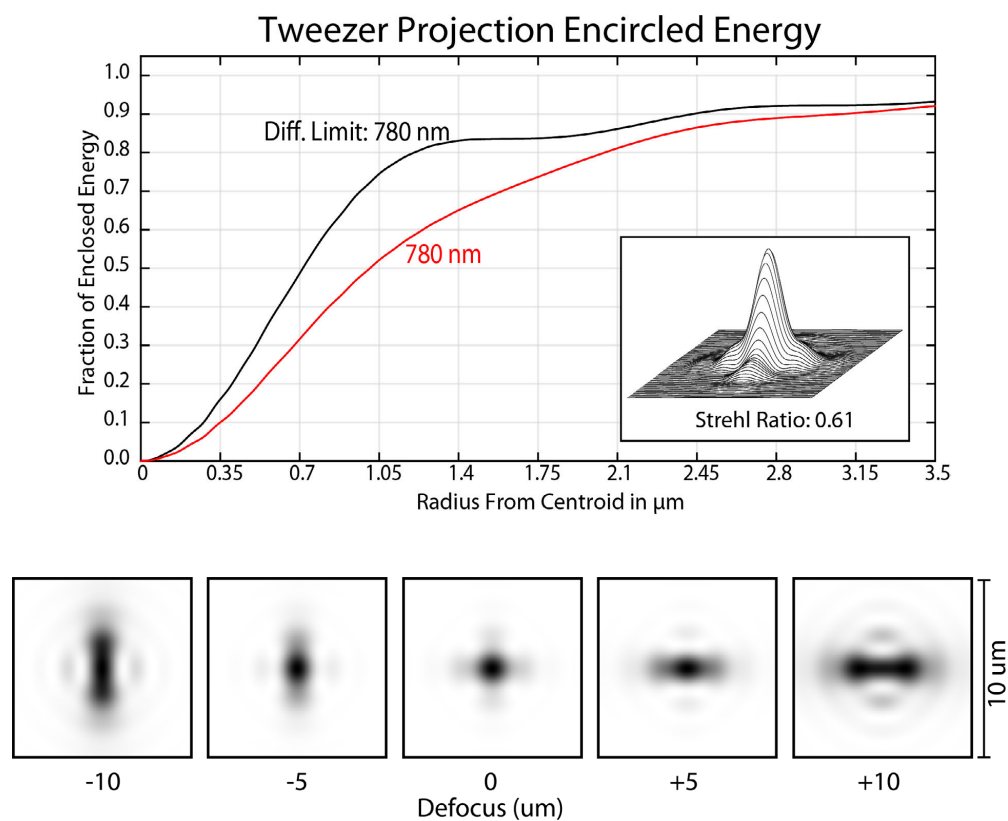
Figure 7.2.8: Projection of 780 nm tweezers. Ray tracing simulations of the effect of this saddle shape curvature.
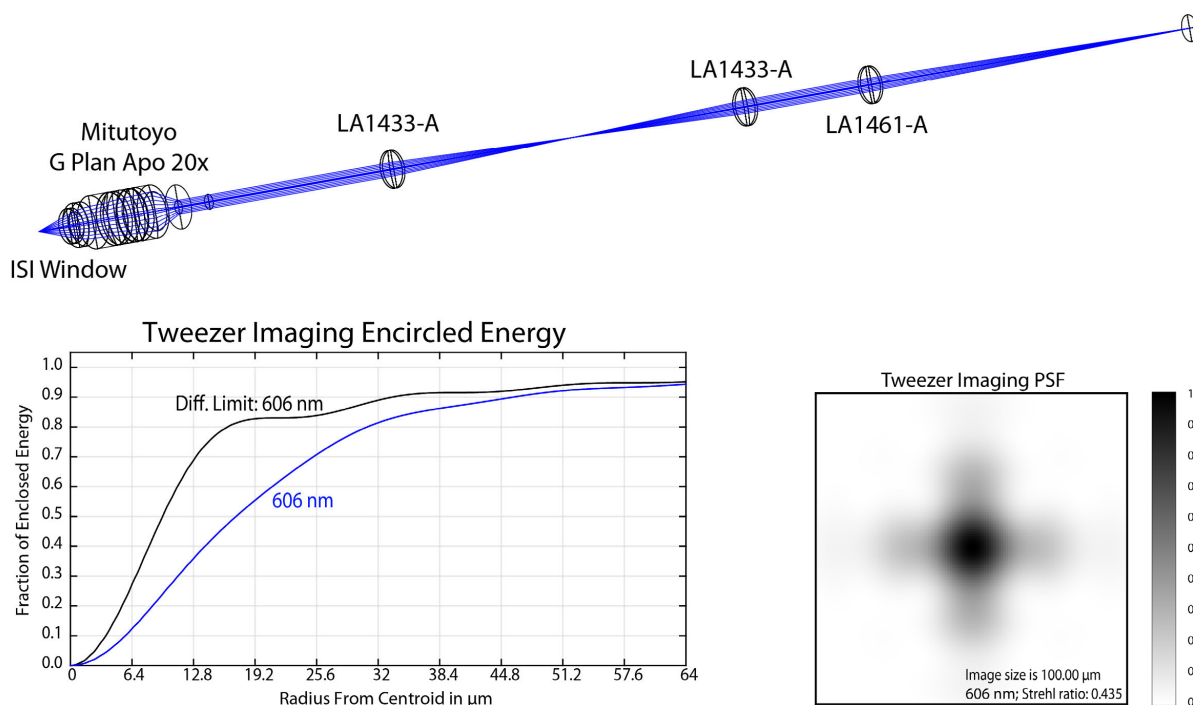
Figure 7.2.9: 606 nm imaging ray tracing simulations of the effect of this saddle shape curvature.

The curvature was about $\pm 1.5 - 2\,\lambda$ over an 8 mm region. The effect of such a curvature can be modeled in ray tracing software, for both the projection of the 780 nm light, Figure 7.2.8, and the imaging of the 606 nm light, Figure 7.2.9. While an overall curvature of the window leads to a focal length shift to first order (as caused by atmospheric pressure), a saddle shape curvature changes the focus of the X and Y axis in opposite direction. One can see this leads to an astigmatic aberration which enlarges the spot size considerably. We have measured and confirmed that the spot size agrees with these simulated aberrations.

Homemade Re-Entrant Window

We decided to solve this problem by making our own re-entrant windows, Figure 7.2.11. This was done by machining a tube with a 0.5 mil gap to the outer diameter of a round glass substrate. The
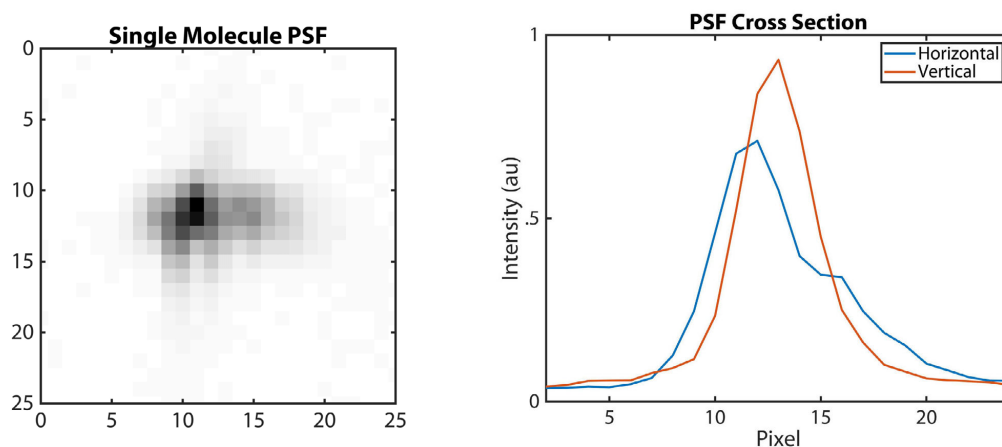
Figure 7.2.10: Measured 606 nm PSF. It appears that the image is slightly defocused.

gap should be just big enough that the new window should be a snug push fit. The side walls were 5 mil thick over a 1 inch distance as a stress relief in the event of temperature changes. This type of design has been used previously for cryogenic application [169]. The window was placed into this tube and glued in place. Due to the very small gap between the tube and the window, capillary forces will suck the glue into the gap, assuming the right viscosity epoxy is used. In this case we tried both Stycast 1266, which was used previously for cryogenic applications, but had untested outgassing properties, and Epotek 302-3M, which we had previously used for the MOT chamber windows.

There are a few important things to keep in mind when assembling these windows. First, the epoxy should be degassed to prevent air bubbles from appearing inside of the gap. The glue should be applied in one spot, and one must wait until the glue reaches the bottom of the window. Then start applying glue in one direction. It is important to go slowly and wait for the glue to fill in the gap before moving forward. If one apples glue too quickly, this will lead to trapped air bubbles and the window will need to be scrapped. The gluing process can cause the window pointing to shift so this should be continuously monitored. Shooting a laser pointer off the surface is a good way to ensure the surface does not tilt. Ensure that all surfaces are UHV clean before gluing. The tube of the window was also glued with the same glue into a CF flange. Again, the gap was left fairly small for the
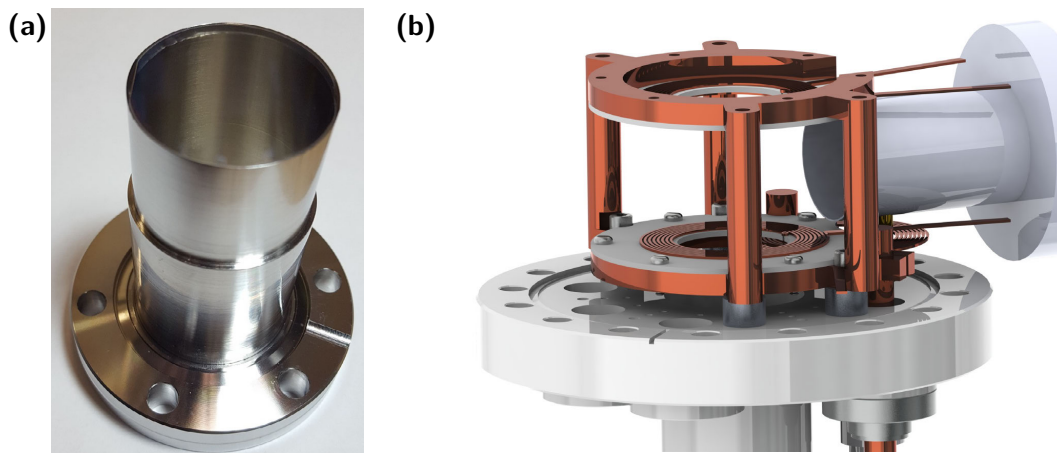
Figure 7.2.11: (a) Homemade window. (b) Overview of re-entrant window placement.
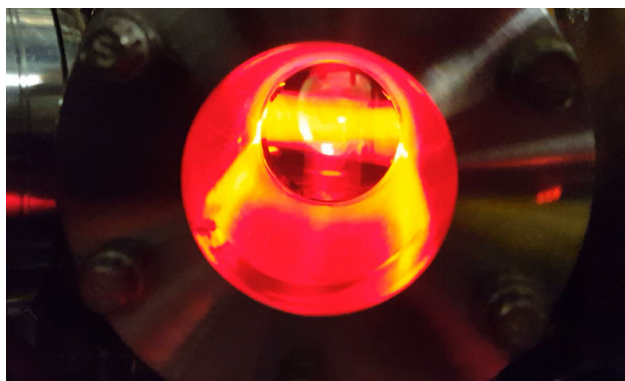
Figure 7.2.12: Not something you see ever day in your UHV chamber...(Yes, that is smoke.)

glue to fully fill the gap. These windows were tested and found to be leak tight at room temperature. However, an anomalous heating effect described in the next section caused these windows to fail.

EDDY CURRENT HEATING

We installed the re-entrant window on the UHV chamber and began trying to make an RF MOT. The MOT coils were turned on for 20 ms every second and operated at 1.4 MHz with a gradient of 15 G/cm. However, on the very first shot, the MOT chamber pressure skyrocketed. We suspected
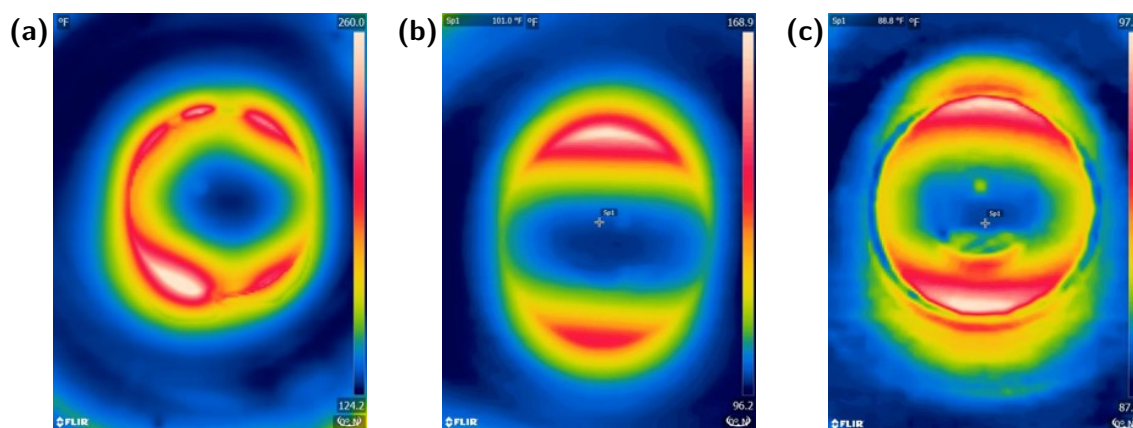
Figure 7.2.13: Thermal Images of the heating pattern of the various windows (a) Stycast window, Peak:260 °F. (b) Epotek window, Peak:169 °F. (c) ISI window, Peak:97 °F.

something had heated up and sprung a leak. After turning off the turbo pumps and shutting the gate valve, we ran the sequence a few more times and looked at the re-entrant tube with a thermal imager (of course a thermal imager was not needed to know something was getting hot, the smoke gave that away, Figure 7.2.12). We found that with the duty cycle we were running at, the temperature was shooting up to 260 °F!. The more interesting thing was how it was heating up, Figure 7.2.13 (a). One would expect from eddy current heating of the coils, a dipole distribution, as is seen with the Epotek and ISI window which were tested afterwards. However, the very odd heating pattern seen on the Epotek window seems to point to something that was wrong most likely in the machining of the thin wall tube. It is possible the thickness of the tube was not uniform and this was causing heat islands which caused the anomalously high temperatures.

We had done back of the envelope calculations to estimate the effects of heady current heating and had found it negligible. Full FEM simulation were done and also showed agreement with the much lower estimated heating rates than had been observed. However these simulations did show some interesting features. Namely, if copper rather than stainless steel were used, the total heating would be an order of magnitude lower, and the heat could be more easily conducted away. The copper
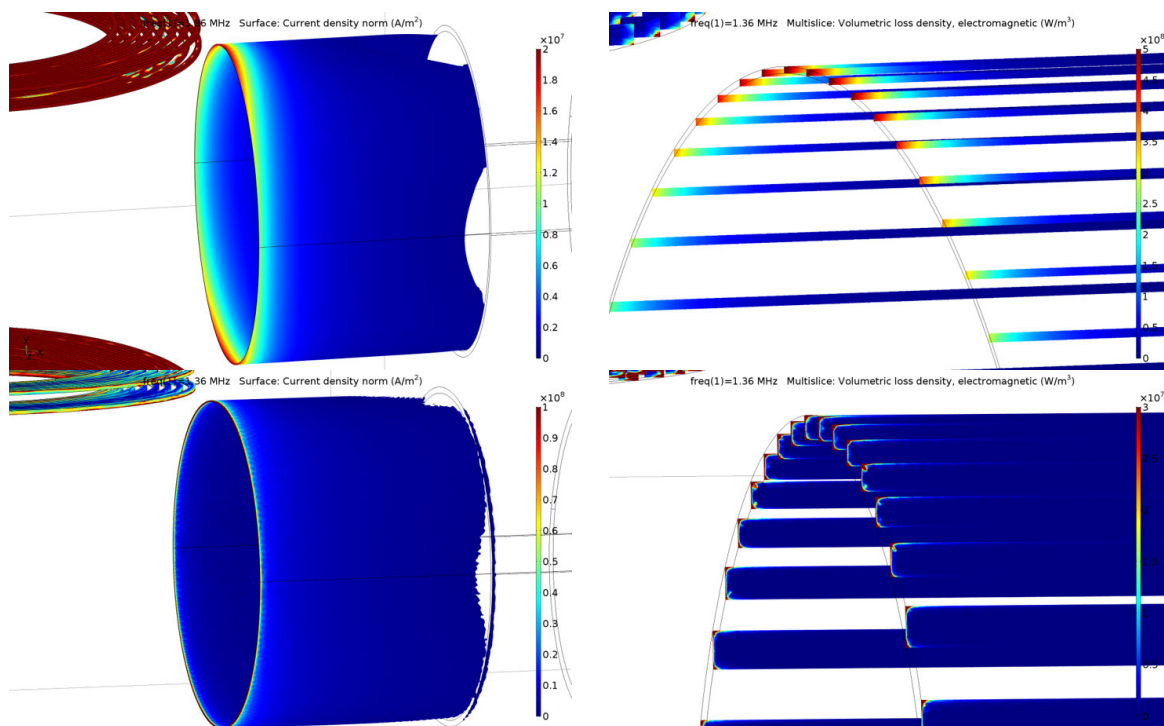
Figure 7.2.14: FEM simulations of eddy current heating on re-entrant tube at 1.36 MHz. Top: stainless steel, dissipating 5.5 W. Bottom: Copper, dissipating 0.4 W. The effect of the small skin depth of copper can be clearly seen, reducing the heating experienced by the copper tube.

tube could also be made much thicker since the skin depth is only 65 μm, the center region of the tube acts as a cold finger puling heat away from the heated surface. It is highly recommended that all future re-entrant windows of this type use copper rather than stainless steel.

We decided that for the time being, we would accept the higher aberrations and use the ISI window. Based on the thermal measurements, the ISI window had by far the least heating.

Electric Fields

With the new re-entrant tube installed we once again began looking for a MOT. However, we quickly discovered a new problem. The lifetime of the MOT was very short lived, Figure 7.2.15, which
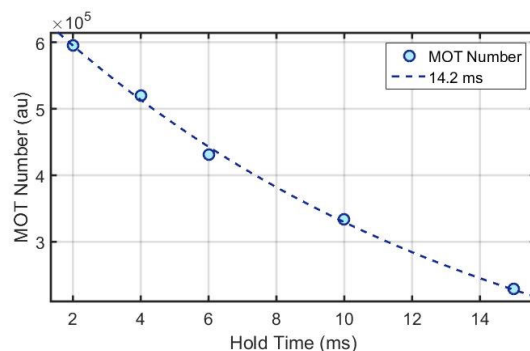
Figure 7.2.15: RF MOT lifetime with the re-entrant window installed.
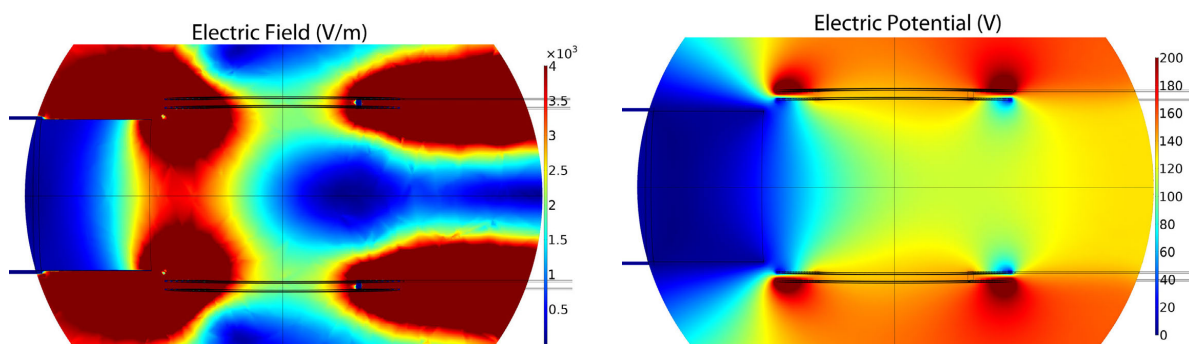
Figure 7.2.16: Reentrant tube electric field and potential. The field at the center of the MOT coils is about 1300 V/m.

indicated we most likely had an electric field issue.

Simulations of the electric fields from the RF MOT agree with the lifetime seen. The fundamental issue is that the re-entrant tube was grounded, but the RF MOT coils were being driven between with ±V on one end and ground on the other. This means that the midpoint voltage is not ground, but rather V/2. This can be clearly seen by looking at the electric field potential, Figure 7.2.16. When the grounded tube was installed between the coils, it caused a large electric field, on the order of 1300 V/m in the MOT region. This corresponds to a lifetime of 15 ms, as observed, Figure 7.2.15.

A solution to the problem is to float the RF coils, such that the midpoint voltage is at ground and
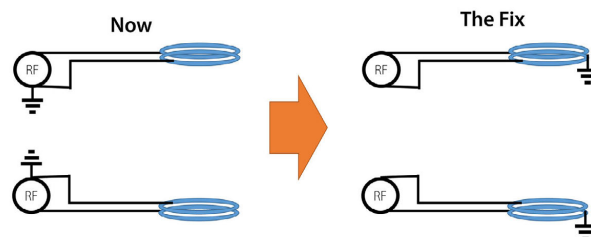
Figure 7.2.17: Driving the MOT coils such that the midpoint voltage is grounded.
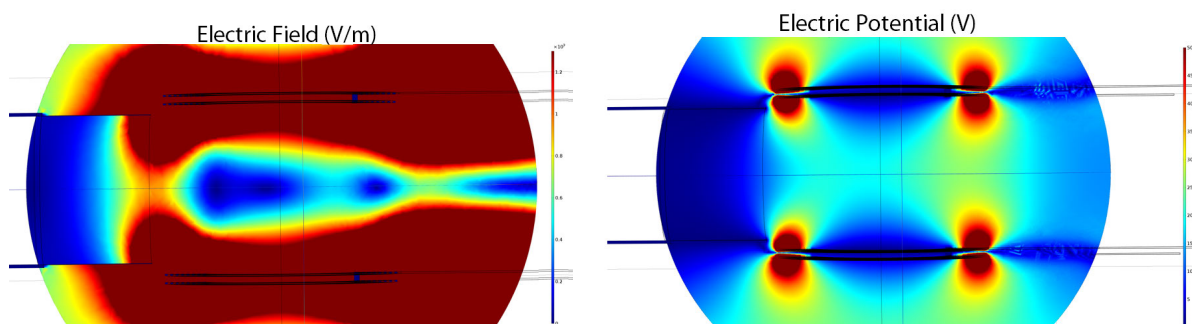
Figure 7.2.18: Electric field and electric potential using this floating coil fix. The peak electric field in the region of interest is decreased by a factor of over 5.

the coils are driven as $\pm$ V/2 on one end and $\pm$ V/2 on the other side Figure 7.2.17. This would decrease the electric field by over a factor of 5, Figure 7.2.18 , meaning a factor of 25 in MOT lifetime. This is quite simple to implement, with only needing at high power transformer to be added at the input of the impedance matching circuit. However, we did not have such a transformer on hand, and only thought about this solution about a week later, so instead we decided to switch to a DC MOT. The DC MOT eliminates both this and the heating problem. However, as we did not want to reopen the UHV chamber, we decided to continue operating with the ISI window. The DC MOT switch does come at a cost of about an order of magnitude in density, but because we planned to load from the ODT rather than the molasses, we decided we had the density to spare.

(a)

(b)
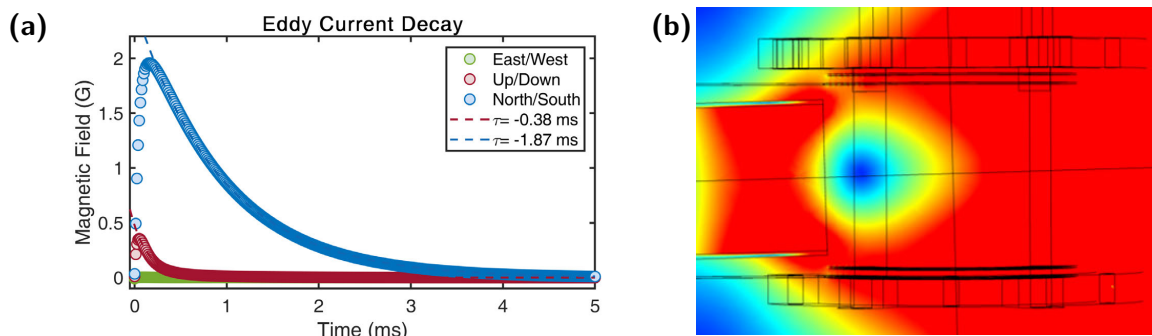
Figure 7.2.19: Eddy current decay of MOT coil holder (a) All 3 components of the field. (b) Side view of the magnetic field mid-decay. The re-entrant tube also creates a small decaying eddy current in the opposite direction. See Footnote[2].

Eddy Current Decays

Unfortunately, that was not the end of the unanticipated problems. There was one final problem that arose with the decision to switch from the RF to the DC MOT, eddy currents. The issue is simple–the MOT coil holder is made of copper, but is not symmetric due to a cut on one side where the electrical feedthroughs are located. This means when the DC MOT is shut off, the eddy current decays over a few milliseconds, and causes a large field which disrupts the sub-Doppler cooling process, Figure 7.2.19. This allows the MOT cloud to rapidly expand due to its high temperature, before the sub-Doppler cooling can kick in. We had been immune to this problem with the RF MOT since the RF MOT switches fields much faster than the time scale that this eddy current can build up. Note that the re-entrant tube also creates a decaying eddy current, but is made of steel so the effect is small.[2]

We decided to add a high current shim coil on the exterior of the MOT coils in the North/South direction. This was the primary direction of the non-symmetric field. Simulations were done to

---

[2]Note there is a cute trick that could be played to compensate for this non-symmetric eddy current decay. The re-entrant tube itself creates a decaying eddy current which is in the opposite direction of the holder. With a copper tube of the right thickness and size, one in principle could use this to compensate the eddy current decay. Of course, just designing the system to run with an RF MOT is probably a better idea.
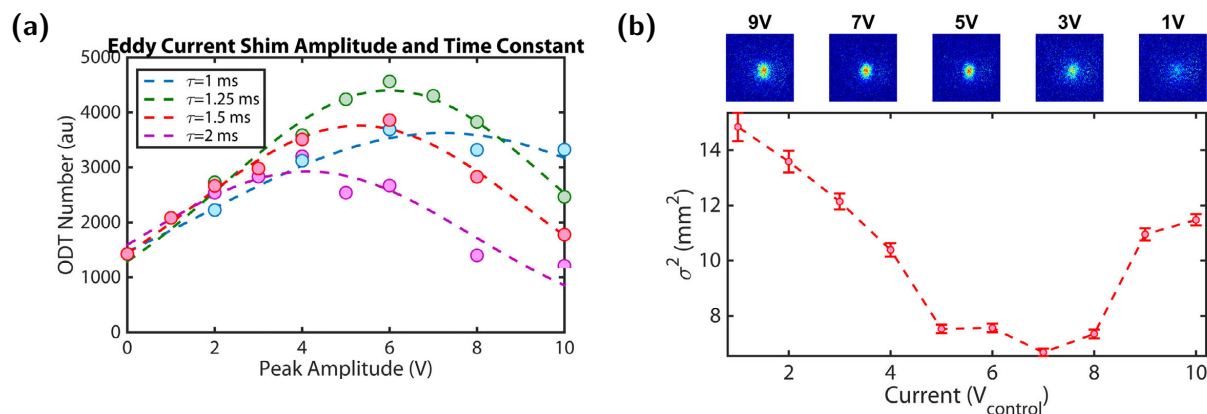
Figure 7.2.20: (a) Optimization of the number of trapped molecules in the ODT. (b) Optimization of the grey molasses cloud diameter.

calculate the approximate timescale of the decay to know where in parameter space we should be looking for the shim timing, Figure 7.2.19(a). We programmed the shim coil to follow a decaying exponential with a timescale similar to that of the simulation. The shim coil is driven with a BOP (Bipolar Operational Power Supply). Figure 7.2.20 shows the optimization of this shim current and time constant. This allowed us to regain reasonable numbers in the ODT.

7.3 ROAD TO A TWEEZER ARRAY

To start looking for molecules in our tweezer, we first began by sending in a small 780 nm beam (0.85 mm waist) into the objective to achieve a fairly large, 4 μm spot size. This was done to increase the chances of capturing a molecule. After finding the optimal focus for loading and imaging the tweezer trap and optimally overlapping the ODT with the tweezer, we could reliably load the tweezer, Figure 7.3.1(a). We knew from loading the 780 nm ODT that for optimal transfer, ramping the 1064 nm ODT was important for transfer efficiency. We did this for various rates, shown in Figure 7.3.1(b). What we saw was, in retrospect, a clear sign of light induced collisions happening. However, we could not confirm this at the time. What was seen was that there was some optimal

(a)

(b)
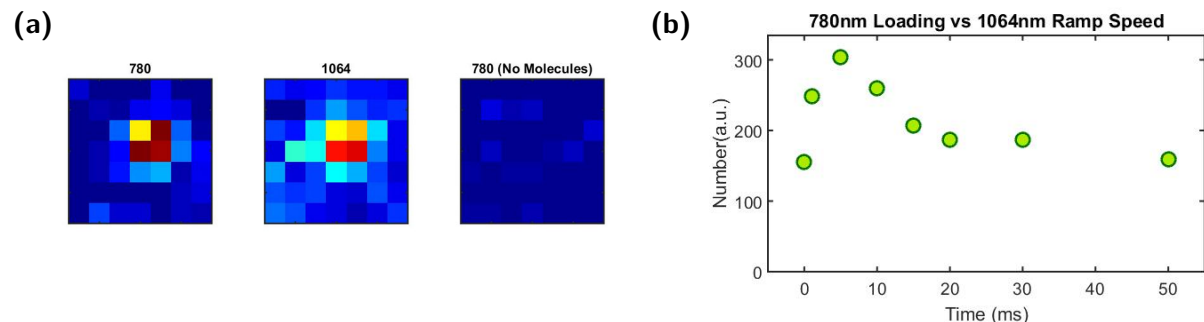
Figure 7.3.1: (a) First loading of a large 4 μm tweezer. (b) First hint of light induced collisions. We looked at the loading of the tweezer as a function of ramp down time of the 1064 nm trap. During this time, the cooling light was on, allowing light assisted collisions to take place.
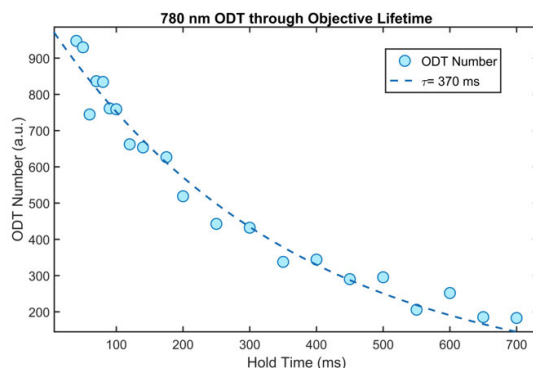
Figure 7.3.2: Lifetime of the 780 nm 4 μm tweezer though the objective ensuring we didn't have any anomalous heating effects.

ramp time for which if we went slower, the molecules had time to undergo light induced collisions and be kicked out from the trap. At short times, the light assisted collision rates were slow enough to sometimes load more than one molecule in the tweezer. We verified that the lifetime of the large 780 nm ODT was at the level of the vacuum lifetime, which it was, and we looked for any non-exponential decay behavior to indicate the presence of inelastic collisions occurring, Figure 7.3.2.

To investigate how far away from the collision blockage regime we were, we scanned the tweezer fluorescence as we varied the density of the ODT we were loading from. This was done by applying a MOT "killing pulse" of whitelight slowing light for various amounts of time. The number loaded

(a)

(b)
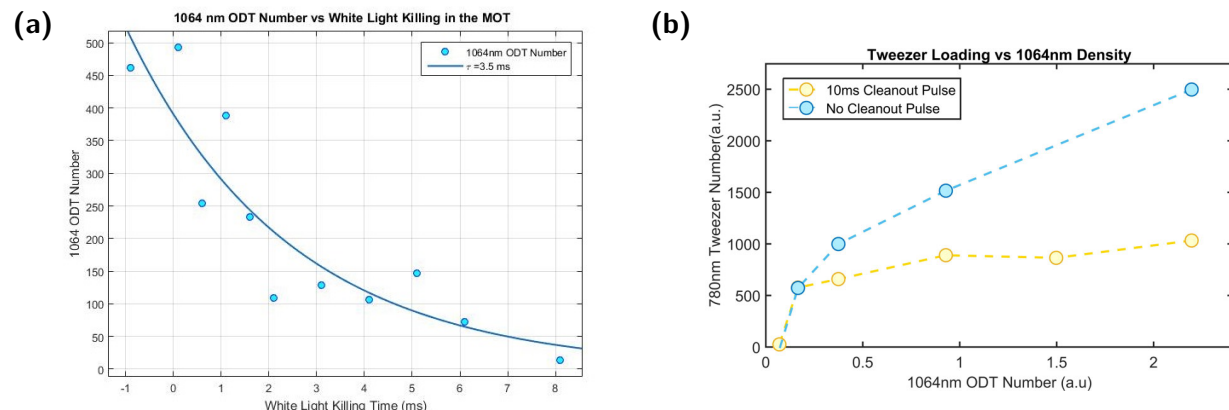
Figure 7.3.3: (a) Number of molecules in the ODT vs a pulse of the slowing light to kill the MOT. (b) Fluorescence from the tweezer vs loading rate, with and without the addition of a light assisted collision pulse. The plateau vs loading rate shows that we have entered the collisional blockage regime.

into the ODT following this pulse is shown in Figure 7.3.3(a). We then looked at the florescence of the tweezers, both directly after loading and with an additional 10 ms "cleanout" pulse to induce light assisted collision prior to the imaging. What we saw is shown in Figure 7.3.3(b). With this cleanout pulse, we were able to kick out molecules from the tweezers and reach a flat loading rate. This gave use some indication of the light-induced rate, as well as the loading rates into the tweezer.

Looking at a histogram of the tweezer fluorescence over many experimental cycles, one would expect a bi-modal histogram, with one peak for no molecules loaded, and one for a single molecule loaded, within the collisional blockade regime. The histogram for a large 3.4 μm tweezer trap, Figure 7.3.4(a), does not show a clear distinction of zero and one molecule peak since the trap to too large to have sufficiency density for fast light induced collisions. We began shrinking the tweezer trap size to speed up the light induced collision rate and enter the collisional blockade regime, Figure 7.3.4(b).

We typically operate with a tweezer waist around 2 μm. To ensure that at most one molecule is contained in each trap, we made use of a short "clean out" pulse by leaving the Λ-cooling light on
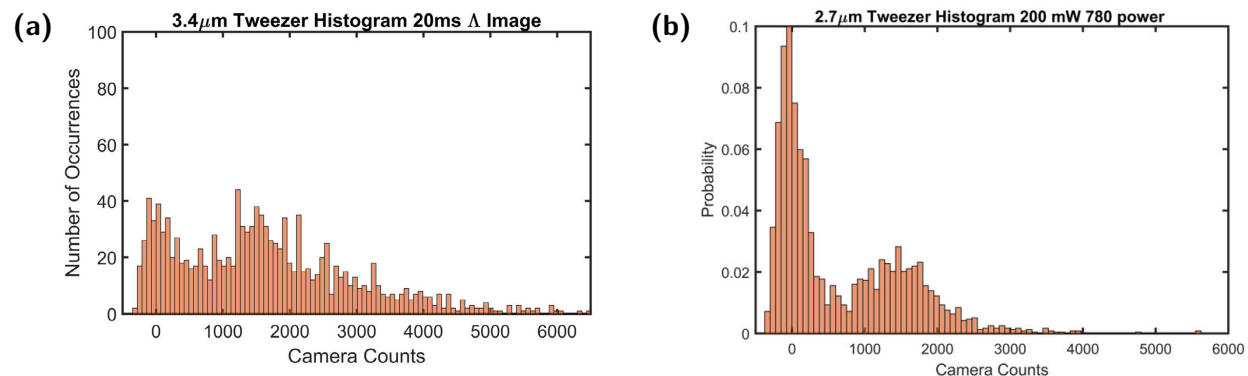
Figure 7.3.4: Histograms of the tweezer fluorescence over many experimental cycles for a (a) 3.4 μm tweezer (b) 2.7 μm tweezer.

for an additional 5 ms after loading to prevent multiple occupancies. This provides a clean starting point, where uniform defect-free arrays of single molecules can be created simply by rearranging the positions of occupied traps.

To ensure we only have at most one molecule per trap, we looked at the histograms for various loading probabilities. These histograms reveal a peak centered at zero counts corresponding to zero molecules, and a secondary feature with a peak centered around 1500 camera counts. To verify that this secondary feature corresponds to single molecules, we progressively reduced the loading rate into the tweezers by reducing the initial MOT number. As shown in Figure 7.3.5, the center of the second feature remains unchanged, while its height decreases. When normalized to the area under the secondary feature, the second feature overlaps in all the histograms. This demonstrates that at most one molecule was present in each trap. If there were more than one molecule, the center of the secondary feature would move towards the zero-molecule feature as the average number in the tweezer is reduced.

These histograms also allow us to determine the detection fidelity for single molecules in a single shot. For each image, a tweezer trap is determined to be occupied if the number of photon counts exceeds a certain threshold. Owing to technical noise and background light, multiple photons per
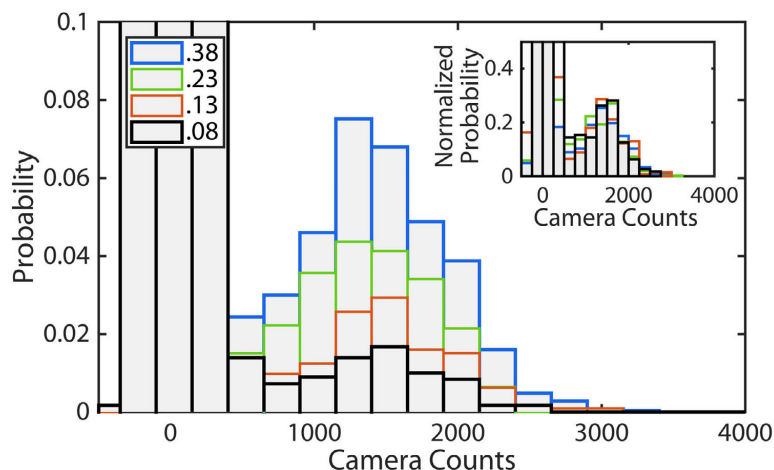
Figure 7.3.5: Histograms for single molecules. Histograms with various tweezer loading fractions as indicated by the legend. Inset: Histogram normalized by camera counts under the secondary feature.

molecule are needed to make a determination, and higher fidelities are obtained with higher number of collected photons. Although the number of photons emitted can be increased with longer imaging durations, durations longer than the imaging lifetime of ~ 100 ms do not help because they lead to increased background light. After optimizing the imaging parameters, we reach a detection fidelity of 92% at an optimal exposure of 30 ms. We would improve this later on, as discussed in the next chapter.

We found that the loading probability and number of photons we could scatter per trapped molecule before losing them was proportional to the trap depth, Figure 7.3.6(a). This caused the initial images to look something like Figure 7.3.6(b) top. After imaging the trap intensities on a CCD in the intermediate plane and compensated the depth of each trap, we were able to make more uniform looking arrays Figure 7.3.6(b) bottom.

We created a tweezer array with 5 traps, shown in Figure 7.3.7. A single shot image is also shown to show the imaging fidelity.
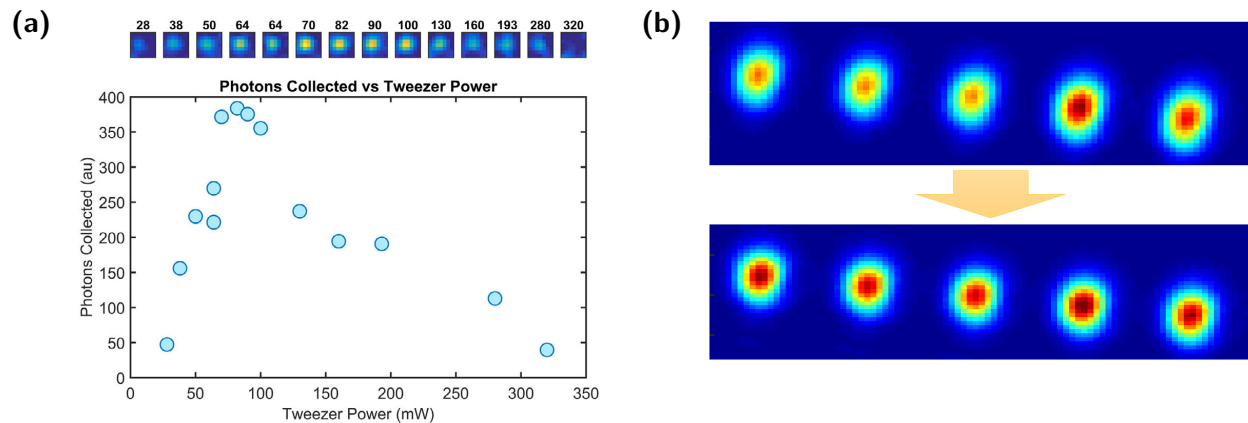
Figure 7.3.6: (a) Collected photons per tweezer vs trap depth. (b) Array of molecules before and after trap depth compensation.
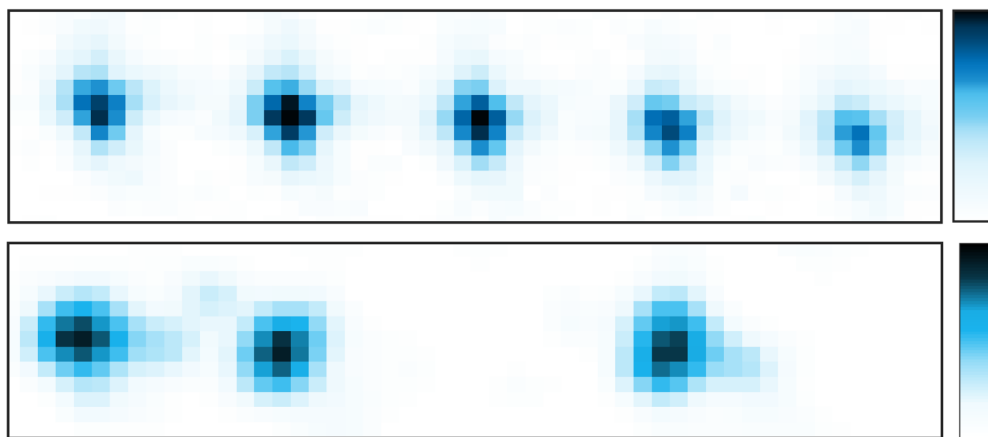
Figure 7.3.7: Molecule Tweezer Array. Top: Image of optical tweezer array of single molecules, averaged over 500 shots. Bottom: Single shot image showing three occupied tweezer traps. A Gaussian filter is added for visual clarity. The tweezers are spaced by 5 μm.
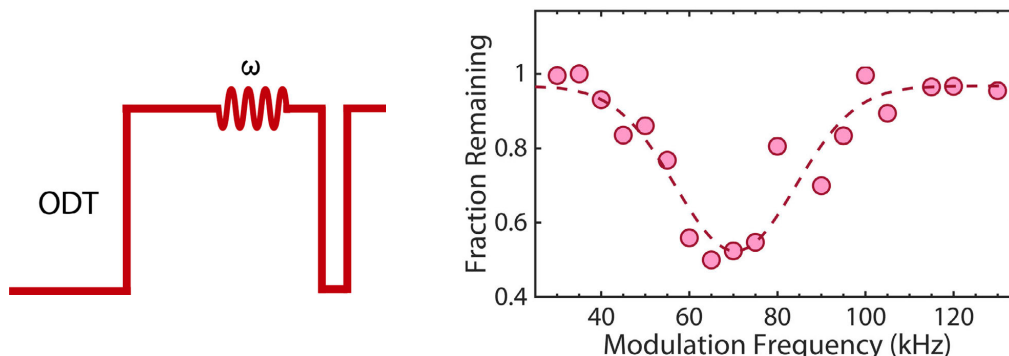
Figure 7.4.1: ODT trap frequency measurement method. The trap depth is modulated for a fixed number of cycles, then turned off briefly for the heated particles to escape. (Modulation only parametric heats while in the harmonic part of the trap) The 2.3 μm radial trap frequency measurement is shown. The loss feature is observed at $2\omega_r$

7.4   Tweezer Trap Characterization

The radial trapping frequency ω_r was measured by parametric heating of the trapped molecules Figure 7.4.1. 2000 cycles of trap modulation with peak-to-peak amplitude of 20% of the trap depth was applied. In parametric heating, a loss feature arises at twice the trap frequency. By fitting the observed loss maximum, we determined the trapping frequencies. For the smaller tweezer trap used to create single molecules, we measured $\omega_r = 2\pi \times 35\,$kHz at a beam power of 65 mW per trap. Using the calculated ac polarizability of CaF, this corresponds to a Gaussian beam waist of 2.3 μm. For the larger tweezer trap used for studying collisions, we measure $\omega_r = 2\pi \times 28\,$kHz at a beam power of 200 mW per trap. This corresponds to a Gaussian beam waist of 3.6 μm. Using the trap frequency and the calculated AC polarizability of CaF at 780 nm, we determine that the tweezer traps have Gaussian beam waists of 2.3 μm, in agreement with the effective numerical aperture of the objective and measured optical aberrations arising from the re-entrant window. Note that for the different hyperfine states, the polarizability varies up to 20%.

The temperature of the molecules was measured via release and recapture, Figure 7.4.2. The
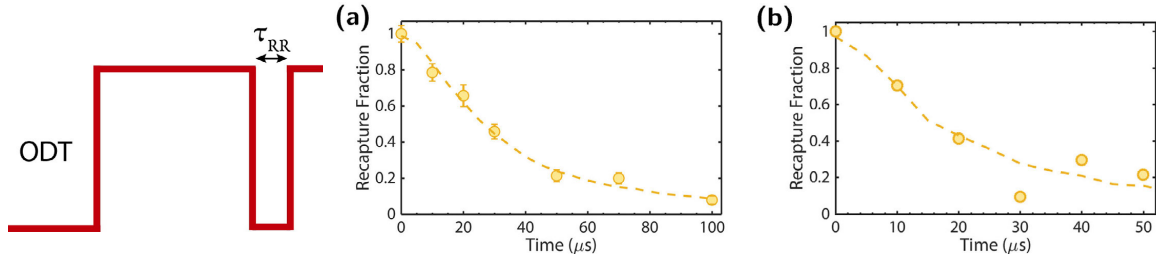
Figure 7.4.2: Release and recapture measurements. (a) Recapture fraction as a function of release time for the $2.3\,\mu$m tweezer trap. Shown in dashed is a Monte-Carlo simulation with the fitted temperature of $80\,\mu$K. (b) Recapture fraction as a function of release time for the $3.6\,\mu$m tweezer trap. Shown in dashed is a Monte-Carlo simulation with the fitted temperature of $106(20)\,\mu$K.

tweezer trap was shut off and molecules were released for a variable amount of time, and then switched back on. The number of recaptured molecules is measured as a function of release time. This is then fit to Monte-Carlo simulations using the measured trap power and full trap profile including the effect of gravity. The smaller tweezer trap has a temperature of $80(20)\,\mu$K. Monte-Carlo simulation gives a peak trapped density for a single molecule of $1.4(6) \times 10^{10}$ cm^{-3}. The larger tweezer trap used to study collisions, has a temperature of $106\,\mu$K. Monte-Carlo simulations give a peak trapped density for two molecules of $4(2) \times 10^{9}$ cm^{-3}. When determining collisional cross-sections, we assume that the average density is $1/2^{3/2} \approx 0.353$ times the peak density, which is the ratio for a harmonic trap.

The vacuum lifetime of the tweezer was 625 ms, Figure 7.4.3. This verified that no anomalous loss mechanisms were present at a timescale we cared about.

In each single shot image, a trap is identified as filled or empty using a threshold. For detecting single molecules, one optimizes for the highest degree of separation in the two histogram features corresponding to zero molecules and single molecules. The width of the zero molecule feature is determined by background light, while the position and the width of the single molecule feature is determined by the number of detected photons. While longer imaging times lead to more detected
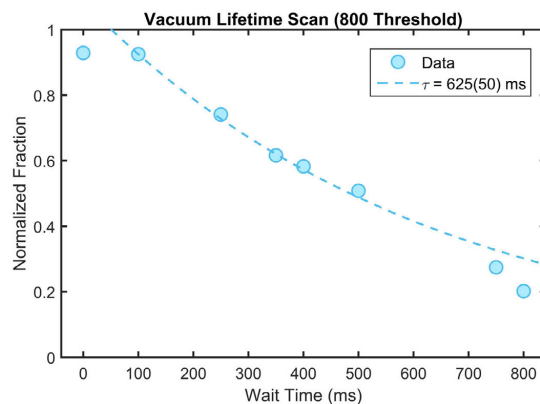
Figure 7.4.3: Lifetime of a molecule in a tweezer. We attribute the loss primarily to collisions with background gas.
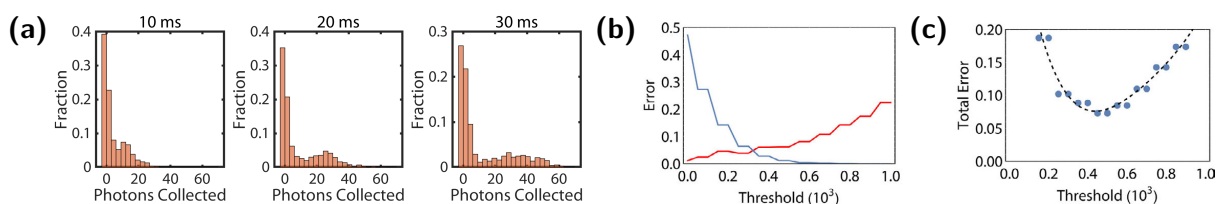
Figure 7.4.4: (a) Histograms of single molecules vs imaging time (b) Misidentification errors versus threshold value for the zero peak, blue, and the single molecule peak, red. (c) Total error as a function of threshold. At the optimal threshold, we obtain a minimum error of $8(1)\%$ corresponding to a fidelity of $92(1)\%$.

photons, imaging times much longer than the imaging lifetime is detrimental, as it leads to a relative increase in the amount of background light, which primarily arise from scattering of imperfections in the vacuum windows. For the smaller tweezer trap, we obtain the highest detection fidelity at an exposure time of 30 ms, and at a single photon detuning of $\Delta = 2\pi \times 24$ MHz. Figure 7.4.4 a shows the histograms obtained with various imaging times. The optimal threshold can be determined by examining the background-subtracted histograms obtained from multiple images. There are two types of identification errors: 1) empty tweezers being identified as occupied 2) filled tweezers being identified as empty. These are shown in Figure7.4.4 b as a function of threshold, with a minimum giving the optimal threshold to use. We find a minimum total error of $8(1)\%$, corresponding to a fidelity of $92(1)\%$, Figure 7.4.4 c.

8

Optimization, Rearrangement and Merging of Molecular Tweezers, and Ultracold Collisions

Having successfully loaded single molecules in a tweezer array, work turned to optimizing the imaging and cooling to improve the detection fidelity. High fidelities are not only important for higher data rates when studying collisions, but will become critical when scaling up to larger arrays. We then worked on moving of the tweezer traps, without inducing heating or experiencing additional loss. This dynamic rearrangement is necessary to create defect free arrays in the future. The first
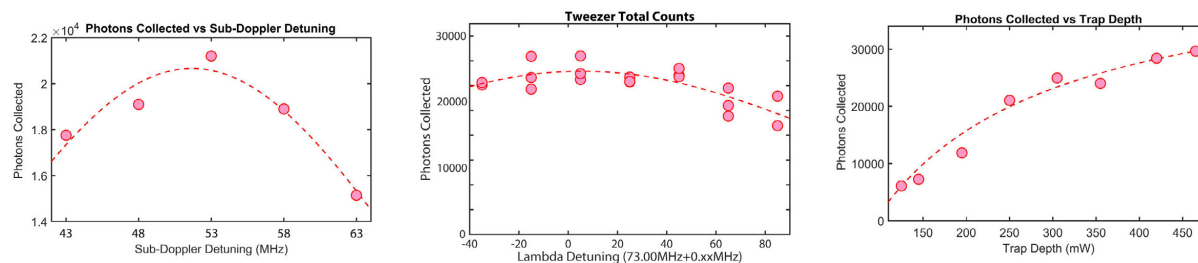
Figure 8.1.1: Optimum sub-Doppler detuning and Λ imaging detunings for a fixed 600 ms image illuminated with X & Y imaging beams.

application of our dynamical rearrangement was to merge tweezers to study collisions.

8.1 IMAGING OPTIMIZATION

To optimize the imaging parameters, we took 600 ms images, which was our known vacuum lifetime, and worked to optimize the total number of photons collected during this exposure. Since our vacuum lifetime sets a hard limit to how long of an exposure we can take, this was a useful metric to maximize. Even if we could find an imaging parameter which gave us very long imaging lifetimes, but scattered slowly, this would not be useful to us since the molecule would already be lost before scattering the same number of photons.

We first scanned the sub-Doppler detuning and found that operating further detuned was highly beneficial to the total number of photons collected, Figure 8.1.1(a). The optimal of the two-photon Λ detuning was fairly broad and not significantly different from the free space optimum, Figure 8.1.1(b).

Since we had been operating with small imaging beams in the X and Y arms, but not in the Z direction, where we simply used the MOT beam to image, we added a small Z beam to match the intensity of the X and Y imaging beams. We aligned this beam by looking at depletion of the ODT signal without the retro-reflection. We then rescanned the various parameters and found that this

(a)

(b)
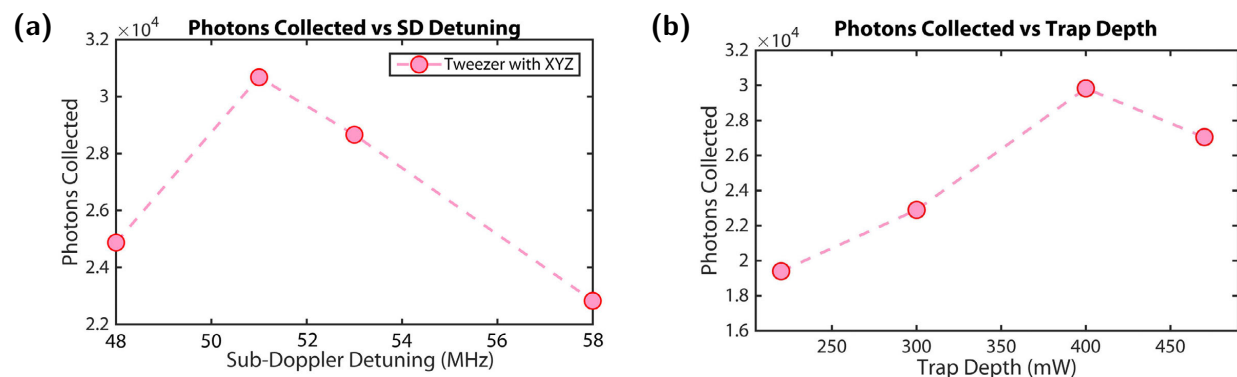
Figure 8.1.2: (a) Optimum sub-Doppler detuning and (b) trap depths for a fixed 600 ms image illuminated with X & Y & Z imaging beams. We can scatter up to 30,000 photons per trapped molecule.

Parameter	Setting
Single Photon Detuning	51 MHz blue detuned
Lambda Detuning	200 kHz blue from free space
X,Y,Z Imaging Beams Intensity	40 mW/cm^2
Trap Depth	2 mK

Table 8.1.1: Optimum imaging parameters.

beam helped, but only by around 30% or so in photons collected.

We also scanned many other parameters, including trap depth, where we generally found deeper traps were better. With all three imaging beams, an optimum occurred at a trap depth of 400 mW. The intensity of the small beams did not have a large effect and neither did the Λ detuning. These scans are shown in Figure 8.1.2. The new optimal imaging parameters are shown in Table 8.1.1.

This gave an imaging lifetime of 530 ms, Figure 8.1.3(a), nearly the same as the vacuum lifetime of 600 ms. We can scatter 30,000 photons at a scattering rate of 70,000 s^{-1}. 30,000 photons scattered seems to be the limit and no other parameter scanned seemed to be able to increase this with the vacuum lifetime we have. It is very possible that with a longer vacuum lifetime, this number can be pushed up to the limitations of our repumping lasers.

(a)

(b)
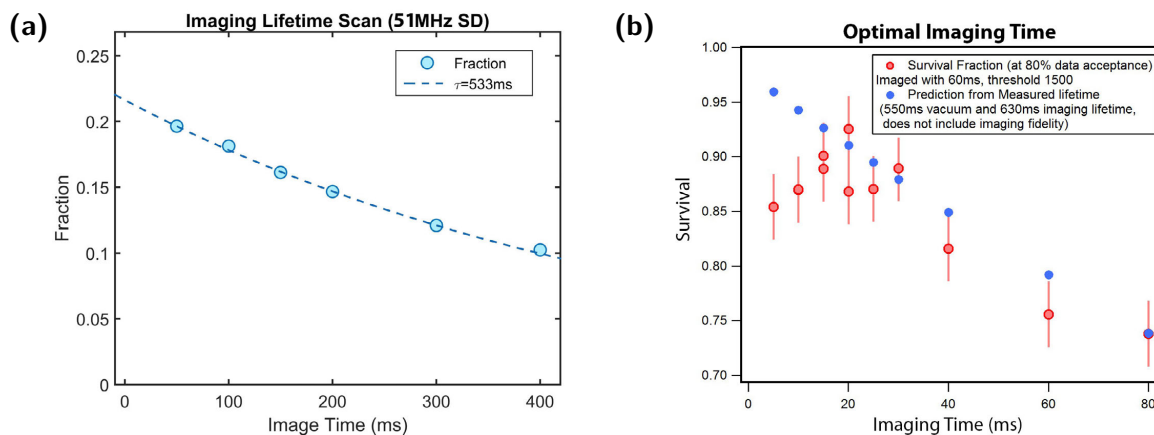
Figure 8.1.3: (a) Imaging lifetime under optimal conditions, with vacuum canceled out. The achieved lifetime is very close to that of the vacuum lifetime, and hence further optimizations lead to diminishing returns. (b) Optimal imaging time for repeat imaging. The blue trace shows the survival fraction expected due solely to the vacuum lifetime. As longer images are taken, the vacuum lifetime starts to play a significant role in the re-imaging fidelity. The red points show the measured re-imaging fidelity.

With these imaging parameters, we now determined the optimal imaging time. This is a question of maximizing our ability to detect ones from zeros in the first image, but not lose too many molecules such that we can then re-image, for example, after rearrangement or collision studies. With the scattered light level we have, which dominates our background noise, we find that an imaging time around 20 ms is optimal, Figure 8.1.3(b).

Two sequential images are shown in Figure 8.1.4, showing our greatly improved ability to separate ones from zeros, and to re-image without too many losses. We find a single image fidelity of 97%.

8.2   Λ-Cooling Optimizations

Unfortunately, the temperatures inside the tweezers were quite hot, over 100 μK, while in free space we were able to cool over an order of magnitude colder. To see whether we were able to cool the molecules further, we began investigating the tweezer temperatures after an additional cooling pulse between the two images. By taking release and recapture measurements and fitting them to a Monte
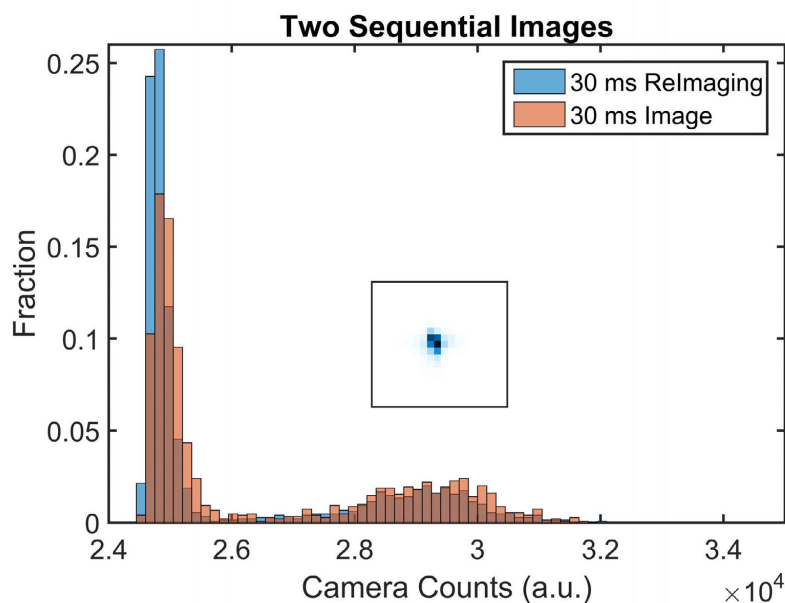
Figure 8.1.4: Two sequential images of a single molecule. Note the much improved separation of the one and zero molecule peaks.

Carlo simulation assuming a Gaussian waist and taking into account gravity, we are able to measure the temperatures of the trapped molecules and measure the effects of the cooling pulse independently of the imaging. We first began by scanning the sub-Doppler detuning and found that the optimal detuning was fairly close to that of the optimal imaging, Figure 8.2.1.

Figure 8.2.2(a) shows the effect of the Λ frequency on the cooling, which we find is optimal around 73.15 MHz, the same as for imaging. One interesting behavior we found is that the scattering rate seems to vary fairly linearly over the Λ frequency we scanned over, Figure 8.2.2(b). This was fairly surprising since one would naively expect the Λ-cooling, which utilizes a VSCPT dark state, would be at the point of lowest scattering rate. It turns out this is not the case. This is most likely explained by the fact that the system is much more complicated than a three-level system and the rate of pumping into the other non-dark states is affected by the Λ frequency.

The greatest impact to temperature was achieved by decreasing the intensity. Figure 8.2.3 shows
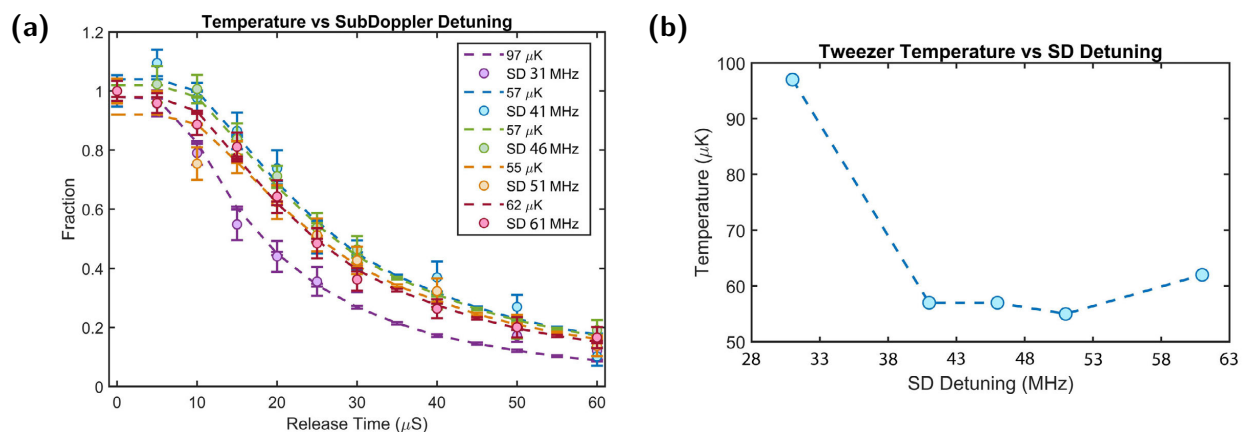
Figure 8.2.1: Tweezer temperature vs sub-Doppler detuning. (a) Release and recapture traces fit to a Monte Carlo. (b) Resulting temperatures vs sub-Doppler detuning.
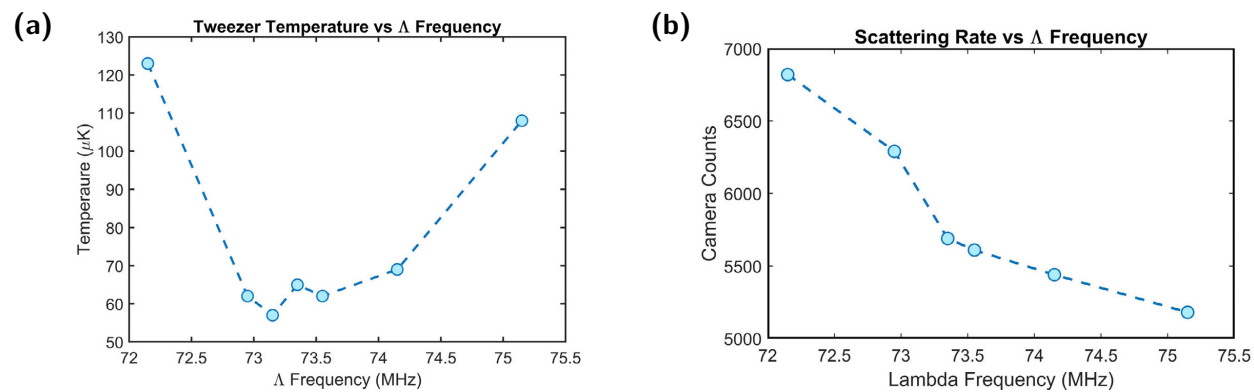
Figure 8.2.2: (a) Temperature vs Λ detuning. (b) Number of scattered photons vs Λ detuning for a 30 ms image.

(a)

(b)
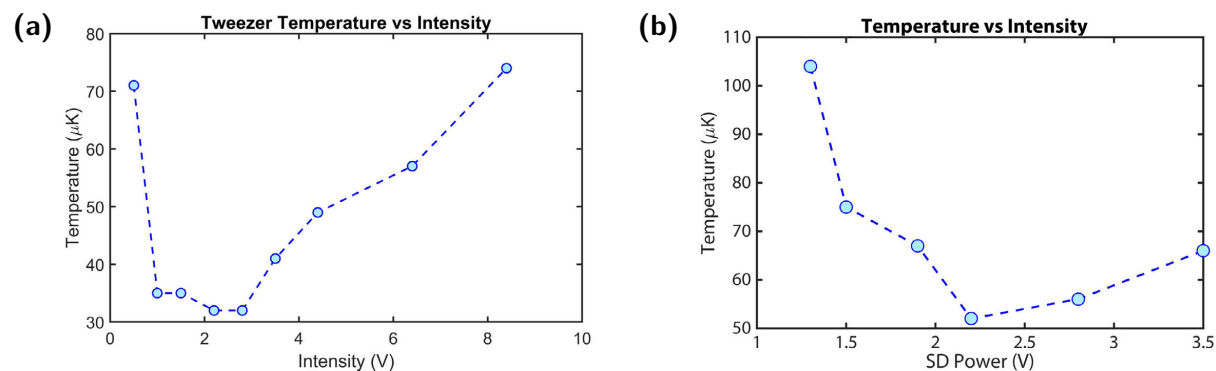
Figure 8.2.3: Tweezer temperature vs intensity for (a) SD=46 MHz and (b) SD=38 MHz.
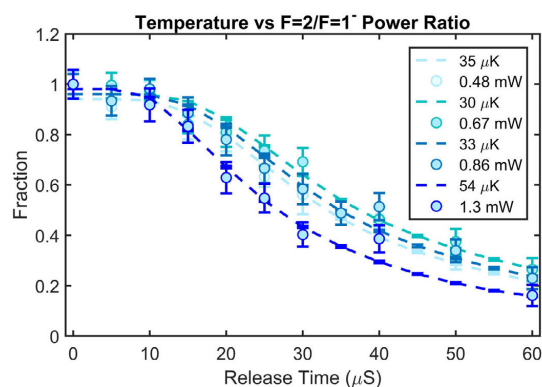
Figure 8.2.4: Tweezer temperature vs ratio of F=2/F=1- power. The F=2 power is fixed at 3.5 mW. The power of F=1- is plotted.

the temperature of the tweezers for various sub-Doppler detunings. It is possible that the rising temperature on the low intensity side is a combination of higher final temperature and slower cooling which may not have been left on for long enough.

In light of this, we rescanned the Λ frequency optimal at lower intensity and found that the minimum had not moved from the high intensity point. Finally we scanned the ratio of the F=2 and F=1- and found that the optimal ratio from the free space optimization (5:1) still gave the lowest temperature, Figure 8.2.4.

The last characterization required was to measure the cooling time inside the trap. For this we
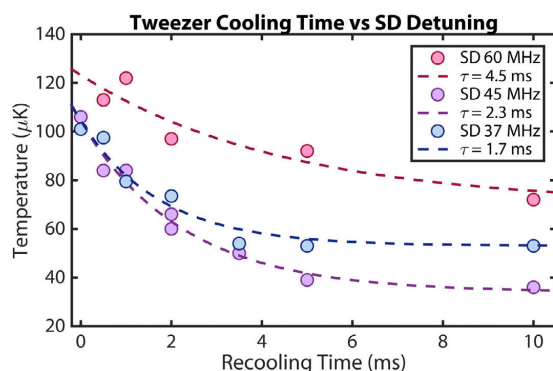
Figure 8.2.5: Cooling timescale for molecules in the optical tweezer.

heated the molecules up by parametric heating, and then applied light for a variable amount of time before remeasuring the temperature. We find that the cooling times scale slightly with sub-Doppler detuning, Figure 8.2.5. For the optimal cooling it seems like the cooling time is on the order of 2 ms. This cooling time will be used later to find an optimal in parameter space for the relative rates for cooling and losses to light induced collisions.

8.3 TWEEZER REARRANGEMENT

In order to either create defect free arrays, or merge tweezers together, we must be able to move the trapped molecules in the tweezers. The position of tweezers are determined by the frequencies generated by the USRP, which must be changed in such a way that the phase of the programmed waveform does not jump when the frequency is moved. We found that such a phase jump could cause a large amount of heating in the moving process. We began by loading three tweezer traps and moving the molecules to one side, Figure 8.3.1.

We found that the move process could be nearly lossless if cooling light was applied during the movement, Figure 8.3.2. We tried various acceleration profiles, but none of them made much of
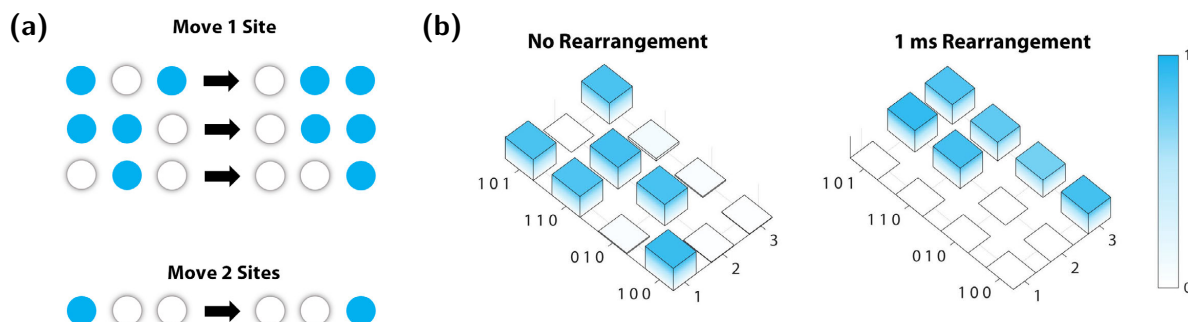
Figure 8.3.1: (a) Outline of the rearrangement. (b) Results of the rearrangement.
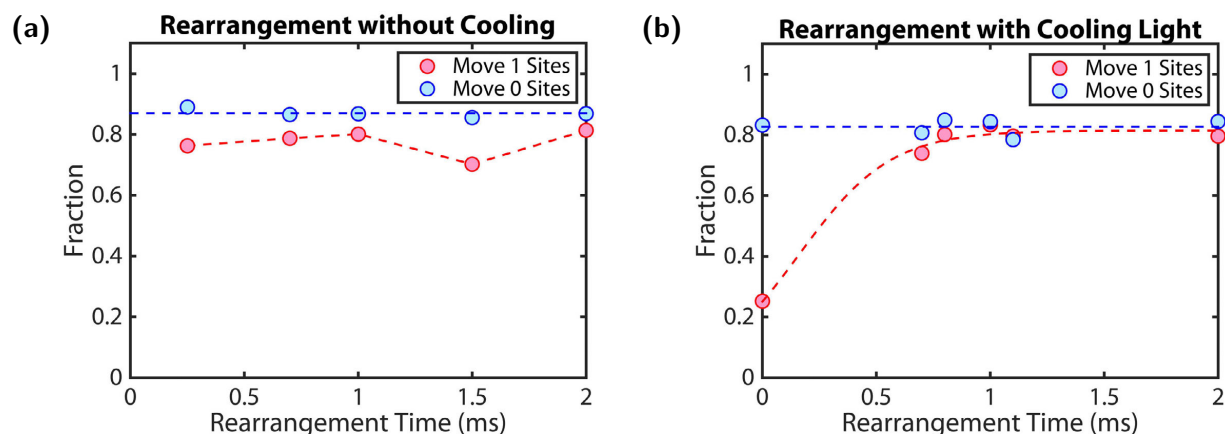
Figure 8.3.2: Tweezer moving success vs number of sites moved for (a) no cooling light and (b) with cooling light.

a difference. We settled on using a constant jerk to constant velocity to constant jerk deceleration profile. The reason we went with constant velocity for the main travel distance was such that any residual acoustic etaloning within the AOD crystal would be traversed at a fixed rate. We can tune this rate such that the power fluctuation does not lead to parametric heating. We can move in 1-2 ms with little loss. Figure 8.3.2 shows the moving success.
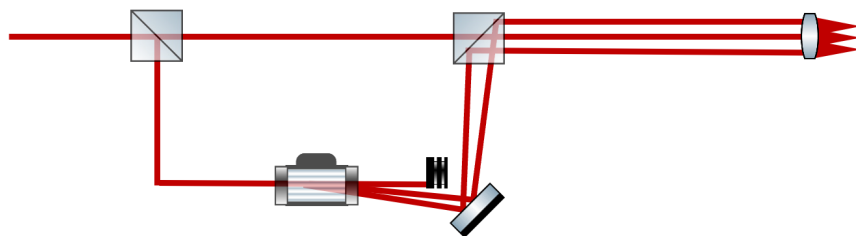
Figure 8.4.1: Beam path for tweezer merging. The ODT power has the opposite polarization than that of the undeflected beam and is 100 MHz apart in frequency.

8.4   Tweezer Merging

We cannot directly merge tweezers since overlapping the two beams would mean sweeping over all beat frequencies which would cause massive heating. To get around this, we split the tweezer light with a PBS before the AOD. One trap bypasses the AOD and two other traps go through the AOD and are recombined with the unshifted beam with a PBS, Figure 8.4.1. After proper alignment and power balancing, we are able to combine two traps and have a 50% probability of reseparating them. This is necessary in order to image the results after a collision takes place. If we were to try to image a trap with two molecules, they would simply undergo light assisted collisions and it would appear that the traps were empty. If the reseparation is exactly 50/50, then half the time they will reseparate as 1-1 and we will be able to detect them. It should be noted that for the resperation to be balanced to within 5%, the power in the AOD trap must be controlled to the 0.05 dB level or less. This is accomplished with tuning a variable attenuator with 0.1 dB step size and using different cable length to introduce attenuation. Figure 8.4.2 shows the typical reseparation ratio.

(a)

(b)
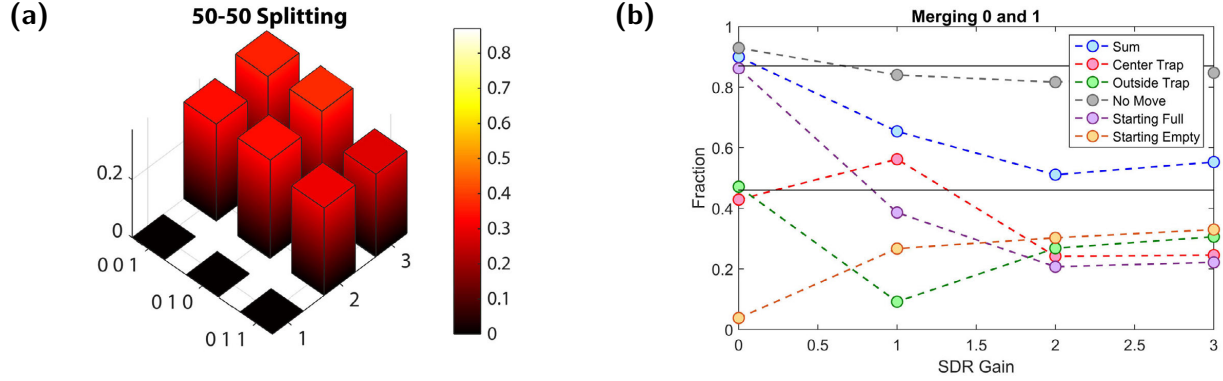
Figure 8.4.2: (a) Re-separation ratio for the initial 1-0 and 0-1 loaded traps. (b) Reseparation ratios for the various initial trap configurations.

8.5 COLLISIONS

Studying molecular collisions is important for gaining a better understanding of molecular dynamics which plays a critical role in determining the stability of ultracold gasses [170]. The theory of collisions between ultracold atoms and molecules is typically described in the partial wave basis [170, 171]. $^{40}Ca^{19}F$ is a bosonic species, hence only even partial wave contribute to collisions when in a single quantum state. However, initial collisional studies were done in the presence of multiple hyperfine states. Here all partial waves are possible so long as they are energetically accessible. As the temperatures of collisions are reduced, fewer and fewer partial waves are present in the collisions. Above s-wave collisions, a centrifugal barrier of height $\hbar^2 l(l+1)/(2m_r r^2)$ exists. For $l > 0$ there can also exist quasi bound states which can lead to what are called shape resonances, which strongly enhance the effect of higher partial waves not typically energetically allowed [171]. In the absense of external fields, long range interactions are typically dominated by Van der Waals forces, which has an interaction potential of C_6/r^6. For CaF-CaF collisions, this can be estimated to be $2.28 \times 10^5 \, E_h a_0^6$ [146]. This leads to a centrifugal barrier height $U = \left(\frac{l(l+1)}{m_r}\right)^{3/2} \left(\frac{1}{54C_6}\right)^{1/2}$, translating to d-wave barrier height of 100 μK (p-wave is 20 μK when particles are distinguishable) for CaF-

CaF collisions. This leads to a threshold behavior, called Wigner laws [172] where the cross section scales as $\sigma \propto E^{l-1/2}$ and the rate constant scales as $B \propto E^l$. What happens when a molecule has enough energy to pass this barrier and come to short range is not clear. The Langevin limit assumes complete loss of anything that crosses the barrier. Sticky collisions, where long lived complexes may be formed at short range have also been theorized [173]. In this section, we study CaF-CaF collisions in an optical trap, first in a large 3.4 μm tweezer, and then in merged 2 μm tweezers.

8.5.1   COLLISIONS IN A 3.4 μM TWEEZER

The first collisions studies were inadvertently conducted in the large 3.4 μm tweezer. This was done at the time due to the fact we were slightly outside the collisional blockade, where we had a chance of loading more than one molecule in a single trap. We could use these occurrences of two molecules being loaded to study CaF-CaF molecules both in the presence of Λ-cooling light and in the dark. To determine when we had more than one molecule loaded in a single tweezer, a threshold was set above the single molecule feature. The camera counts collected for single molecules ($\sim$ 1000) had negligible counts above ($\sim$ 2000). In theory, loading any number more than one would have counts at this level, but from simulations, the contribution of these can be neglected. Different molecule numbers can lead to different decay rates. Assuming that decay originates only from two-body processes, the decay rate for N_t molecules is determined by $\Gamma_2 N_t (N_t - 1)/2$, where Γ_2 is the decay rate for 2 molecules. Due to the combinatorial factor, the decay rate of 3 and 4 molecules is 3 and 6 times faster than the decay of 2 molecules. This means that the longest observed decay timescale of $n > 1$ must correspond to either single-body loss or two-body loss arising from 2 molecules.

For the case of molecules illuminated by Λ-imaging light, we find that the single molecule feature decays with exponential decay time constant of 129(12) ms, Figure 8.5.1. This is the imaging lifetime. The two molecule count decays much faster, with a time constant of 26(6) ms. To deter-
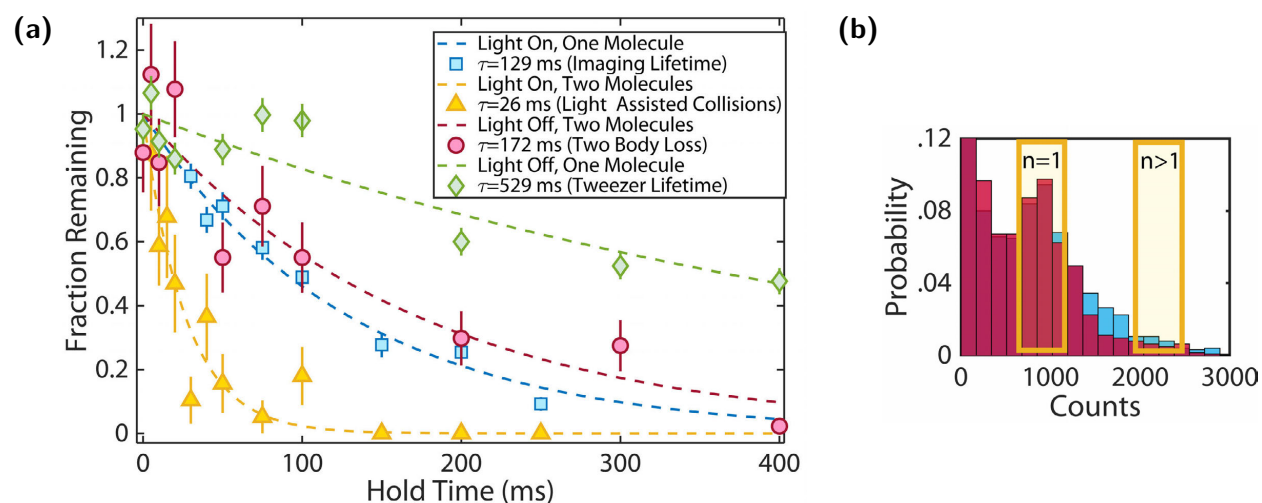
Figure 8.5.1: (a) Collisions in the large 3.4 μm trap. Loss curves for a single molecule (green diamonds) and two molecules (red circles) in the absence of light. The single molecule lifetime of $\tau = 530$ ms and the two molecule lifetime is $\tau = 180$ ms. Loss curves for a single molecule (blue squares) and two molecules (yellow triangles) in the presence of Λ-cooling light, reflect the imaging lifetime and light induced collisional loss rate, respectively. The imaging lifetime is $\tau = 130$ ms and the light induced collision lifetime is $\tau = 26$ ms. (b) Histograms of camera counts after short (blue) and long (red) hold times. The highlighted region $n = 1$ ($n > 1$) denotes the range used to compute the fraction remaining for single (double) molecules.

mine whether collisions are occurring in the absence of light, we perform the same measurements

by holding the molecules in the dark. Under these conditions, the single molecule lifetime is 530 ms,

Figure 8.5.1, whereas two molecules have a lifetime of 180 ms, which indicates that collisions are also

present in the absence of light, albeit at a much lower rate. Because the collisional loss rate scales

with molecular density, with the smaller 2.3 μm used in the array, Λ-cooling of a few milliseconds

is sufficient to induce light-assisted collisions. This is consistent with the observed absence of mul-

tiple molecules in the smaller trap. Assuming that the decay seen is primarily from two molecules,

we obtain a light induced collision rate of $\gamma = 2.7(14) \times 10^{-8}$ cm^{3}s^{-1}, corresponding to a cross sec-

tion of $\sigma = 10(5) \times 10^{-10}$ cm^2, assuming $\Gamma = n\sigma v$. This is similar to that measured for Rb atoms in

optical tweezers [119]. Light-induced collisions arise from dipolar interactions, which result from

an electric dipole moment induced by near-resonant light [121, 174]; this dipole moment has a

similar size of about 1 Debye in both atomic and molecular systems, suggesting that molecular sys-

tems should have similar collision rates to atomic systems. We note that the light-assisted collisional

cross-section indicates a density limit of $\sim 10^{11}$ cm^{-3} for the typical ms timescales for laser cooling.

In the absence of light, the fitted loss rate is $\gamma = 4(2) \times 10^{-9}$ cm^{3}s^{-1}, corresponding to a cross section

of $\sigma = 1.4(7) \times 10^{-10}$ cm^2. There are multiple possible loss mechanisms, ranging from hyperfine and

rotational relaxation to long-lived complex formation to evaporation from elastic collisions.

8.5.2 STUDYING COLLISIONS BY MERGING TWEEZERS

After optimizing the moving tweezers, we had the ability to merge tweezers to study collision and

re-separate them to image. We can use this to study collisions in a more controlled fashion than

our previous method of looking in the tail of the histogram. With this configuration, we only have

one non-moving(static) trap, with which we can merge either side trap. We typically operate using

just one side trap to prevent any technical differences from affecting the measurement(for exam-

ple from saturation effects of the AOD or amplifier). The possible merging scenarios are shown in
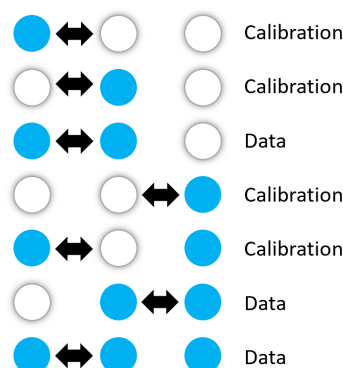
Figure 8.5.2: Table of merging options for studying collisions

Figure8.5.2. Since the loading of the tweezers is stochastic, we do not always load one molecules in each trap. In fact, loading both traps simultaneously occurs less than 25% of the time, and the probability of loading only one trap is more likely. The occurrences where we load only one tweezer can be used as interleaved calibration data, ensuring that the reseparation fraction, or anything else, impacts the survival over time.

Light Assisted Collisions

By turning on light (Λ-cooling light) for a variable amount of time after the tweezers are merged, we can study light assisted collisions against various parameters. Here we measure the light induced collision rate versus sub-Doppler detunings and intensities of the Λ-cooling light. This was done by merging the tweezers for a fixed amount of time, while applying light for a variable time while the tweezers were merged. In this way, any effects of loss to either background gas or inelastic molecule-molecule collisions are canceled out. Prior to the merging, the tweeezers were prepared by applying the same parameters of Λ-cooling light as that was used for the light induced collisions. This was done to prevent any heating or cooling effects to occur while the light assisted collisions are taking place, ensuring the density is constant in time. We find that the light induced collision rates decrease
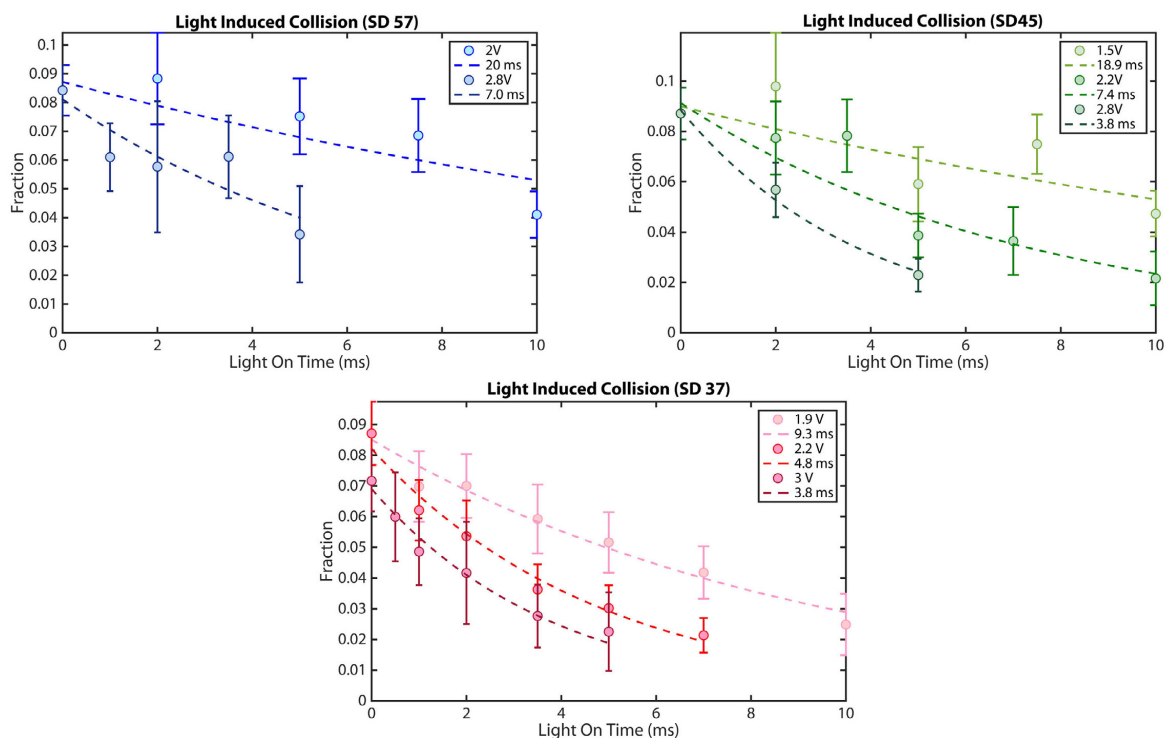
Figure 8.5.3: Light induced collisions vs sub-Doppler detuning and intensity

with larger sub-Doppler detunings and increase with intensity, Figure 8.5.3, as one would expect.

These light induced collision rate, combined with the cooling time scales from Figure 8.2.5, allows us to find a parameter space where the cooling timescale is faster than the light induced loss. We found that at a sub-Doppler detuning of 45 MHz, and an intensity of 2.2 V, the light induced collision lifetime is 7.4 ms, while the recooling time is on the order of 2 ms. This allows for rethermalization of the molecules in a tweezer after merging without significant losses. This was used next to study CaF-CaF collisions.

From the measured light induced collision rate and a measure of temperature to attain density, we can plot the rate constant and cross section as a function of intensity for various sub-Doppler detunings, shown in Figure 8.5.4. We find that the cross section and rate constants increase with both smaller sub-Doppler detunings and with intensity. These measurements are consistent with
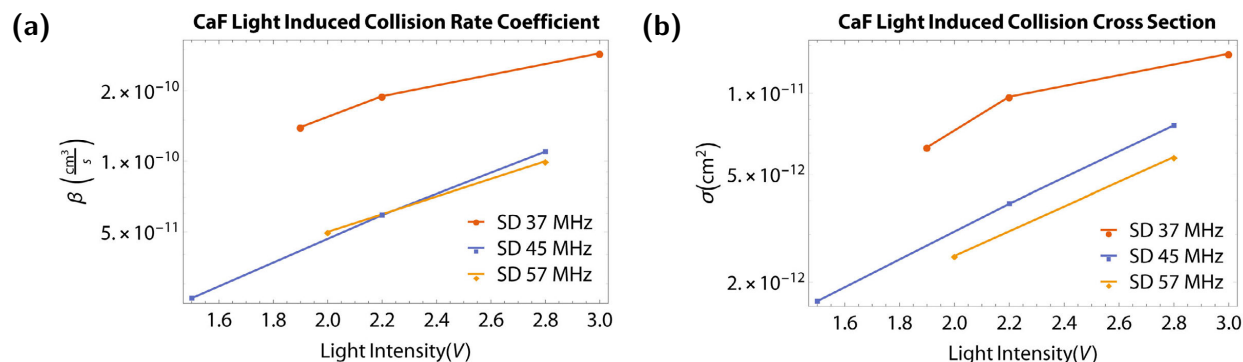
Figure 8.5.4: CaF light induced collisions (a) rate constants and (b) cross sections as a function of sub-Doppler detuning and intensity.

the large light induced rates measured in the previous section, where the sub-Doppler detuning was much closer to resonance, and the intensity was higher.

CaF-CaF Ground State Collisions

Having found the optimal recooling parameters, we could now follow a similar sequence, but varying the overlap time of the two tweezers. Since no light was present now, we had to make sure the two molecules were both still in thermal equilibrium. This was critical to extract an accurate estimate of the cross section. When two tweezers are merged, if the overlap is not perfect, it is possible that the molecule from the AOD trap was dropped off to the side of the static trap. This could potentially lead it to have substantially higher energy than the second molecule. This in theory is protected against since we adiabatically ramp down the depth of the second trap. Just to make sure this was the case, we also turned on the recooling light for a short 3 ms pulse, at the cost of about 20% in data rate. The full sequence is as follows: (1) image(25 ms) (2) wait(1 ms) (3) recool (SD 45 MHz; 2.2 V; 5 ms) (4) merge (5) recool (SD 45 MHz; 2.2 V; 3 ms) (6) hold in dark (7) separate and image 60 ms. We found a decay with a time scale of 21 ms, corresponding to a inelastic rate constant of 3×10^{-11} cm^{3}s^{-1} and a cross section of 2×10^{-12} cm^2, Figure 8.5.5. We then repeated this without
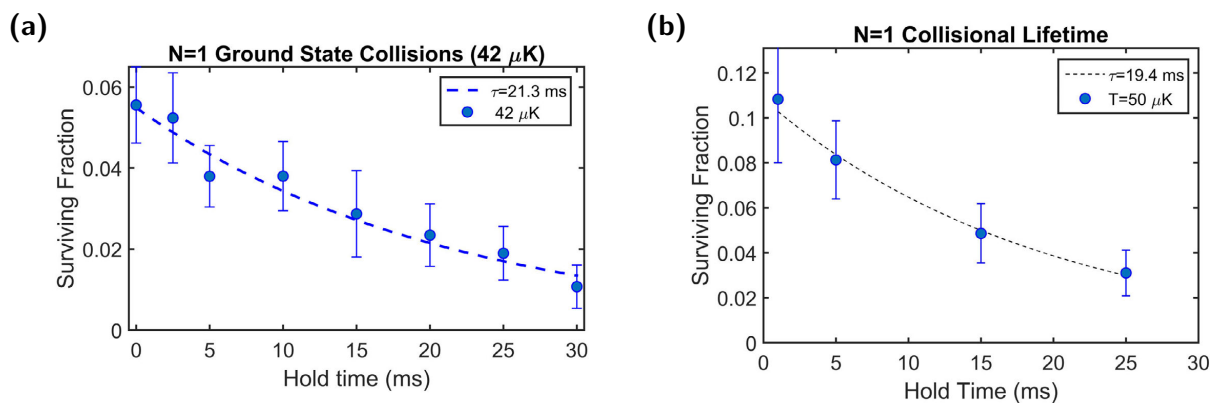
Figure 8.5.5: (a) Inelastic collision rate of CaF at 42 μK with (a) and without (b) recooling.

the second recooling pulse. The timescale was unchanged, indicating that the overlap of the merged traps was good enough for this application.

The ability to skip the rethermalizing pulse meant we could observe the behavior the the trapped molecules at shorter merging times. We found a decay shown in Figure 8.5.6. The molecules are predominantly found in the F=1- and F=2 states after the Λ-cooling. While the F=1- state is stable against hyperfine relaxation, it is not the case for the F=2 state. However, we do not see any evidence of a second time scale arising from the various initial hyperfine distributions. To further explore the effects of hyperfine relaxation, we applied an optical pumping pulse to pump the population into the F=0 state and repeated the measurement. We observed no significant change in the decay. This suggests that hyperfine relaxation is not the dominant decay pathway. A complete understanding of the dynamics will require further investigation. Preliminary results indicate that rotational relaxation may not be orders of magnitudes faster than other loss channels. Sticky collisions [175, 176], chemical reactions, or photoinduced two-body loss [177] may be to blame.
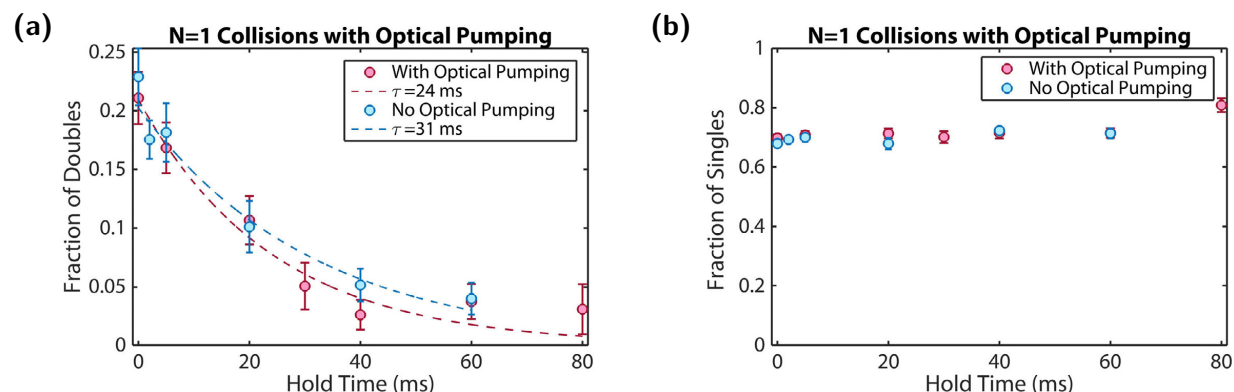
Figure 8.5.6: (a) Inelastic collision rate of CaF with and without optical pumping into F=0. Optical pumping was verified with microwaves. (b) Survivals of ones showing that the loss is only present when two molecules are present.

8.6 COHERENT CONTROL OF CaF MOLECULES

We also demonstrate coherent control of CaF molecules with microwave pulses between rotational states. This can be used to prepare clean signal quantum state samples, important for us to gain a better understanding of the collisions seen. It also allows us to transfer molecules to the absolute ground state, where we can prevent any loss arising from either rotational or hyperfine relaxation. Transitions between the N=1 and N=0 states in CaF are separated by 20.5 GHz, located in the K band of microwaves. We can drive an E1 transition with a microwave photon, and hence achieve high Rabi rates.

8.6.1 MICROWAVE CHARACTERIZATION

To deliver the microwaves to the molecules, we built our own microwave pyramid horn antenna. The back of a microwave horn has a waveguide region where microwaves are fed from a $\lambda/4$ dipole. The antenna was designed to have a gain of 10 dB. The far-field radiation pattern is shown in Figure 8.6.1. The emission follows the expected radiation pattern and is well polarized. The horn is driven by a
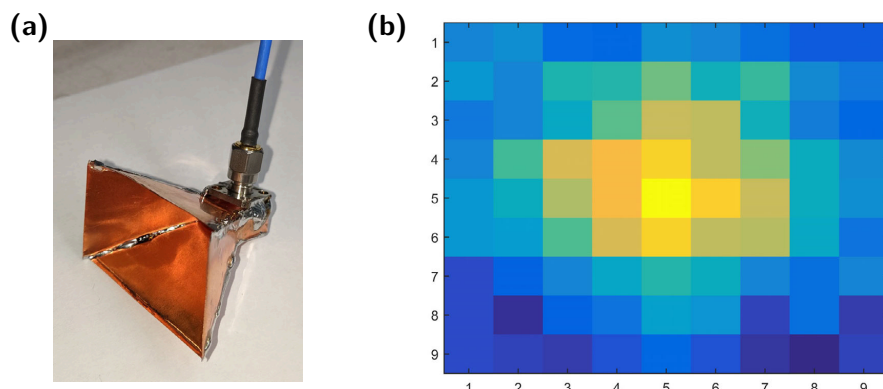
Figure 8.6.1: (a)Homebuilt microwave horn. The measured return loss is 14 dB. (b)Far-field radiation pattern measured at 16.5 GHz at a distance of 12.5 in. The field of view is 18 in.
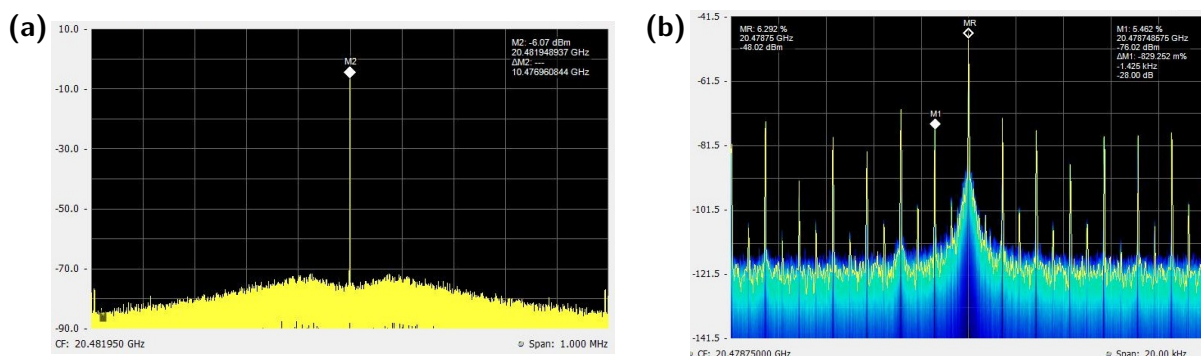
Figure 8.6.2: (a) Microwave spectrum after amplifier. (b) Microwave spectrum as measured with an antenna near the chamber. The multiple peaks are harmonics or the turbo pump on the MOT chamber.

40 GHz signal generator (Hittite HMC-T2240) and amplified by a 5 Watt amplifier (PE15A4020).

Two directional couples monitor both the power delivered and reflected from the microwave horn.

Careful characterization has shown that the microwaves are very clean, as shown in Figure 8.6.2(a).

When switched off with a PIN switch (ATM S1517D), the measured attenuation is over 80 dB.

(a)

(b)
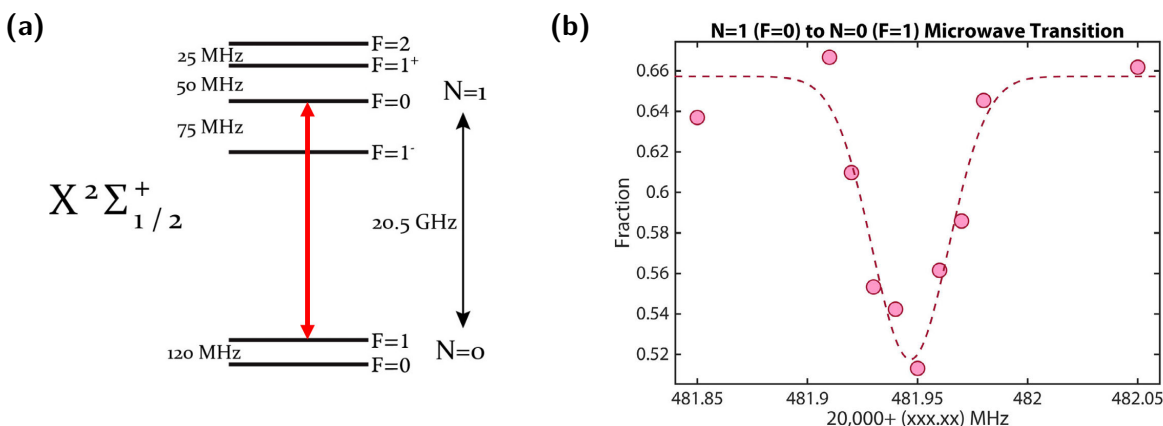
Figure 8.6.3: (a) Transitions addressed with microwaves. Due to the lack of a magnetic field, all m_F states in the F=1 ground state are degenerate. (b) F=0(N=1) to F=1(N=0) line center.

8.6.2   Microwave Transfer to N=0

We began by first driving the molecules from the N=1, F=0 state, to the N=0, F=1 state, Figure 8.6.3.

At high powers, the width of the transition is power broadened to [140] $\Delta\omega_{FWHM} = \Gamma\left(1 + \frac{2\Omega^2}{\Gamma^2}\right)^{1/2}$.

At low microwave powers, the broadening of the transition due to ac Stark shifts begins to dominate. With fairly low powers, we were able to drive molecules with a π pulse duration of 70 μs, Figure 8.6.4(a). However, there was significant decay in the Rabi oscillations, on the order of $\tau = 170$ μs. We decided to try to beat this decoherence by cranking up the drive power. Unfortunately, this did not buy us much in terms of the observed number of Rabi oscillations. With a π pulse duration of now just under 500 ns Figure 8.6.4(b), we are able to see about 10 oscillations at most, rather than the 100s expected from a decoherence time of $\tau = 170$ μs. This indicated that something was not quite right with the microwaves themselves.

After quite some confusion, we found that while the microwaves sent to the horn were perfectly clean (Figure8.6.2(a)), the molecules saw something drastically different, Figure 8.6.2(b). A forest of side-bands were visible when measured with an antenna near the chamber. These side-bands are separated by exactly twice the turbo frequency (715 Hz). It appears that the metal chamber
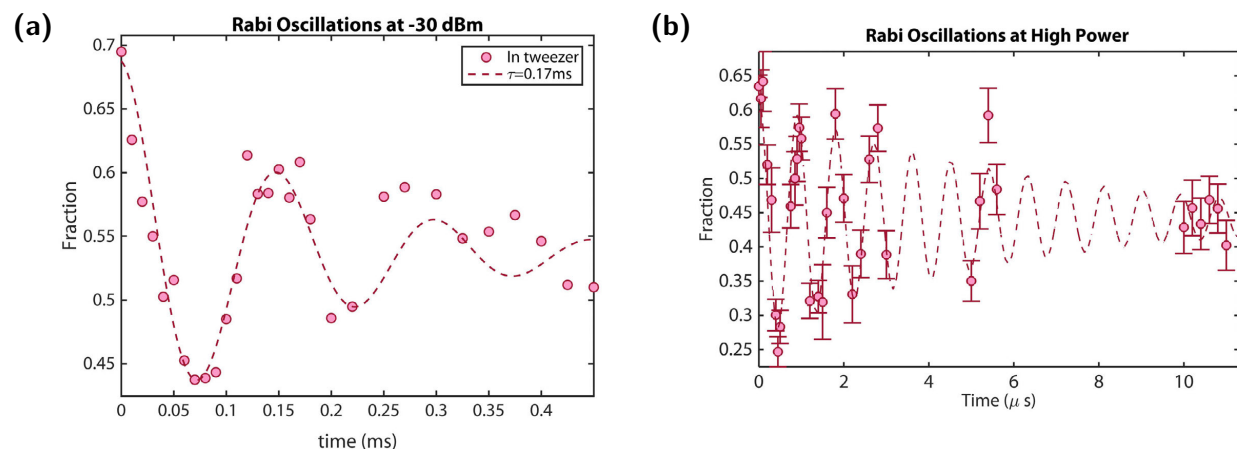
Figure 8.6.4: Rabi oscillations from N=1,F=0 to N=0,F=1. (a) Decaying Rabi oscillations at low power. (b) Decaying Rabi oscillations with a higher drive power. This suggest that the decay in coherence is not environmental, but due to our microwave drive.

is not only acting as a reflector of the microwaves, but is also modulating them due to vibrations. This may not be completely surprising, as the turbo pump (Agilent V551) is audibility loud and the MOT chamber is mounted on a large nipple at the end of the turbo. This problem is made worse with the fact that there was no direct line of sight between the molecules and the horn due to space constraints. We attempted to move the horn further away and place it behind the last mirror of the slowing beam path such that some direct line of sight existed, but that did not seem to help. It is possible we could synchronize the microwave pulse to the turbo pump, which should reduce the decoherence shot to shot. For the time being, since we are simply studying collisions, this is not as critical. In future experiments with large arrays, it will be important to consider this. Limiting metal near the chamber, using glass cells and microwave absorbing material is one possibility. Also relying on near-field coupling of the microwaves is another option.

With the microwaves, we are able to characterized the optical pumping time and efficiency, Figure 8.6.5. We find that with a laser intensity of $I_{MOT}/10$, and with all hyperfine components on except for F=0, we can transfer about 75% of the population into the F=0 state in 50 μs.
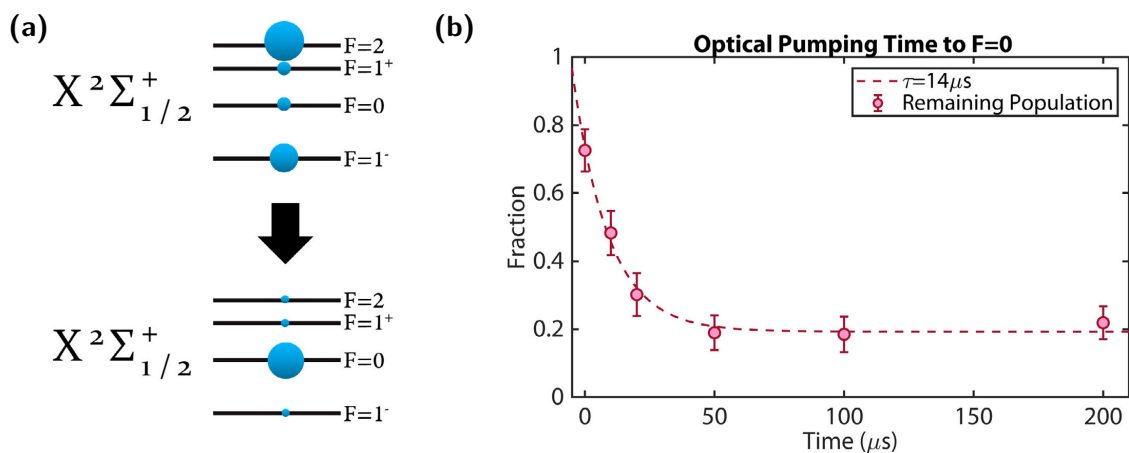
Figure 8.6.5: (a) Optical pumping into F=0. (b) Optical pumping timescale at $I_{MOT}/10$. Population remaining after a π pulse is plotted.
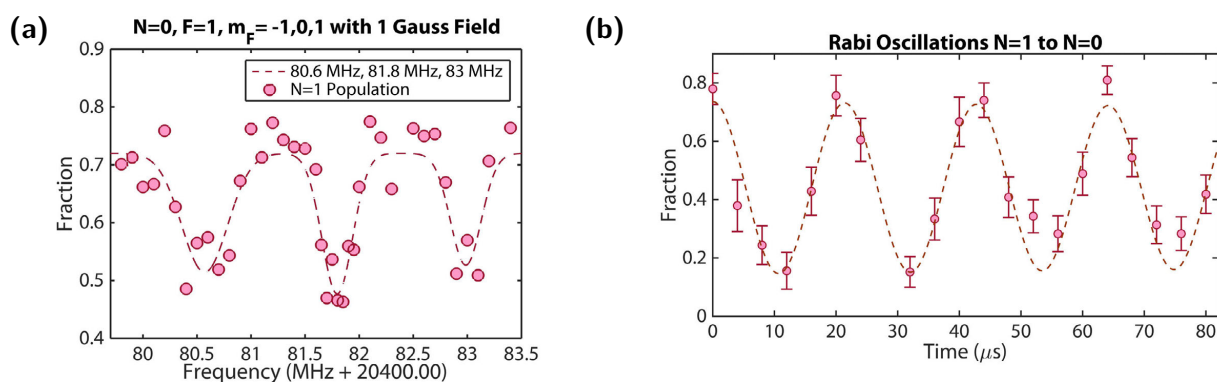
Figure 8.6.6: (a) Splitting of F=1, m_F=1,0,-1 in the ground N=0 state. (b) Rabi oscillations between N=1,F=0 and N=0,F=1,m_F=0 with a static magnetic field to split the m_F states.
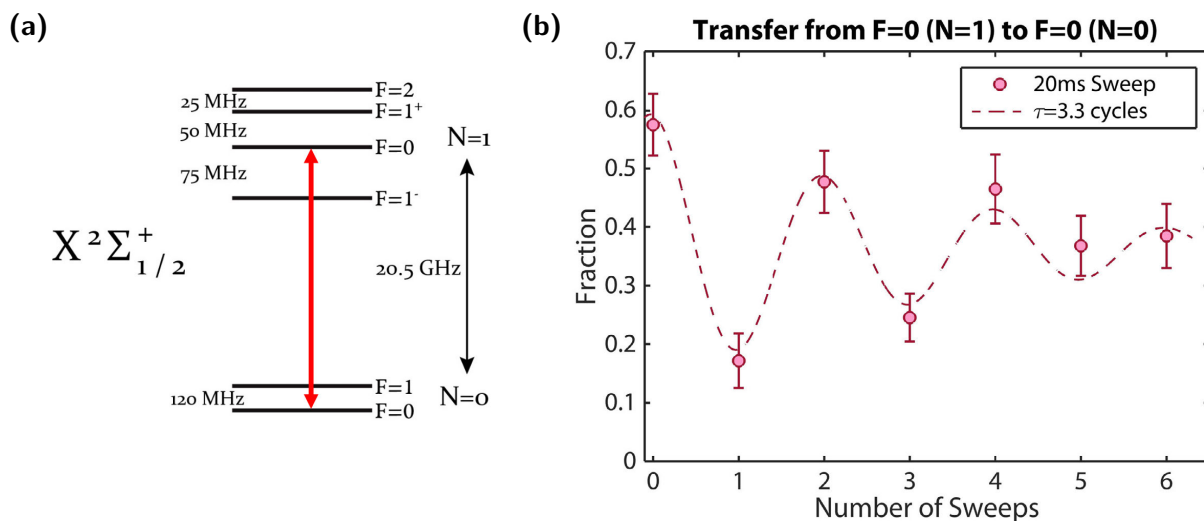
Figure 8.6.7: (a) Microwave transition swept to perform Landau–Zener transfer. (b) Transfer of ultracold CaF molecules to and from the absolute ground state (N=0, F=0). The single sweep efficiency is 86%.

To split the different m_F states of the F=1 manifold of the ground rotational state, we apply a small magnetic field. Since the shift of F=1, m_F=0 is quadraticaly sensitive, applying small fields is important for decoherence. Instabilities of this shim magnetic field at high fields was found to be a major source of decoherence. This splitting is shown in Figure 8.6.6(a). With this field, we could now drive Rabi oscillation between F=0 and F=1, m_F=0, Figure 8.6.6(b).

8.6.3 Absolute Ground State CaF Molecules

The final thing which could be done was to drive molecules to the absolute ground state (N=0, F=0). While we could drive molecules from F=1 (N=1) to F=0 (N=0), the optical pumping only purifies F states, not m_F. This would mean that when driving down to N=0, only one third of the populations would follow. If trying to do collisions experiments, this would mean that with two traps, the data rate is then reduced by atleast a factor of 9, plus all other imperfections associated with the microwave transfer. This leads us to want to optically pump into F=0 and drive directly the

E1 forbidden transition. The external magnetic field, applied to split m_F levels, also mixes the F=1, m_F=0 and the F=0 state in the N=1 state. Due to this mixing, we are then able to preform a Landau–Zener sweep, adabatically transferring population from the N=1, F=0 to the N=0, F=0. This was done by sweeping the magnetic field across the transition in about 20 ms. Sequential transfers to and back from the absolute ground state is shown in Figure 8.6.7, with a single sweep efficiency of 86%.

9

Conclusion and Outlook

9.1   Progress in Laser cooling of Molecules

Over the development of the experiment, we increased the phase space density by ten orders of magnitude from the MOT to the tweezers. Figure 9.1.1 shows the phase space density at various stages of the experiment. The overall progress in laser cooled molecules has also skyrocketed over the past years. Figure 9.1.2 shows the best densities achieved by laser cooling experiments since the start of my PhD. These improvements, as discussed, have allowed us to move from the technical
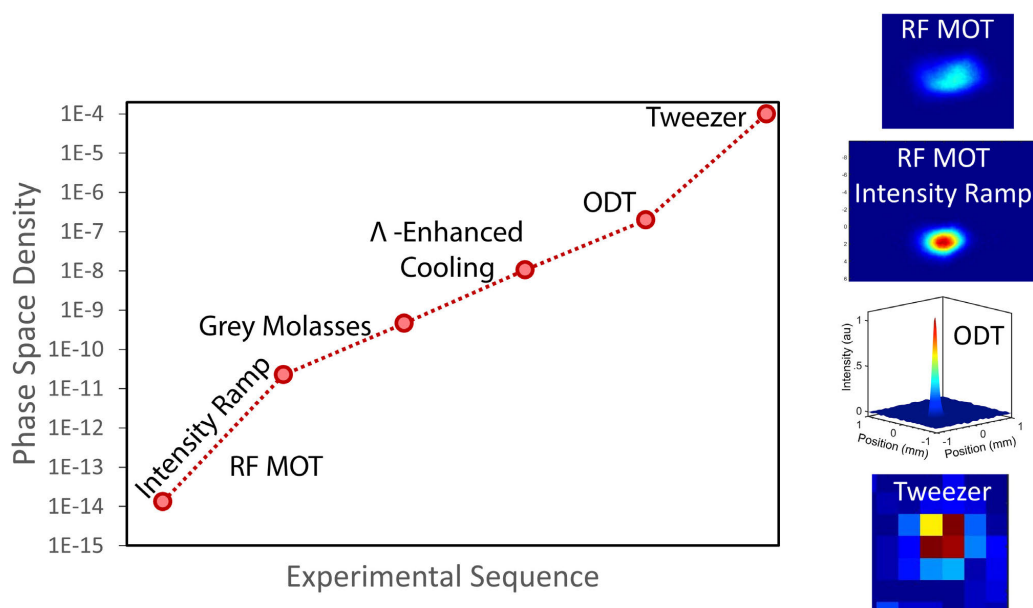
Figure 9.1.1: Phase space density throughout the experiential cycle.

aspects of laser cooling to being able to study the physics of collisions, and bringing into reality the long sought after dream of quantum computation and simulation with molecules.

With the ability to load single molecules into tweezers arrays, molecules, for the first time, are on the same footing as laser cooled atoms. Laser cooling large samples to degeneracy remains as an exercise for the reader.

9.2   FUTURE IMPROVEMENTS

Many future improvements could be implemented in the future, allowing for much lager samples of laser cooled molecules. Currently, by far the most inefficient step is the laser slowing process. In the future transverse cooling could be added, Figure 9.2.1, either in the form of molasses cooling, Sisyphus cooling, or a 2D MOT for compression. Transverse cooling has already been attempted in nearly all of the molecule laser cooling experiments with limited success. However, most were
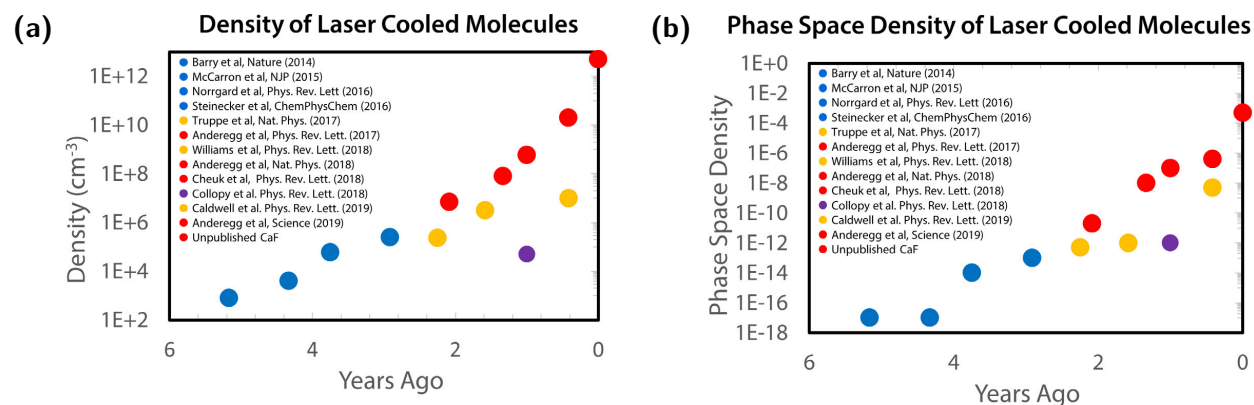
Figure 9.1.2: (a) Density of laser cooled molecules over the past 5+ years. The red dots indicate work presented in this thesis.(b) Phase space density of laser cooled molecules over the past 5+ years. The red dots indicate work presented in this thesis.
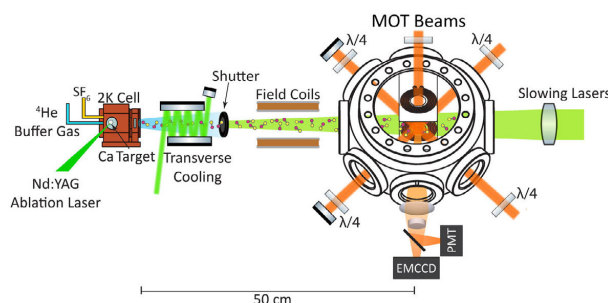
Figure 9.2.1: Transverse cooling implantation to the existing apparatus.

incomplete attempts (at least our attempt was incomplete), and gains, especially with new laser technologies, should be achievable.

9.3   A Novel Slowing Method

There are other ways of improving the slowing process. A Zeeman slower for molecules has recently been proposed requiring high fields to push the molecules into the Paschen–Back regime [136–138]. Here we present another idea to make a positional space dependent decelerator. Such a decelerator could be used also for a CW source or for multiple loading.
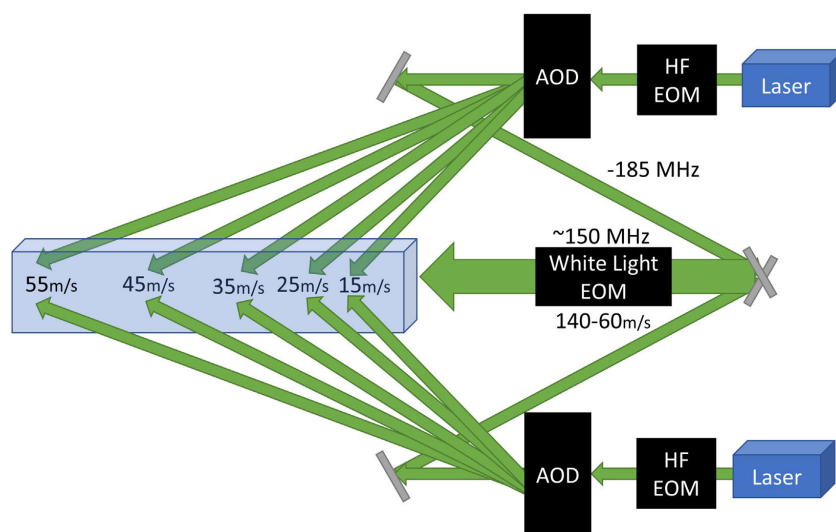
Figure 9.3.1: A "rainbow" slower for molecules. Whitelight slowing is used for deceleration of high velocity molecules down to around 60 m/s. To decelerate molecules to the MOT capture velocity, an AOD generates positional dependent slowing light. Due to the angle of this light, it also provides a transverse cooling force to prevent pluming of the molecular beam.

The basic idea is to have a whitelight slowing beam which piles all the molecules up to around 60 m/s. The final velocity should be set such that this beam can be left on continuously without affected the MOT. An AOD with multiple differences frequencies creates a rainbow of light, with each frequency exiting at a different angle. This angle is then exaggerated with some optics, eg. a spherical mirror, and aimed at the molecular beam with some shallow angle. The shallow angle avoids beams of near resonate light from destroying the MOT and also gives a transverse cooling force. In this way, you have the positional dependence slowing of a Zeeman slower, but with the addition of transverse cooling the entire distance. Due to the nature of this arrangement, the transverse cooling increases and the velocity slows, which is when transverse confinement against pluming is most important. Figure 9.3.1 gives an overview of this slower as well as some important considerations.

9.4   FUTURE DIRECTIONS

We are already well on our way towards studying ground state molecular collisions. Preliminary results indicate similar loss rates to the excited roational states. By applying an electric field in the current experiment, we could study shielding effects [24]. These large electric fields give rise to a long-range repulsion above a critical value. This however requires quite large electric fields, on the order of 15 kV/cm for CaF, which may be difficult to accomplish in the existing apparatus. Also care must be taken to prevent patch potentials on the glass surfaces, which are fairly close to the molecules. Other shielding schemes where by microwaves may be used have also been proposed [26, 178, 179]. In these schemes, microwave fields are used to either cancel out the dipole interaction or engineer repulsive long-range interactions which forms a three-dimensional repulsive shield. We could also apply magnetic fields during the collisional process in order to study molecule-molecule Feshbach resonances [180, 181]. These resonances could then be used in the future for rapid direct evaporation cooling of CaF molecules.

With a few improvements in initial number, we could try evaporative cooling the molecules directly in the ODT. This will most likely require pumping molecules into a single state to suppress the rate of inelastic collisions. Once could also study atom molecule collisions and sympathetic cooling. This is best done by co-loading an atomic species into the ODT. Lithium appears to be an optimal candidate due to it low mass, and thus high centrifugal barrier.

The optical tweezer platform is also ideal for studying dipolar exchange [182]. By polarizing the molecules, either by applying an external electric field, or with microwaves, we can expect exchange rates on the order of 10-100 Hz between tweezers. For future applications, such as quantum simulations and computation, it will become important to perform Raman sideband cooling [183] of the molecules. This prevents dephasing from the motion within the trap. The right application of magnetic fields and polarizations will be needed to compensate the tensor stark shifts present in
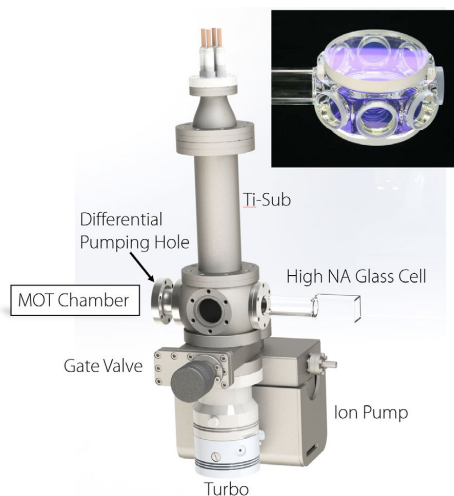
Figure 9.4.1: Concept for a next generation molecular tweezer experiment. Molecule will be optically transported from the MOT chamber to a glass cell, allowing for high NA imaging and trapping. A glass octagonal cell (pictured from Precision Glassblowing), may also be used.

optical traps. Two qubit gates may be implemented in a various ways [12–14, 184, 185]. A dipolar blockade scheme [13] may be used were the dipolar interactions will lead to an energy shift leading to a blockade effect. The error rate for this type of gate is given by [115, 186] $\varepsilon = \frac{\Omega^2}{8E_{DDI}^2}\left(1 + 6\frac{\Omega^2}{\omega_{10}^2}\right)$ where Ω is the Rabi coupling and ω_{10} is the splitting between the qubit 1 and 0 states, ~ 100 MHz for CaF. This leads to an error rate on the order of 10^{-3}. A dipolar exchange scheme [15] may also be used to preform a two qubit gate, where the coupling between molecules is set by changing the internal state. Theoretical estimates for achievable gate fidelities range from 10^{-3} to 10^{-6} [13, 14, 184], making molecules competitive alternative to current platforms.

Finally, to perform quantum simulation and computation with molecules, improvements in the detection fidelity and trap array size will need to be made. A next generation molecular tweezers experiment (Figure 9.4.1) is currently underway. It will feature high NA allowing for high fidelity detection and large arrays with moderate power. With two objectives of NA 0.65, a factor of 10 more photons will be collected than the current 0.28 system. This means that imaging can be a factor of

10 shorter, and hence reduce the imaging losses by a factor of 10. Also, shorter images will mean faster sequences, reducing the effects of vacuum loss. With the improved vacuum lifetimes, imaging fidelities well over 99.9% should be achievable. 2D arrays can be made with a crossed AOD or SLM. The experiment will feature a transport stage to allow for high vacuum and large optical access. The transport must be compatible with a high repetition rate, on the order of 2 Hz. Clean microwave polarizations may be added with either nearfield coupling or careful design of metallic parts. Two molecules, i and j, with a dipole moment $\hat{d}$ and position r will interact with a Hamiltonian [8],

$$H_{ij} = \frac{1}{4\pi\varepsilon_0} \left(\frac{\hat{d}_i \hat{d}_j - 3(\hat{r}_{ij} \cdot \hat{d}_i)(\hat{r}_{ij} \cdot \hat{d}_j)}{|r_i - r_j|^3} \right) \tag{9.1}$$

with $\hat{r}_{ij} = \frac{r_i - r_j}{|r_i - r_j|}$. Since the dipole moment is set by the molecules, reducing the spacing between molecules will be necessary to decrease gate times. While optical tweezers typically can only be brought to a few microns before heating due to interference of tweezer light overlap, using an interleaved array of two different trapping frequencies may be used. One could load the tweezers into an accordion lattice, which could then reduce the particle spacing. Such approaches may allow for dipolar rates on the order of 10's to 100's of kHz. Blackbody stimulated vibrational transitions will limit the coherence times to around 3-4 seconds at room temperature, as discussed in Chapter 2. Cooling the apparatus to 77 K will extend this decoherence time to minutes. In the future, other species could be used, such a polyatomics, where even more complexity can further expand the range of Hamiltonians simulated.

A

CaF Molecular Constants and Properties

This appendix will serve as a reference for the properties of CaF.

A.1   Vibration Levels

$$E_v = \omega_e(v + \tfrac{1}{2}) - \omega_e x_e(v + \tfrac{1}{2})^2 + \omega_e y_e(v + \tfrac{1}{2})^3 + \dots \tag{A.1}$$

Constant	$X^2\Sigma^+$	$A^2\Pi$	$B^2\Sigma^+$	$C^2\Pi$	$D^2\Sigma^+$
ω_e	588.644	594.513	572.424	480.595	657.33
$\omega_e x_e$	2.91194	3.031	3.101	1.81335	2.85
$\omega_e y_e$	8.41499×10^{-3}	-	-	-	-

Table A.1.1: Vibrational constants for CaF. [129, 188]

A.2   ROTATIONAL LEVELS

$$E_{rot} = B_v R(R+1) - D_v R^2(R+1)^2 + H_v R^3(R+1)^3 + ... \quad \text{(A.2)}$$

$$B_v = B_e - a_e\left(v + \frac{1}{2}\right) + \gamma_e\left(v + \frac{1}{2}\right)^2 ... \quad \text{(A.3)}$$

Constant	$X^2\Sigma^+$	$A^2\Pi$	$B^2\Sigma^+$	$C^2\Pi$	$D^2\Sigma^+$
B_e	0.343704	0.348744	0.342604	0.32439	0.3656
a_e	2.436×10^{-3}	2.529×10^{-3}	2.63×10^{-3}	2.05×10^{-3}	2.1×10^{-3}
γ_e	4.9299×10^{-6}	-	6.3×10^{-6}	-	-
D_v	4.68×10^{-7}	4.81×10^{-7}	4.83×10^{-7}	-	-
H_v	-1.9×10^{-14}	-3.8×10^{-14}	-6.7×10^{-14}	-	-

Table A.2.1: Rotational constants for CaF. (Note: D_v and H_v are depended on the rotational state, however, due to the small size of these terms, we ignore it here.) [129, 188, 189]

A.3   Λ DOUBLING

	$X^2\Sigma$	$A^2\Pi$	$B^2\Sigma$	$C^2\Pi$	$D^2\Sigma$
Λ (GHz)	-	1.3346	1.3722	0.254	0.270

Table A.3.1: Λ doubling splittings [189].

A.4 Dipole Moments

Table A.4.1 shows the dipole moments and transition moments of CaF for the lowest lying states relent to laser cooling.

State	Dipole Moment (D)
$X^2\Sigma$	-3.08
$A^2\Pi$	-2.44
$B^2\Sigma$	-2.06
$C^2\Pi$	-9.25
$D^2\Sigma$	4.50
$E^2\Sigma$	-9.68

Transition	Transition Moment (D)
X-A	5.95
X-B	4.70
X-C	1.30
X-D	0.79
X-E	0.61
A-B	1.09
A-C	3.00
B-C	18.6

Table A.4.1: Dipole moments and transition moments of CaF (1D $=0.3934$ ea_0) [190–192].

A.5 g Factors

Table A.5.1 shows the g-factors for the X, A, and B states.

State	Hyperfine state	g_F Factor
$X^2\Sigma^+$	F=2	0.5
	F=1	0.795
	F=0	0
	F=1$^-$	-0.295
$A^2\Pi_{1/2}$	F=1	-0.021
	F=0	0
$B^2\Sigma^+$	F=1	1.022
	F=0	0

Table A.5.1: CaF g_f factors [144].

A.6 Frank Condon factors

The tables A.6.1, A.6.2, and A.6.3 give the Frank Condon factors for the X- A,B,C transitions. These have been calculated with a symplectic integrator, which can be found on the DeMille group website. The results of this integrator have been surprisingly accurate for CaF against measured values.

$A\,^2\Pi$	$v'=0$	$v'=1$	$v'=2$	$v'=3$
$v=0$	0.978	0.0223	1.74×10^{-5}	4.22×10^{-7}
$v=1$	0.0216	0.935	0.0435	4.58×10^{-5}
$v=2$	0.000711	0.0407	0.895	0.0636
$v=3$	2.67×10^{-5}	0.00201	0.0575	0.858
$v=4$	1.11×10^{-6}	0.000101	0.0038	0.0723
$v=5$	5.05×10^{-8}	5.29×10^{-6}	0.000239	0.00598

Table A.6.1: A state Frank Condon factors.

$B\,^2\Sigma$	$v'=0$	$v'=1$	$v'=2$	$v'=3$
$v=0$	0.998	0.00195	1.66×10^{-5}	1.16×10^{-6}
$v=1$	0.00192	0.993	0.00457	4.11×10^{-5}
$v=2$	5.02×10^{-5}	0.00442	0.988	0.00792
$v=3$	2.97×10^{-8}	0.000157	0.00757	0.98
$v=4$	3.39×10^{-9}	7.98×10^{-8}	0.000326	0.0114
$v=5$	4.78×10^{-11}	1.62×10^{-8}	1.19×10^{-7}	0.000569

Table A.6.2: B state Frank Condon factors.

$C\,^2\Pi$	$v'=0$	$v'=1$	$v'=2$	$v'=3$
$v=0$	0.694	0.258	0.0441	0.00387
$v=1$	0.249	0.282	0.35	0.105
$v=2$	0.0508	0.322	0.0834	0.345
$v=3$	0.00643	0.115	0.304	0.00977
$v=4$	0.000554	0.0206	0.172	0.244
$v=5$	3.12×10^{-5}	0.00227	0.0411	0.214

Table A.6.3: C state Frank Condon factors.

A.7 Molecular Potentials

Figure A.7.1 shows the potential curves for the X, A ,B, and C states, all layered on top of one another.
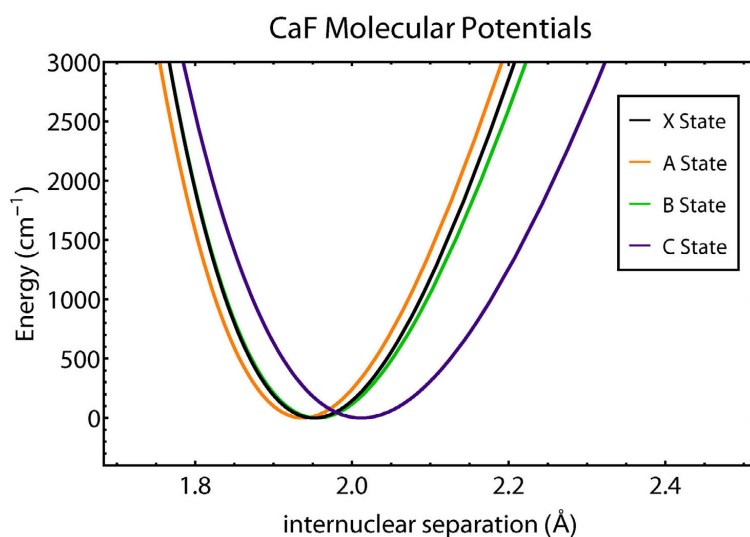
Figure A.7.1: CaF Levels relevant in this thesis.

	$X^2\Sigma$	$A^2\Pi$	$B^2\Sigma$	$C^2\Pi$	$D^2\Sigma$
r_e (Å)	1.9516403	1.9374	1.9555	2.012	1.893

Table A.7.1: Equilibrium internuclear separation [129, 188].

A.8 Transitions

The measured transitions for CaF are shown in Figure A.8.1.
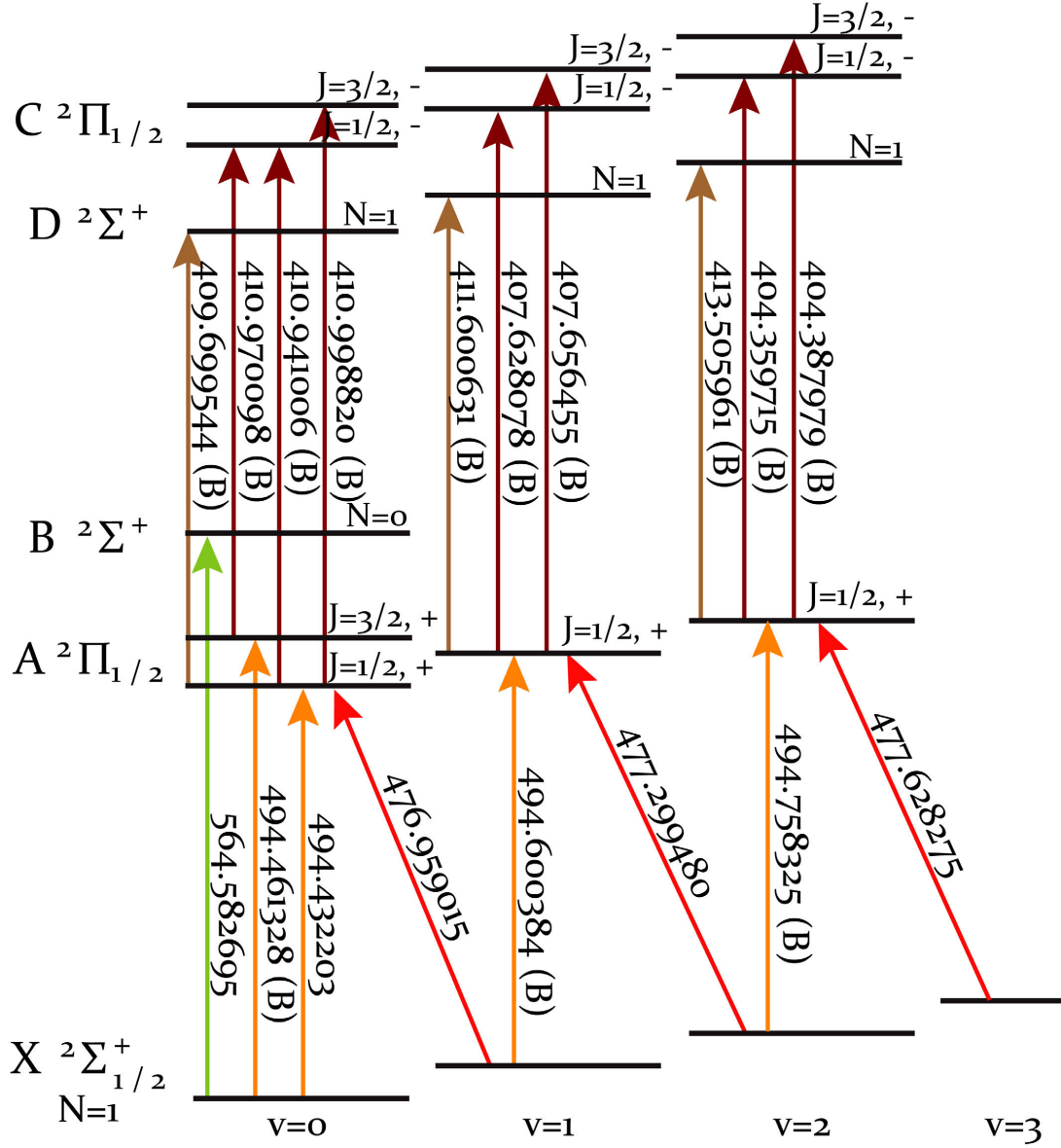
Figure A.8.1: CaF electronic transition in THz. Unless noted, frequencies reference the center of the transition. (B) Indicates the frequency addressing the blue most hyperfine state. Frequencies are referenced to our wavemeter, which has an unknown offset.

B

Galvo Based Single Mode Fiber Switcher

Stable lasers over a wide wavelengths is critical to laser cooling molecules. ULE cavities and frequency combs are often used in many AMO labs today, however ULE cavities tend to be limited in their wavelengths range once purchased and require high frequency AOMs to bridge the free spectral range of the cavities. Frequency combs are often not quite as turn key and reliable as manufactures claim them to be, are costly and require external locking electronics for each laser. They also require a wavemeter for each channel to know the absolute position of the laser. Wavemeters turn out to be a good alternative for both wide wavelengths ranges and turn key operation delivering
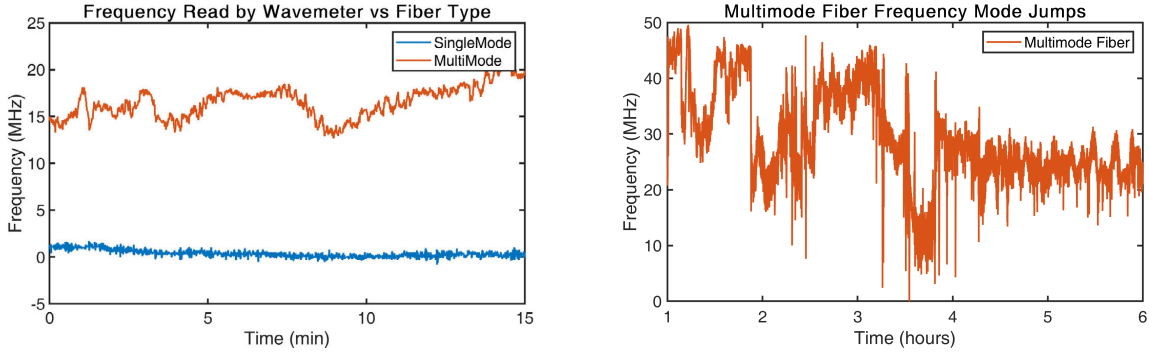
Figure B.0.1: Long term frequency reading of a HeNe from a multimode fiber into the wavemeter.

frequency stability in the range of 100's of kHz. Specifically we use a High Finesse WS-7 wavemeter which is specified to have an absolute accuracy of 60 MHZ and a measurement resolution of 10 MHZ for 248 nm to 1180 nm at a speed of 500 Hz. We find however that we are able to attain frequency stability to the 100's of kHz level with a few simple modifications. These wavemeters have a Fizeau interfrometer inside which is projected onto a camera to image the fringes and calculate the wavelengths.

Originally multimode fibers into a multimode switch was used, which was read by the wavemeter. This was found to be highly unstable and rendered the experiment highly unreliability. Figure B.0.1 shows the fundamental problem of using multimode fibers into the wavemeter. Due to the many different modes in a multimode fiber, and the changing mode profile versus time, temperature, pressure, etc. The Fizeau interferometer misreads this changing mode structure as a change in frequency of the laser. This causes frequency changes on on the 50 MHz level with large jumps if the multimode fibers are touched. If a single mode fiber is used instead, these jumps disappear and the stability is greatly increased. Figure B.0.2 shows the Allan deviation of the stability of both a single mode fiber and a multimode fiber.
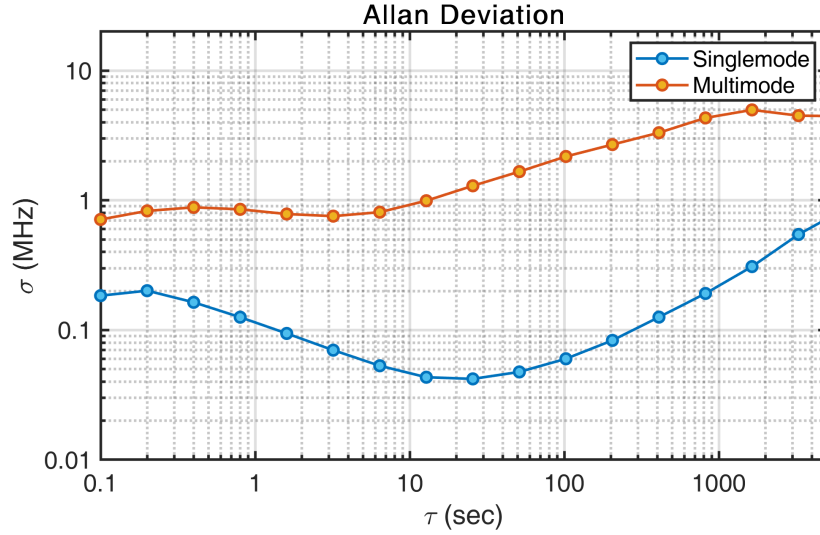
Figure B.0.2: Allan deviation for both the singlemode fiber and multimode fiber into the wavemeter looking at the HeNe.

As a long term frequency reference, we originally used a frequency stabilized HeNe. [1] We later switched to a vapor cell locked lithium reference for improved frequency stability.

The reference frequency is sent into one of the wavemeter channels and all of the frequencies read out by the wavemeter are then referenced to that frequency. This removes all first order drifts presents in the wavemeter, but still allows for wavelength dependent drifts to occur.

While single mode switchers are sold, they are quite pricey, have long lead times, switch in several milliseconds and are not expandable if more lasers need to be added and have limited wavelength ranges. Recently we also have some evidence that the single modes switches degrade when 400 nm light is used. We decided instead to build out own switcher which was based on a galvo. We used a Cambridge technology PSI-10 galvo which has a step response of 220 μs, a resolution of 12 μrad

---

[1]Note:Never buy a HeNe from Melles Griot. A typical frequency stabilized HeNe looks at two adjacent laseing modes which have opposite polarizations [193, 194]. A PBS then is used to monitor the amplitudes of both of these peaks and locks the cavity such that these peaks are of equal height. Melles Griot shockingly does not do this. They only look at one peak and lock the amplitude of that peak, which means if the power from the laser changes, the frequency changes.
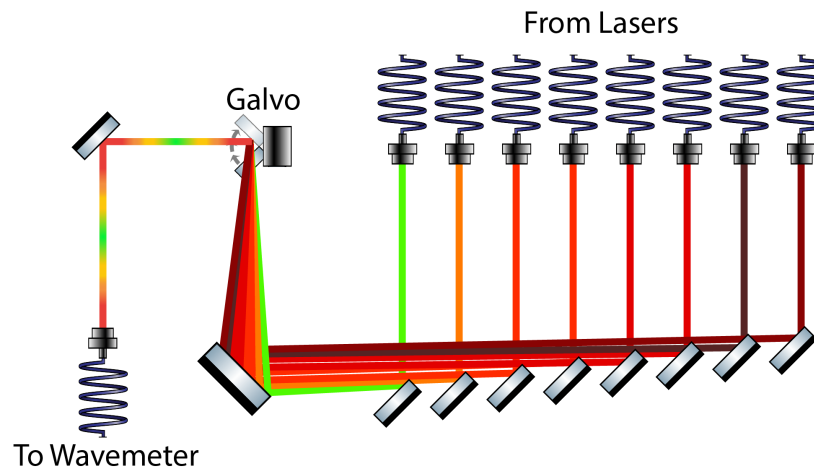
Figure B.0.3: Layout of the galvo based fiber switcher

a temperature drift of 30 μrad/$^\circ$C and a long term drift of only 100 μrad. The galov based switched employed 8 fibers which were collimated with 15 mm focal length aspheres and aligned onto the galvo mirror. The fairly large beam size was used to reduced sensitivity to alignment drifts. The galvo mirror switches between 8 preset locations to sequentially couple each fiber into a single fiber to enter the wavemeter. The position of each galvo step is controlled by a multiplexer (MAX354) which takes the 4 wire serial connection high finesse uses and has 8 adjustable potentiometers which can each be adjusted to any value from 0-5 V.

Figure B.0.4 shows the switching speed of the galvo between two different lasers. We find that the galvo matches its specs and switches between channels in 200 μs with limited ringing.

The galvo switcher has now been operated for 4 years with nearly no realignments needed (with the exception of falling objects).
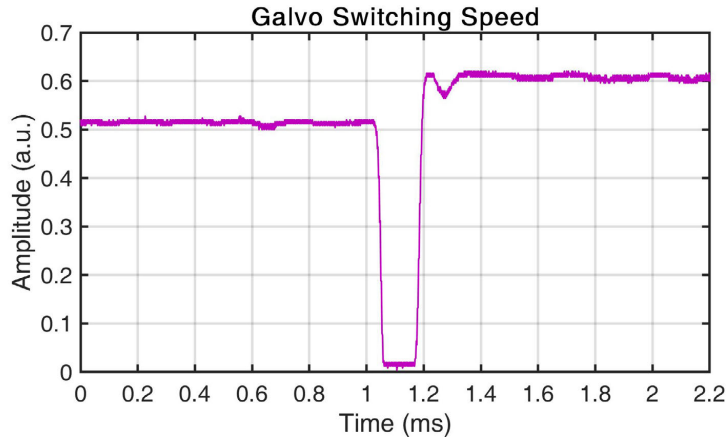
Figure B.0.4: Switching speed between two fiber coupled beams.

B.1   Improving the Stability of the WS7

In order to reach long term stability at below the MHz level, several environmental parameters must be controlled. First it was found that the frequency read out by the wavemeter was proportional to the air pressure, Figure B.1.1(a). It was also found that High Finesse has some sort of internal temperature stabilization which corrects in 3 MHz steps, Figure B.1.1(b). While the wavemeter is always compared in relation for a stabilized frequency reference as one of its channels, the large fluctuations seen with the changes in pressure and temperatures still presented a problem for our long term stability.

We decided to enclose the wavemeter inside of a large LF 12 nipple to prevent changes in air pressure affecting frequency stability. Both a single mode fiber feedthrough and a usb/serial feedthough were needed to control the wavemeter. Once again, due to long lead times, we decided to make these ourselves. To make an air tight singe mode fiber feedthough we bought a custom FC/APC to FC/PC bare fiber which we slid into a notch of a KF blank. The modified blank was then glued to another larger blank with Torr-Seal. This worked until multiple openings and closings stressed the

(a)

Wavemeter Pressure Drifts

(b)

Wavemeter Temperature Compensation
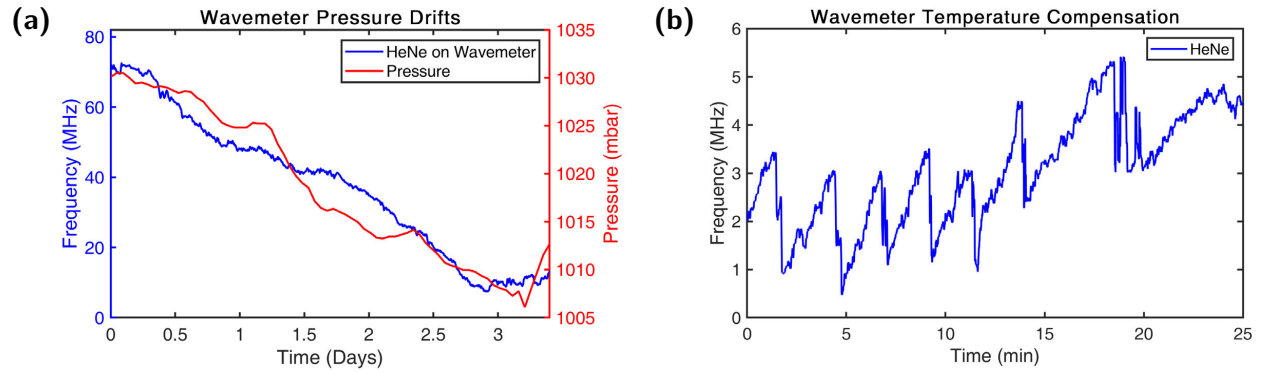
Figure B.1.1: (a) Pressure data overlapped with the drift of the HeNe as measured by the wavemeter. (b) Internal temperature compensation of the wavemeter.

blank and caused small cracks in the Torr-Seal. This was solved by adding the Torr-Seal after the bank was already tightened in place.

The 4 wire Serial+USB feedthrough proved to be a bit more tricky than anticipated. The waveme-ter uses high speed USB which communicates at 480 Mbits/ second. In order to have USB compliant device such that the rising and flailing edges don't blur together, one needs a rise time on the order of 500 ps! At these frequencies corresponding to a few GHz, it is very easy to couple in a little bit of stray inductance or capacitance which will cause the device to fail. The feedthrough used was built from a 9 pin Amphenol connector, 5 used for the USB + shield and 4 for the serial connection to the wavemeter. The first iteration had fairly long untwisted wires on both the input and output side. This degraded the signal to a point where the device could no longer communicate. Once we realized the frequencies involved, we ensured that all of the twisted pairs were twisted directly in and out of the connector and made sure the ground shield was properly installed. These improve-ments allowed the USB connection to function properly. The eye diagram from signals from the wavemeter is shown in Figure B.1.2.
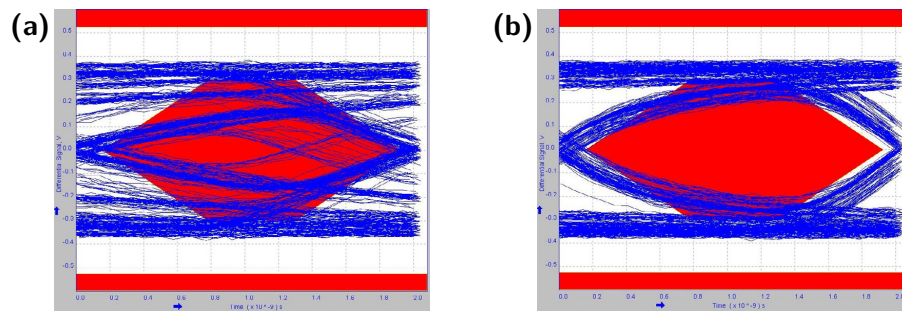
Figure B.1.2: (a) Signal degradation from a 3 in. break in shielding and poorly twisted pairs. (b)The performance of the home-built USB feedthrough.

B.2   ASIDE: TESTING USB COMPLIANCE

USB devices can be easily tested via programming from a computer via a USB test fixture (This is simply a relay which switches from the host computer to the oscilloscope without depowering the USB). All USB devices have a controller inside which may be programmed to output various test sequences with software from the USB website (www.usb.org). In order to test a device, follow these steps.

1. Connect both the $Data_+$ and $Data_-$ connectors to a fast oscilloscope.

2. Connect the device under test (DUT) to the test board.

3. Connect the power and USB connection form the test board to the computer.

4. Flip the toggle switch on the test board to program.

5. Using xHCI HSETT, select the correct host controller for testing the device.

6. Select the desired device and select the "TEST_PACKET" command.

7. Execute.
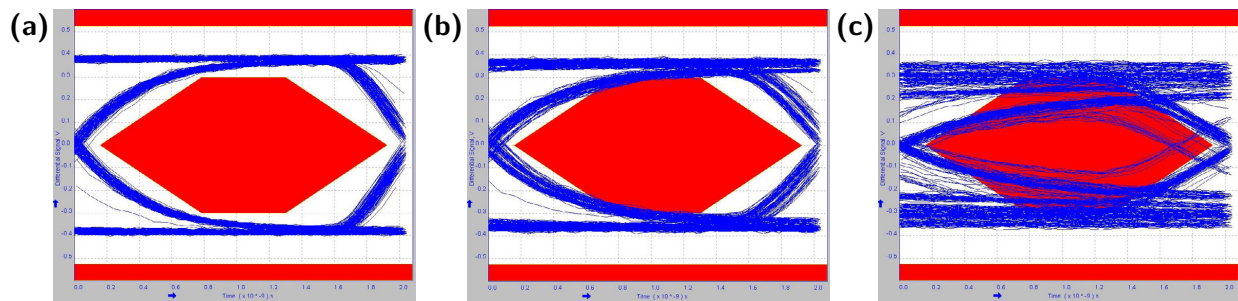
Figure B.3.1: Degradation of USB signal vs cable length. The signal is from a USB 3.0 thumb drive. (a) Direct connection. (b) Short 3 ft. USB cable. (c) Long 15 ft. USB cable with repeater hub.

8. Switch the text board to test mode. This flips a relay and which switches the connection of the DUT from the computer to the scope.

9. Plot an eye diagram to analyze the signal.

10. Once done, the DUT will need to be power cycled before it can be used again.

B.3   USB Eye Diagrams vs Shielding and a USB Feedthrough

As mention previously proper shielding is crucial to maintaining signal integrity. Figure B.3.1 shows the effects of USB cable length on single integrity. Surprisingly even your typical long USB cable, depending on how it was manufactured, is enough to cause sporadic communications issues.

C

Optical Blackening Reflectivity and Outgassing

Optical blackening was vital to improve signal to noise in the experiment. Here the reflectivity and outgassing rates are plotted for various methods. We find that Acktar (Spectral Black), MH2200 (Alion), and copper blackening [195] all have similar performances for reflectivity. MH2200 is the best for shallow angles, while Acktar is the best for higher angles. MH2200 is recommended for most applications as it is easy to apply with an air brush, has very low outgassing, and is less delicate than the other methods.
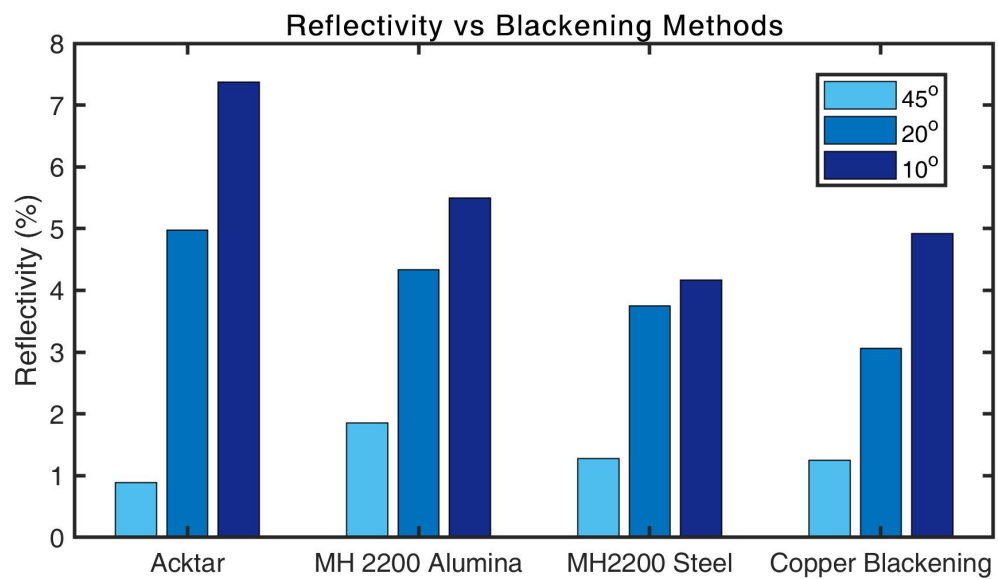
Figure C.0.1: Reflectivity of various blackening method vs angle of incidence. Measured at 650 nm.
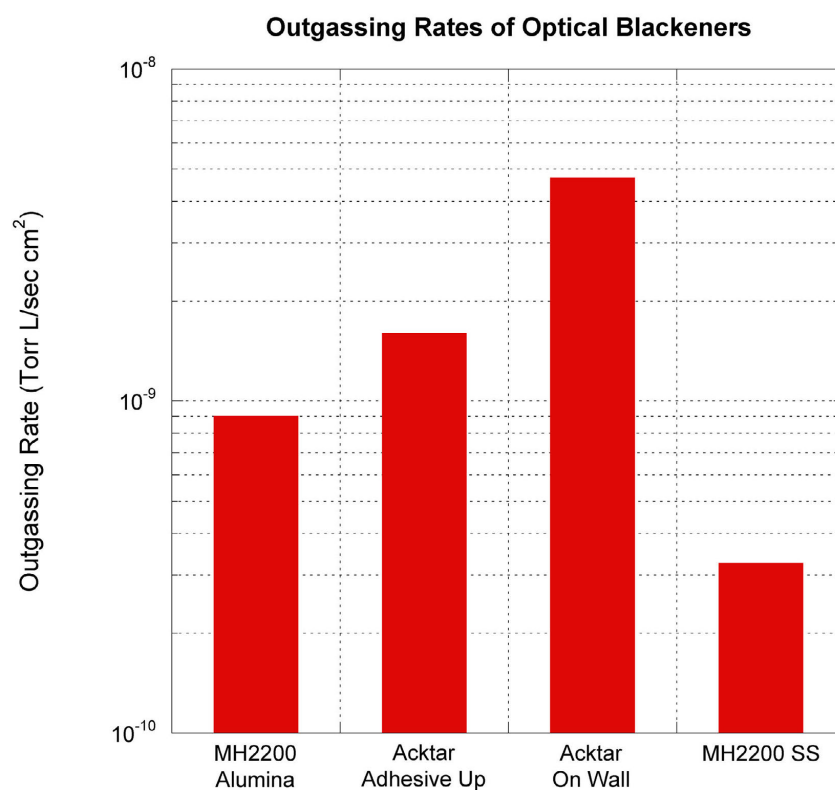
Figure C.0.2: Outgassing rates of various blackeners. Note: The outgassing rates measured for the MH2200 on alumina is limited by the alumina. The outgassing plotted for the MH2200 on stainless steel is an upper limit, as the measurement was limited by the ultimate pressure of the turbo-pump.

D

Dye Lasers - Tips and Tricks

Dye lasers are a versatile tool for producing high laser power across the visible spectrum. They do however require some knowledge for proper operation, which has created a negative reputation for these lasers. Still today, their ability to continuously tune with several watts of power across the visible spectrum still has yet to be matched by solid-state systems. This tunability and high power is critical for molecules as one may easily address different lines with a turn of a knob (and maybe a quick dye change as well). We will specifically cover the Coherent 899's in this section as those are the lasers found in our lab. The basic operation method will be universal across dye lasers, but
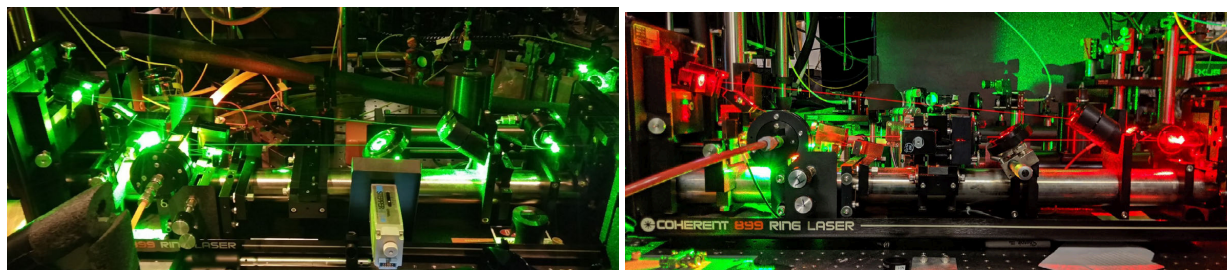
Figure D.0.1: Not many lasers can tune over multiple colors. (Lasing at 548 nm on the left and 630 nm on the right.)

specific tricks will apply only to 899s. The general steps to align the dye laser is well document in the 899 manuals, so initial lasing will not be covered here. When properly tuned, a dye laser can achieve a linewidth of $\sim$ 1 MHZ RMS.

D.1 Overview of Dye Lasers and the Coherent 899

A CW dye laser uses organic dye molecules as the gain medium for the lasing to occur. Due to the presence of meta-stable states, fresh molecules must be continuously replenished, which is done in the form of a dye jet. Around the dye jet, a bow-tie cavity, which creates a traveling wave, supports the lasing. Single direction lasing is achieved with an optical diode (same working principle as an optical isolator). With the cavity and the broad gain medium, the laser may support multiple cavity modes and thus be very broad. A birefringent filter selects the allowed lasing modes over a range on the order of 2 THz. To turn this laser into a single frequency laser, an intra cavity assembly (ICA), contains both a thick and thin etalon which selects only one cavity mode, Figure D.1.2.

Organic dye molecules have strong emission and absorption bands in the visible spectrum due to an extended system of conjugate bonds(alternating single and double bonds). Without such bonds, the absorption is below 200 nm [196]. There are two sub-classes of dyes, uncharged, which feature
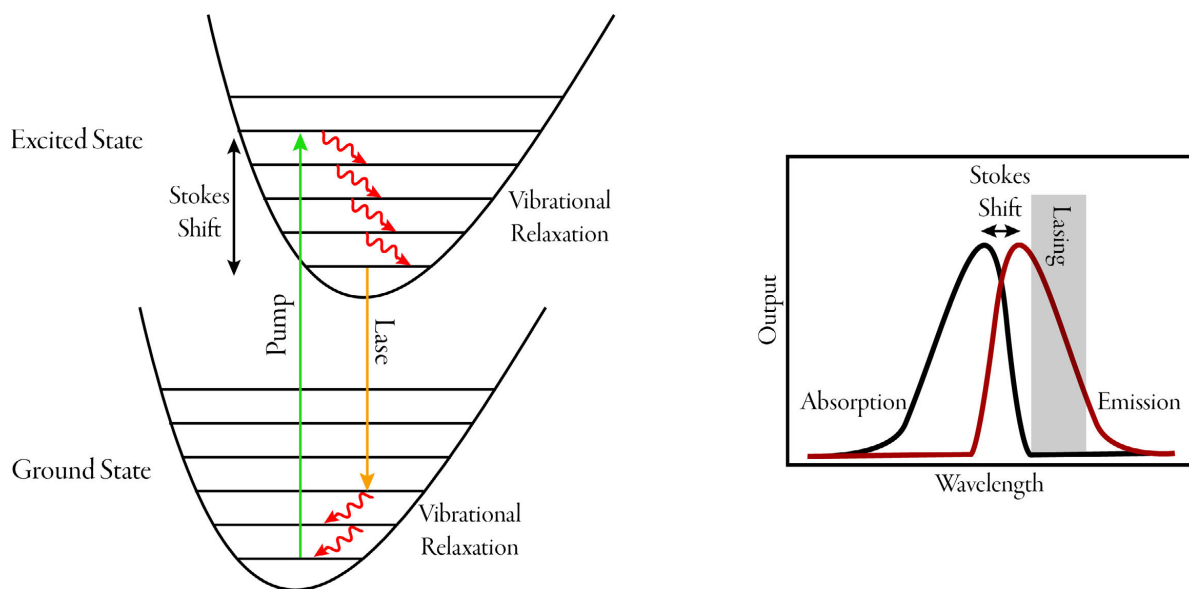
Figure D.1.1: Dye laser level structure. The absorption wavelength is set by the overlap of Franck Condon factors of the ground stat and excited states. Rapid relaxation occurs once excited up due to the fluid nature of the dye (Collisions happen on the picosecond time scale). Decay occurs and lasing between the excited ground state and a lower state with good wavefunction overlap occurs. The wavelength difference between the absorption and emission is called the Stokes shift (typically around 20 nm for the rhodamines and 10 nm for the pyronins [196]). Lasing can occur in a range where where is strong emission, but no absorption.
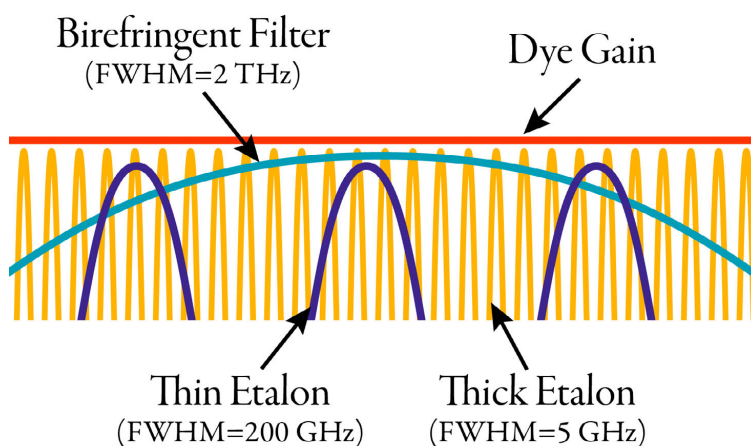
Figure D.1.2: Filters in a Coherent 899 Dye Laser. (Adapted from Coherent manual)

good solubility to non-polar solvents, and cationic dyes which are soluble in polar solvents, such as alcohols [196]. Collisions occur on the picosecond timescale. This broadens the spectrum as the rotational moment of the molecules is affected. This also sets the timescale for nonradiative decays in the excited state. A pump laser is used to excite the dye molecules to create a population inversion. Originally dye lasers were designed to be pumped with argon-ion laser, but now days solid state DPSS lasers are typically used. The dyes we typically use, Rhodamines, have a peak absorption around 530 nm, make a 532 nm DPSS an ideal pump laser. Some dyes have slightly bluer absorption lines were new 488 nm solid state lasers can be used. In order for lasing to occur, the absorption at that wavelength must be low and the emission line strong. Molecules must also not be lost too quickly to long lived triplet states which would destroy the lasing. Dye molecules are damaged over time by the high power pump light, and thus dyes have a finite lifetime. For a dye to lose 25% of its initial power can be as short as a few days, as in the case of Rhodamine 560, to several months, for Rhodamine 6G and 640. The difference between the absorption and emission band is called the Stokes shift. Dye with large Stoke shift allow for a broad wavelength tuning.

The dye is in suspended in a carrier liquid, typical Ethylene glycol. The dye must first be dissolved, however. The choice of solvents depends on the dye. Methanol is often used, but some dyes require other solvents. The dye must be well dissolved in the solvent with no visible trace of any particulates. Figure D.1.3 shows the effect of using Benzyl alcohol vs methanol for Rhodamine 560 Chloride. It should be noted that by contrast, R560 Perchlorate dissolved well in both Methanol and Benzyl alcohol. The choice of carrier liquid and solvent can be used to change the absorption and lasing wavelength and properties, including the quantum yield of the dye. The solvent should be viscous, and cooling the dye typically increases lasing power. The viscosity of Ethylene glycol is very sensitive to temperature, so keeping it cold is critical to reliable operation. A viscous liquid also allows the dye jet to be run at higher pressures without turbulence. The onset of turbulence occurs with large Reynolds number, which is lowered by higher viscosity. A turbulent jet will add noise to the laser
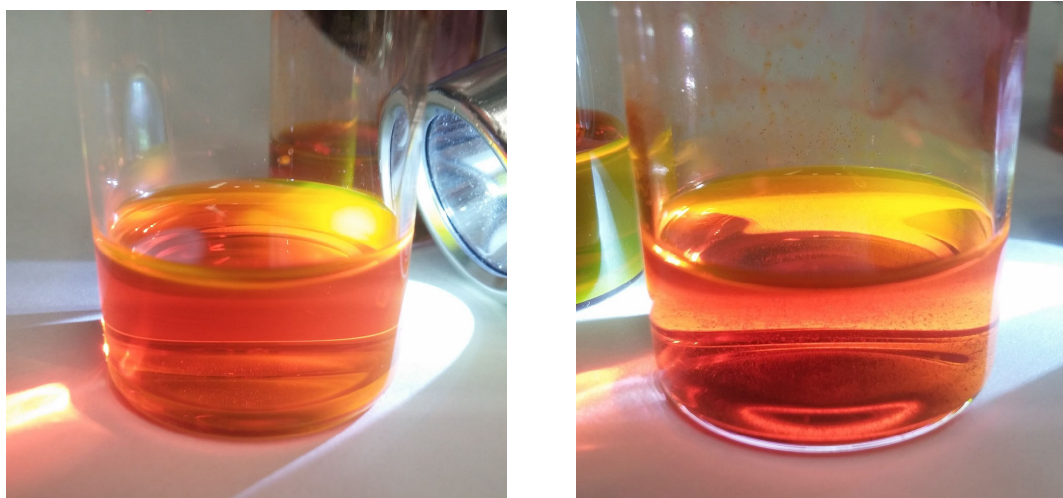
Figure D.1.3: R560 Chloride dissolved in Benzyl alcohol on the left; Very good, clear, and no particulates. On the right methanol was used; Not good, many particulates left.

and often make lasing unreliable.

The polarization of the pump light must be set to match that of the lasing cavity. The reason behind this is not at all obvious. The dye molecule can be modeled as an oscillating dipole, with the emission patter being a dipole [197]. The molecules in the ground state which are aligned such that their dipole moment matches the polarization of the pump light will be preferentially excited. Because the molecules are in a liquid rather than a gas, the molecules orientations change with Brownian motion. This drastically slows the rate at which molecules change orientation and thus molecules remain in the same orientation from the time they absorb a photon until they re-emit. Thus the emission of dye molecules in preferential in the same direction as the pump light.

The dye jet is typically operated in a pressure range of 5 to 10 bar depending on the nozzle and circulator used. We used the modified Radiant Dyes nozzles which allow for much higher pressure operation than the original Coherent nozzles, which are limited around 3 bar for non-turbulent operation. The dye jet should be flat with raised edges on either side. At a distance of around 3-6
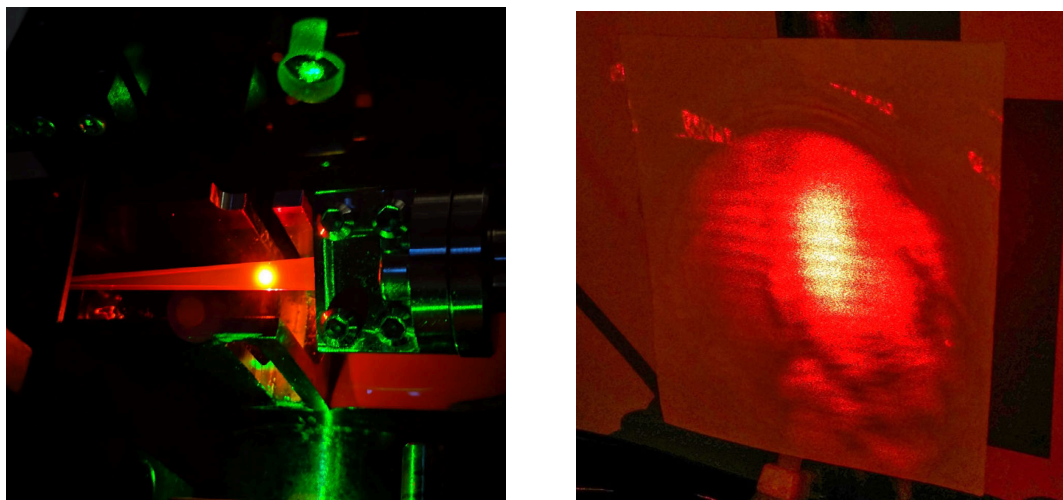
Figure D.1.4: Left: Typical dye jet with radiant dye nozzle. Right: Fringes from the dye jet when lasing backwards. These fringes should be stable.

inches, the sides should merge together. The pump laser should be focused onto the flat portion of the dye jet. There should be no streaks in the jet. Streaks are typically caused by blockages by small particulates in the nozzle. Dye which is left out can dry over time and crystallize. It is important to run dye lasers weekly, even when they are not in use. When lasing has been established, one can check the stability of the dye jet by flipping the orientation of the magnet on the optical diode. This will cause the laser to lase the opposite direction and project a spot onto the ceiling off of the dye jet, as shown in Figure D.1.4. since the dye jet should be interferometrically flat, fringes should be visible. If all is in order, these fringes should be stable. Oscillations/movement of these fringes indicate something is wrong with the dye jet, most likely due to the circulator. If the dye jet appears to have low pressure, this indicate the impedance to the jet is low. The filter having a clog is the most likely culprit. Air bubbles in the dye jet can be cause by a variety of things. The filter, whose job is primary to remove air bubbles, could be torn. There may be cavitation happening inside of the screw pump due to damaged parts or too high of a pressure. There could also be a leak in a connection on the input side to the pump, which would suck air in. Finally, if the return tube is not well aligned

bubbles can be formed from turbulence in this tube.

The absorption of the dye should be around 80-85%. One can alter the absorption and emission curve of dyes by pH tuning them. Adding a base, such as KOH, will shift the laser to lase at a longer wavelength by 5-10 nm, which adding an acid will shift the laser to shorter wavelength by 5-10 nm. In the Rhodamines, this large shift is due to a free COOH group, which in a polar solvent will undergo dissociation based on the pH to satisfy the acid-base equilibrium [196]. It should be noted that pH tuning can shorten the lifetime of the dye and affect the viscosity over time. Increasing the concentration of dye tends to shift the peak emission to longer wavelengths. (This effect is shown in Figure D.2.1 for Rhodamine 19.)

The focus of the pump laser should be slightly in front of the dye jet. If the focus is too far forward, this causes thermal lensing inside of the jet and causes instabilities. Stability can also be increased by moving the focus of the upper-fold mirror up away from the jet, making a smaller spot size on the output coupler. By looking at the expanded output mode of the laser, one can check the position of the pump focus. The output mode of the laser should be a very nice TEM 00 Gaussian mode. If the mode has a brighter center and is diffuse around, it may be unstable. This is due to the focus being too close to the jet. If a star shaped pattern around the output mode exists, then the focus is too far from the dye jet. Any mode other than this is most likely due to a dirty optic causing absorption.

D.1.1 TUNING THE 899/699 LOCK BOX

There are few adjustable potentiometers which can be tuned for optimal locking of the Coherent 899. Table D.1.1 gives an overview of the tuning process. For optimal locking performance, the submarine cavity should be properly aligned. Note, large fridges does not necessarily mean it is properly aligned. Make sure to also minimize the reference photodetector signal as much as possible while still maintaining fringes >1 V.

PCB	Control Box Settings	Trace (30 GHz)	Pot #	Comments
1A1	Thick Etalon Free Run Internal		R107	Football shape Make horizontal
1A3	Reference Cavity Zero Servo Internal		R7	5 Modes +5V Peak
1A4	Reference Cavity Free Run Internal		R51	Flat and Smooth Not jumps
1A5	Laser Power Free Run Internal		R56	Flat and Smooth Not jumps

Table D.1.1: 899 lock box tuning guide.

D.2 DYE CURVES

Figure D.2.1 shows the dye tuning curves for various dyes lasing from 540 to 660 nm for single frequency operation. All of these curves were measured with a 10 W 532 nm DPSS pump. These curves should serve as a guide to select the right dye. They are not absolute maximums; they have simple been achieved by me at some point in time. A useful resource for dye absorption and emission curves is the Kodak Laser Dye Handbook.
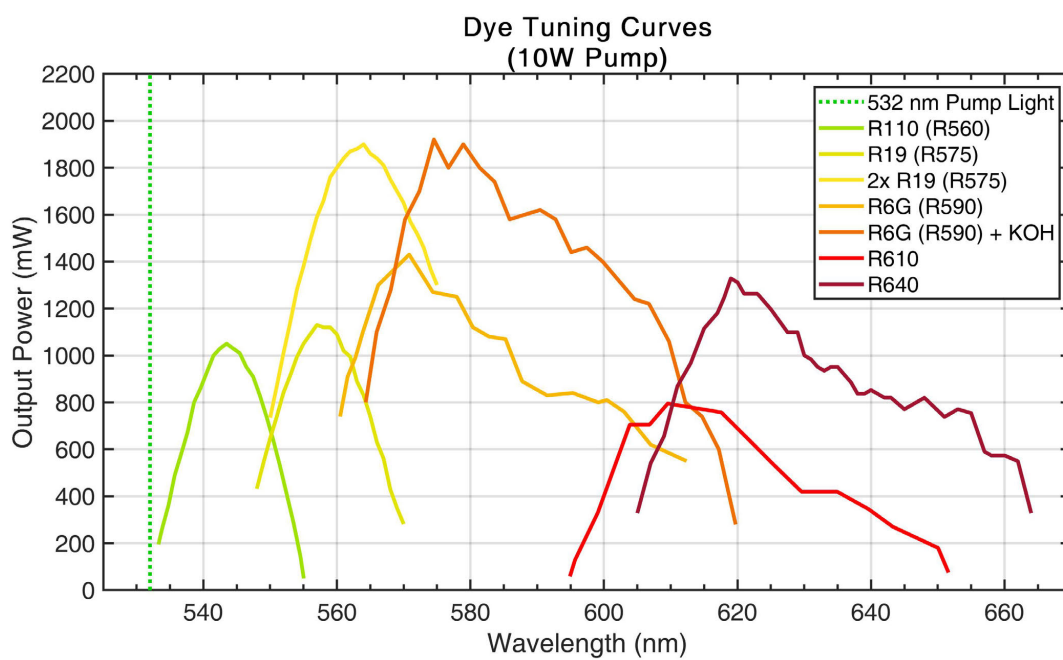
Figure D.2.1: Output power for single frequency operation with a 10 W 532 nm DPSS pump. These curves are not absolute maximums, they have simple been achieved by me at some point in time.

E

Experimental Control Software

The experiment is controlled with multiple programs on multiple computers. This is partly for historical reasons and partly out of necessity. An overview is shown in Figure E.0.1.

All of the experimental control is done with Cicero. Due to the fast 2 Hz rep rate, our version was modified to reduce the buffer generation time. The EMCCDs are controlled with MATLAB via the Andor SDK. The Matlab routine acquires the images, analyses which tweezers are occupied, and sends a data string to the USRP control computer. The USRP has a lookup table as for all
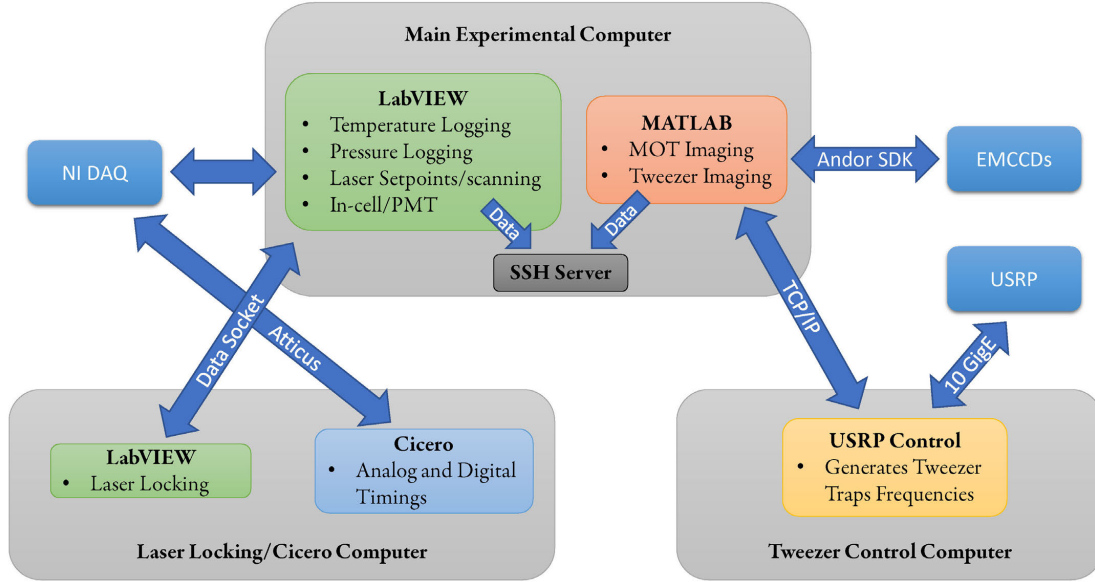
Figure E.0.1: Overview of the experimental control system

of the initial configures with pre-computed paths for rearrangement. At the moment, there is no communication between the USRP control software and Cicero, so the timing jitter (typically $\sim$ms) must be minimized to achieve reliable rearrangement. The USRP control software was originally written in the Lukin lab for their tweezers control. They graciously lent us their code which we modified for our experiment.

Figure E.0.2 shows the timing sequence of the experiential sequence and Figure E.0.3 shows the values and timings of the analog variables that are time dependent.
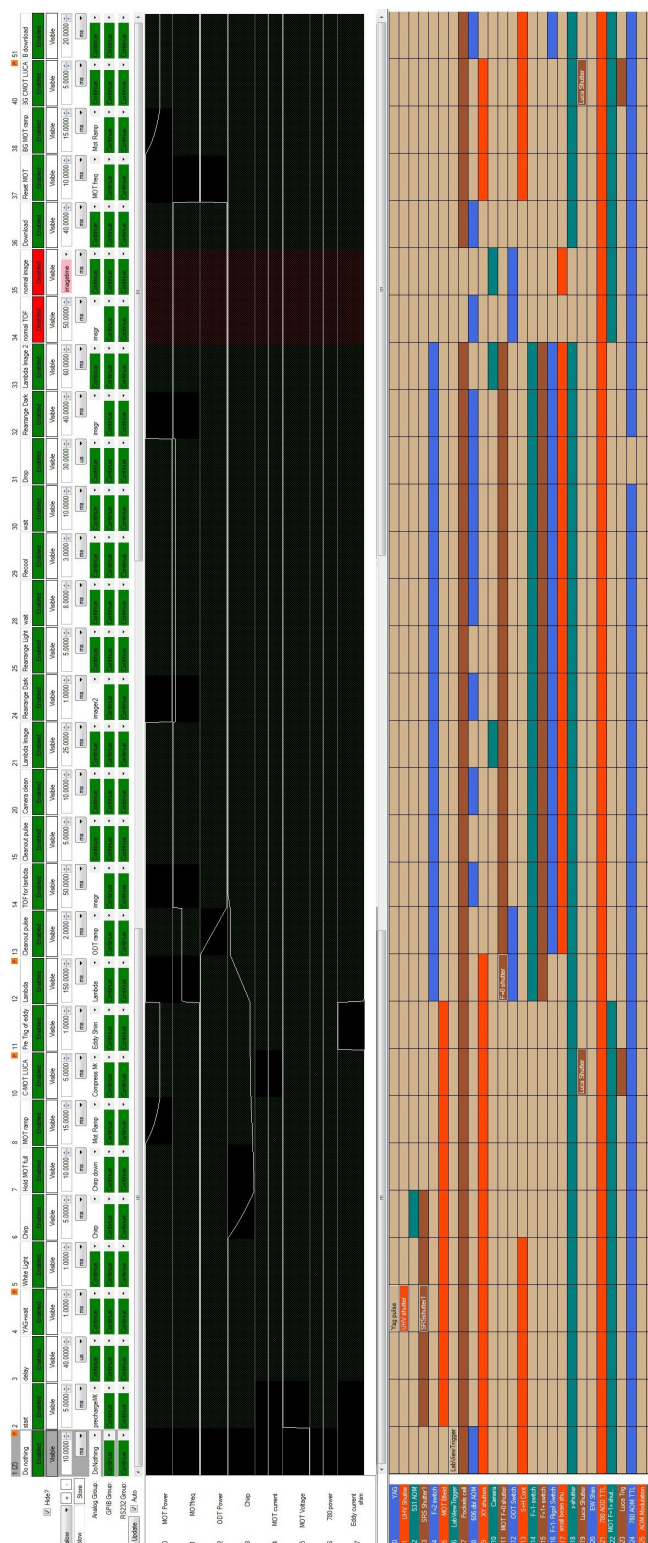
Figure E.0.2: Full timing sequence for measuring collisions in tweezers.
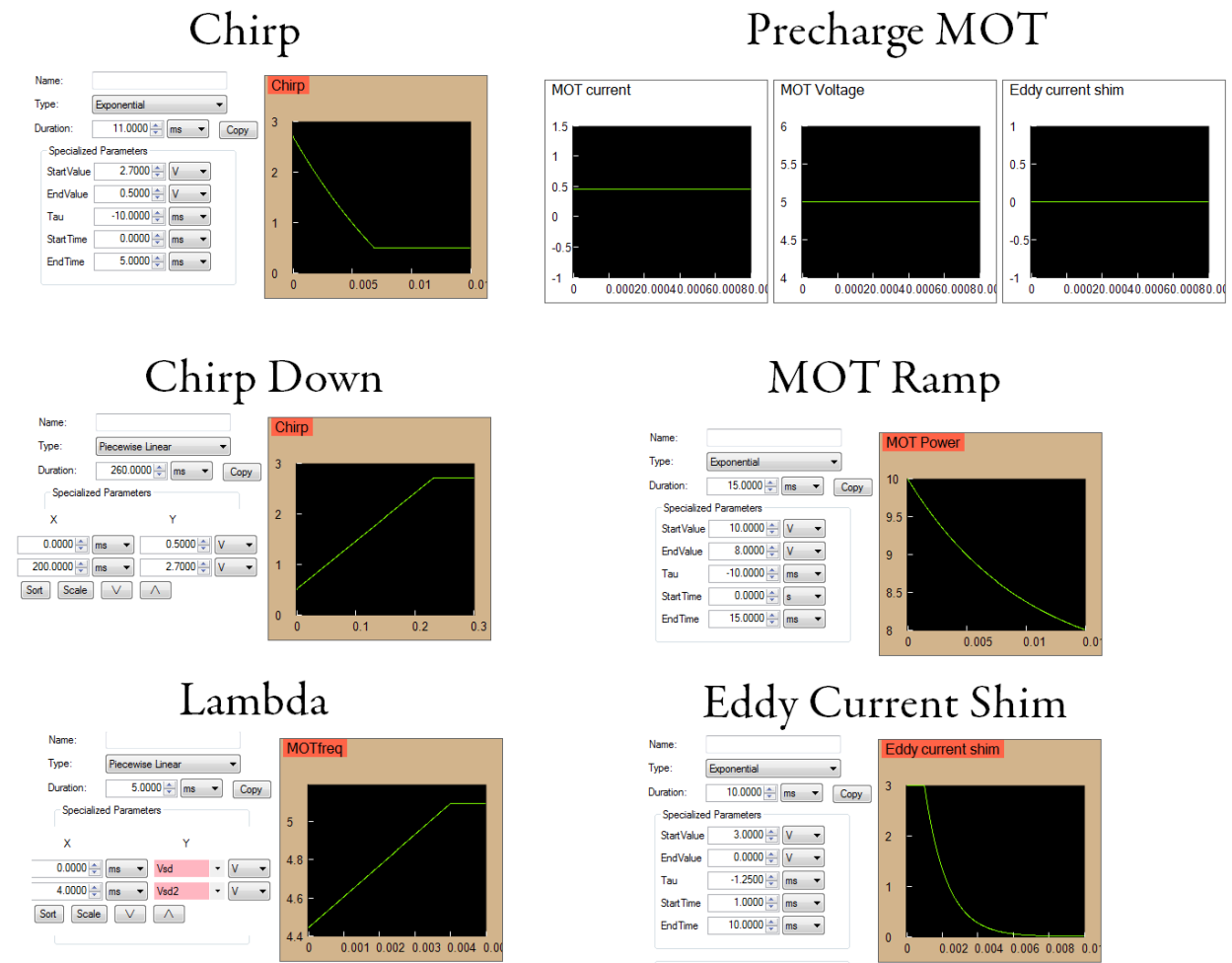
Figure E.0.3: Cicero analog variables.

References

[1] William D. Phillips. Nobel lecture: Laser cooling and trapping of neutral atoms. *Reviews of Modern Physics*, 70(3), 1998. doi: 10.1103/revmodphys.70.721.

[2] Andrew D. Ludlow, Martin M. Boyd, Jun Ye, E. Peik, and P. O. Schmidt. Optical atomic clocks. *Reviews of Modern Physics*, 87(2), 2015. doi: 10.1103/revmodphys.87.637.

[3] Immanuel Bloch, Jean Dalibard, and Sylvain Nascimbène. Quantum simulations with ultracold quantum gases. *Nature Physics*, 8(4), 2012. doi: 10.1038/nphys2259.

[4] William Stwalley, Roman Krems, and Bretislav Friedrich, editors. *Cold Molecules*. CRC Press, 2009. doi: 10.1201/9781420059045.

[5] Lincoln D Carr, David DeMille, Roman V Krems, and Jun Ye. Cold and ultracold molecules: science, technology and applications. *New Journal of Physics*, 11(5), 2009. doi: 10.1088/1367-2630/11/5/055049.

[6] Bretislav Friedrich and John M. Doyle. Why are cold molecules so hot? *ChemPhysChem*, 10(4), 2009. doi: 10.1002/cphc.200800577.

[7] Steven A. Moses, Jacob P. Covey, Matthew T. Miecnikowski, Deborah S. Jin, and Jun Ye. New frontiers for quantum gases of polar molecules. *Nature Physics*, 13(1), 2016. doi: 10.1038/nphys3985.

[8] John L. Bohn, Ana Maria Rey, and Jun Ye. Cold molecules: Progress in quantum engineering of chemistry and quantum matter. *Science*, 357(6355), 2017. doi: 10.1126/science.aam6299.

[9] A. Micheli, G. K. Brennen, and P. Zoller. A toolbox for lattice-spin models with polar molecules. *Nature Physics*, 2(5), 2006. doi: 10.1038/nphys287.

[10] H. P. Büchler, A. Micheli, and P. Zoller. Three-body interactions with cold polar molecules. *Nature Physics*, 3(10), 2007. doi: 10.1038/nphys678.

[11] G. Pupillo, A. Griessner, A. Micheli, M. Ortner, D.-W. Wang, and P. Zoller. Cold atoms and molecules in self-assembled dipolar lattices. *Physical Review Letters*, 100(5), 2008.

[12] D. DeMille. Quantum computation with trapped polar molecules. *Physical Review Letters*, 88 (6), 2002.

[13] S. F. Yelin, K. Kirby, and Robin Côté. Schemes for robust quantum computation with polar molecules. *Physical Review A*, 74(5), 2006. doi: 10.1103/physreva.74.050301.

[14] Mallikarjun Karra, Ketan Sharma, Bretislav Friedrich, Sabre Kais, and Dudley Herschbach. Prospects for quantum computing with an array of ultracold polar paramagnetic molecules. *The Journal of Chemical Physics*, 144(9), 2016. doi: 10.1063/1.4942928.

[15] Kang-Kuen Ni, Till Rosenband, and David D. Grimes. Dipolar exchange quantum logic gate with polar molecules. *Chemical Science*, 9(33), 2018. doi: 10.1039/c8sc02355g.

[16] Jacob A Blackmore, Luke Caldwell, Philip D Gregory, Elizabeth M Bridge, Rahul Sawant, Jesús Aldegunde, Jordi Mur-Petit, Dieter Jaksch, Jeremy M Hutson, B E Sauer, M R Tarbutt, and Simon L Cornish. Ultracold molecules for quantum simulation: rotational coherences in CaF and RbCs. *Quantum Science and Technology*, 4(1), 2018.

[17] A. André, D. DeMille, J. M. Doyle, M. D. Lukin, S. E. Maxwell, P. Rabl, R. J. Schoelkopf, and P. Zoller. A coherent all-electrical interface between polar molecules and mesoscopic superconducting resonators. *Nature Physics*, 2(9), 2006. doi: 10.1038/nphys386.

[18] R. V. Krems. Cold controlled chemistry. *Physical Chemistry Chemical Physics*, 10(28), 2008. doi: 10.1039/b802322k.

[19] N. Balakrishnan. Perspective: Ultracold molecules and the dawn of cold controlled chemistry. *The Journal of Chemical Physics*, 145(15), 2016. doi: 10.1063/1.4964096.

[20] Jun Ye, Sebastian Blatt, Martin M. Boyd, Seth M. Foreman, Eric R. Hudson, Tetsuya Ido, Benjamin Lev, Andrew D. Ludlow, Brian C. Sawyer, Benjamin Stuhl, and Tanya Zelevinsky. Precision measurement based on ultracold atoms and cold molecules. In *AIP Conference Proceedings*. AIP, 2006. doi: 10.1063/1.2400637.

[21] Matthew T. Hummon, Timur V. Tscherbul, Jacek Kłos, Hsin-I Lu, Edem Tsikata, Wesley C. Campbell, Alexander Dalgarno, and John M. Doyle. Cold N NH collisions in a magnetic trap. *Physical Review Letters*, 106(5), 2011. doi: 10.1103/physrevlett.106.053201.

[22] J. F. E. Croft, N. Balakrishnan, and B. K. Kendrick. Long-lived complexes and signatures of chaos in ultracold K2 Rb collisions. *Physical Review A*, 96(6), 2017. doi: 10.1103/physreva.96.062707.

[23] Mikhail Lemeshko, Roman V. Krems, John M. Doyle, and Sabre Kais. Manipulation of molecules with electromagnetic fields. *Molecular Physics*, 111(12-13), 2013. doi: 10.1080/00268976.2013.813595.

[24] Goulven Quéméner and John L. Bohn. Shielding $^2\Sigma$ ultracold dipolar molecular collisions with electric fields. *Physical Review A*, 2015. doi: 10.1103/PhysRevA.93.012704.

[25] Jie Cui and Roman V. Krems. Elastic and inelastic collisions of $^2\Sigma$ molecules in a magnetic field. *Physical Review A*, 2013. doi: 10.1103/PhysRevA.88.042705.

[26] A. V. Gorshkov, P. Rabl, G. Pupillo, A. Micheli, P. Zoller, M. D. Lukin, and H. P. Büchler. Suppression of inelastic collisions between polar molecules with a repulsive shield. *Physical Review Letters*, 101(7), 2008. doi: 10.1103/physrevlett.101.073201.

[27] Jongseok Lim, Matthew D. Frye, Jeremy M. Hutson, and M. R. Tarbutt. Modeling sympathetic cooling of molecules by ultracold atoms. *Physical Review A*, 92(5), 2015. doi: 10.1103/physreva.92.053419.

[28] M. A. Baranov, M. Dalmonte, G. Pupillo, and P. Zoller. Condensed matter theory of dipolar quantum gases. *Chemical Reviews*, 112(9), 2012. doi: 10.1021/cr2003568.

[29] Bryce Gadway and Bo Yan. Strongly interacting ultracold polar molecules. *Journal of Physics B: Atomic, Molecular and Optical Physics*, 49(15), 2016. doi: 10.1088/0953-4075/49/15/152002.

[30] M. L. Wall, K. R. A. Hazzard, and A. M. Rey. Quantum magnetism with ultracold molecules. In *From Atomic to Mesoscale*. World Scientific, 2015. doi: 10.1142/9789814678704_0001.

[31] Wolfgang Lechner, Hans-Peter Büchler, and Peter Zoller. Role of quantum fluctuations in the hexatic phase of cold polar molecules. *Physical Review Letters*, 112(25), 2014. doi: 10.1103/physrevlett.112.255301.

[32] Wolfgang Lechner and Peter Zoller. From classical to quantum glasses with ultracold polar molecules. *Physical Review Letters*, 111(18), 2013. doi: 10.1103/physrevlett.111.185306.

[33] M Ortner, A Micheli, G Pupillo, and P Zoller. Quantum simulations of extended hubbard models with dipolar crystals. *New Journal of Physics*, 11(5), 2009. doi: 10.1088/1367-2630/11/5/055045.

[34] B. Capogrosso-Sansone, C. Trefzger, M. Lewenstein, P. Zoller, and G. Pupillo. Quantum phases of cold polar molecules in 2D optical lattices. *Physical Review Letters*, 104(12), 2010. doi: 10.1103/physrevlett.104.125301.

[35] H. P. Büchler, E. Demler, M. Lukin, A. Micheli, N. Prokof'ev, G. Pupillo, and P. Zoller. Strongly correlated 2D quantum phases with cold polar molecules: Controlling the shape of the interaction potential. *Physical Review Letters*, 98(6), 2007.

[36] Mikhail Lemeshko, Roman V. Krems, and Hendrik Weimer. Nonadiabatic preparation of spin crystals with ultracold polar molecules. *Physical Review Letters*, 109(3), 2012. doi: 10.1103/physrevlett.109.035301.

[37] N. Y. Yao, C. R. Laumann, A. V. Gorshkov, S. D. Bennett, E. Demler, P. Zoller, and M. D. Lukin. Topological flat bands from dipolar spin systems. *Physical Review Letters*, 109(26), 2012. doi: 10.1103/physrevlett.109.266804.

[38] M. Ortner, Y. L. Zhou, P. Rabl, and P. Zoller. Quantum information processing in self-assembled crystals of cold polar molecules. *Quantum Information Processing*, 10(6), 2011. doi: 10.1007/s11128-011-0301-7.

[39] Jing Zhu, Sabre Kais, Qi Wei, Dudley Herschbach, and Bretislav Friedrich. Implementation of quantum logic gates using polar molecules in pendular states. *The Journal of Chemical Physics*, 138(2), 2013. doi: 10.1063/1.4774058.

[40] Peter W. Shor. Scheme for reducing decoherence in quantum computer memory. *Physical Review A*, 52(4), 1995. doi: 10.1103/physreva.52.r2493.

[41] Daniel Barredo, Sylvain de Léséleuc, Vincent Lienhard, Thierry Lahaye, and Antoine Browaeys. An atom-by-atom assembler of defect-free arbitrary two-dimensional atomic arrays. *Science*, 354(6315), 2016. doi: 10.1126/science.aah3778.

[42] Manuel Endres, Hannes Bernien, Alexander Keesling, Harry Levine, Eric R. Anschuetz, Alexandre Krajenbrink, Crystal Senko, Vladan Vuletic, Markus Greiner, and Mikhail D. Lukin. Atom-by-atom assembly of defect-free one-dimensional cold atom arrays. *Science*, 354(6315), 2016. doi: 10.1126/science.aah3752.

[43] Hannes Bernien, Sylvain Schwartz, Alexander Keesling, Harry Levine, Ahmed Omran, Hannes Pichler, Soonwon Choi, Alexander S. Zibrov, Manuel Endres, Markus Greiner, Vladan Vuletić, and Mikhail D. Lukin. Probing many-body dynamics on a 51-atom quantum simulator. *Nature*, 551(7682), 2017. doi: 10.1038/nature24622.

[44] David DeMille, John M. Doyle, and Alexander O. Sushkov. Probing the frontiers of particle physics with tabletop-scale experiments. *Science*, 357(6355), 2017. doi: 10.1126/science.aal3003.

[45] M. S. Safronova, D. Budker, D. DeMille, Derek F. Jackson Kimball, A. Derevianko, and Charles W. Clark. Search for new physics with atoms and molecules. *Reviews of Modern Physics*, 90(2), 2018. doi: 10.1103/revmodphys.90.025008.

[46] B. C. Regan, Eugene D. Commins, Christian J. Schmidt, and David DeMille. New limit on the electron electric dipole moment. *Physical Review Letters*, 88(7), 2002. doi: 10.1103/physrevlett.88.071805.

[47] ACME Collaboration. Order of magnitude smaller limit on the electric dipole moment of the electron. *Science*, 343(6168), 2014.

[48] ACME Collaboration. Improved limit on the electric dipole moment of the electron. *Nature*, 562(7727), 2018. doi: 10.1038/s41586-018-0599-8.

[49] William B. Cairncross, Daniel N. Gresh, Matt Grau, Kevin C. Cossel, Tanya S. Roussy, Yiqi Ni, Yan Zhou, Jun Ye, and Eric A. Cornell. Precision measurement of the electron's electric dipole moment using trapped molecular ions. *Physical Review Letters*, 119(15), 2017. doi: 10.1103/physrevlett.119.153001.

[50] Cari Cesarotti, Qianshu Lu, Yuichiro Nakai, Aditya Parikh, and Matthew Reece. Interpreting the electron EDM constraint. *Journal of High Energy Physics*, 2019(5), 2019. doi: 10.1007/jhep05(2019)059.

[51] Ivan Kozyryev and Nicholas R. Hutzler. Precision measurement of time-reversal symmetry violation with laser-cooled polyatomic molecules. *Physical Review Letters*, 119(13), 2017.

[52] Paul Jansen, Hendrick L. Bethlem, and Wim Ubachs. Perspective: Tipping the scales: Search for drifting constants from molecular spectra. *The Journal of Chemical Physics*, 140(1), 2014. doi: 10.1063/1.4853735.

[53] D. DeMille, S. Sainis, J. Sage, T. Bergeman, S. Kotochigova, and E. Tiesinga. Enhanced sensitivity to variation of m_e/m_p in molecular spectra. *Physical Review Letters*, 100(4), 2008. doi: 10.1103/physrevlett.100.043202.

[54] Marko Gacesa and Robin Côté. Photoassociation of ultracold molecules near a feshbach resonance as a probe of the electron–proton mass ratio variation. *Journal of Molecular Spectroscopy*, 300, 2014. doi: 10.1016/j.jms.2014.03.005.

[55] M R Tarbutt, B E Sauer, J J Hudson, and E A Hinds. Design for a fountain of YbF molecules to measure the electron's electric dipole moment. *New Journal of Physics*, 15(5), 2013. doi: 10.1088/1367-2630/15/5/053034.

[56] K.-K. Ni, S. Ospelkaus, M. H. G. de Miranda, A. Pe'er, B. Neyenhuis, J. J. Zirbel, S. Kotochigova, P. S. Julienne, D. S. Jin, and J. Ye. A high phase-space-density gas of polar molecules. *Science*, 322(5899), 2008. doi: 10.1126/science.1163861.

[57] Luigi De Marco, Giacomo Valtolina, Kyle Matsuda, William G. Tobias, Jacob P. Covey, and Jun Ye. A degenerate fermi gas of polar molecules. *Science*, 363(6429), 2019.

[58] Jee Woo Park, Sebastian A. Will, and Martin W. Zwierlein. Ultracold dipolar gas of fermionic Na23K40 molecules in their absolute ground state. *Physical Review Letters*, 114(20), 2015. doi: 10.1103/physrevlett.114.205302.

[59] Peter K. Molony, Philip D. Gregory, Zhonghua Ji, Bo Lu, Michael P. Köppinger, C. Ruth Le Sueur, Caroline L. Blackley, Jeremy M. Hutson, and Simon L. Cornish. Creation of Ultra-cold Rb87Cs133 molecules in the rovibrational ground state. *Physical Review Letters*, 113(25), 2014. doi: 10.1103/physrevlett.113.255301.

[60] Mingyang Guo, Bing Zhu, Bo Lu, Xin Ye, Fudong Wang, Romain Vexiau, Nadia Bouloufa-Maafa, Goulven Quéméner, Olivier Dulieu, and Dajun Wang. Creation of an ultracold gas of ground-state dipolar Na23 Rb87 molecules. *Physical Review Letters*, 116(20), 2016. doi: 10.1103/physrevlett.116.205303.

[61] Timur M. Rvachov, Hyungmok Son, Ariel T. Sommer, Sepehr Ebadi, Juliana J. Park, Martin W. Zwierlein, Wolfgang Ketterle, and Alan O. Jamison. Long-lived ultracold molecules with electric and magnetic dipole moments. *Physical Review Letters*, 119(14), 2017. doi: 10.1103/physrevlett.119.143001.

[62] Juris Ulmanis, Johannes Deiglmayr, Marc Repp, Roland Wester, and Matthias Weidemüller. Ultracold molecules formed by photoassociation: Heteronuclear dimers, inelastic collisions, and interactions with ultrashort laser pulses. *Chemical Reviews*, 112(9), 2012. doi: 10.1021/cr300215h.

[63] G. Savard, St. Becker, G. Bollen, H.-J. Kluge, R.B. Moore, Th. Otto, L. Schweikhard, H. Stolzenberg, and U. Wiess. A new cooling technique for heavy ions in a penning trap. *Physics Letters A*, 158(5), 1991. doi: 10.1016/0375-9601(91)91008-2.

[64] Nicholas R. Hutzler, Hsin-I Lu, and John M. Doyle. The buffer gas beam: An intense, cold, and slow source for atoms and molecules. *Chemical Reviews*, 112(9), 2012. doi: 10.1021/cr200362u.

[65] Hendrick L. Bethlem, Giel Berden, and Gerard Meijer. Decelerating neutral dipolar molecules. *Physical Review Letters*, 83(8), 1999. doi: 10.1103/physrevlett.83.1558.

[66] Andreas Osterwalder, Samuel A. Meek, Georg Hammer, Henrik Haak, and Gerard Meijer. Deceleration of neutral molecules in macroscopic traveling traps. *Physical Review A*, 81(5), 2010. doi: 10.1103/physreva.81.051401.

[67] Nitzan Akerman, Michael Karpov, Liron David, Etay Lavert-Ofir, Julia Narevicius, and Edvardas Narevicius. Simultaneous deceleration of atoms and molecules in a supersonic beam. *New Journal of Physics*, 17(6), 2015. doi: 10.1088/1367-2630/17/6/065015.

[68] N. J. Fitch and M. R. Tarbutt. Principles and design of a Zeeman-Sisyphus decelerator for molecular beams. *ChemPhysChem*, 17(22), 2016. doi: 10.1002/cphc.201600656.

[69] Hsin-I Lu, Ivan Kozyryev, Boerge Hemmerling, Julia Piskorski, and John M. Doyle. Magnetic trapping of molecules via optical loading and magnetic slowing. *Physical Review Letters*, 112(11), 2014. doi: 10.1103/physrevlett.112.113006.

[70] S. Chervenkov, X. Wu, J. Bayerl, A. Rohlfes, T. Gantner, M. Zeppenfeld, and G. Rempe. Continuous centrifuge decelerator for polar molecules. *Physical Review Letters*, 112(1), 2014. doi: 10.1103/physrevlett.112.013001.

[71] Xing Wu, Thomas Gantner, Manuel Koller, Martin Zeppenfeld, Sotir Chervenkov, and Gerhard Rempe. A cryofuge for cold-collision experiments with slow polar molecules. *Science*, 358(6363), 2017. doi: 10.1126/science.aan3029.

[72] Mehdi Hamamda, Pierre Pillet, Hans Lignier, and Daniel Comparat. Universal deceleration of highly polar molecules. *New Journal of Physics*, 17(4), 2015. doi: 10.1088/1367-2630/17/4/045018.

[73] Mark G. Raizen, Dmitry Budker, Simon M. Rochester, Julia Narevicius, and Edvardas Narevicius. Magneto-optical cooling of atoms. *Optics Letters*, 39(15), 2014. doi: 10.1364/ol.39.004502.

[74] Martin Zeppenfeld, Barbara G. U. Englert, Rosa Glöckner, Alexander Prehn, Manuel Mielenz, Christian Sommer, Laurens D. van Buuren, Michael Motsch, and Gerhard Rempe. Sisyphus cooling of electrically trapped polyatomic molecules. *Nature*, 491(7425), 2012. doi: 10.1038/nature11595.

[75] M. S. Elioff. Subkelvin cooling NO molecules via "billiard-like" collisions with argon. *Science*, 302(5652), 2003. doi: 10.1126/science.1090679.

[76] Hyungmok Son, Juliana J. Park, Wolfgang Ketterle, and Alan O. Jamison. Observation of collisional cooling of ultracold molecules. 2019.

[77] T.W. Hänsch and A.L. Schawlow. Cooling of gases by laser radiation. *Optics Communications*, 13(1), 1975. doi: 10.1016/0030-4018(75)90159-5.

[78] D.J. Wineland and Hans Dehmelt. Proposed 10^{-14} $\Delta\nu/\nu$ laser fluorescence spectroscopy on Tl + mono-ion oscillator. In *Bulletin of the American Physical Society*, volume 20, 1975.

[79] D. J. Wineland, R. E. Drullinger, and F. L. Walls. Radiation-pressure cooling of bound resonant absorbers. *Physical Review Letters*, 40(25), 1978. doi: 10.1103/physrevlett.40.1639.

[80] W. Neuhauser, M. Hohenstatt, P. Toschek, and H. Dehmelt. Optical-sideband cooling of visible atom cloud confined in parabolic well. *Physical Review Letters*, 41(4), 1978. doi: 10.1103/physrevlett.41.233.

[81] M. H. Anderson, J. R. Ensher, M. R. Matthews, C. E. Wieman, and E. A. Cornell. Observation of Bose-Einstein condensation in a dilute atomic vapor. *Science*, 269(5221), 1995. doi: 10.1126/science.269.5221.198.

[82] K. B. Davis, M. O. Mewes, M. R. Andrews, N. J. van Druten, D. S. Durfee, D. M. Kurn, and W. Ketterle. Bose-Einstein condensation in a gas of sodium atoms. *Physical Review Letters*, 75 (22), 1995. doi: 10.1103/physrevlett.75.3969.

[83] C. C. Bradley, C. A. Sackett, and R. G. Hulet. Bose-Einstein condensation of lithium: Observation of limited condensate number. *Physical Review Letters*, 78(6), 1997. doi: 10.1103/physrevlett.78.985.

[84] M. D. Rosa. Laser-cooling molecules. *The European Physical Journal D*, 31(2), 2004. doi: 10.1140/epjd/e2004-00167-2.

[85] Benjamin K. Stuhl, Brian C. Sawyer, Dajun Wang, and Jun Ye. Magneto-optical trap for polar molecules. *Physical Review Letters*, 101(24), 2008.

[86] E. S. Shuman, J. F. Barry, and D. DeMille. Laser cooling of a diatomic molecule. *Nature*, 467 (7317), 2010. doi: 10.1038/nature09443.

[87] Matthew T. Hummon, Mark Yeo, Benjamin K. Stuhl, Alejandra L. Collopy, Yong Xia, and Jun Ye. 2D magneto-optical trapping of diatomic molecules. *Phys. Rev. Lett.*, 110, 2013.

[88] Eunmi Chae, Loic Anderegg, Benjamin L Augenbraun, Aakash Ravi, Boerge Hemmerling, Nicholas R Hutzler, Alejandra L Collopy, Jun Ye, Wolfgang Ketterle, and John M Doyle. One-dimensional magneto-optical compression of a cold CaF molecular beam. *New Journal of Physics*, 19(3), 2017. doi: 10.1088/1367-2630/aa6470.

[89] J F Barry, E S Shuman, E B Norrgard, and D Demille. Laser radiation pressure slowing of a molecular beam. *Phys. Rev. Lett.*, 108, 2012.

[90] Boerge Hemmerling, Eunmi Chae, Aakash Ravi, Loic Anderegg, Garrett K Drayna, Nicholas R Hutzler, Alejandra L Collopy, Jun Ye, Wolfgang Ketterle, and John M Doyle. Laser slowing of CaF molecules to near the capture velocity of a molecular MOT. *J. Phys. B: At. Mol. Opt. Phys.*, 49, 2016.

[91] Valentina Zhelyazkova, Anne Cournol, Thomas E Wall, Aki Matsushima, Jonathan J Hudson, EA Hinds, MR Tarbutt, and BE Sauer. Laser cooling and slowing of CaF molecules. *Physical Review A*, 89(5), 2014.

[92] Ivan Kozyryev, Louis Baum, Kyle Matsuda, Benjamin L. Augenbraun, Loic Anderegg, Alexander P. Sedlack, and John M. Doyle. Sisyphus laser cooling of a polyatomic molecule. *Physical Review Letters*, 118(17), 2017. doi: 10.1103/physrevlett.118.173201.

[93] J. F. Barry, D. J. McCarron, E. B. Norrgard, M. H. Steinecker, and D. DeMille. Magneto-optical trapping of a diatomic molecule. *Nature*, 512(7514), 2014. doi: 10.1038/nature13634.

[94] DJ McCarron, EB Norrgard, MH Steinecker, and D DeMille. Improved magneto–optical trapping of a diatomic molecule. *New J. Phys.*, 17(3), 2015.

[95] EB Norrgard, DJ McCarron, MH Steinecker, MR Tarbutt, and D DeMille. Sub-millikelvin dipolar molecules in a radio-frequency magneto-optical trap. *Phys. Rev. Lett.*, 116(6), 2016.

[96] Matthew H. Steinecker, Daniel J. McCarron, Yuqi Zhu, and David DeMille. Improved radio-frequency magneto-optical trap of SrF molecules. *ChemPhysChem*, 17(22), 2016. doi: 10.1002/cphc.201600967.

[97] S. Truppe, H. J. Williams, M. Hambach, L. Caldwell, N. J. Fitch, E. A. Hinds, B. E. Sauer, and M. R. Tarbutt. Molecules cooled below the doppler limit. *Nature Physics*, 13(12), 2017. doi: 10.1038/nphys4241.

[98] Loïc Anderegg, Benjamin L. Augenbraun, Eunmi Chae, Boerge Hemmerling, Nicholas R. Hutzler, Aakash Ravi, Alejandra Collopy, Jun Ye, Wolfgang Ketterle, and John M. Doyle. Radio frequency magneto-optical trapping of CaF with high density. *Physical Review Letters*, 119(10), 2017.

[99] H J Williams, S Truppe, M Hambach, L Caldwell, N J Fitch, E A Hinds, B E Sauer, and M R Tarbutt. Characteristics of a magneto-optical trap of molecules. *New Journal of Physics*, 19(11), 2017. doi: 10.1088/1367-2630/aa8e52.

[100] Alejandra L. Collopy, Shiqian Ding, Yewei Wu, Ian A. Finneran, Loïc Anderegg, Benjamin L. Augenbraun, John M. Doyle, and Jun Ye. 3D magneto-optical trap of yttrium monoxide. *Physical Review Letters*, 121(21), 2018.

[101] Jonathan D. Weinstein, Robert deCarvalho, Thierry Guillet, Bretislav Friedrich, and John M. Doyle. Magnetic trapping of calcium monohydride molecules at millikelvin temperatures. *Nature*, 395(6698), 1998. doi: 10.1038/25949.

[102] H. J. Williams, L. Caldwell, N. J. Fitch, S. Truppe, J. Rodewald, E. A. Hinds, B. E. Sauer, and M. R. Tarbutt. Magnetic trapping and coherent control of laser-cooled molecules. *Physical Review Letters*, 120(16), 2018.

[103] D. J. McCarron, M. H. Steinecker, Y. Zhu, and D. DeMille. Magnetic trapping of an ultracold gas of polar molecules. *Physical Review Letters*, 121(1), 2018.

[104] Loïc Anderegg, Lawrence W. Cheuk, Yicheng Bao, Sean Burchesky, Wolfgang Ketterle, Kang-Kuen Ni, and John M. Doyle. An optical tweezer array of ultracold molecules. *Science*, 365(6458), 2019. doi: 10.1126/science.aax1265.

[105] D. DeMille, D. R. Glenn, and J. Petricka. Microwave traps for cold polar molecules. *The European Physical Journal D*, 31(2), 2004. doi: 10.1140/epjd/e2004-00163-6.

[106] D P Dunseith, S Truppe, R J Hendricks, B E Sauer, E A Hinds, and M R Tarbutt. A high quality, efficiently coupled microwave cavity for trapping cold molecules. *Journal of Physics B: Atomic, Molecular and Optical Physics*, 48(4), 2015. doi: 10.1088/0953-4075/48/4/045001.

[107] S. C. Wright, T. E. Wall, and M. R. Tarbutt. Microwave trap for atoms and molecules. 2019.

[108] Richard P. Feynman. Simulating physics with computers. *International Journal of Theoretical Physics*, 21(6-7), 1982. doi: 10.1007/bf02650179.

[109] J. I. Cirac and P. Zoller. Quantum computations with cold trapped ions. *Physical Review Letters*, 74(20), 1995.

[110] D. J. Wineland, C. Monroe, W. M. Itano, B. E. King, D. Leibfried, C. Myatt, and C. Wood. Trapped-ion quantum simulator. *Physica Scripta*, T76(1), 1998. doi: 10.1238/physica.topical. 076a00147.

[111] R. Blatt and C. F. Roos. Quantum simulations with trapped ions. *Nature Physics*, 8(4), 2012. doi: 10.1038/nphys2252.

[112] M. H. Devoret and R. J. Schoelkopf. Superconducting circuits for quantum information: An outlook. *Science*, 339(6124), 2013. doi: 10.1126/science.1231930.

[113] Markus Greiner and Simon Fölling. Condensed-matter physics: Optical lattices. *Nature*, 453 (7196), 2008. doi: 10.1038/453736a.

[114] Christian Gross and Immanuel Bloch. Quantum simulations with ultracold atoms in optical lattices. *Science*, 357(6355), 2017. doi: 10.1126/science.aal3837.

[115] M. Saffman, T. G. Walker, and K. Mølmer. Quantum information with rydberg atoms. *Reviews of Modern Physics*, 82(3), 2010. doi: 10.1103/revmodphys.82.2313.

[116] Waseem S. Bakr, Jonathon I. Gillen, Amy Peng, Simon Fölling, and Markus Greiner. A quantum gas microscope for detecting single atoms in a hubbard-regime optical lattice. *Nature*, 462 (7269), 2009. doi: 10.1038/nature08482.

[117] P.S. Julienne. Cold binary atomic collisions in a light field. *Journal of Research of the National Institute of Standards and Technology*, 101(4), 1996. doi: 10.6028/jres.101.050.

[118] D. Frese, B. Ueberholz, S. Kuhr, W. Alt, D. Schrader, V. Gomer, and D. Meschede. Single atoms in an optical dipole trap: Towards a deterministic source of cold atoms. *Physical Review Letters*, 85(18), 2000. doi: 10.1103/physrevlett.85.3777.

[119] A. Fuhrmanek, R. Bourgain, Y. R. P. Sortais, and A. Browaeys. Light-assisted collisions between a few cold atoms in a microscopic dipole trap. *Physical Review A*, 85(6), 2012.

[120] Y H Fung and M F Andersen. Efficient collisional blockade loading of a single atom into a tight microtrap. *New Journal of Physics*, 17(7), 2015. doi: 10.1088/1367-2630/17/7/073011.

[121] N. Schlosser, G. Reymond, and P. Grangier. Collisional blockade in microscopic optical dipole traps. *Physical Review Letters*, 89(2), 2002.

[122] John M. Brown and Alan Carrington. *Rotational Spectroscopy of Diatomic Molecules*. Cambridge University Press, 2003. doi: 10.1017/cbo9780511814808.

[123] Charles Jean Joachain Brian H. Bransden. *Physics of Atoms and Molecules*. Prentice Hall, 2003. ISBN 058235692X.

[124] W. Gordy and R. L. Cook. *Techniques of Chemistry, Microwave Molecular Spectra (Volume 18)*. Wiley-Interscience, 1984. ISBN 0-471-08681-9.

[125] N. Vanhaecke and O. Dulieu. Precision measurements with polar molecules: the role of the black body radiation. *Molecular Physics*, 105(11-12), 2007. doi: 10.1080/00268970701466261.

[126] Stefan Yoshi Buhmann, M. R. Tarbutt, Stefan Scheel, and E. A. Hinds. Surface-induced heating of cold polar molecules. *Physical Review A*, 78(5), 2008. doi: 10.1103/physreva.78.052901.

[127] Eunmi Chae. *Laser Slowing of CaF Molecules and Progress towards a Dual-MOT for Li and CaF*. PhD thesis, Harvard University, 2015.

[128] Rudolf Grimm, Matthias Weidemüller, and Yurii B. Ovchinnikov. Optical dipole traps for neutral atoms. In *Advances In Atomic, Molecular, and Optical Physics*. Elsevier, 2000. doi: 10.1016/s1049-250x(08)60186-x.

[129] C.M. Gittins, N.A. Harris, R.W. Field, J. Verges, C. Effantin, A. Bernard, J. Dincan, W.E. Ernst, P. Bundgen, and B. Engels. Analysis and deperturbation of the c2Π and d2Σ+ states of caf. *Journal of Molecular Spectroscopy*, 161(1), 1993. ISSN 0022-2852. doi: https://doi.org/10.1006/jmsp.1993.1236.

[130] Albert G. Tobin, Douglas W. Sedgley, Thomas H. Batzer, and Wayne R. Call. Evaluation of charcoal sorbents for helium cryopumping in fusion reactors. *Journal of Vacuum Science & Technology A: Vacuum, Surfaces, and Films*, 5(1), 1987. doi: 10.1116/1.574141.

[131] S. Truppe, M. Hambach, S. M. Skoff, N. E. Bulleid, J. S. Bumby, R. J. Hendricks, E. A. Hinds, B. E. Sauer, and M. R. Tarbutt. A buffer gas beam source for short, intense and slow molecular pulses. *Journal of Modern Optics*, 65(5-6), 2017. doi: 10.1080/09500340.2017.1384516.

[132] E. Verdasco, V. Saez Rabanos, F. J. Aoiz, and A. Gonzalez Urena. Chemiluminescence from the calcium ca sulfur hexafluoride reaction: absolute cross section, photon yields, and electronic branching. *The Journal of Physical Chemistry*, 91(8), 1987. doi: 10.1021/j100292a018.

[133] *Selectivity in Chemical Reactions.* Springer Netherlands, 2011. ISBN 940107870X.

[134] Alejandra Collopy. *A Three-Dimensional MOT of YO Towards Narrow-Line Cooling.* PhD thesis, University of Colorado, 2018.

[135] William D. Phillips and Harold Metcalf. Laser deceleration of an atomic beam. *Physical Review Letters*, 48(9), 1982. doi: 10.1103/physrevlett.48.596.

[136] M Petzold, P Kaebert, P Gersema, M Siercke, and S Ospelkaus. A Zeeman slower for diatomic molecules. *New Journal of Physics*, 20(4), 2018. doi: 10.1088/1367-2630/aab9f5.

[137] M. Petzold, P. Kaebert, P. Gersema, T. Poll, N. Reinhardt, M. Siercke, and S. Ospelkaus. Type-II Zeeman slowing: Characterization and comparison to conventional radiative beam-slowing schemes. *Physical Review A*, 98(6), 2018. doi: 10.1103/physreva.98.063408.

[138] Qian Liang, Wenhao Bu, Yuhe Zhang, Tao Chen, and Bo Yan. A general Zeeman slower for type-ii transitions and polar molecules. 2019.

[139] E. L. Raab, M. Prentiss, Alex Cable, Steven Chu, and D. E. Pritchard. Trapping of neutral sodium atoms with radiation pressure. *Physical Review Letters*, 59(23), 1987. doi: 10.1103/physrevlett.59.2631.

[140] C.J. Foot. *Atomic Physics.* Oxford University Press, 2004. ISBN 0198506961.

[141] K. N. Jarvis, J. A. Devlin, T. E. Wall, B. E. Sauer, and M. R. Tarbutt. Blue-detuned magneto-optical trap. *Physical Review Letters*, 120(8), 2018. doi: 10.1103/physrevlett.120.083201.

[142] Matthew Harvey and Andrew James Murray. Cold atom trap with zero residual magnetic field: The ac magneto-optical trap. *Physical Review Letters*, 101(17), 2008. doi: 10.1103/physrevlett.101.173201.

[143] A. Collopy, M. Hummon, M. Yeo, B. Stuhl, B. Hemmerling, G. Drayna, E. Chae, A. Ravi, H.-I. Lu, J. Doyle, and J. Ye. Towards a 3-D magneto-optical trap for molecules. In *APS Division of Atomic, Molecular and Optical Physics Meeting Abstracts*, 2013.

[144] M. R. Tarbutt and T. C. Steimle. Modeling magneto-optical trapping of CaF molecules. *Physical Review A*, 92(5), 2015. doi: 10.1103/physreva.92.053401.

[145] M R Tarbutt. Magneto-optical trapping forces for atoms and molecules with complex level structures. *New Journal of Physics*, 17(1), 2015. doi: 10.1088/1367-2630/17/1/015007.

[146] Eric B. Norrgard. *Magneto-optical trapping of diatomic molecules.* PhD thesis, Yale University, 2006.

[147] John F Barry. *Laser cooling and slowing of a diatomic molecule.* PhD thesis, Yale University, 2013.

[148] D. A. Kleinman, A. Ashkin, and G. D. Boyd. Second-harmonic generation of light by focused laser beams. *Physical Review*, 145(1), 1966. doi: 10.1103/physrev.145.338.

[149] Eryn C. Cook, Paul J. Martin, Tobias L. Brown-Heft, Jeffrey C. Garman, and Daniel A. Steck. High passive-stability diode-laser design for use in atomic-physics experiments. *Review of Scientific Instruments*, 83(4), 2012. doi: 10.1063/1.3698003.

[150] J. Dalibard and C. Cohen-Tannoudji. Laser cooling below the doppler limit by polarization gradients: simple theoretical models. *Journal of the Optical Society of America B*, 6(11), 1989. doi: 10.1364/josab.6.002023.

[151] D. Boiron, A. Michaud, P. Lemonde, Y. Castin, C. Salomon, S. Weyers, K. Szymaniec, L. Cognet, and A. Clairon. Laser cooling of cesium atoms in gray optical molasses down to 1.1 uk. *Physical Review A*, 53(6), 1996. doi: 10.1103/physreva.53.r3734.

[152] G Grynberg and J.-Y Courtois. Proposal for a magneto-optical lattice for trapping atoms in nearly-dark states. *Europhysics Letters (EPL)*, 27(1), 1994. doi: 10.1209/0295-5075/27/1/008.

[153] D. Rio Fernandes, F. Sievers, N. Kretzschmar, S. Wu, C. Salomon, and F. Chevy. Sub-doppler laser cooling of fermionic40k atoms in three-dimensional gray optical molasses. *EPL (Europhysics Letters)*, 100(6), 2012. doi: 10.1209/0295-5075/100/63001.

[154] Franz Sievers, Norman Kretzschmar, Diogo Rio Fernandes, Daniel Suchet, Michael Rabinovic, Saijun Wu, Colin V. Parker, Lev Khaykovich, Christophe Salomon, and Frédéric Chevy. Simultaneous sub-doppler laser cooling of fermionic Li6 and k40 on the D1 line: Theory and experiment. *Physical Review A*, 91(2), 2015. doi: 10.1103/physreva.91.023426.

[155] J A Devlin and M R Tarbutt. Three-dimensional doppler, polarization-gradient, and magneto-optical forces for atoms and molecules with dark states. *New Journal of Physics*, 18(12), 2016. doi: 10.1088/1367-2630/18/12/123017.

[156] M Weidemüller, T Esslinger, M. A Ol'shanii, A Hemmerich, and T. W Hänsch. A novel scheme for efficient cooling below the photon recoil limit. *Europhysics Letters (EPL)*, 27(2), 1994. doi: 10.1209/0295-5075/27/2/006.

[157] A. Aspect, E. Arimondo, R. Kaiser, N. Vansteenkiste, and C. Cohen-Tannoudji. Laser cooling below the one-photon recoil energy by velocity-selective coherent population trapping. *Physical Review Letters*, 61(7), 1988. doi: 10.1103/physrevlett.61.826.

[158] Andrew T. Grier, Igor Ferrier-Barbut, Benno S. Rem, Marion Delehaye, Lev Khaykovich, Frédéric Chevy, and Christophe Salomon. Λ-enhanced sub-doppler cooling of lithium atoms in d1 gray molasses. *Physical Review A*, 2013. doi: 10.1103/PhysRevA.87.063411.

[159] Giacomo Colzi, Gianmaria Durastante, Eleonora Fava, Simone Serafini, Giacomo Lamporesi, and Gabriele Ferrari. Sub-doppler cooling of sodium atoms in gray molasses. *Physical Review A*, 93(2), 2016. doi: 10.1103/physreva.93.023421.

[160] Alban Urvoy, Zachary Vendeiro, Joshua Ramette, Albert Adiyatullin, and Vladan Vuletić. Direct laser cooling to Bose-Einstein condensation in a dipole trap. *Physical Review Letters*, 122 (20), 2019. doi: 10.1103/physrevlett.122.203202.

[161] Xiao Zhang, Yang Chen, Jianxiong Fang, Tishuo Wang, Jiaming Li, and Le Luo. Beam pointing stabilization of an acousto-optic modulator with thermal control. *Optics Express*, 27(8), 2019. doi: 10.1364/oe.27.011503.

[162] A. Mazurenko, S. Blatt, F. Huber, M. F. Parsons, C. S. Chiu, G. Ji, D. Greif, and M. Greiner. Implementation of a stable, high-power optical lattice for quantum gas microscopy. *Review of Scientific Instruments*, 90(3), 2019. doi: 10.1063/1.5066623.

[163] T. A. Savard, K. M. O'Hara, and J. E. Thomas. Laser-noise-induced heating in far-off resonance optical traps. *Physical Review A*, 56(2), 1997. doi: 10.1103/physreva.56.r1095.

[164] Roman V. Krems. *Molecules in Electromagnetic Fields*. John Wiley & Sons, Inc., 2018. doi: 10.1002/9781119382638.

[165] Lawrence Cheuk. Private communication.

[166] L. R. Liu, J. D. Hood, Y. Yu, J. T. Zhang, N. R. Hutzler, T. Rosenband, and K.-K. Ni. Building one molecule from a reservoir of two atoms. *Science*, 360(6391), 2018. doi: 10.1126/science.aar7797.

[167] Wenwen Zhang and Qian Chen. Signal-to-noise ratio performance comparison of electron multiplying CCD and intensified CCD detectors. In *2009 International Conference on Image Analysis and Signal Processing*. IEEE, 2009. doi: 10.1109/iasp.2009.5054588.

[168] Leon K. Harding, Richard T. Demers, Michael Hoenk, Pavani Peddada, Bijan Nemati, Michael Cherng, Darren Michaels, Leo S. Neat, Anthony Loc, Nathan Bush, David Hall, Neil Murray, Jason Gow, Ross Burgon, Andrew Holland, Alice Reinheimer, Paul R. Jorden, and Douglas Jordan. Technology advancement of the CCD201-20 EMCCD for the WFIRST coronagraph instrument: sensor characterization and radiation damage. *Journal of Astronomical Telescopes, Instruments, and Systems*, 2(1), 2015. doi: 10.1117/1.jatis.2.1.011007.

[169] Clinton Reed Brome. *Magnetic Trapping of Ultracold Neutrons*. PhD thesis, Harvard University, 2000.

[170] Goulven Quéméner. Ultracold collisions of molecules. 2017.

[171] Dalibard J. Collisional dynamics of ultra-cold atomic gases. *Proceedings of the International School of Physics; Enrico Fermi*, 140(Bose-Einstein Condensation in Atomic Gases), 1999. ISSN 0074-784X. doi: 10.3254/978-1-61499-225-7-321.

[172] Eugene P. Wigner. On the behavior of cross sections near thresholds. *Physical Review*, 73(9), 1948. doi: 10.1103/physrev.73.1002.

[173] James F. E. Croft and John L. Bohn. Long-lived complexes and chaos in ultracold molecular collisions. *Physical Review A*, 89(1), 2014. doi: 10.1103/physreva.89.012714.

[174] Nicolas Schlosser, Georges Reymond, Igor Protsenko, and Philippe Grangier. Sub-poissonian loading of single atoms in a microscopic dipole trap. *Nature*, 411(6841), 2001. doi: 10.1038/35082512.

[175] Michael Mayle, Brandon P. Ruzic, and John L. Bohn. Statistical aspects of ultracold resonant scattering. *Physical Review A*, 85(6), 2012. doi: 10.1103/physreva.85.062712.

[176] Michael Mayle, Goulven Quéméner, Brandon P. Ruzic, and John L. Bohn. Scattering of ultracold molecules in the highly resonant regime. *Physical Review A*, 87(1), 2013. doi: 10.1103/physreva.87.012709.

[177] Arthur Christianen, Martin W. Zwierlein, Gerrit C. Groenenboom, and Tijs Karman. Photoinduced two-body loss of ultracold molecules. *Physical Review Letters*, 123(12), 2019. doi: 10.1103/physrevlett.123.123402.

[178] Tijs Karman and Jeremy M. Hutson. Microwave shielding of ultracold polar molecules. *Physical Review Letters*, 121(16), 2018. doi: 10.1103/physrevlett.121.163401.

[179] Tijs Karman and Jeremy M. Hutson. Microwave shielding of ultracold polar molecules with imperfectly circular polarization.

[180] Cheng Chin, Rudolf Grimm, Paul Julienne, and Eite Tiesinga. Feshbach resonances in ultracold gases. *Reviews of Modern Physics*, 82(2), 2010. doi: 10.1103/revmodphys.82.1225.

[181] Alisdair O. G. Wallis and Roman V. Krems. Magnetic feshbach resonances in collisions of non-magnetic closed-shell $^1\Sigma$ molecules. *Physical Review A*, 2012. doi: 10.1103/PhysRevA.89.032716.

[182] Bo Yan, Steven A. Moses, Bryce Gadway, Jacob P. Covey, Kaden R. A. Hazzard, Ana Maria Rey, Deborah S. Jin, and Jun Ye. Observation of dipolar spin-exchange interactions with lattice-confined polar molecules. *Nature*, 501(7468), 2013. doi: 10.1038/nature12483.

[183] Vladan Vuletić, Cheng Chin, Andrew J. Kerman, and Steven Chu. Degenerate raman sideband cooling of trapped cesium atoms at very high atomic densities. *Physical Review Letters*, 81(26), 1998. doi: 10.1103/physrevlett.81.5768.

[184] Eric Charron, Pérola Milman, Arne Keller, and Osman Atabek. Quantum phase gate and controlled entanglement with polar molecules. *Physical Review A*, 75(3), 2007. doi: 10.1103/physreva.75.033414.

[185] Chaohong Lee and Elena A. Ostrovskaya. Quantum computation with diatomic bits in optical lattices. *Physical Review A*, 72(6), 2005. doi: 10.1103/physreva.72.062321.

[186] M. Saffman and T. G. Walker. Analysis of a quantum logic device based on dipole-dipole interactions of optically trapped rydberg atoms. *Physical Review A*, 72(2), 2005. doi: 10.1103/physreva.72.022347.

[187] Alexander Franzen. Multiple figures employ diagrams from the gwoptics componentlibrary.

[188] Leonid A. Kaledin, Jonathan C. Bloch, Michael C. McCarthy, and Robert W. Field. Analysis and deperturbation of the A2Π and B2Σ+ states of CaF. *Journal of Molecular Spectroscopy*, 197(2), 1999. ISSN 0022-2852. doi: https://doi.org/10.1006/jmsp.1999.7909.

[189] J Verges, C Effantin, A Bernard, A Topouzkhanian, A R Allouche, J d'Incan, and R F Barrow. The b $^2\delta$ state of CaF. *Journal of Physics B: Atomic, Molecular and Optical Physics*, 26(2), 1993. doi: 10.1088/0953-4075/26/2/011.

[190] S. Raouafi, G.-H. Jeung, and Ch. Jungen. Permanent and transition dipole moments in CaF and CaCl. *The Journal of Chemical Physics*, 115(16), 2001. doi: 10.1063/1.1405118.

[191] Stephen R. Langhoff, Charles W. Bauschlicher, Harry Partridge, and Reinhart Ahlrichs. Theoretical study of the dipole moments of selected alkaline-earth halides. *The Journal of Chemical Physics*, 84(9), 1986. doi: 10.1063/1.450651.

[192] W. J. Childs, L. S. Goodman, U. Nielsen, and V. Pfeufer. Electric-dipole moment of caf (x 2Σ+) by molecular beam, laser-rf, double-resonance study of stark splittings. *The Journal of Chemical Physics*, 80(6), 1984. doi: 10.1063/1.447005.

[193] Ester K. Halse. Polarization properties of He-Ne-lasers. *Optics Communications*, 31(2), 1979. doi: 10.1016/0030-4018(79)90305-5.

[194] D. Lenstra and G.C. Herman. Saturation-induced polarization preferences in two-mode oscillating gas lasers. *Physica B C*, 95(3), 1978. doi: 10.1016/0378-4363(78)90062-1.

[195] E. B. Norrgard, N. Sitaraman, J. F. Barry, D. J. McCarron, M. H. Steinecker, and D. DeMille. In-vacuum scattered light reduction with black cupric oxide surfaces for sensitive fluorescence detection. *Review of Scientific Instruments*, 87(5), 2016. doi: 10.1063/1.4949503.

[196] Fritz Peter Schäfer, editor. *Dye Lasers*. Springer Berlin Heidelberg, 1973. doi: 10.1007/978-3-662-11579-4.

[197] Lee W. Casperson, W. J. Sandle, A. C. Wilson, D. M. Warrington, and R. J. Ballagh. Pump polarization effects in cw dye lasers. *Journal of Applied Physics*, 69(12), 1991. doi: 10.1063/1. 347496.